The University of Strathclyde

Glasgow

Department of Mechanical & Aerospace Engineering

The Development of an Integrated Modelling Framework to Aid with the Design of Endovascular Devices

Martin van Zyl

A thesis in fulfilment of the requirements for the degree of Doctor of Philosophy

2015

Copyright statement

Acknowledgements

I would like to start by thanking Dr William Dempster and Prof David Nash for their supervision, patience and guidance. It was a privilege to be part of the dynamic research team created by these two inspirational individuals.

I would then like to thank Terumo Vascutek for part funding this project. A special thanks to Mr Tim Ashton and Mr David Stevenson whose trust in the academic process allowed for continuous industry support.

Within the University of Strathclyde, I would like to thank Dr Phil Riches for his supervision over all bioengineering aspects of this project. Without his support, large sections of this thesis would not have been feasible. I would also like to thank my academic colleagues Alan Jappy, Lewis Brown, James Ure and Peter Jenkins for their advice and friendship.

Finally I would like to convey a special thanks to my mother, Lizette van Zyl. Without her continuous love, support and motivation this body of work would not have been possible.

Abstract

In product design environments where safety is critical, industries can often be reluctant to adopt emerging technologies. This is the case for many endovascular device manufacturers, where advanced non-linear Finite Element Analysis methods are still to be incorporated into their product design functions. To encourage adoption this thesis explores the merits and limitations of newly developed constitutive models as implemented into leading numerical analysis software suites. Specific attention is given to the Holzapfel soft tissue and Auricchio Nitinol constitutive models.

Limitations and merits are explored through the development of an integrated modelling framework. This framework was constructed around a case study for which Vascutek's Anaconda^{TM} stent graft system was chosen. In its final iteration the framework took the form of a series of python scripts which could be imported into Abaqus 6.11 to generate a variety of FE studies.

For the development of the python scripts, a generalised artery material model was required for which a vascular characterisation programme was initiated. This programme mechanically characterised three human abdominal aortas using uniaxial and biaxial characterisation methods. By deploying Anaconda proximal ring devices within cadaver specimens and recording deformations, the programme produced detailed out-of-plane deformation data for vascular tissue. Where possible, results obtained were combined with those found in the academic literature. From this, comprehensive data sets were created from which a generalised mechanical description for the abdominal aorta was proposed. In this study, the accuracy of such a generalised arterial description was also explored for the first time.

The work herein present a range of advanced Finite Element modelling techniques. These techniques range from a bespoke three layered abdominal aorta arterial model to novel wire bundle modelling methods. A comprehensive study into Nitinol's load path dependency effects is also presented. The study correlated the

effect as captured within experimental results against those predicted by Finite Element Analysis. Findings of this study highlight limitations within the Auricchio constitutive model as implemented into Abaqus 6.11 and emphasise the need to model the entire loading regime when conducting Finite Element studies.

The extensive validation procedures used to determine the accuracy of the integrated modelling framework are presented. It is shown for the case study chosen, that the framework is capable of capturing a range of complex device-artery interactions. It is also shown that the model is capable of predicting deformations within 35% of that measured during device deployment and cadaver specimen pressure-inflation experiments.

It is a conclusion of this thesis, that from an understanding of the limitations involved, current FE technologies could be feasibly integrated into product design methodologies through the development of robust, computationally efficient design tools.

Foreword

This study follows a thesis completed by Dr Emma McCummiskey for the fulfilment of a PhD degree. It continues and expands upon the work presented within her thesis with the aim of addressing realistic artery simulations.

Contents

Nomenclature

AAA	-	Abdominal Aortic Aneurysm
ABT	-	Abdominal Test
CAD	-	Computer Aided Design
COF	-	Chronic Outward Force
DVE	-	Digital Video Extensometer
EVAR	-	Endovascular Aneurysm Repair
FDA	-	Food and Drug Administration
FE	-	Finite Element
FEA	-	Finite Element Analysis
NHS	-	National Health Service
NL FEA	-	Nonlinear Finite Element Analysis
LPD	-	Load Path Dependency/Dependant
ISO	-	International Organization for Standards
IMA	-	Inferior Mesenteric Artery
SMA	-	Superior Mesenteric Artery
RRF	-	Radial Resistive Force

1.0 Introduction

Medically, aneurysms are defined as a dilation of the arterial vessel wall due to localised weakening. They are often asymptomatic, in many cases going undetected. If left untreated aneurysms can rupture, resulting in disability or death. Aneurysms are common in the western world with smoking, hypertension and poor diet being factors thought to contribute to their development. Their serious nature and commonality results in 12,000 related deaths each year in the UK [1].

Of these 12,000 deaths, approximately 6,000 are attributed to Abdominal Aortic Aneurysm (AAA). In developed countries, AAA's occur in approximately 6% of men and 1% of women aged over 65 [2]. Rupture of AAA's can lead to severe pain, tachycardia, hypotension, poor perfusion, loss of consciousness and in many cases rapid death. The high mortality rates associated with AAA rupture results in 2% of all male deaths in the UK [3].

Within the UK's National Health Service (NHS), a monitoring programme is normally initiated once a developing AAA has been detected. During this monitoring programme aneurysm growth is monitored until an unacceptable size is reached or symptoms develop. For abdominal aneurysms, an arterial diameter of between 5 to 5.5 cm is generally regarded as the stage at which intervention is required [4].

Once intervention is required, there are two methods of treatment; open surgical and endovascular repair. Open surgical repair has historically been the treatment of choice, with the first documented procedure in 1951 [5]. Since then, open repair procedures have remained relatively unchanged with cross clamping of the aorta, removal of the affected region, and the insertion of a knitted graft to replace the removed section [6]. This surgical technique is complex and traumatic to the human body due its invasive nature. Records indicate that in 2004, the 30-day mortality rates for open surgery were approximately 4.7% [1].

Compared against open surgery, endovascular repair is a relatively modern method of AAA intervention. The first documented procedure was conducted by Parodi in 1991 [7]. Since then the fundamentals of Endovascular Aneurysm Repair (EVAR) has remained largely unchanged, with the insertion of a modular woven bifurcated graft which acts as a conduit for blood flow outlining the procedure. In most cases, the endovascular device is implanted through a small incision in both femoral arteries, using a sheath and catheter system to manoeuvre the device in place. As a minimally invasive procedure, live x-ray guidance is used for identification of the aneurysm and positioning of the device. The procedure can often be administered under spinal, epidural or simply local anaesthesia.

Patient suitability for EVAR is normally assessed by a specialist based on patient anatomy and risk factors which include cardiac, pulmonary and renal status [8]. With the current state of EVAR, 50 to 60% of patients can be treated by endovascular means [8], although these figures are subject to constant change due to developments within the field.

Neither open nor endovascular surgery have been definitively proven to be superior. When looking at post four year recovery rates, several studies have shown similar all-cause mortality rates between the two methods [9], [10]. Whilst endovascular surgery has a shorter post-operation recovery period, re-intervention rates for this treatment tend to be higher. With both open surgery and EVAR procedures carrying merit and associated risks, the choice of treatment is patient specific to be determined by a specialist.

In the case that a vascular surgeon elects for endovascular treatment for an AAA, a variety of endovascular devices are available. These devices are manufactured by a host of medical device companies situated in various countries. Current EVAR device manufacturing leaders within Britain are Cook Medical, Medtronic and Terumo Vascutek. In this study, an EVAR device offered by Terumo Vascutek will be examined in detail.

For the design of their products, Vascutek uses classic design methodologies rooted largely in experimental based procedures. These methods tend to be supported by empirical data and rigorous validation procedures. Although time consuming, endovascular device manufacturers often prefer proven design methodologies, due to the safety critical nature of their products. This can hamper the adoption of modern CAD techniques, a problem reinforced by the highly complex nature of the materials involved.

To further encourage adoptions of CAD techniques, academic research groups have worked on producing improved vascular tissue constitutive models over the last decade. Due to the progress made, these advanced constitutive models have recently become commercially available within leading FEA suites. This has brought with it the opportunity to implement these technologies within endovascular product design.

Although improved constitutive models are now available, reluctance to adopt new methods still remains within the industry [11]. This reluctance will remain until such time the merits and limitations of emerging technologies are clearly defined through an independent assessment. To carry out such an assessment, the project presented herein was created. It was the aim of this project to investigate the use of emerging technologies in the field of numerical analysis for the design of future endovascular devices. This assessment was conducted around a case study, for which the Terumo Vascutek Anaconda^{TM} device was chosen. The Anaconda device is a successful EVAR device which have been used in over 17,000 treatments with a 94% procedural success rate according to clinical trials [12] .

The study was conducted through the development of an integrated modelling framework which could be used to study the interactions between the Anaconda^{TM} and an arterial wall. In its final iteration, the framework was in the form of a series of python scripts. The scripts could be imported into Abaqus 6.11 in a prescribed manner to generate a variety of FE studies. The FE model created by the framework focussed on the simulation of three critical stages of the Anaconda's life cycle being;

The forming stage of the proximal ring during which key manufacturing steps were captured; a device compaction stage during which the proximal ring is compacted into sheath-like diameters; and a deployment stage during which the device is deployed into a simulated arterial vessel. Once deployed the device could be subjected to the cardiac cycle from which key strain-stress data could be obtained.

1.1 The Anaconda™

The Anaconda device received CE certification in April 2004 and has since become a popular choice for endovascular surgeons. Since certification it has gone through six commercially available design generations. Although much has changed since 2004 and product variations exist, the basic design principles have remained broadly unchanged. The device is comprised of three components being a bifurcated main body into which two legs are coupled (Figure 1.1). Each of these three components consists of a super-elastic Nitinol scaffold onto which knitted polyester graft fabric is sutured. The skeleton consists of an intricate pattern of wire strands and bundles. Key to the performance of the device is the skeleton's ability to allow for compaction into a catheter, remote deployment, device anchorage and adequate sealing of the aneurysm sacs whilst accommodating cardiac compliance. The skeleton, therefore, dictates much of the mechanical characteristics of the device whilst the polyester graft acts as a conduit for blood flow.

The Anaconda is available in a range of sizes to provide the best patient specific fit possible. A total of eight body sizes are available, enabling treatment of an aortic diameter range of 16 mm to 32 mm. Further customization through a number of leg sizes and configurations are available.
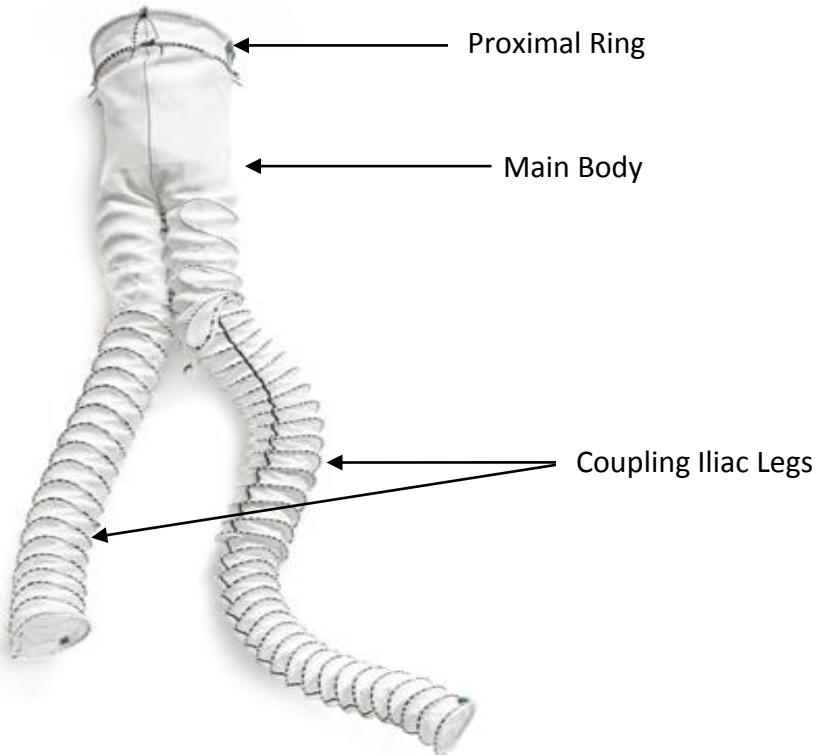
Figure 1.1: **The Anaconda device manufactured by Terumo Vascutek.**

A number of engineering challenges have to be considered when designing endovascular devices. For the Anaconda stent graft device, primary considerations are that of strength and fatigue characteristics, which must be balanced against the functional requirement of sealing. To meet the design requirements, a property referred to as "oversize" is carefully considered per patient. The property of "oversize" refers to various elements of the Anaconda but essentially refers to the proximal ring having a nominal diameter larger than the artery into which it is delivered. Through this, when deployed within the vessel, the device applies a radial force to the surrounding tissue. This outward force is crucial to the device's overall performance and is strongly linked to the diameter ratio between the vessel and device. If the device's outward force is too low, conditions such as a type 1 endoleak or stent migration can occur [13]. If, however, the radial force is too high, the device could damage the vessel.

In addition to the proximal ring's wire diameter, oversizing also influences the mean strain a device experiences *in situ*. The device's stiffness in turn, dictates its

compliance to the cardiac cycle, and through this, dictates the strain amplitude it experiences. These two elements of mean strain and strain amplitude are then strongly related to the device's fatigue life, which must be optimised per patient to meet regulatory standards. ISO 25539-1 dictates that the device should have a minimum life span of ten years which corresponds to a minimum of 400 million cycles. The need for any new design iteration of the Anaconda to comply with ISO 25539-1 can result in experimental methods being slow and impractical. FE methods provide the opportunity of an efficient preliminary assessment of new designs, by allowing detailed strain and stress calculations to be compared against fatigue performance data. In addition to this, for current design iterations, radial force estimations can be produced for combinations of ring diameter, wire diameter and number of wire turns, in simulations using patient-specific geometry. This data has the potential to be used by design engineers to reduce the size of the Anaconda device which could allow a broader spectrum of patients to be treated, many of whom are currently rejected due to risk factors associated with the size of the catheter required for device delivery. For these reasons, an Integrated Modelling Framework, which can be used to effectively assess device combinations and explore new designs, has significant value.

1.2 Research goals and objectives

The principal goal of this project was to assess current constitutive and FE capabilities for the use in the design process of endovascular devices. The motivation for this assessment came from the rapid advance in the constitutive modelling of soft tissue and Nitinol over the last decade. Further incentive came from advantages a FE capability could bring into the proposed context.

As an additional goal, the research project aimed to contribute to the growing number of data sets available for vascular tissue material model development. Areas within vascular tissue characterisation requiring further study were to be highlighted through an extensive literature review. Once highlighted, areas were to be addressed through a dedicated experimental programme.

In addition to furthering knowledge within the field of soft tissue characterisation, the project had the goal of furthering knowledge of Nitinol FE modelling. Novel modelling techniques were to be proposed for the modelling of endovascular products constructed from the alloy.

Objectives of this body of work could be stipulated as follows:

- Development of a reliable and computationally efficient integrated modelling framework.
    - This project was to build upon previous studies to move towards the development of an endovascular device product design tool.
    - During development of the integrated modelling framework, focus was to be placed on the efficiency of FEA simulations. Efforts were to be made to reduce computational expense without a compromise on simulation accuracy.
    - The framework was to be robust, being able to successfully solve for the entire design envelope of the Anaconda device.
    - The framework was to have quantified levels of accuracy determined through rigorous validation procedures.
- Explore the use of an arterial constitutive model formulated around the micromechanics of arterial tissue for use in the framework.
    - The framework was to include a generalised arterial model based on the typical patient age at which AAA intervention is required.
    - Material models developed through this project were to be validated.
- Limitations of current Nitinol constitutive modelling were to be explored
    - A FEA investigation into Nitinol load history effects were to be conducted.
    - Novel Finite Element modelling techniques were to be suggested for wire bundle representation.

1.3 Thesis structure

A complexity of this project was the broad range of topics which were to be addressed in unison. With this in mind, chapter 2 is dedicated to a broad and comprehensive literature review. The review initially covers the endovascular repair of aneurysms and studies relevant to the one presented herein. The subjects of Nitinol and Vascular tissue are then addressed in turn, focussing on the micromechanics, mechanics and FE modelling of each.

With the literature review presented, chapter 3 presents the vascular tissue characterisation programme. As characterisation activities were imperative to the overall accuracy of the integrated modelling framework developed, emphasis is placed on the experimental techniques and experimental equipment used. Experimental results are presented per specimen before being collated and compared against relevant data obtained from the literature.

Chapter 4 addresses the development of the integrated modelling framework. The framework is presented in its final form with the various iterations leading to its final form omitted for conciseness. Data fitting procedures required for the development of material models are also presented within this chapter.

Chapter 5 presents work conducted to validate the framework. Validation procedures focussed on the comparison of FE predictions against experimental results. Where possible, comparisons against analytical solutions were also made.

With the validation work presented, focus in chapter 6 turns towards Finite Element studies conducted using the framework created. The first of these is a relevant study into Nitinol's load history dependency effects, a study during which its impact on design is clarified. The chapter is concluded with an investigation into the limitations and merits of a generalised soft tissue model.

Chapter 7 will conclude the present work through a discussion on the suitability of FE within the proposed context. This discussion draws from the multitude of studies conducted during this research project and through this, identify its novelty. The

contributions made to the academic field will also be clearly identified. Finally, recommendations for further study will be made before closing remarks are given.

An outline of the thesis is provided in figure 1.2.

Chapter 1: Research goals and objectives are introduced and motivation is provided.

Chapter 2: A Literature review is presented highlighting current research gaps.

Chapter 3: An experimental programme is completed to establish material modelling and validation data using human aortic specimens.

Chapter 4: The framework is developed using data obtained from the experimental programme.

Chapter 5: The design tool is validated and its merits and limitations explored.

Chapter 6: FEA studies are completed using the developed tool and novel modelling methodologies are proposed.

Chapter 7: Thesis conclusions are provided.

Figure 1.2: **Schematic representation of this thesis's structure**

2.0 Literature review

The FE simulation of endovascular devices and their interaction with the arterial wall combines a broad range of complex academic fields. A thorough literature review was therefore required, the main findings of which are presented in this chapter.

Within the review knowledge gaps are first identified through assessing published literature. The review then focuses on aspects of endovascular device design, Nitinol and vascular tissue mechanics. Each of these topics are addressed in detail, providing background to studies presented in following chapters.

2.1 Numerical modelling of device-artery interactions

When conducting the literature review, a lack of studies was found which considered stent-graft interactions with the arterial wall. This finding was not unique, with a recent publication in the Journal of Endovascular Therapy stating; "Published reports on simulation of the mechanical behaviour of stent-graft are almost non-existent" [11]. Another finding by the current author, which was supported by this publication, is that the studies which are available through published literature, are often subject to severe simplifications regarding their representation of the arterial wall. The lack of published studies on stent-graft interactions highlights knowledge gaps in device-artery deformation data and the need for accurate computational frameworks to conduct such studies.

Recognising the knowledge gap which exists, a report published in 2015 by Perrin *et al.,*[14] examined the interactions between a stent constructed from Nitinol and a hyper-elastic arterial model. Although clearly driven by the same academic questions as the current work, no statements of simulation accuracy were provided within the published study. Crucially, the model created within the publication was never validated. To this extent, the publication only demonstrates that a FE solution is possible when conducting these complicated studies. Furthermore, the arterial model used within the publication does not address the multi-layered nature of the

arterial wall and is based on a Mooney-Rivlin constitutive model, a purely phenomenological formulation. To the present work, comments on the feasibility of FEA within the endovascular device design process can only be made after having explored the accuracy of the simulations conducted.

A report published in 2013 which produced a comprehensive, three layered arterial model with patient specific geometry, considered the deformations imparted onto the arterial system when catheter-like devices are inserted into the lumen [15]. As a conclusion of this work, the suitability of using FE analysis to preoperatively identify patient specific procedure risks was supported. As a framework which was also to some extent validated, the study is a valuable contribution to the academic field of endovascular device design. With relation to the present study, the publication, however, focussed on catheter systems and the macroscopic deformation of the arterial system. The work herein is in contrast focussed on localised effects and stent-graft devices.

A peer reviewed article which provides a good summation of the current state (up to 2012) of stent-graft numerical analysis is a publication by Roy *et al.,* [16]. The publication summarises and praises the advances made in constitutive modelling over the last decade, yet calls for realistic stent-graft models to be created to improve design. The article specifically calls for more attention to be given to the device-artery anchoring locations, suggesting that interactions at these locations are still poorly understood. The knowledge gaps identified within this paper is central to the present study.

A number of studies were found which aimed at determining the behaviour of coronary stents *in situ* [17]–[20]. In most of these, the object of the study was to investigate wall stresses. In this context, contact forces between endovascular devices and arterial wall is well addressed due to its relevance to restenosis [21]. Overall, however, it was found that a limited number of these publications attempted an accurate arterial model based on human arterial data. Those who had, such as Lally *et al.,* [18], commonly used 316L stainless steel as the alloy in

question. The work herein is differentiated by its focus on graft-stent devices manufactured from super-elastic alloys and their interactions with the arterial wall represented by a layer specific, hyper-elastic arterial model.

A study which has attempted a validated hyper-elastic arterial model is a publication by Brand *et al.,* [22]. Within this study an Ogden hyper-elastic arterial model was used in an attempt to investigate stent/artery interactions. The object of the research was again to ascertain the wall stresses induced by stents for the purpose of investigating restenosis pathology. Although relevant, linear material models were used in device representations.

Pelton *et al.* conducted a study into the NLFEA modelling of Nitinol medical devices [23]. The study confirms that FE can produce agreeable results to that measured in experiment when testing Nitinol specimens of different A_f temperatures at 37$^{\text{o}}$C. The study also confirms that FEA can adequately predict force displacement results of Nitinol diamond-shape fatigue specimens. Although a valuable contribution, the study did not address stent/artery interactions. This omission is central to the work presented within this thesis.

The work presented herein follows a study conducted by McCummiskey *et al.,* [24]. Within the study McCummiskey addressed the development of a product design tool around the Anaconda device as a case study. The study laid a foundation for the modelling of the Anaconda device but was unfortunately subject to several limitations. Foremost of these limitations were:

- The tool was computationally expensive. This made the tool impractical for commercial implementation.
- The Device/Artery model employed a silicone material model to simulate the behaviour of the artery. This was seen as a significant limitation with speculative accuracy.
- The model suffered from robustness issues, with the complex contact conditions resulting in element distortion and contact surface penetrations.

- Problematic boundary conditions resulted in reduced accuracies.
- The tool was inflexible, modelling a single deployment case.

In spite of these limitations, a reliable approach was established. Since the submission of the thesis in 2008, further developments within the field of FEA have brought forward the opportunity to address limitations through the work presented herein.

2.2 The use of Nitinol in endovascular devices

Nitinol is a so-called "super-elastic" alloy, capable of elastic strains of up to 8%. This ability to cope with large strains has resulted in Nitinol being increasingly used in medical applications where large scale deformations are likely to occur [25]. Common applications include products deployed through minimally invasive procedures and endovascular devices which are prone to *in situ* crushing [26]. Consequently, although general in nature, the findings of this thesis are especially relevant to the growing number of endovascular devices with Nitinol incorporated into their design [27].

The most common endovascular device is the stent which has been used for vascular intervention since 1960 [28]. Stents were initially commonly manufactured from stainless steel with Nitinol variations appearing in the early 1990s. Early applications of endovascular devices were limited to the treatment of stenosis which is still a common medical procedure. Since the advent of the stent in the 1960's the approach has improved dramatically with modern drug eluting stents becoming common [29], [30]. Stent grafts, the sub category under which the Anaconda is placed, were eventually used for the first time in 1991 for the treatment of an aortic aneurysm [28].

Within 10 years of the first endovascular stent graft treatment, a further 11 FDA approved stent graft devices were available on the market in the United States alone [26]. Most of these had Nitinol incorporated into their design. First generation devices commonly had an intent-to-treat success ratio of up to 93.8% [13]. As is still

the case with modern generations, early failures were mostly attributed to type 1 endoleaks, emphasising the importance of adequate sealing of the devices [31].

Nitinol possesses a wide range of unique mechanical properties which makes it remarkably well suited for use in a variety of endovascular devices. A distinctive feature of Nitinol is its stress-strain hysteresis which is characterised by pronounced upper and lower stress plateaus. Product design engineers have found that through correct design and delivery procedures, medical devices can be made to operate on the lower plateau of the stress-strain curve [27]. As the nominal stress states at which the plateaus are encountered can be controlled by material processing techniques, engineers are able to control the force that stents exert on the vessel wall. The exceptionally large strain range over which the plateaus exist also entails that the stent can easily cope with variable *in situ* conditions whilst still applying the same predicted force on the vessel wall. This feature, often referred to as the Chronic Outward Force (COF) [24], [32], provides immense consistency for designers and provides reassurance for medical practitioners on crucial matters such as the sealing properties of devices.

Accompanying Nitinol's COF is another favourable property referred to as the radial resistive force (RRF). The RRF property refers to the tendency of Nitinol specimens, operating on the lower plateau, to resist further loading through another linear modulus. This modulus is approximately equal in magnitude to that of the first linear modulus and aims to return the specimen to the upper plateau. Through this characteristic, stents can be thought to have a biased stiffness, exerting a force according to its COF, yet resist further deformation by the vessel wall through a greater RRF.

Further endovascular medical products that have made use of Nitinol's unique mechanical properties include vena cava filters which are used to prevent pulmonary emboli [33]. Nitinol based occlusion devices have also become more popular in recent years, a trend driven by the opportunity for simplified delivery procedures [27]. The number of endovascular devices continues to grow with a host

of devices already available. Amongst others, current leaders within the field of endovascular device design are Boston Scientific, Cook Medical and Terumo Vascutek.

Nitinol has been used to make guidewires for the deployment of catheters since the 1980's [8]. Its superior performance in this application is largely thanks to its excellent kink resistance and flexibility which provides advantages over stainless steel and titanium. Nitinol's kink resistance is attributed to its super-elastic properties and idiosyncrasies associated with its stress-strain curve. It can be shown that continual loading beyond the upper plateau results in another elastic region, where the modulus increases dramatically until slip and limit load are incurred. Through this property kinks are resisted through a more uniformly spread strain distribution [27]. Nitinol's kink resistance has also provided further grounds for its use in stent manufacturing where there is a perceived risk that once implanted the stent could become deformed through externally applied forces. Lastly, Nitinol's kink resistance has made it exceptionally suitable for the use in Homer Mammalok devices, organ retrieval systems, snares and embolic protection devices [34].

Further non-endovascular medical applications are bone staples, spinal cages, suture anchors, heart valve sizers and flexible micrograspers [35]. Non-medical applications range from spectacle frames to under wires for bras. All of these applications make use of Nitinol's unique properties to some extent and continual research into the metal's application must be seen as warranted.

2.3 Nitinol

For the purpose of conciseness, focus is placed on Nitinol in its super-elastic state and the accompanying "shape-memory" effect has been largely omitted from discussion. The alloy's micromechanical behaviour is discussed in detailed, focussing on the alloy's molecular structure. Effects such as stress-strain behaviour, fatigue properties and load dependency effects are also addressed.

2.3.1 Crystallographic structure of Nitinol

The feasibility of using endovascular devices as a method of aneurysm repair quite often relies on the use of exotic materials to cope with the challenging delivery methods and in situ conditions. Nitinol, developed by the Naval Ordnance laboratory in 1960, has been used with great success for many of these applications as discussed in section 2.1.

Although often referred to as a Shape-Memory Alloy (SMA) it is Nitinol's accompanying pseudoelastic property that makes it of particular use for endovascular devices. It is observed that under the right conditions these SMA's display super-elastic behaviour which enables them to withstand strains in excess of 8% without incurring plastic deformation. This property makes SMAs especially well-suited to catheter delivery systems, enabling minimally invasive surgery.

Nitinol (NiTi) is a near-equiatomic alloy of Nickel and Titanium. The ratio is commonly 49.0 to 50.7 at.% titanium, where super-elastic alloys lie in the region of 49.0 to 49.4 at.% [36]. In its stable condition, Nitinol has a body centred cubic structure referred to as austenite. Under loading, a remarkable crystallographic solid-state phase change occurs. During this phase change the parent austenitic structure is transformed into an unstable face centred cubic structure referred to as martensite. The resulting martensitic lattice represents a more staggered, irregular molecular structure when compared to the parent austenitic structure (figure 2.1). The martensitic lattice shown in figure 2.1 is heavily twinned and can easily be deformed through the process known as detwinning [37], [38]. Through the detwinning process atomic bonds in the structure are not broken under increased loading. Instead, the twin boundaries move to produce a shape that better accommodates the applied load [39]. Due to crystallographic restriction, with the removal of load the initial orientation of atoms can be restored. It is thus through Nitinol's remarkable molecular phase change that the metal can cope with strains of up to 8% without plastic slip occurring.
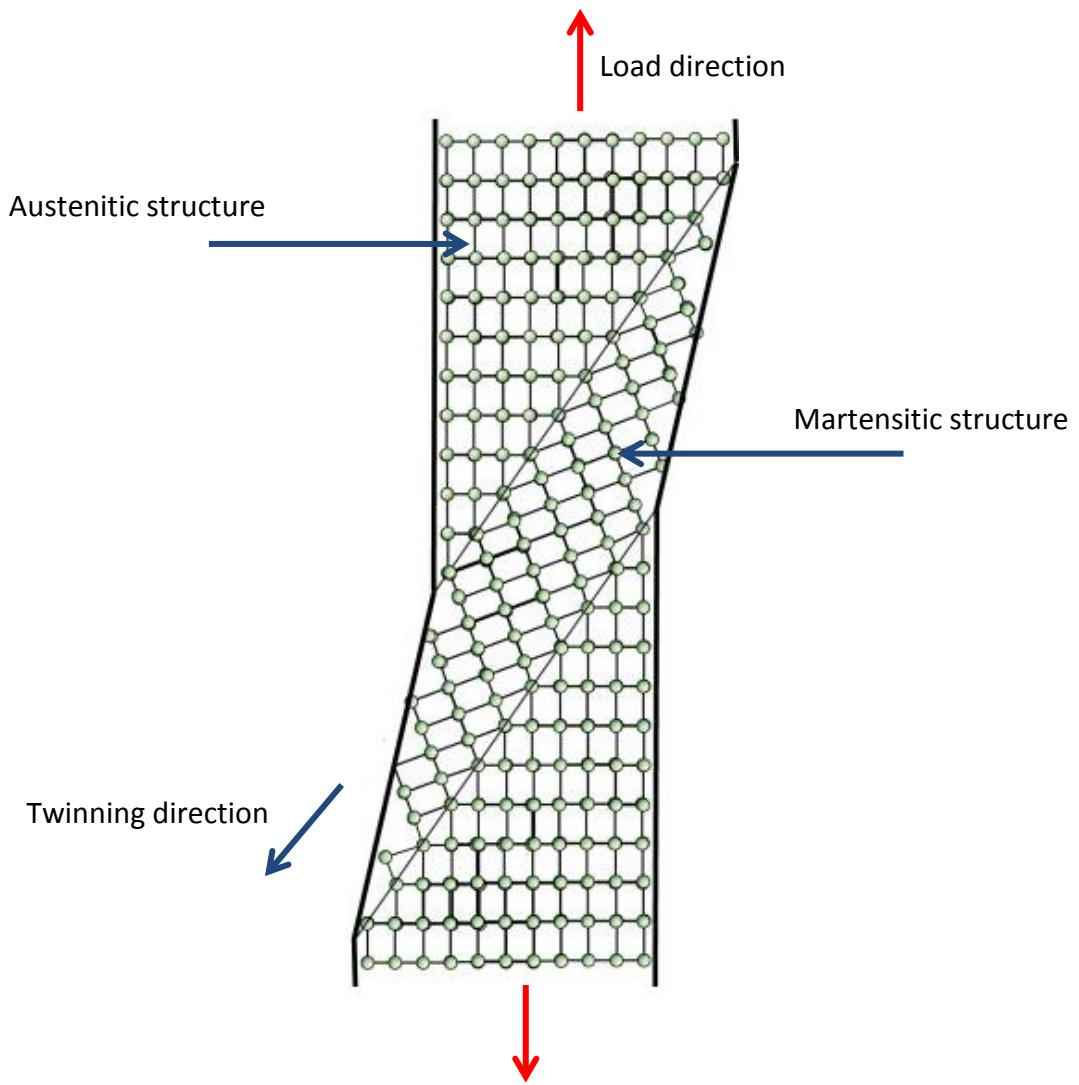
Figure 2.1: **Image representing a Nitinol specimen in tension.**

The phase atomic shift is accomplished through a shear type process at a predetermined strain and temperature state. The exact states at which the atomic shift will occur are sensitive to specimen manufacturing processes and are also load direction dependant. The transformation process itself is a complex and widely researched topic. It is understood that in polycrystal specimens transformation is initiated through nucleation. The transformation then propagates through regions of large strain and crystals of preferred orientation. Authors studying this behaviour of Nitinol in thin sheets [40] have reported Lüders-like bands developing under load. It is hence thus that the transformation from austenite to martensite is complex and heterogeneous in nature.

Digital Image Correlation (DIC) techniques have shown that during loading, even upon apparent complete transformation of the material, small pockets of austenitic crystals can still be found [41]. The heterogeneous behaviour of Nitinol at a microscopic level is mostly attributed to material defects, crystal orientation and geometric instabilities [40].

Without any mechanical loading a solid-state phase transformation from austenite to martensite can be achieved through temperature control of a Nitinol specimen. Figure 2.2 displays the austenitic/martensitic ratio as a function of temperature in a Nitinol specimen. What can be seen from this graph is that for each specimen of Nitinol, a series of key temperatures exists which marks the onset of various stages of the austenite-martensite transformation. To this body of work the most relevant of these is the A_f temperature, above which Nitinol is in its stable austenitic phase and is said to be in its super-elastic state. For the Anaconda devices, specifications to suppliers generally demand A_f temperatures of between 10^0C to 15^0C. This specification ensures that super-elastic behaviour is observed when operating within the human body at 37^0C.
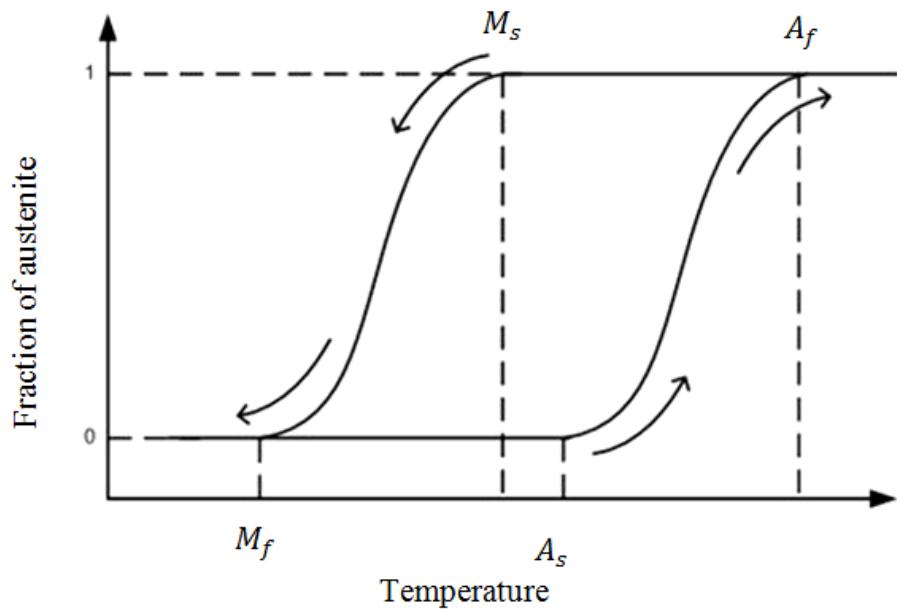

Figure 2.2: **Schematic representation of the fraction of martensite as a function of temperature. Subscripts *s* and *f* represents the transformation of start and finish points of either austenite (A) or martensite (M).**

18

An important but often neglected constituent of the austenite-martensite cycle is an intermittent phase. The phase, referred to as the R-phase, only develops under certain conditions during the transition between Nitinol's body centred cubic to face centred forms. The phase develops when the parent cubic phase elongates along one of its diagonals, reducing the cube angle and producing a rhombohedral structure [42]. The formation of R-phase crystals within the austenite lattice has a notable effect on the materials stress-strain response, generally delaying the onset of the martensitic lattice. In practice the R-phase is generally unwanted and can be eliminated through correct Nitinol grade selection.

Effective control of ageing processes and temperature control of Nitinol specimens also plays a key role in avoiding the onset of the R-phase. It has been noted within this study that the primary interest lies in specimens 15 degrees above their A_f temperatures at which onset of the R-phase constituents is understood not to be an issue [42], [43].

An important aspect of Nitinol is that both the transformation and reorientation processes dissipate energy [44], [45]. The energy is released in the form of heat which can have consequences for a metal where the properties are highly temperature dependant. In experiments involving Nitinol, active temperature control is often employed to compensate for thermal effects. Loading at sufficiently slow loading rates to simulate near quasi-static loading conditions has also been shown to be sufficient to compensate for the exothermic effects. Nitinol's mechanical properties have been found to be largely strain rate independent if isothermal conditions are established during testing [46].

As previously mentioned, Nitinol's energy dissipative processes result in pronounced hysteretic behaviour. This behaviour can, for instance, be clearly observed in the materials stress-strain response an example of which can be seen in figure 2.3. The stress-strain response provides a convenient platform for discussion and as such is frequently referenced within this thesis.

2.3.2 Uniaxial stress-strain behaviour of NiTi specimens

The stress-strain regime can be divided into phases as marked by points A through E in figure 2.3. As can be seen in figure 2.3, initial loading of a specimen is met by a conventional linear elastic modulus (A-B). This elastic modulus is commonly between 40GPa and 75GPa, similar to that of Aluminium. Once a nominal state of stress is reached (B), the energy required for nucleation of martensitic participates is provided. Twin pairs are established and any additional loading is met through little resistance as the specimen deforms through the detwinning mechanics described in section 2.2.1. Once the entire specimen has transformed and detwinned (assumed here to be point C) any further deformation is met with conventional mechanisms of linear elasticity and slip until failure occurs. Unloading from the upper plateau, is met by a linear elastic response referred to as the second elastic modulus. At nominal stress value (D) a lower plateau is reached along which any further unloading will propagate. Continual unloading results in the complete transition back to the parent austenitic phase (E), at which point another linear elastic region is encountered.

The exceptionally large hysteresis loop (A, B, C, D, E) displayed by Nitinol's stress-strain curve indicates that a significant amount of energy is dissipated during a loading cycle. It is worth noting that the stress-strain behaviour of 'as drawn' specimens differs remarkably from that shown in figure 2.3. Typically a level of cold working and heat treatment is required before super-elastic behaviour is noted [32]. Furthermore, figure 2.3 represents the stress-strain behaviour of a specimen at temperatures above its A_f temperature which is typically between -20°C and 100°C. It is observed that above 100°C Nitinol alloys gradually lose their super-elastic properties and behave in more conventional terms.

As shown in figure 2.3, Nitinol's stress-strain response in compression and tension is asymmetric. Most notable is that in compression Nitinol does not exhibit the distinct flat plateaus normally associated with the alloy. When compared with its

tensile response, the transformation stress tends to be significantly higher and the strain at which the second elastic modulus is countered lower.

Nitinol's asymmetry is well researched with a host of publications available on the topic [41], [47]. For the present work, Nitinol's asymmetry presents significant FE challenges. Foremost of these is that the asymmetric response is yet to be adequately captured within constitutive modelling. Currently the Auricchio constitutive model, as implemented within leading numerical software suites, offers the option of capturing asymmetry effects through a single parameter [48]. This lack of control offered to end users can lead to an ill-fitting material model with a compressive response that is not representative of experimental data. In addition to these issues, the use of an asymmetric material definition within FE analysis introduces a significant additional computational burden through the introduction of an asymmetric stiffness matrix within the numerical analysis process.
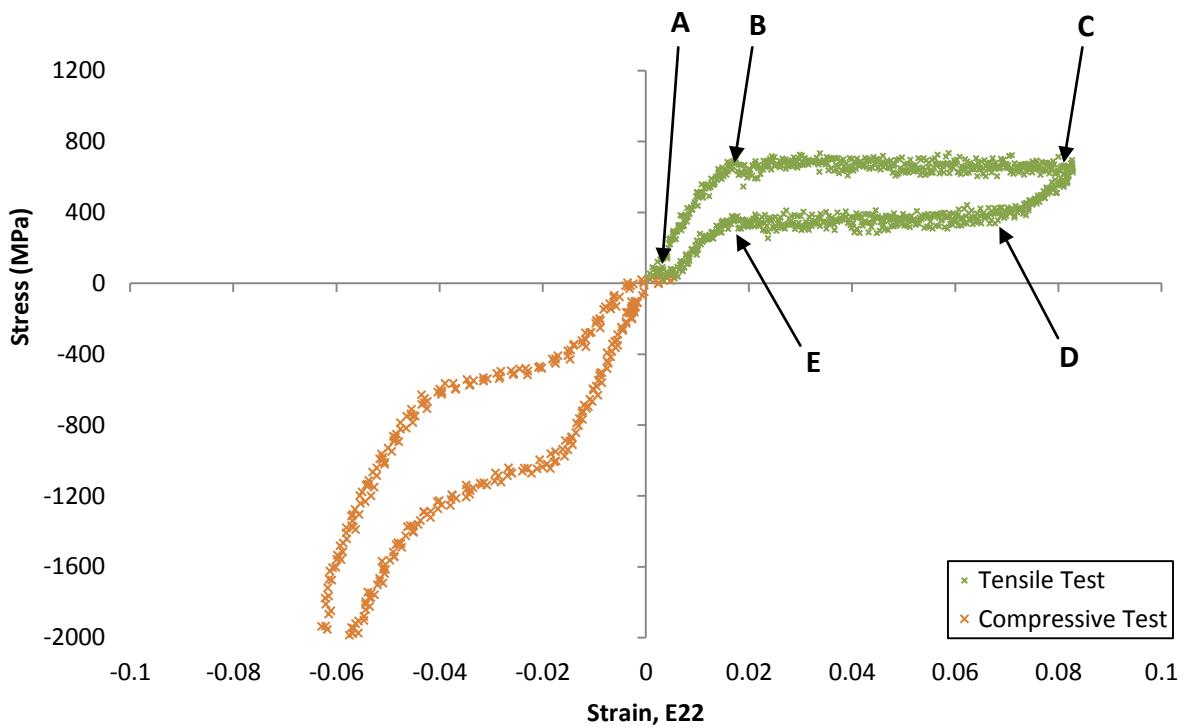

Figure 2.3: **Stress-strain curve for a 1 mm diameter Nitinol wire in both compression and tension. Nitinol's distinctive hysteretic behaviour is clearly visible.**

2.3.3 Fatigue properties of Nitinol

As with many aspects of Nitinol, its fatigue characteristics are multivariable and complex. However, much of the literature available on the topic [45], [49], [50] concludes that Nitinol excels within strain controlled environments, whilst relatively poor results are obtained under stress controlled conditions. This trend is an effect of the super-elastic mechanism where high strains generate relatively low stresses, whilst high stresses result in excessively high strains. As the Anaconda's *in situ* conditions are representative of a strain controlled loading environment such findings further supports Nitinol's popularity within the endovascular device industry.

Published studies into the fatigue properties of Nitinol can be found as far back as 1981, with an early study by McNichols *et al.* into the fatigue behaviour of thermal shape memory Nitinol up to 2.2×10^5 cycles [51] . Results through this study produce a linear S-N curve, a finding which was later supported in a more recent publication [52]. These results differ from linear elastic materials for which a power law S-N curve are common. Nitinol's unconventional S-N curve results are closely linked to its atomic phase shift which affects mechanisms of crack propagation, and Nitinol's response to mean strain and temperature as discussed below.

Crack propagation: Although the literature available on crack propagation induced through cyclic loading in Nitinol is by no means extensive, a growing number of papers are available for study. In general, tests examining Nitinol's fatigue crack propagation resistance have found that non transforming microstructures far outperform transforming microstructures [53]. The low fatigue crack growth resistance in transforming microstructures is believed to be associated with the small negative dilation (.5%) associated with the transformation from austenite to martensite. Through this it can be shown that additional cyclic tensile stresses are established around the crack tips, promoting crack growth [54].

Machereach *et al.* correlated crack growth with deformation modes within Nitinol [50]. Through this study correlations were established between the deformation modes and fatigue performance of Nitinol specimens. Using X-ray microdiffraction techniques, Robertson *et al.,* [55] completed an in depth study into this topic and found that the areas in the wake of an advancing crack tip would transform back into the parent austenitic phase. The paper continues in support of the notion that crack tip propagation investigations, even during the development of fatigue test data, must be under loading conditions representative of the intended application to be relevant. This is in part due to the way in which crack propagation mechanisms can change in transformation microstructures depending on specific loading states. The study also highlighted the large crystallographic anisotropy that exists within each Nitinol specimen and the crucial role grain alignment plays in crack propagation.

Mean strain effects: The proximal ring of the Anaconda device is generally oversized compared to the lumen in which it is implanted. For this reason it is vital that the bending fatigue characteristics of Nitinol should be studied at non-zero-mean values. On this topic various authors [56], [57] have published several studies, the results and conclusions of which are all in relative agreement. It has been found that unlike conventional engineering material Nitinol's cyclic fatigue endurance gradually increases with increasing mean strain (trend seen up to 7-8 % mean strain for super-elastic specimens). A publication by Robertson *et al.,* [55] ascribed this effect to increasing volume fractions of martensite present within specimens which has been shown to have better fatigue properties than the parent austenitic phase. With this it was also shown that strain amplitude has a greater effect on fatigue life than mean strain, with constant life diagrams as shown in figure 2.4 indicating that strain amplitudes below 0.40 result in a fatigue life above ten million cycles. Although the effect has been attributed to increased volumes of martensite, this trend shown on figure 2.4 could also be partly explained through the previous discussion on transforming and non-transforming microstructures.

Relative temperature effects: As the properties of Nitinol have been shown to be strongly temperature dependant, several authors have studied the correlation between fatigue performance and A_f temperatures [55], [58]. The most relevant findings to the work herein are that for specimens experiencing transforming microstructures, specimens operating at 10°C above their A_f temperatures have been shown to perform best.
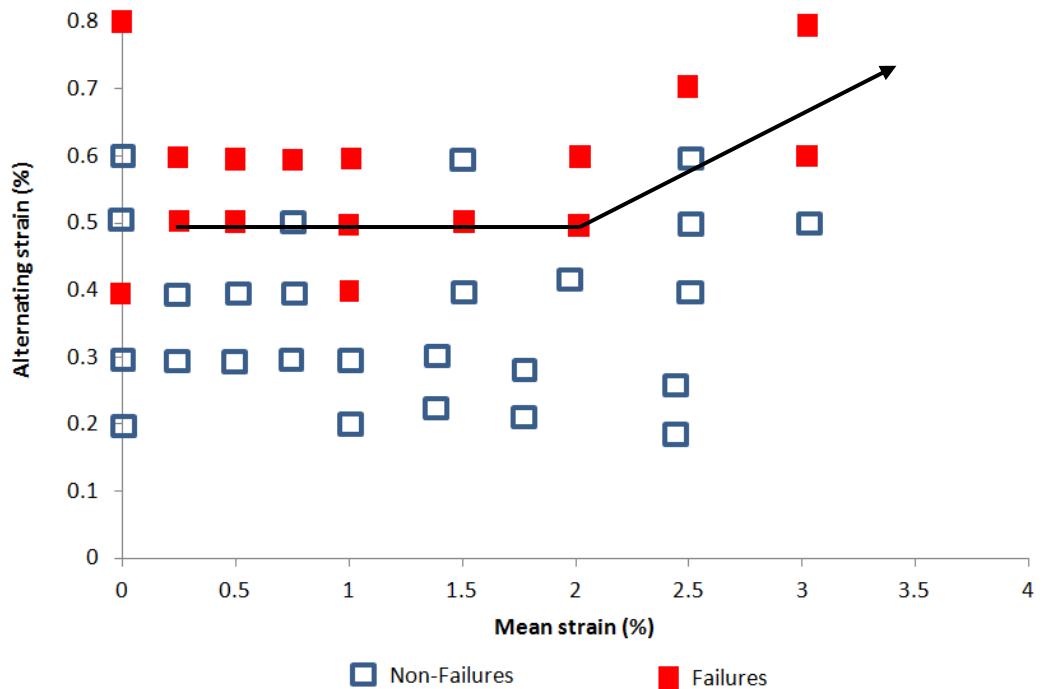

Figure 2.4: **Constant life diagram of an axial specimen under displacement controlled loading conditions produced by Duerig *et al.*, [56]. Squares marked in red indicate failures whilst squares left blank surpassed a ten million cycle benchmark.**

2.3.4 Nitinol's load path dependency

Load path dependency has recently been highlighted as a property requiring further study by a number of authors [24], [59]. The property refers to the phenomenon where Nitinol's state variables are load history dependent whilst operating within the super-elastic regime. For the present study this property was especially relevant due to its potential influence on fatigue characteristics.

Within the published literature, the topic of load path dependency has been touched upon on the side of larger experimental programmes. *Rebelo et al.,* [60] have, for example, shown through investigations that modern material models are able to capture the behaviour of Nitinol specimens subject to non-uniform cyclic loading regimes. As an idiosyncrasy that stems from the energy dissipative nature of the phase transformation, this implies that empirical-based Nitinol constitutive models do capture load history effects. To this author's knowledge, however, no study has solely addressed the property whilst exploring the impact it might have on effective product design.

2.3.5 Biocompatibility

In addition to its pseudoelastic behaviour, Nitinol exhibits several additional properties that make it particularly suitable to the biomedical fields. Foremost of these properties is Nitinol's biocompatibility which comes despite of its high nickel content that is considered to be toxic. Nitinol's biocompatibility is thought to be a result of being an intermetallic compound rather than an alloy in a pure metallurgical sense [32]. Through being a compound, stronger bonds are established between Nickel and Titanium within Nitinol than in Nickel precipitates often found in steel. Testing conducted by *Zollikofer et al.,* [61] have consistently shown that Nitinol is less corrosive and more chemically stable than stainless steel which is used in many medical applications. During tests in which Nickel-Titatnium were submerged in synthetic saliva at 37^0C for 72 hours, corrosion rates in the order of $10^{-5}\ mpy$ have been recorded which again perform favourably against many grades of stainless steel.

As Nitinol is less magnetic than stainless steel, image distortion is less likely to occur during MRI scanning. In this regards, NiTi displays suitability comparable to pure titanium [27].

2.3.6 Auricchio Nitinol constitutive model

A host of constitutive models are available for the material modelling of Nitinol. Integrated into the industry-leading FEA software suites, Abaqus 11.2 and ANSYS 4, is the Auricchio constitutive model [48], [62]. This model was chosen for use within this project due to its commercial accessibility.

The material model is based on an internal-variable formulation known as generalized plasticity. It is this framework that is used for the construction of the constitutive model. The model is created to take into account various key features including dissimilar material behaviour in compression and tension and the martensitic reorientation processes. What is important to note is that the material model is not based on phase-transition micromechanics. Instead it is formulated from thermo-mechanical continuum theory based on the aforementioned internal-variable formulation technique (generalised plasticity). The micromechanics are captured through evolutionary equations used to describe internal variables.

A key aspects of the internal variables within the Auricchio model is that they relate to the phase transition and reorientation processes. Through this the micromechanics of the transition is captured. Aspect upon which the formulation is based include:

- Initial and final stress-strain conditions for each phase transition
- Dependence of the phase transition on temperature
- The pressure dependence of the phase transition

2.3.6.1 3D model formulation

Stress (τ) and Temperature (T) are used as control variables. In order to create the transformation and hysteretic behaviour, a transformation strain (ε^{tr}) is used. The transformation strain is added to each element when phase transformation conditions are met in such a form that the total strain can be expressed as shown in equation 2.1.

$$\varepsilon = \varepsilon^e + \varepsilon^{tr}$$

(2.1)

Where ε^e is the elastic portion of the strain as calculated by the Young's modulus whilst ε^{tr} is a term representing the recoverable plastic deformation. The term ε^{tr} can be expressed as shown in equation 2.2.

$$\varepsilon^{tr} = \varepsilon_L u$$

(2.2)

Variable ε^{tr} within equation 2.2 is in turn dependant on three terms captured within the tensor u and the maximum elastic strain ε_L. These three terms, as expressed in equation 2.3, refer to three super-elastic processes: the Austenite to Martensite transformation (AS); the Martensite to Austenite transformation (SA); and the Martensite reorientation processes (SS).

$$\dot{u} = \dot{u}^{AS} + \dot{u}^{SA} + \dot{u}^{SS}$$

(2.3)

Another relation used within the formulation is the fractions of Austenite (ζ_A) and Martensite(ζ_S) present within an element, the sum of which is assumed to be unity.

$$\zeta_S + \zeta_A = 1$$

(2.4)

These equations stated above are used as a base to create the material model. From these equations the more complex evolutionary equations are derived which are used to model the balance of ζ_A and ζ_S, the derivation of which can be found in [62].

Equation 2.5, as proposed by *Auricchio et al.,* [62], forms a key part in the material model formulation. The variable H is a logic parameter (H = 1 or 0) which contains

the phase transition activation conditions. β Is a material parameter influencing the speed of transformations whilst F is a function of the stress state, deviatoric stresses and internal pressures.

$$\zeta_S = \zeta_{S,n} + \left(\left(\int_t^{t_{n+1}} H^{AS} \beta (1 - \zeta_s) \frac{\dot{F}^{AS}}{(F_f{}^{AS})^2} \right) dt + \left(\int_t^{t_{n+1}} H^{SA} \beta \zeta_s \frac{\dot{F}^{SA}}{(F_f{}^{SA})^2} \right) dt \right) \quad (2.5)$$

Within equation 2.5, the first term marked in red is the source term for the Martensite (A-S) fraction within each element whilst the second term in blue can be interpreted as a sink term for the Martensite fraction (S-A). These terms are activated through parameter H, at conditions coinciding with positions B, C D and E in figure 2.3. Through this the fraction of Martensite, and hence the fraction of strain induced through the super-elastic mechanism, is established.

Through this review of the Auricchio Nitinol constitutive model it can be seen that the model is highly phenomenological, with a notable disregard to underlying micromechanics. The constitutive model has however been subjected to extensive peer revision with numerous studies indicating that the model is capable of replicating tensile experimental results to reasonable degrees of accuracy [47], [60], [63]. Less information is available on the models ability to replicate compressive results, especially that of thin wire [41].

2.3.7 Nitinol literature summary

This section reviewed academic studies relevant to the present work. It was clear from the literature available that the fundamental micromechanical behaviour of Nitinol has been intensively studied. As a result a wealth of knowledge is available on the subject through publication. Distinct areas requiring further work have however been highlighted by leading authors in more advanced micromechanical topics. These topics include crack tip propagation mechanisms which is fundamental for the full understanding of fatigue properties.

With the current understanding of Nitinol's fatigue performance, the literature suggests caution when it comes to applying generalised fatigue data [55]. A strong

case can be made that load case-specific yield criteria and fatigue data must be produced for devices manufactured from Nitinol operating in safety critical applications. With several publications which support this reasoning, custom designed studies to assess fatigue performance must be seen as the only responsible way to assess the performance of medical devices. As experimental methods can be impractical when assessing the life span of prototype devices, these findings give support to the use of alternative methods such as the Finite Element Method during design. This argument applies specifically to the Anaconda device where the proximal ring is subject to complex loading. This also further supports research into FE design tools which can be used for both adequate product design and device optimisation.

The lack of information regarding Nitinol's load history dependency is seen as an area requiring further investigation relevant to the present body of work. The relevance comes from the complex loading regimes imposed onto the device during delivery and the ambiguity this might have on stress and strain states. Further investigations into the effect were therefore warranted within this thesis.

Through the literature review it has been seen that Nitinol's asymmetry is a well-documented metallurgical effect. In spite of this, it is currently inadequately captured within constitutive modelling. This inadequacy could have a significant influence on the accuracies of simulations conducted through the integrated modelling framework. As with these findings, the present project was given an additional objective of addressing Nitinol's asymmetry as captured within FEA.

2.4 Vascular tissue

Within this section relevant literature on the topic of vascular tissue is assessed. Focus within the review is initially placed on general mechanics before data on the abdominal aorta is provided. A brief review of arterial constitutive modelling is made available in section 2.3.10.

The pathology and mechanics of aneurysms is complex. As the Anaconda device anchors in healthy tissue and bypasses the aneurysm sack, this thesis will not address the mechanics of diseased tissue. Interested readers are referred to references [64], [65] and [66] for further information.

2.4.1 Arteries

Arteries form part of the cardiovascular system, which also includes the heart and venous system as displayed in figure 2.5. The work herein is primarily concerned with the characteristics of arteries and as such the other forms of cardiovascular tissue will be omitted from discussion.

The most prominent of all arteries is the aorta which is a single systemic artery emerging from the heart. It can be seen as the origin of oxygenated blood flow which feeds the entire body through successive branching. As the largest arterial form, it is segmented for referencing purposes with a descriptive naming convention. The aorta leaves the heart as the ascending aorta before curving around to form the aortic arch. At the aortic arch the first major branch vessels are found namely the brachiocephalic, left common and left subclavian arteries (figure 2.5). The aorta then descends down into the chest cavity as the descending aorta until the diaphragm is reached. The aortic region below the diaphragm is referred to as the abdominal aorta from which major branching vessels are the renal, superior and inferior mesenteric arteries (SMA, IMA). From the abdominal aorta the vessel bifurcates into the common iliac which eventually, after further bifurcation becomes the femoral arteries. Here the successive branching continues until capillary beds and arterioles eventually feed soft tissue with nutrients in the outer

limbs. Once nutrients have been supplied to the soft tissue, blood returns to the heart through the venous system.
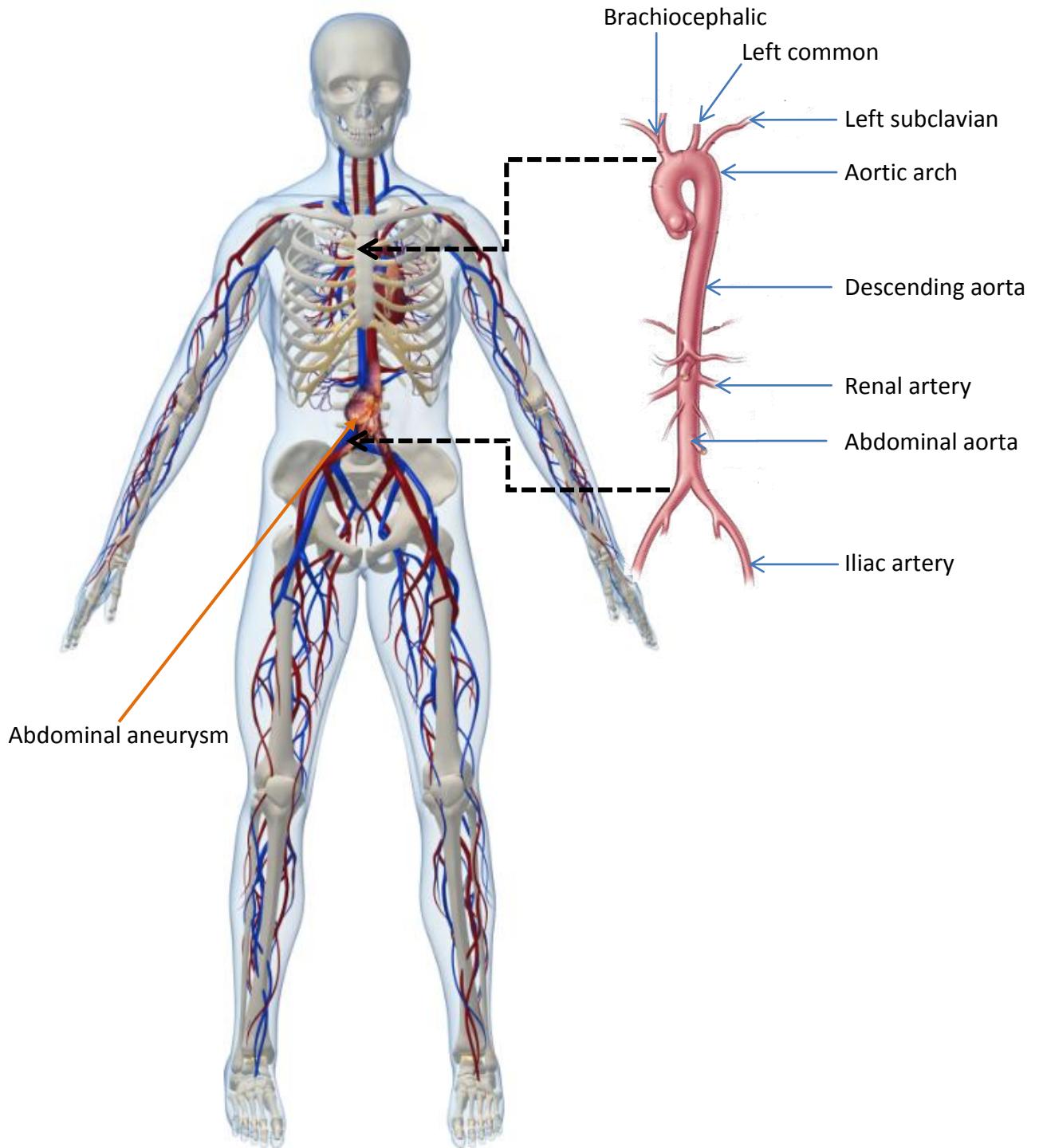

Figure 2.5: **Cardiovascular system of the human body. To the right the aorta is shown along with the naming convention used. Within the body shown, an abdominal aneurysm has been superimposed, showing the typical location and structure of this arterial disease.**

2.4.2 Function of arteries

The main function of the arterial system is to distribute nutrient rich oxygenated blood throughout the body. Within the cardiovascular system arteries acts as a pressure reservoir, supplying constant blood flow to capillary beds throughout the cardiac cycle. The arterial system thus forms a crucial part in regulating blood pressure within sections of artery, for instance near the common carotid bifurcation, carrying baroreceptors for this purpose.

2.4.3 Components of arteries

As seen in figure 2.6 the structure of arterial tissue is complex. The main components are smooth muscle cells, elastin, collagen, endothelium, connective tissue and a glycosaminoglycan-rich ground substance. These constituents of the arterial wall can be grouped into active and passive components. Of the passive components the most structurally significant are elastin and collagen. It is these passive components that give arterial tissue its passive mechanical properties which are often measured under laboratory conditions.
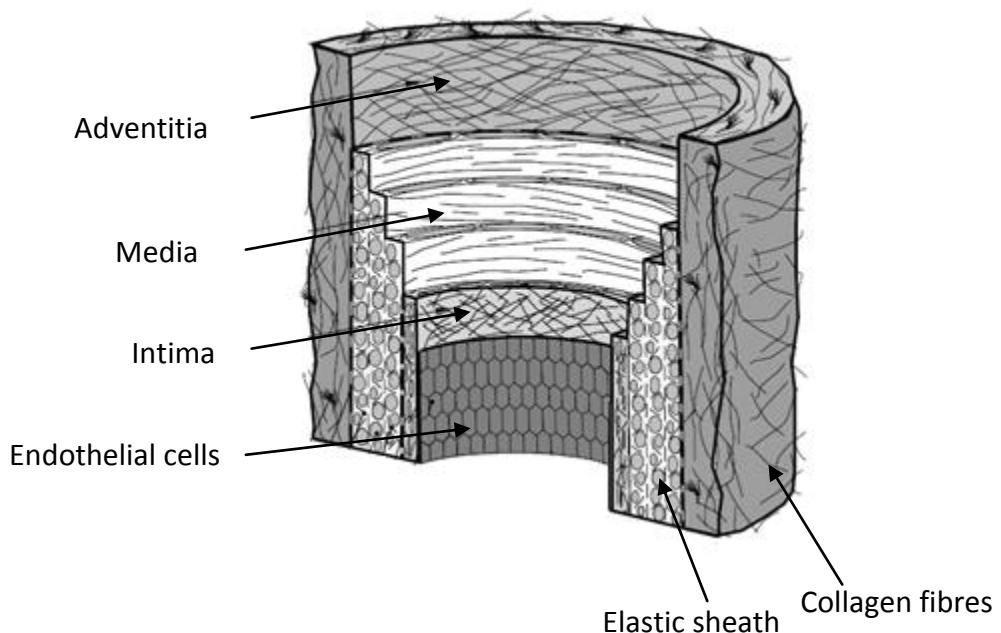

Figure 2.6: **Structure of the artery** [67]**.**

Muscle cells: Muscle cells found in the arterial system are known as involuntary muscle. With a helical arrangement, muscle contraction is used to control the lumen diameter of medium and small arteries through a process called vascoconstriction/vascodilatation. Muscle tissue is therefore clearly an active component that influences the mechanical properties of the artery to meet blood pressure and flow requirements.

As an additional function, muscle cells are responsible for the synthesizing of elastin and collagen. Through this they are also responsible for the maintenance and remodelling of the arterial extracellular matrix.

Elastic Fibres: Elastic fibres consists of two components: a core of elastin, surrounded by fibrillin microfibrils in a sheath-type arrangement. The elastin is the principle component within this arrangement, making up approximately 88-92% of the fibre [68]. With a Young's modulus of approximately .45 MPa the fibres are highly elastic and can stretch in excess of 150% without breaking.

Collagen: In humans there are over 28 known types of collagen. Only two of these, type 1 and 3, accounts for the majority found in arterial tissue [69]. With an ultimate tensile strength of 50 to 100 MPa, it is collagen which adds stiffness and strength to organic structures [70]. With its high tensile strength collagen fibres are the most mechanically significant constituents within the arterial wall. Due to its mechanical importance, collagen is often the focus during the study of vascular mechanics and vascular constitutive modelling.

Each collagen fibre is complex in nature, being made from fibrils and microfibrils. This construction increases flexibility and reduces the risk of rupture due to crack propagation [71]. Within stress free vascular tissue collagen is found to be undulated. With collagen's limited elasticity (10%), the crimped arrangement provides a level of extension to the artery before dramatically stiffening the macroscopic response. The specific arrangement and orientation of collagen within the artery is an important factor influencing vascular mechanics.

Collagen within vascular tissue is controlled through a balanced mechanism of synthesis and degradation [69]. These mechanisms are adjusted to respond to local stimuli, being it mechanical or disease. An example of this adjustment is for instance seen in the pathology of aneurysms, where it is found that increased proteolactic activity breaks down elastin, whilst the collagen production increases in an attempt to strengthen the diseased structure.

2.4.4 Structure of arteries

At any one topographical site, the various constituents listed in sections 2.3.3 can be found in different ratios through the radial thickness of the artery. In mature arteries these variations are of such nature that they effectively create three distinct layers referred to as the tunica intima, tunica media and tunica adventitia. Each of these layers, due to their specific ratio of components, plays a distinctive role in the overall mechanics of the artery. Throughout the vascular system, the relative size of these layers change to adapt to the specific function that the arterial segment fulfils and the mechanical stimuli it will experience.

In general it is observed that arteries closer to the heart are more elastic in nature, whilst arteries further along the vascular tree appear more muscular. This variation in attributes often leads to arteries being divided into one of three groups being elastic, muscular and arterioles. These groupings have relevance to the additional functions that these arteries often perform, with elastic arteries acting as a pressure reservoir and muscular arteries controlling blood flow and pressure. Arterioles are the smallest type of arteries and relatively the most muscular.

The three layers mentioned (Intima, Media and Adventitia) often play a key role in FE modelling of the arterial wall. The layers provide a convenient method of grouping the heterogeneous wall properties into manageable subgroups which can be assumed to be orthotropic in nature. Little is published on the accuracy of the FE modelling of individual layers as opposed to capturing the global response of the vascular wall as a single entity. The reason for this might lie with the relatively recent development of constitutive models which are able take into account

histological features. Collagen fibre angle directions have only recently been incorporated into commercially available FE codes (2006) [48]. The common assumption would be that a more detailed three layered FE model would be more accurate. This however might not be the case due to the complexities introduced when doing so. A high quality study focussed on comparing the merits of individual arterial layer modelling as opposed to single entity modelling can be seen as overdue when considering current constitutive capabilities.

Each of the three layers is further discussed here in terms of their components and mechanical contribution. In spite of the commonality of the three-layered arterial representation, dissimilarities in their exact definitions can often be found within publications. As such, the following section conveys how each layer has been divided in this study.

Tunica Intima: The intima has at its inner surface (next to the lumen) a thin layer of endothelial cells held onto a basal lamina mostly constructed from collagen. In young healthy arteries, it provides a negligible mechanical contribution due to its relative thickness [72]. The intima's main function is to provide a non-clotting surface for blood flow and allow for molecule transfer. In elderly patients, or patients with significant arterial disease, it has been found that intimal hyperplasia thickens this layer with the net effect of increasing the layer's mechanical contribution. In the present work the intima extends from the lumen to the first elastic lamina.

Tunica media: The first elastic lamina is seen as the boundary between the intima and media. The media extends to a less prominent external second elastic lamina which acts as the boundary to the adventitia. Between these lamina sheets the media exists as a concentric pattern of elastic fibres and smooth muscle cells. Woven in between the elastin are bundles of collagen fibrils.

Tunica Adventitia: In young arteries the adventitia is approximately 1/5 of the wall thickness and as such is relatively small. It has however, in spite of its size, a significant influence on the overall behaviour of the vascular wall. This is due to high

collagen content which is arranged as a dense network interspersed with fibroblast and elastic fibres. Collagen fibres within the adventitia are generally thought to be orientated longitudinally, providing protection against over dilation.

Arterial perivascular tissue: Perivascular tissue surrounds the adventitia and anchors it to surrounding features. The prevalence of perivascular tissue is dependent on its topographical site. Vertebral arteries, for instance, are partially encased in the spine whilst cerebral arteries are partially surrounded by cerebrospinal fluid. This study will not include the mechanical effects of perivascular tissue and as such will exclude their effect from further discussions.

2.4.5 Local arterial adaptability

Vascular tissue is well known to be adaptive to local mechanical stimuli. Regions experiencing excess mechanical stimulus have been shown for instance to recruit collagen to stiffen the arterial response. The heart too also offers examples of localised adaptability; the left ventricle is often found to be thicker in patients who suffer from high blood pressure, whilst it is relatively larger in patients with a leaking aortic valve [73].

The vascular property of local adaptability provides further complications when attempting to characterise vascular tissue mechanics. This is of particular concern when consideration is given to the mechanical stimuli present in uniform cylindrical regions that might exist in the region of an arterial feature. The abdominal aorta provides a good example of this where regions around the SMA and renal arteries are branch feature intense, whilst the region distal to this is uniformly cylindrical in nature.

Supporting the need for local characterisation is an investigation conducted by Kim *et al.,* [74] which studied the local variation of mechanical properties in arteries. The investigation was specifically aimed at comparing the anterior and posterior side of porcine arteries at the same topographical site. Variations in properties were noted which further highlights the localised heterogeneity. Previous studies [73] on this subject have shown an increase in wall thickness around branch features on canine

iliac femoral arteries. Although data published on this matter is preliminary in nature, evidence has suggested significant macro and microscopic variations in regions containing structural features.

Although histological adaptability is clearly well documented, the impact of branch features on the mechanical properties of surrounding tissue is not. If significant variations are found to exist, current methods of regional characterisation might be inadequate for material modelling purposes. The assumption of mechanical consistency over large regions should hence be further investigated and associated errors better quantified.

Limited mechanical characterisation data is available for arteries. As this is the case, and human arterial samples scarce, regional characterisation has remained prevalent in spite of local variations that might exist due to local adaptability. Furthermore, due to the precious nature of human samples, regional characterisation has typically been conducted in regions of straight segments where uniaxial specimens can easily be harvested. As the Anaconda device anchors just distal to the renal arteries, ambiguity exists around the applicability of characterisation data not taken from this region. A study aimed at clarifying the mechanical variations that might exist in the presence of arterial features could therefore be seen as much needed. This study could also further clarify the specific pathology of abdominal aneurysms. It has indeed been observed that suprarenal aneurysms are much less common than infrarenal aortic aneurysms [75] yet little has been done to clarify the reasons for this. Some reference to this phenomenon is made in the literature [76] but often, as in the referenced papers, pressure wave mechanics are listed as a possible contribution to this trend without much justification.

2.4.6 Relative behaviour of arteries *in situ* against *in vitro*

An issue pertinent to this project was that of the relative behaviour between arterial tissue *in situ* and *in vitro*. This issue was a concern as characterisation data available through studies are generally obtained through *in vitro* studies. As the end

objective of this research project was to produce simulations representative of *in situ* conditions, the errors associated with this approach had to be clarified.

Active and Passive Behaviour: As the arterial wall contains muscle cells its mechanical properties are variable. In spite of this, an invariant material model is required for FE implementation. This introduces considerable complications to material model development, as all characterisation activities must occur around a single activation state.

Relevant to this issue is an in depth investigation conducted by *Wagner et al.,* [77]. This study was aimed at quantifying the effects of muscle activation in both muscular and elastic arteries. Within this study several arteries were characterised in their activated, basal and passive states. Active and passive states were achieved through treating specimens with endothelin-1 and sodium nitroprusside solutions prior to characterisation. Specimens characterised without interference were considered to be in their basal state.

The study found that for elastic arteries, the active and basal response were very similar in nature. This meant that for elastic arteries, the level of activation post basal conditions, has little effect on the overall behaviour of specimens. In muscular arteries this trend was reversed with the active response being much stiffer than both the basal and passive response.

As this work was predominantly interested in the abdominal aorta, which is a highly elastic artery, the basal response tested in the laboratory was deemed to be representative of *in situ* conditions.

In situ environment: Overall, the influence that surrounding organs have on *in situ* vascular mechanics is still poorly understood. Only in recent studies has this issue been addressed to any significant extent.

On this subject Kim *et al.,* [78] produced a study in which the effects that surrounding tissue has on vascular mechanics were investigated. Several conclusions relevant to the present work were made. Most significant of these were

findings suggesting that the arterial wall thickness is closely linked to the mechanical significance of surrounding tissue. Although a valued contribution, the study stopped short of detailed mechanical characterisation.

With an appreciation of basic mechanics, the organs surrounding the arterial vessel will likely influence device-artery interactions through resisting arterial deformation. Data which quantifies the magnitude of this influence around the abdominal aorta is, however, not yet available. With current computing capabilities, FEA, and even the computational framework developed herein, could feasibly be used in a parameter study to investigate the likely significance of surrounding tissue. This parameter study could be basic in nature, for example, representing organs through boundary conditions placed on the adventitia. With current computing capabilities, this method of representation would also be the only feasible way of accounting for surrounding tissue within detailed device-artery interaction simulations. Accounting for the effects of surrounding organs within device-artery interaction simulations is seen as an objective which should be met once ex-vivo device-artery interactions are successfully modelled, and as a result, will not be included in the modelling framework developed herein.

The abdominal aorta is mostly surrounded by soft tissue organs, with only the spinal column in close proximity to its anterior side. The spindle nature of abdominal aneurysms, which can grow to diameters three times the original aortic size, further provides evidence that the abdominal aorta is not rigidly constrained on any one side.

Dynamic Loading: The loading conditions to which the arterial system is subject are dynamic in nature. This is mostly due to the constant variation in blood pressure induced by the cardiac cycle and external forces. Studies have shown that during the cardiac cycle, arterial motion within the body is predominantly in the circumferential direction [69]. This implies little or no shear stresses resulting from twisting and suggests that the pressure pulse can be assumed to be radial in direction.

It should be noted that local blood pressure can vary greatly depending on the orientation of the human body. A person standing has a significant blood pressure differential between their head and feet due to hydrostatics. Studies have for instance shown that blood pressure within the dorsalis pedis arteries of a healthy man standing can be as high as 154.3 mmHg. This is well above what is typically assumed for the abdominal region [79].

In this study, a pressure range of 100 ±20 mmgh was assumed for the abdominal region. Studies have shown this to be a valid assumption for a healthy adult, supine in posture [79].

2.4.7 Residual stresses within arteries

Arteries contain a significant level of *in situ* residual stresses which is generally well documented [76], [80], [81]. The axial component of these stresses can most easily be observed as arteries are seen to retract longitudinally by up to 30% when first dissected from the body. Residual stresses are also common in the circumferential direction which is believed to exist in an attempt to homogenise stresses within the wall when pressurised.

The axial and circumferential residual stresses of arteries are often separately referred to as "internal stretch" and "residual stresses" respectively. For clarity this convention was adhered to in this thesis. Within the literature, internal stretch is also commonly quantified by a single percentage stretch value whilst residual stresses are characterised through the opening angle a dissected tubular section takes.

In recent published investigations, comprehensive studies have aimed at quantifying residual stresses in each of the arterial layers [82]. Through the studies published the extraordinary complexity of the arterial wall has further been revealed. Unfortunately, results published on this issue tend to be subject to high values of standard deviation. This can partly be attributed to the complexity involved in residual stress characterisation.

Trends within results however suggest that each individual layer is subject to a unique set of 3D residual stresses. Stresses within each layer also seem anisotropic in nature with planar sections showing various degrees of *in situ* stretch in different directions. These results suggest that the simplistic method of opening angle measurements might be insufficient in capturing the true nature of *in situ* residual stresses in specimens.

Parallel to publications on 3D residual stresses in the arterial wall have been studies attempting to incorporate this data into FE models. Unfortunately only a very limited number of these are available for scrutiny and those which are tend to be subject to severe material simplifications [83].

2.4.8 The effects of ageing

Aging has a profound effect on the vascular system, the effects of which have been well documented within the literature [84], [85]. Typical effects of aging can be listed as follows:

- Increased wall thickness
- Increased stiffness related to the relative increase in collagen content
- Increase of the number, and thickness, of elastic lamellar units
- Blood pressure within arteries tend to increase
- Longitudinal *in situ* stretch decreases
- Increased susceptibility to arterial disease

The mechanical influence of the effects listed above can be dramatic. Ideally then when performing FE simulation studies, material models should be based on characterisation data from specimens of relevant age. Age effects also then drives the need for improved vascular characterisation data sets as it provides yet another variable which should be limited during statistical analysis.

2.4.9 The abdominal aorta

The type and degree of loading an endovascular device is subjected to *in situ* depend largely on the topographical site into which the device is implanted. For devices implanted into the abdominal aorta, the cyclic loading imparted is predominantly caused by the motion of the vessel due to the cardiac cycle. It is well known that during ventricular ejection the aorta, pulmonary arteries and other large distribution arteries distend rapidly, accommodating 50% of the stroke volume [69]. The vessel then retracts, maintaining a flow through the smaller muscular arteries and capillary beds. During this cycle of dilation and contraction the abdominal aorta can typically experience a diameter change of 9 to 12%.

As a valuable contribution, Weisbecker *et al.,* [72] completed an in-depth study on the mechanical properties of the abdominal aorta. The study completed was comprehensive in the sense that layer-specific samples were mechanically characterised into supra-physiological regions. Results are published in parameter form, allowing for the integration of results into finite element material models. Although comprehensive in nature, a regional form of characterisation was adopted (obtaining specimens from across the abdominal aorta), with ambiguity existing around the exact location from where specimens were harvested. With reference to discussions within this thesis regarding local variations in vascular mechanics (section 2.3.5), this information is essential to the work herein. Furthermore, as these comprehensive studies are rare, further investigations are required in order to produce meaningful datasets.

Collagen content ratio, fibre orientation and distribution have been extensively studied in the past. Data available on this topic for the aorta tends to be comprehensive in manner, with site and layer-specific data available for several locations. Generally, results suggest that within the abdominal aorta, the mean angles of collagen fibres increases through the radial thickness of the wall (from approximately 20^0 to 60^0) [71]. The level of dispersion around the mean angle also tends to increase through the radial thickness. Although this would imply that an

asymmetric fibre layup is present within the aorta, no published study could be sourced which specifically studied the coupling effects which could arise from this. With the arterial motion being predominantly in the circumferential direction during the cardiac cycle [69], it is reasonable to suspect that potential coupling effects are somehow counteracted, possibly through residual stresses or attachment to perivascular tissue. Further research on this topic is however required.

2.4.10 Vascular constitutive modelling

Recent advances in the constitutive modelling of vascular tissue has signalled the onset of models driven by underlying micromechanics, moving away from pure phenomenological models. Advanced models tend to be based on collagen fibre angle and distribution, recognising the mechanical importance of these constituents.

Although a number of models are available for the modelling of arterial tissue [86]–[88] this project used the Holzapfel constitutive model. This is mainly due to the model's commercial availability and the peer revision to which the model has as a result been subjected. A brief overview of the Holzpafel constitutive model is presented herein as a basic understanding of the model structure is beneficial for later sections of this thesis. As derivations can be extensive, they are omitted. Instead, derived expressions and a description of terms are provided. Interested readers are referred to references [80], [89] for further details.

2.4.10.1 Holzapfel's constitutive framework

The approach taken within the Holzapfel description is to use a free-energy function to describe the materials anisotropic hyper-elastic response. The artery's structural complexity is reduced to a non-collagenous ground matrix which is reinforced by two families of collagen. Within this representation, the non-collagenous matrix is assumed to be isotropic.

Collagen is represented by two families that are symmetrically disposed to each other with respect to a circumferential axis by an angle γ. The angle γ, and the

dispersion of fibres around this angle is set through a user inputs parameter. It is the angle and distribution of the collagen fibres that invokes and dictates the level of anisotropic behaviour of the models. With this representation, there is no radial component to fibre families. This assumption in turn renders the model incapable of capturing the orthotropic nature of the arterial wall. To address this issue modelling techniques are required, such as the individual modelling of arterial layers.

2.4.10.2 Continuum description

To form the continuum framework, a general description of deformation is first established. Within this description the variable Ω_0 is taken to be the fixed reference configuration of a body. With this reference, deformations can be described through equation 2.6.

$$\chi : \Omega_0 \longrightarrow \mathbb{R}^3 \tag{2.6}$$

Within equation 2.6 χ is a function that transforms points (x) in the reference configuration, Ω_0, to a position (X) in the deformed configuration Ω. This transformation can be expressed as shown in equation 2.7.

$$x = \chi(X) \in \Omega \tag{2.7}$$

Further the standard deformation gradient and local volume expressions required for numerical integration are stated here in equation 2.8 and 2.9 respectively.

$$F(X) = \frac{\partial \chi(X)}{\partial X} \tag{2.8}$$

$$J(X) = \det F > 0 \tag{2.9}$$

As the vascular tissue is incompressible, the deformation gradient F is placed into a state of multiplicative decomposition. The decomposition consists of its dilatational and distortional parts which can be expressed as shown in equation 2.10, where I denotes a standard second order unit tensor.

$$F = \left(J^{1/3} I \right) \bar{F} \tag{2.10}$$

The right and left Cauchy-Green tensor (C and b) associated with equation 2.10 can be expressed as shown in equation set 2.1.

$$C = F^T F = J^{2/3}\bar{C}, \qquad\qquad \bar{C} = \bar{F}^T\bar{F}$$

$$b = FF^T = J^{2/3}\bar{b}, \qquad\qquad \bar{b} = \bar{F}\bar{F}^T$$

Equation set 2.1

The strain is characterised by the Green-Lagrange strain tensor E, where the associated modified counterpart is represented by $\bar{E}$ as shown in equation 2.11 and 2.12.

$$E = J^{\frac{2}{3}}\bar{E} + \frac{1}{2}\left(J^{\frac{2}{3}} - 1\right)I \qquad\qquad \textbf{(2.11)}$$

$$\bar{E} = \frac{1}{2}(\bar{C} - I) \qquad\qquad \textbf{(2.12)}$$

To characterise the hyper-elastic response of vascular tissue second order tensors (A_α) is used and the existence of Helmholtz free-energy function Ψ is proposed. As the energy function is dependent on the structural tensors and the Green-Lagrange Strains, the free energy function can be expressed in terms of its volumetric $U(J)$ and isochoric contributions ($\bar{\Psi}$) as shown in equation 2.13.

$$\Psi(E, A_1, \dots, A_n) = U(J) + \bar{\Psi}(\bar{E}, A_1, \dots, A_n) \qquad\qquad \textbf{(2.13)}$$

With it demonstrated how the expression of strain is related to the free energy function, the stress-strain relationship can be expressed in terms of the second Piola-Kirchhoff stress as shown in equation 2.14.

$$S = \frac{\partial \Psi(E, A_1, A_2)}{\partial E} \qquad\qquad \textbf{(2.14)}$$

With the basic relationship between stress, strain and the free energy term presented, equation 2.13 can be restated using the Cauchy Green tensor as a measure of deformation. The free energy function can also be further specialised to

vascular mechanics by assuming incompressibility, which leads the volumetric contribution to be purely a Lagrange contribution. $\overline{\Psi}$ Is thus taken to be purely isochoric and based on the two families of collagen. Through this, the structural tensors can be reduced to two second order tensors which describe the structure of the tissue at any unit volume. Through applying these steps equation 2.13 can be transformed into equation 2.15.

The energy function as stated in equation 2.15 was first presented by Holzapfel *et al.,* [90]. At the core of this description lie simplifications placed on the underlying structure of vascular tissue. Most notable of these is the use of the two families of collagen to represent collagen content (A_1, A_2). Although novel at the time, in the form shown in equation 2.15, the description is limited through failing to take into account collagen distribution around mean orientations. Through this limitation, equation 2.15 describes transversely isotropic conditions instead of the required anisotropic.

$$\Psi(C, A_1, A_2) = U(J) + \overline{\Psi}(\overline{C}, A_1, A_2) \qquad \textbf{(2.15)}$$

In an attempt to address the issue of collagen distribution Holzapfel *et al.* took this description further by modifying the structural tensors. This was accomplished through the introduction of a generalised structure tensor denoted as $\rho(M)$, the expression of which is shown in equation 2.16. In equation 2.16, M is a single unit vector around which distributions of fibres are described through the normalised function whilst variables Θ and ϕ denote mean fibre angles around which the distributions occur.

$$\frac{1}{4\pi} \int \rho\left(M(\Theta, \phi)\right) d\omega = 1 \qquad \textbf{(2.16)}$$

With the introduction of the density function $\rho(M)$, the structural tensors as expressed in equation 2.15 take the new form "H" as shown in equation 2.17. In this compact description, a_0 is the preferred material orientation whilst the parameter *k* is introduced.

$$H = kI + (1 - 3k)a_0 \otimes a_0 \qquad \text{(2.17)}$$

It can be seen from the above expression that the structural tensors rely only on this single parameter k. This parameter is seen as a structural parameter, which characterises the distribution of collagen around the mean fibre angle. During numerical analysis, k is assigned a value between the two limits of 0 and 1/3, the limits of which renders the material either transversely isotropic (0) or fully isotropic (1/3), when considering in plane loading. The parameter k can be expressed as shown in equation 2.18, or alternatively can be determined through histological examination of specimens.

$$k = \frac{1}{4} \int_0^\pi \rho(\Theta) \, sin^3 \Theta d\Theta \qquad \text{(2.18)}$$

Equations 2.7 through to 2.18 provide an overview of the underlying principles on which the constitutive description is based. When implemented within Abaqus 6.11, constituents of the Helmholtz free energy function is grouped into two parts: one which calculates energy contributions from the isotropic ground matrix (Ψ_g) and the other which calculate contributions from the collagen fibres (Ψ_f). With this division, the total Helmholtz free energy function (Ψ) can be expressed as shown in equation 2.19.

$$\Psi = \Psi_g + \Psi_f \qquad \text{(2.19)}$$

$$\Psi_g = \frac{1}{2} c(I_1 - 3) \qquad \text{(2.20)}$$

$$\Psi_f = \sum_{i=1,2} \bar{\Psi}_{fi}\big(\bar{C}, H_i(a_{0i}, k)\big) \qquad \text{(2.21)}$$

Within equation 2.20, isotropic contributions are calculated using a linear function which is only dependant on a structural modulus type parameter c and a second order unit tensor I_1. Expression 2.21 is constructed from elements stated within equation 2.6 through to 2.18. Within Abaqus, the numerical solution process is centred around the reduction of the free energy within a system, where zero results in a solution for a given boundary conditions set.

2.4.11 Vascular tissue summary

It has been shown through the literature review that the mechanical properties of the arterial wall can be highly variable. This feature of arteries provides a major challenge when attempting to develop a general Finite Element model for product optimisation purposes.

To overcome this issue, the variability of arterial tissue must be adequately addressed during model development. Furthermore, to answer questions surrounding applicability, the errors associated with the use of a generalised parameter set should be quantified. As this has not been done in the published literature to any extent, it was an objective of this project to investigate the applicability of generalised arterial models.

Current data available within the literature is comprehensive enough to establish mechanical trends across the vascular system. In spite of this, insufficient characterisation data is available to fully determine the variability between patients at any one topographical site. The data currently available is a product of a previous focus on vascular micromechanics, a trend driven by leading authors' interest in constitutive modelling. Data requirements for the use of the newly developed constitutive models are different however with a focus on macromechanics and comprehensive mechanical characterisation of a large number of specimens required. The development of large characterisation data sets will eventually allow for the creation of generalised, gender specific, topographical, site specific arterial models which are crucial for the development of advanced FE based design tools.

Through the literature review it was found that a three layered biological description of arteries is common (Intima, Media and Adventitia). As the division of these layers are based on structural differences, it can be assumed that mechanical properties per layer will vary greatly. Although current constitutive models are capable of capturing the main underlying features which give rise to layer-specific properties, nothing has been published regarding the benefits or drawbacks of a

layered FE artery model. A comparison between various arterial FE representations was therefore overdue, another area to which this project aimed to contribute.

Supporting the development of a three layered FE arterial model is the variation of residual stresses across the wall thickness. Through basic mechanical appreciation, these residual stresses are seen to be fundamental to the overall mechanics of the arterial wall. In spite of this, little has been done to study *in situ* residual stresses through FEA. This is seen as a product of the complexity of doing so and the infancy of the capability. The development of the integrated modelling framework herein provides an excellent basis for studies such as these. To create such models, however, requires layer-specific data sets, which are rare within published literature.

3.0 The vascular testing programme

This project assessed the suitability of advanced constitutive models within the design process of endovascular devices. Whilst similar assessments to this have been carried out in the past [24], previous studies have tended to focus on the device itself. These studies have, as a result, used extensively simplified arterial models with questionable degrees of accuracy.

Simplifications associated with arterial modelling have often in the past stemmed from the difficulties involved in the FE representation of biological tissue. With these difficulties noted, various academics have over the last decade aimed at further developing vascular constitutive theory, whilst developers have been simplifying its implementation [89]. Extensive progress within this field has now allowed for the suitability of FE to be reassessed within this project.

In spite of progress within the field, making use of modern arterial constitutive descriptions has yet to become a straightforward process. The reason for this lies predominantly with the considerable amount of data required for material model development. If a detailed, layer-specific arterial model is to be created, uniaxial data is required for axial and circumferential directions for all three layers. Histology studies are also needed to verify mean fibre angles and distributions. Furthermore, if the material model created from this uniaxial data is to be used in safety critical applications, additional load-deflection data is required for model validation purposes. Ideally, the load-deflection data gathered should also match the final simulation loading conditions closely. This is especially crucial in the cases where a material model derived from uniaxial (2D) data aims to replicate complex, non-uniform (3D) loading conditions [72], [67].

For use in this project, abdominal aorta material characterisation data were available from the open access literature. With the extensive data requirements needed for FE simulation, this data was, however, not comprehensive enough. With questions around the applicability of data not gathered from the exact topographical site of interest, this issue soon became exacerbated by further limiting the use of published data. A further key issue which was pertinent to the project presented herein is the unique loading conditions imparted by the super-elastic proximal ring of the Anaconda device. These unique loading conditions created the need for bespoke data sets for validation purposes.

A further unanswered question faced by this project was how representative parameters currently available within the literature were of patients to be treated by the Anaconda device. Although material parameters were available for use, a general set representative of averaged properties had not yet been proposed. A study was also required to better judge the applicability of such an averaged set. This study had to investigate whether such a set can be used over entire topographical regions and whether such a set is still representative in the presence of additional arterial features.

With these motivations, a vascular testing programme was initiated within this project. Within this chapter, the main objectives of this programme are first outlined before test setup and protocols are discussed. Results and the conclusions obtained from this study are presented towards the end of the chapter.

All the work done in this section was carried out under full ethical approval by both The Ethics Committee at the University of Strathclyde and Biopta, the supplier of tissue.

3.1 Programme objectives

The aim of the testing programme was to deliver comprehensive data sets, adequate for the FE modelling of the abdominal aorta. Once delivered, the data sets were to be used in the development of a integrated modelling framework which could be used to investigate the interaction between endovascular devices and the arterial wall. Data produced through the programme was to be collated with that which could be found in the literature. Through this, statistically significant data sets were to be created from which generalised Holzapfel material parameters could be suggested.

For the purposes of the programme, three human abdominal aortas were studied. Each of these specimens was subjected to layer-specific characterisation. Anaconda device deployment simulations were also conducted to obtain data that could be used for validation purposes.

 Data sets per specimen were to include information as follows:

- Uniaxial stress-strain data for each arterial layer in both axial and circumferential directions.
- Uniaxial stress-strain data of the intact wall.
- Pressure - Diameter (external) readings of tubular sections.
- Deformation measurements of the arterial vessel with a proximal ring implanted (Device deployment simulations).
- Picrosirius red staining to determine the mean collagen fibre angle and distribution per arterial layer.

Wherever possible, experimental data were to be kept wall layer-specific. For the proposed use of the material models developed, human specimens were to fall within the age range of 40 to 75 years, the age at which most endovascular treatments are administered.

Due to the mechanical importance of the proximal ring, only its interactions with specimens were examined during this programme.

3.2 Experimental setup

The programme objectives of conducting deployment simulations in addition to uniaxial/biaxial characterisation were beyond the capabilities of any single testing rig at the University of Strathclyde. For this reason, a Bose 3200 ElectroForce was utilised for all uniaxial work whilst a custom built environmental chamber was developed in order to carry out pressurisation and deployment simulations. An overview of both rigs will be presented here.

3.2.1 Bose 3200

The Bose 3200, figure 3.1, is a bespoke biological tissue test instrument. It features a single ElectroForce linear actuator with a stroke length of 12 mm. The actuator is capable of displacement increments of .005 mm and frequencies up to 200 Hz. For this project, a Bose 250 g load cell was used with a resolution of $\pm 0.25\%$ FSO.

Figure 3.1: **Bose 3200 Series III test instrument.**

For control software, the Bose WinTest 4.1 programme was utilised. The software is fully comprehensive, allowing for waveform generation, data acquisition and instrument control. The software's block waveform function was used for waveform generation, the likes of which can be seen in figure 3.2. Each specimen tested was subjected to 12 cycles, each consisting of a series of displacement controlled loads. Various displacements and dwells were used for specimen training before three final characterisation cycles were performed. The characterisation cycles were conducted at a rate of 1.2 mm/min, in accordance with rates proposed by previous studies [67].

Data acquisition occurred through the use of data scans. Twenty scans of 60 seconds each were used to cover the generated waveform. 1200 data points were used per scan resulting in 20 data points per second being logged.

TuneIQ control optimisation was used within this project. As a built in function of WinTest 4.1, the TuneIQ function essentially allowed PID control loops to be optimised by using an automatic tuning process. Porcine specimens were used for optimisation.
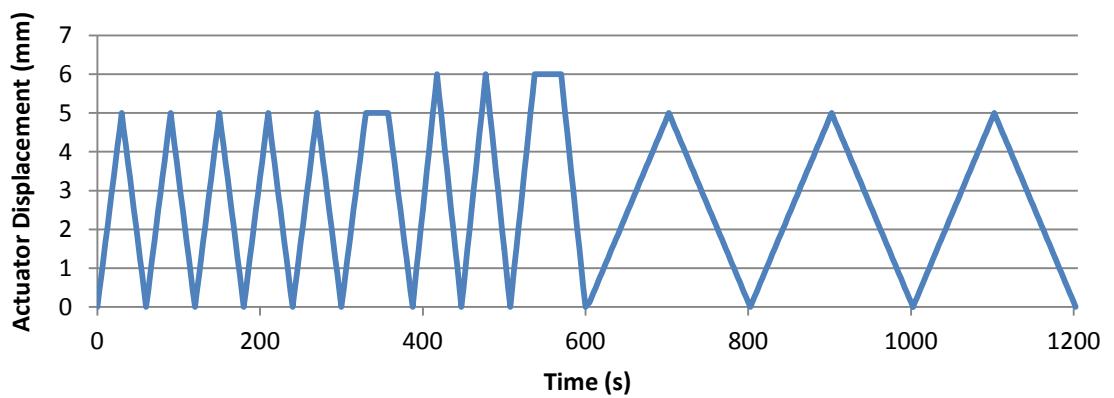

Figure 3.2: **Bose waveform used during experimentation.**

A Digital Video Extensometer (DVE) was used to capture strain data during uniaxial extension. The built-in WinTest 4.1 application, Vision 4.1, was used for this purpose. The DVE application operated by tracking five markers placed on specimens. The markers were tracked using a Prosilica, Allied Vision Technologies fixed lens high shutter speed camera.

Resolution of the DVE system was setup dependent, with optimum conditions allowing a resolution determined by the span of one camera pixel. The span of the pixel could be calculated through equation 3.1 [91], where x is the distance between the camera and specimen in inches, whilst y is the pixel span in millimetres.

$$y = \frac{.66x + .248}{480} \tag{3.1}$$

Within this project, a typical working distance of 12 inches was used, equating to a pixel span of approximately 0.017 mm. With extensions in the region of 5 mm being imparted on uniaxial specimens, theoretical errors of 0.34% within readings could be expected at maximum extension. In practice band noise and external factors resulted in resolutions that were highly setup dependant. During protocol development, resolution typically allowed for strain increments of 0.15% to be measured.

The Allied Vision Technologies camera captured at a rate of 200 frames per second, with strain calculations being performed in real time. As the 200 frames per second were faster than the WinTest 4.1 data acquisition, the camera frame rate had no significant influence on overall accuracy. Strain calculations were transferred from the Vision application to WinTest as Green-Lagrange strains.

3.2.2 Deployment rig

A custom-built pressurisation rig was developed for the purposes of the vascular testing programme. Once developed, porcine specimens were tested to ensure the correct operation of the entire rig. The rig in its final form, as shown in figures 3.3 and 3.4, comprised of various components, all of which were independently calibrated and verified. Figure 3.3 is a schematic representation of figure 3.4.

The rig used 2 syringe drivers (1)(2), to force a pbs solution through a heated water bath (3) into the test specimen (5). Through adjusting syringe driver flow rates, the pressure inside the test specimen could be controlled. Pressures and temperatures inside the specimen were measured through pressure transducers (4) and an implanted thermocouple (9). During experimentation, the specimen was kept in a sealed environmental chamber, the temperature of which was set to 37°C through a feedback controlled air heater (8). Independently, the environmental chamber's atmospheric temperature was verified using a secondary thermocouple (7), instrumentation of which could also be used to measure humidity levels. Specimen diameter readings were recorded through a laser micrometer system (6).
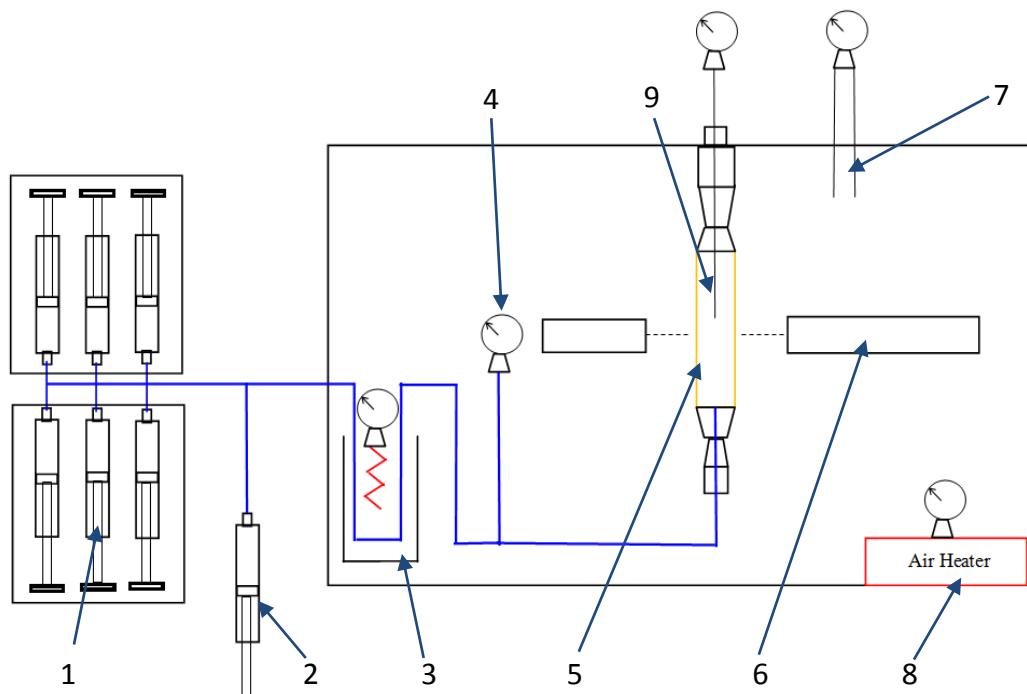

*Figure 3.3:* **Schematic of the custom developed experimentation rig.**
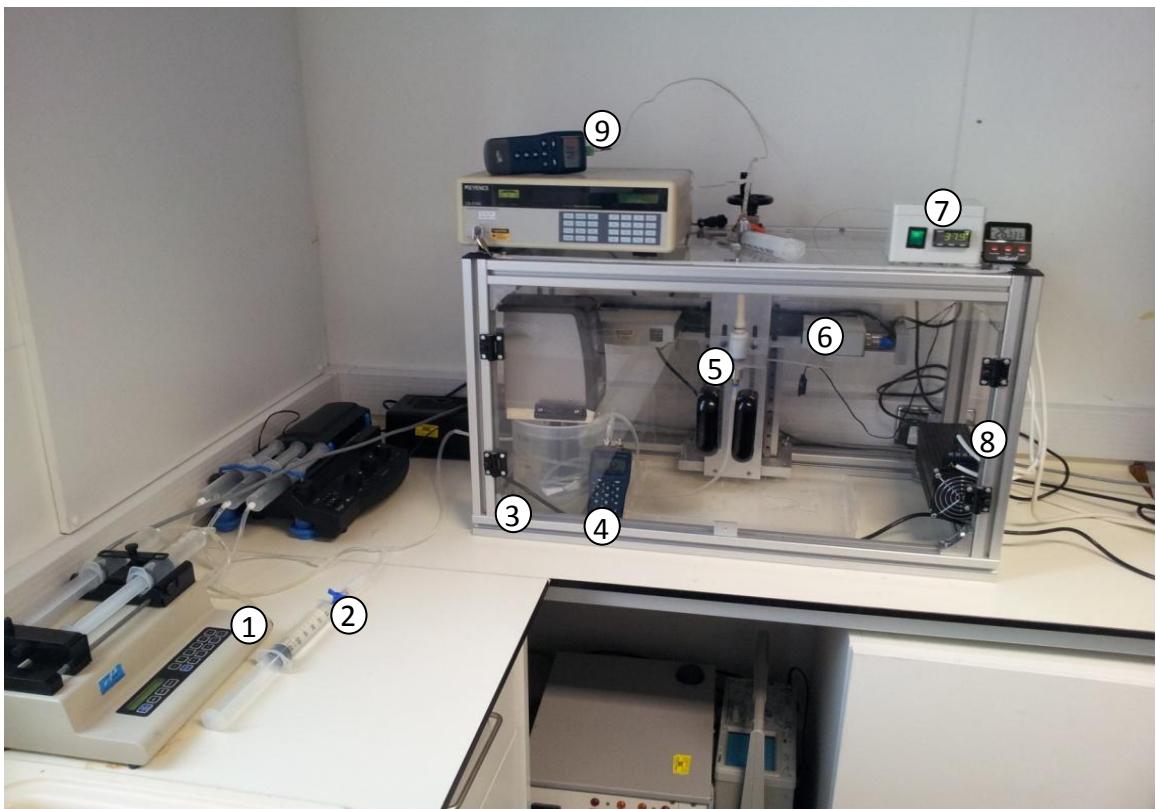
Figure 3.4: **Custom developed pressure-diameter rig.**

With reference to figure 3.4, further details are provided here on the equipment used:

(1) Cole-Parmer dual-syringe infusion/withdrawal pump model 74900-20. The Cole-Parmer syringe pump was used for infusion and withdrawal of the pbs solution into the specimen. A secondary pump was on standby in the event of excessive leaking rates. The Cole-Parmer syringe driver allowed for flow accuracies within .5% of specified values.

(2) An additional in-line syringe was installed. The syringe was typically used during initial infusion. During initial infusion, air within the specimen was vented through a valve and replaced with the heated buffer solution.

(3) Grant Optima^{TM} TX150 high-performance programmemable digital heating circulator. The heating element was placed in a water bath, the temperature of which was held between 50°C and 55°C. The temperature was varied within this range according to that needed to achieve an in

specimen solution temperature of 37$^{\text{o}}$C. The fluid line that passed through the heated water bath was approximately 1500 mm in length.

(4) Digitron Digital 2020P7 pressure meter. Suitable for testing in high humidity and temperatures levels.

(5) Specimens were fixed to the rig using a number of custom designed fittings ranging from 14 to 46 mm in diameter, in 2 mm increments, the drawings of which are provided in appendix 2. The fittings chosen were those that had the same approximate diameter of the artery vessel when pressurised to 100 mmHg. The large range of fittings insured minimal fixture distortion and fittings points.

(6) Keyence LS-3100 laser scan micrometer. The scanning heads, with a sensitivity of .001 mm, were placed within the environmental chamber. During prolonged experimental procedures icepacks were placed on top of the laser heads to avoid overheating. The laser micrometer was fully calibrated using United Kingdom Accreditation Service (UKAS) accredited calibration blocks.

(7) Secondary thermometer and humidity meter for verification purposes.

(8) Air heater operated using a West 3200 single loop controller. A flexible Type-K thermocouple was placed next to the specimen during testing.

(9) Digitron Digital 2029T Thermometer and flexible Type-K thermocouple. The thermocouple was fed through fittings and placed inside the specimen during experimentation.

As listed, three thermocouples were used within the test setup. Only when readings from these three apparatus converged within a 2$^{\text{o}}$C (36.0 to 38.0$^{\text{o}}$C) envelope did experimentation take place. During protocol development, a second analogue pressure meter was also used to verify pressure readings and the correct operation of equipment involved. Placing the heated water bath inside the sealed environmental chamber ensured that humidity levels within the chamber remained above 70%.

3.2.3 Proximal ring devices

Proximal rings commissioned for this project were identical to those used in 3rd generation Anacondas. As with the fresh nature of biological tissue requested, ring devices used during deployment simulations had to be pre-manufactured before specimens could be received.

To ensure correct oversizing of specimens ranging from 17.5 to 31 mm lumen diameters, seven different sized proximal rings were commissioned. For each of these ring sizes, three different Lutz numbers (1.3, 0.9, and 0.5) were commissioned by adjusting wire diameter and the number of turns from which each consisted. The Lutz number, as expressed in equation 3.2 and derived in appendix 5, is a method used by Vascutek to define ring stiffness, first proposed by Prof Karl-Lutz Lauterjung, inventor of the Anaconda ring stent design.

The requirement for different ring strengths was driven by FE model validation requirements as illustrated in figure 3.5 which displays the typical behaviour of an artery during pressurisation. As can be seen, during pressurisation, increasing pressure tends to yield smaller displacement increments. For FE model validation purposes, during device deployment it was beneficial to generate displacements close to the plateau whilst avoiding straying onto it. If deployment simulations were carried out within regions of the plateau, comparison of deformations to FE results would be less effective in ascertaining the accuracy of the FE simulation. It was, however, useful to operate as near to the plateau as possible, as again, for validation purposes, it was beneficial for the ring, not the internal pressure, to be the dominant deformation force.

All devices commissioned for this study are summarised in table 3.1. The table provides device details and introduces a naming convention adhered to for the rest of this thesis. The table also summarises vessel compatibility for each device used. An example of the devices used is provided in figure 3.6.

$$Lutz = \left(\frac{Diameter_{wire}{}^4 \times N_{turns}}{Inner\ Diameter_{ring}{}^3} \right) \times 10^6 \qquad \textbf{(3.2)}$$
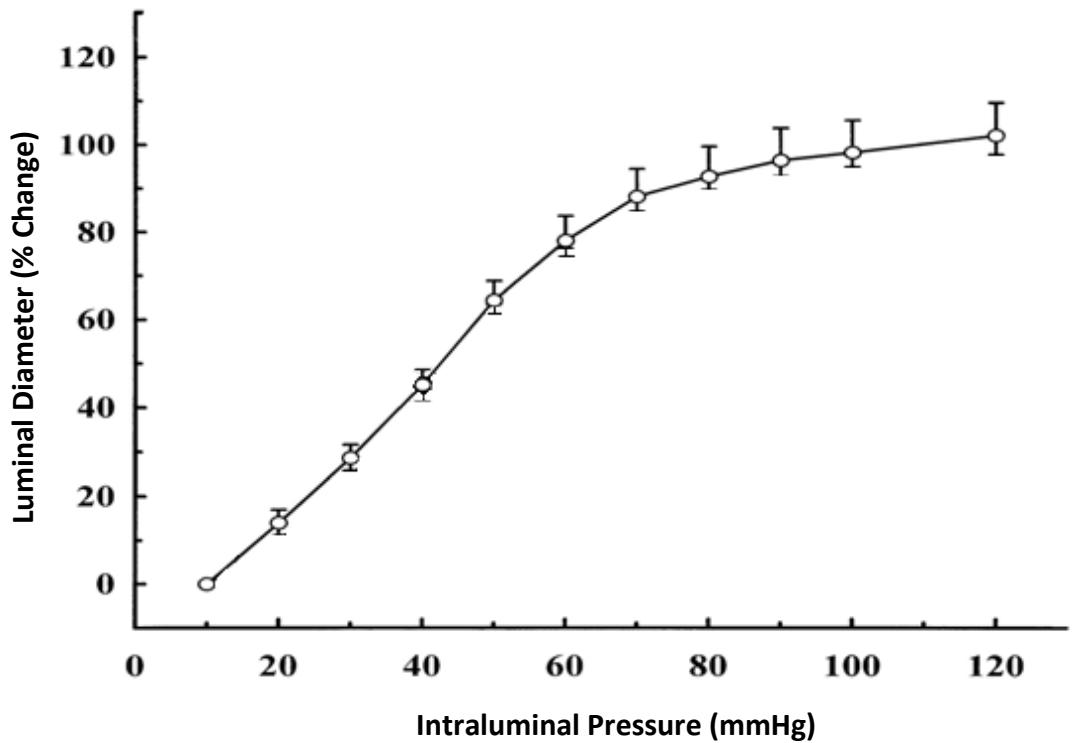
Figure 3.5: **Pressure-Diameter response of a rat mesenteric artery obtain from Ref** [92]**. The initial response of the tissue tends to be elastic, with increased pressurisation leading to diminishing displacement increments.**
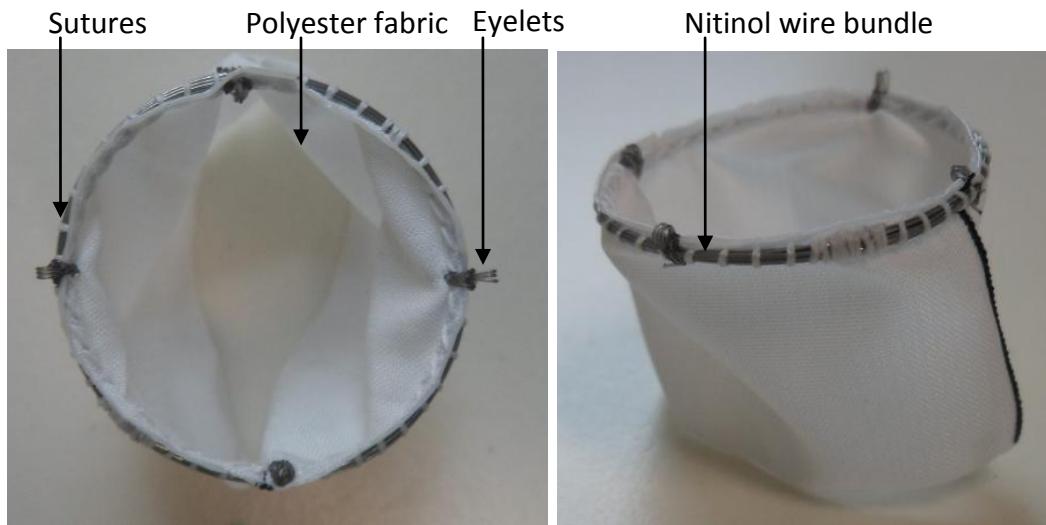

Figure 3.6: **R_23 Lutz 1.3 commissioned for the vascular testing programme. Nitinol wire was wound from a straight drawn condition into a bundle and sutured onto knitted polyester graft fabric material using 1mm suture spacing. Four eyelets, manufactured from nylon, were added to the design to allow for deployment.**

Table 3.1: **List of devices commissioned for the vascular testing programme. The table contains all critical dimensions and specifies ring-specimen compatibility.**

Device outer diameter	Ring No.	Compatible Vessel		Wire Diameter (mm)	No. of turns	Bundle Diameter Theoretical (mm)	Ring Inner Diameter	Flat Ring Mean Diameter (mm)	Flat Ring Outer Diameter (mm)	Lutz Ring Number (from Inner D)
		Min	Max							
21.5	R_21 Lutz 1.3	17.50	19.50	0.18	9.00	0.69	19.70	20.39	21.09	1.24
	R_21 Lutz 0.9	17.50	19.50	0.18	7.00	0.54	19.70	20.24	20.78	0.96
	R_21 Lutz 0.5	17.50	19.50	0.18	4.00	0.31	19.70	20.01	20.32	0.55
23.5	R_23 Lutz 1.3	19.50	21.00	0.18	13.00	1.00	21.70	22.70	23.71	1.34
	R_23 Lutz 0.9	19.50	21.00	0.18	9.00	0.69	21.70	22.39	23.09	0.92
	R_23 Lutz 0.5	19.50	21.00	0.18	5.00	0.39	21.70	22.09	22.47	0.51
25.5	R_25 Lutz 1.3	21.00	23.00	0.20	11.00	0.94	23.70	24.64	25.59	1.32
	R_25 Lutz 0.9	21.00	23.00	0.20	8.00	0.69	23.70	24.39	25.07	0.96
	R_25 Lutz 0.5	21.00	23.00	0.20	4.00	0.34	23.70	24.04	24.39	0.48
28.0	R_28 Lutz 1.3	23.00	25.00	0.22	10.00	0.94	25.70	26.64	27.59	1.38
	R_28 Lutz 0.9	23.00	25.00	0.22	7.00	0.66	25.70	26.36	27.02	0.97
	R_28 Lutz 0.5	23.00	25.00	0.22	4.00	0.38	25.70	26.08	26.45	0.55
30.5	R_30 Lutz 1.3	25.00	27.50	0.22	12.00	1.13	27.70	28.83	29.96	1.32
	R_30 Lutz 0.9	25.00	27.50	0.22	8.00	0.75	27.70	28.45	29.21	0.88
	R_30 Lutz 0.5	25.00	27.50	0.22	5.00	0.47	27.70	28.17	28.64	0.55
32.0	R_32 Lutz 1.3	26.50	29.00	0.22	14.00	1.32	29.70	31.02	32.34	1.25
	R_32 Lutz 0.9	26.50	29.00	0.22	10.00	0.94	29.70	30.64	31.59	0.89
	R_32 Lutz 0.5	26.50	29.00	0.22	6.00	0.57	29.70	30.27	30.83	0.54
34.0	R_34 Lutz 1.3	28.50	31.00	0.24	12.00	1.24	31.70	32.94	34.17	1.25
	R_34 Lutz 0.9	28.50	31.00	0.24	9.00	0.93	31.70	32.63	33.55	0.94
	R_34 Lutz 0.5	28.50	31.00	0.24	5.00	0.51	31.70	32.21	32.73	0.52

Ring devices were manufactured by Terumo Vascutek, by the same technicians whom manufacture Anaconda devices. Anaconda device manufacturing protocols were used when suturing Nitinol wire bundles onto knitted polyester fabric (typically 1.0 mm spacing between sutures). The Nitinol used in the construction of these devices, was again, identical to that used for the Anaconda device (Fort Wayne, Niti#1, Super-Elastic Straight Annealed with etched surface).

3.2.4 Anaconda delivery system

During protocol development for the vascular testing programme, deployment of the ring device into the artery was found to be problematic. The main difficulties were associated with deployment of the device into a suitable position whilst maintaining stability. Once in a suitable position, the device also had to be manipulated into a quarter symmetric shape to meet *in situ* and FE modelling assumptions.

To overcome these issues, the author, alongside Mr David Stevenson Head of Innovation at Vascutek, modified a 1st generation Anaconda delivery system for the delivery of single proximal rings. The delivery system, as seen in figure 3.7, allowed for the compaction of the device into catheter-like diameters, manipulation of the device into position, and deployment of the device. Through a series of tethering wires, the device could be redeployed as necessary until in a satisfactory position and orientation. Once the device was deployed, the tethers could be removed and the delivery system could be extracted. Throughout the deployment process, focus was placed on replicating the load history that the ring would experience in practice.
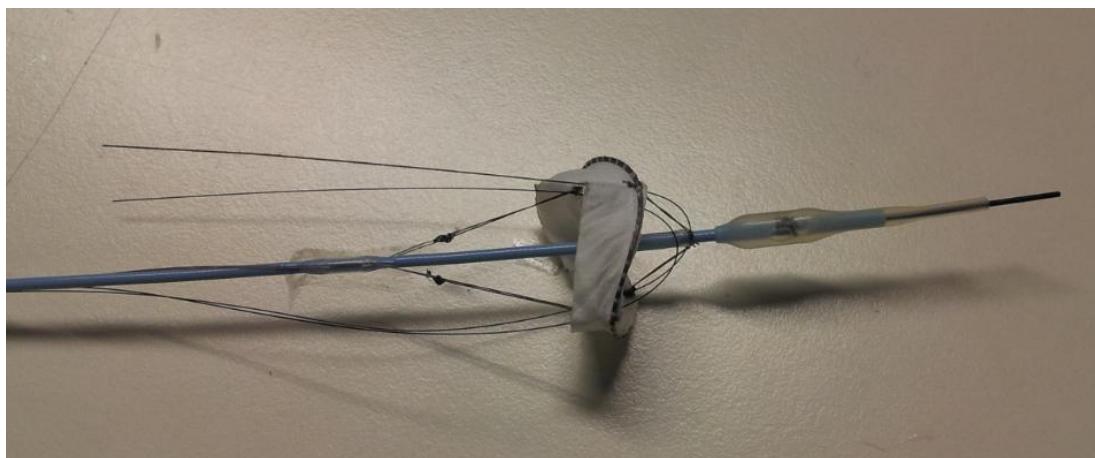
Figure 3.7: **Adapted Anaconda device delivery head. Tethering wires were looped through the nylon eyelets, allowing for compaction into sheath-like diameters. The delivery head was used to place the device into a suitable position. Once in position, the tethering wires were slowly removed, expanding the device.**

3.3 Protocol

This section of the thesis will outline the protocol that was adhered to during the Vascular testing programme. The protocol was established through comprehensive experimentation with porcine specimens. Only when the protocol was fully verified were human specimens acquired for the presented work. The protocol was independently scrutinised by Dr Philip Riches (Department of Biomedical Engineering, The University of Strathclyde) a licensed practitioner in human anatomy and dissection.

3.3.1 Specimen acquisition and preparation

An agreement was set in place with Biopta Ltd, a company that specialises in the acquisition of human vascular tissue. The agreement was subject to an ethical review by an internal body within Biopta and the University of Strathclyde's own ethical review board.

An agreement was set in place for three abdominal specimens, each specimen being defined as the aortic tissue between the diaphragm and the aortic bifurcation as shown in figure 3.8. In accordance to characterisation studies [93]–[95], all characterisation experiments were done within 48 hours of specimen extraction. Patient data on age, sex and relevant medical records were supplied with every sample provided. From the moment of extraction specimens were kept in a phosphate buffered solution (pH 7.4) at 4°C.

On reception, the specimen was dissected into two regions as shown in figure 3.9. Region ABT.1 was identified as the region spanning axially 30 mm above the superior mesenteric artery, whilst region ABT.2 was identified as the region between the lower renal artery and the aortic bifurcation. Excessive perivascular tissue was removed by Biopta staff members.

Through an axial incision through sample ABT.1, a rectangular patch was produced. This patch was then separated into its three wall layer constituents using a microscope, scalpel and tweezers. Once each of the layers was separated, the

microscope was used to identify any damage caused by the procedure. Tissue samples with excessive damage or visible disease were rejected from later characterisation work.

Layer separation work was conducted by a trained Biopta staff member after developing their techniques using bovine specimens.
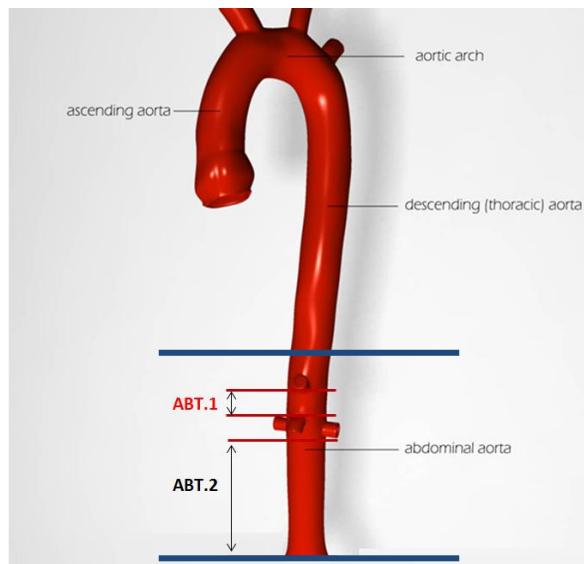

*Figure 3.8:* **Labelled human aortic system**
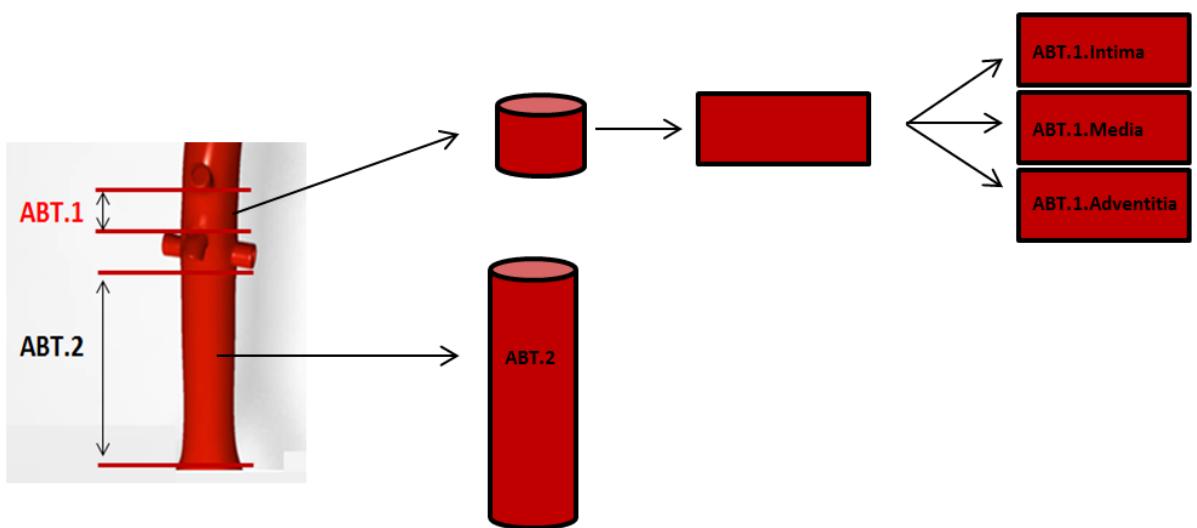
Figure 3.9: **Preparation requirements for experimental work.**

3.3.2 Experimental procedures

This section will summarise experimental procedures as used during the testing.

3.3.2.1 Uniaxial experimentation procedures

1. Surfaces were sterilised and necessary equipment gathered.
2. The Bose 3200 was prepared and fitted with a heated (37°C) water bath.
3. The DVE was installed as shown in figure 3.10.
4. Four Specimens, two in an axial and two in the circumferential direction, were produced from each arterial layer. Each specimen measured roughly 40 mm in length and 5 mm in width.
5. Excess moisture was removed from the sample using absorbent paper. Five markers were placed on each sample. Small sections of emery paper were glued to the edges of each sample to minimise slipping once clamped. Care was taken not to affect the gauge length which was defined by the edges of the paper.
6. The sample was then placed into the Bose 3200 rig and left to equilibrate for 20 minutes before executing the actuator waveform, as shown in figure 3.2.
7. The waveform could be adjusted to optimise for the specimen's specific gauge length and stress-strain response.
8. Detailed measurements of sample length, width, and gauge length were recorded using a digital vernier caliper.
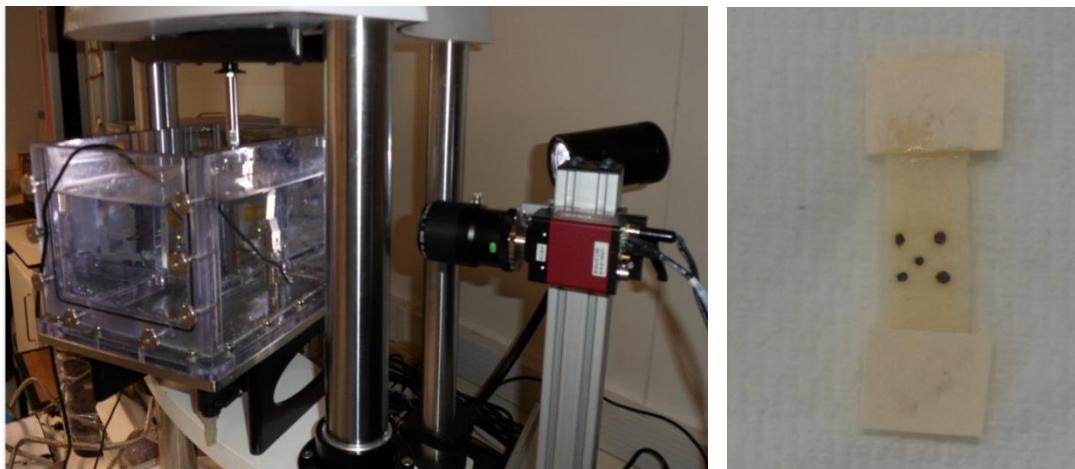
Figure 3.10: **Left, Bose 3200 test setup for uniaxial charaterisation. Right, prepared porcine protocol development specimen.**

3.3.2.2 Pressure-diameter and deployment procedures

1. The inflation rig was prepared through filling syringes with a calcium free pbs solution. Air and water heaters were used to set the environmental chamber temperature to 37°C. During protocol, development high humidity levels were found to help keep specimens hydrated. Care was therefore taken to ensure that the humidity levels rose above 70% before work commenced.

2. Tubular sample ABT.2 was inspected for features and arterial disease. A careful note of the specimen's condition and detailed geometric measurements were taken.

3. To allow for pressurisation, all major branching vessels were plugged and sutured. Branching vessels were plugged using resin, taking care as to not affect gauge sections. Cotton balls or absorbent paper towels were additionally used for larger branching vessels to minimise leaking.

4. The tubular section was then fixed onto the rig at 15% axial stretch and filled with the saline solution using syringe drivers.

5. Leaking rates were checked before allowing the specimen to equilibrate for 30 minutes. Specimens were occasionally damped using a spray bottle containing a heated buffer solution.

6. Once equilibrated for 20 minutes, the specimen was subjected to 15 training cycles, in which internal pressure was varied between 0 and 160 mmHg, at an approximate rate of 2 mmHg/per second

7. With leaking through small branching vessels and capillary beds inevitable, syringe drivers were refilled as necessary.

8. Using the laser micrometer, pressure-diameter readings were recorded at two locations: the location where the proximal ring device was to be deployed and the other just distal of the inferior mesenteric artery.

9. The vessel was removed from the rig and the chosen device was deployed. The device choice was based on the ring size which would give a Ring/Vessel diameter oversize of between 10 to 20%. The ring's Lutz number was based on vessel compliance as measured during pressurisation.

10. The vessel was reattached to the rig with a 15% axial stretch and allowed to equilibrate for 10 minutes.

11. After five training cycles, deformations imparted by the ring were captured using the laser micrometer at pressures of 0, 60, 80, 100 and 120 mmHg. The recording process involved noting vessel diameter measurements at 1 mm axial increments and then repeating the process at various angles of rotation. Through this methodology a 3D deformation map was obtained as illustrated in figure 3.11. As specifics regarding data collection were dependant on a host of factors such as the nature of arterial surface features, details regarding the data collected will be provided per specimen in section 3.4.

(a)   (b)   (c)
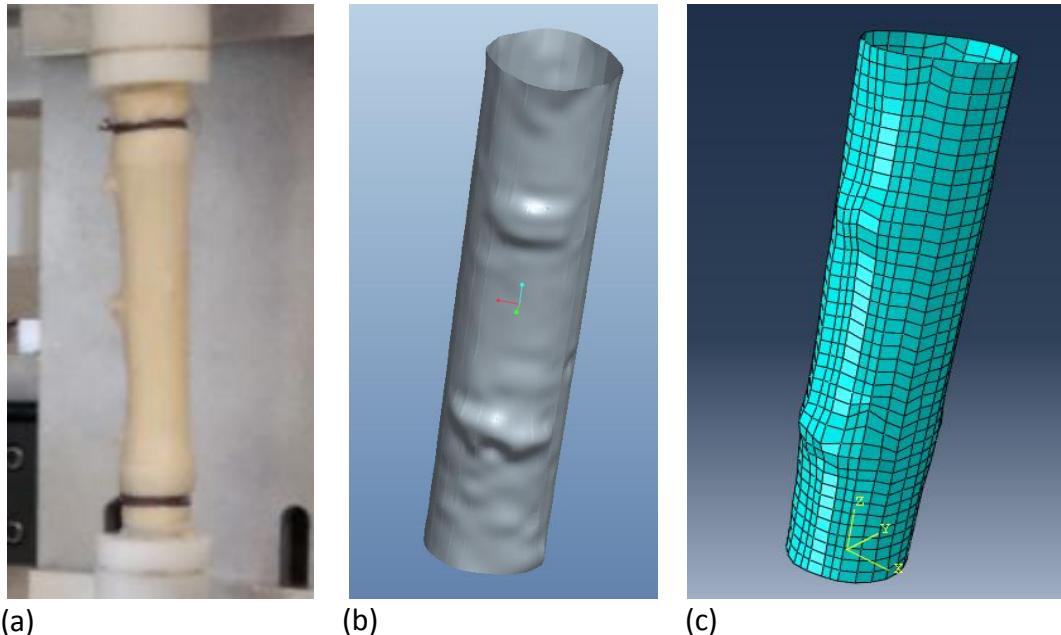
Figure 3.11: **Process capability outline for 3D reconstruction of deformed specimens. Data points were obtained during testing (a). These data points could then be imported into CAD software for the generation of a surface (b). Created models could then be imported into FE software for mesh development and load applications (c).**

3.4 Results

Results presented here illustrates major findings of the testing program and represents the data used for FE modelling purposes. Data for all specimens tested can be found appendix 3.

3.4.1 Specimen 1

Table 3.2 summarises specimen 1's donor information. These details are provided here due to their potential influence on vascular mechanics. With a study of the cause of death, medical history and medication, only diabetes was highlighted as having a possible impact on vascular mechanics as it has been shown to lead to stiffening of the arterial wall [96]. Due to the patient's relatively young age, this was, however, only a minor concern. On first appearance, the specimen seemed healthy with only a slight irregular shape below the inferior mesenteric artery, as shown in figure 3.12.

Table 3.2: Specimen 1's donor information

Age	43
Sex	Female
Race	Caucasian
Height	1.61 Meters
Weight	102 kg
Cause of Death	Intraparenchymal haemorrhage
Medical History	Factor 5 Leiden deficiency, diabetes for 14 years starting as gestational diabetes. Diverticulitis for 4 years
Medications	Glucophage, Coumadin, Paxil, vitamin B12, Cipro for UTI 2 weeks prior to admission
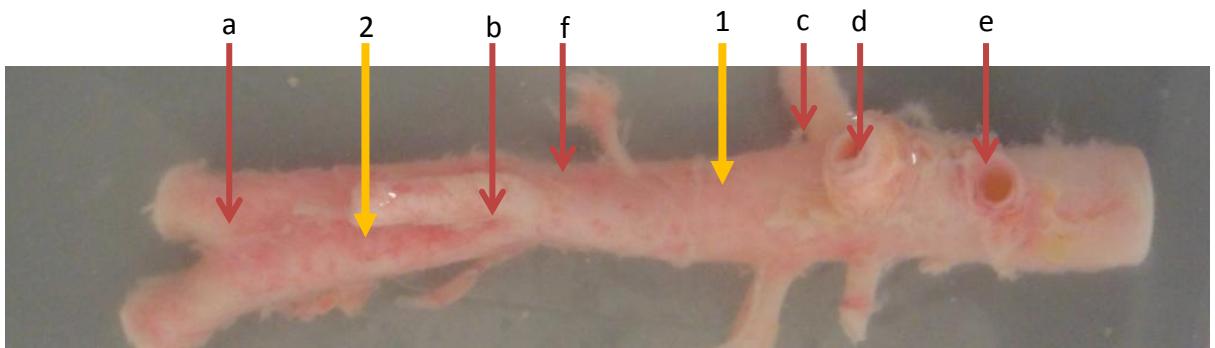
Figure 3.12: **Image of specimen 1. Aortic features were identified as follows: aortic bifurcation (a), inferior mesenteric artery (b), renal artery (c), superior mesenteric artery (d) and finally the celiac trunk (e). Irregular narrowing of the aorta was noted (f). Notations 1 and 2 point towards locations at which pressure-diameter readings were obtained.**

3.4.1.1 Separation of individual layers

On receipt of specimen 1, the donor's young age raised concerns about the layer separation process. Studies have found that in young patients the intimal layer can be thin [73]. This was thought could lead to the intima tearing during separation. Indeed, as can be seen in figure 3.13, layer separation was difficult with tearing unavoidable. Tearing generally occurred around arterial features, such as small branching vessels, leaving only small patches useable for uniaxial characterisation. Once identified, medial and adventitial layers separated without any difficulty.

A much larger number of branching vessels were encountered within the ABT.1 sample region than what was expected. This was seen as a patient specific variation. Separation of layers did, however, confirm that the section was relatively healthy with no significant disease noted.
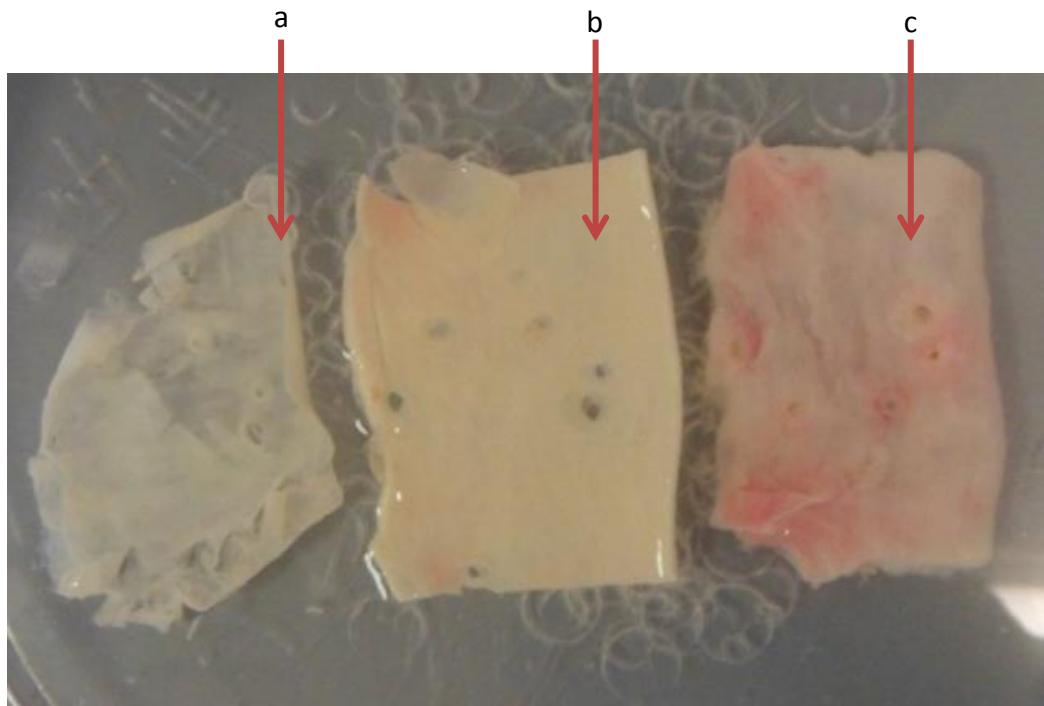
Figure 3.13: **Specimen 1's arterial layers separated. Layers were identified as the intima (a), the media (b) and adventitia (c). The intimal layer was damaged during separation whilst the media and adventitia separated with more ease. Holes within the layers are the location at which branching vessels were removed.**

3.4.1.2 Layer-specific uniaxial results

With arterial layers separated, the protocol as defined in section 3.4 of this report was followed to obtain uniaxial stress-strain results. Due to the difficulties encountered during intimal separation, only two uniaxial samples could be harvested from this layer (one circumferential and one axial).

Figure 3.14 depicts stress-strain (engineering) results obtained from each layer characterised. The results are comparable in nature to other publications addressing the stress-strain properties of vascular tissue [72]. In contrast to other published studies, which report nonlinear stiffening around 12%, was the elastic nature of the intima which was seen to stiffen between 20 and 30%.

With reference to the limited data available, the response of the intima is commonly dominated by collagen alignment at low strain values. The elastic response of specimen 1's intima can be linked to the patient's age and relative health of the samples tested. Intimal thickening is common with age, with the layer becoming more mechanically significant with time. The results can therefore be explained when noting that most of the abdominal aorta data available for comparison in the literature are from much older donors. Furthermore, results shown here are topographically site specific, for which no published stress-strain data exists. Until further data becomes available on the mechanical variability across aortic regions, little value can be placed in direct comparison against other studies.

Specimen's 1 intimal layer was very thin in nature. It should be noted that surface damage, due to layer separation, could also have had an impact on the results. Although microscopic studies of the samples suggested minimal detectable damage, tears and voids created during the separation process were unavoidable. The results shown in figure 3.14 confirm the highly orthotropic nature of vascular tissue, and emphasises the need for a layer-specific approach to vascular FE modelling.
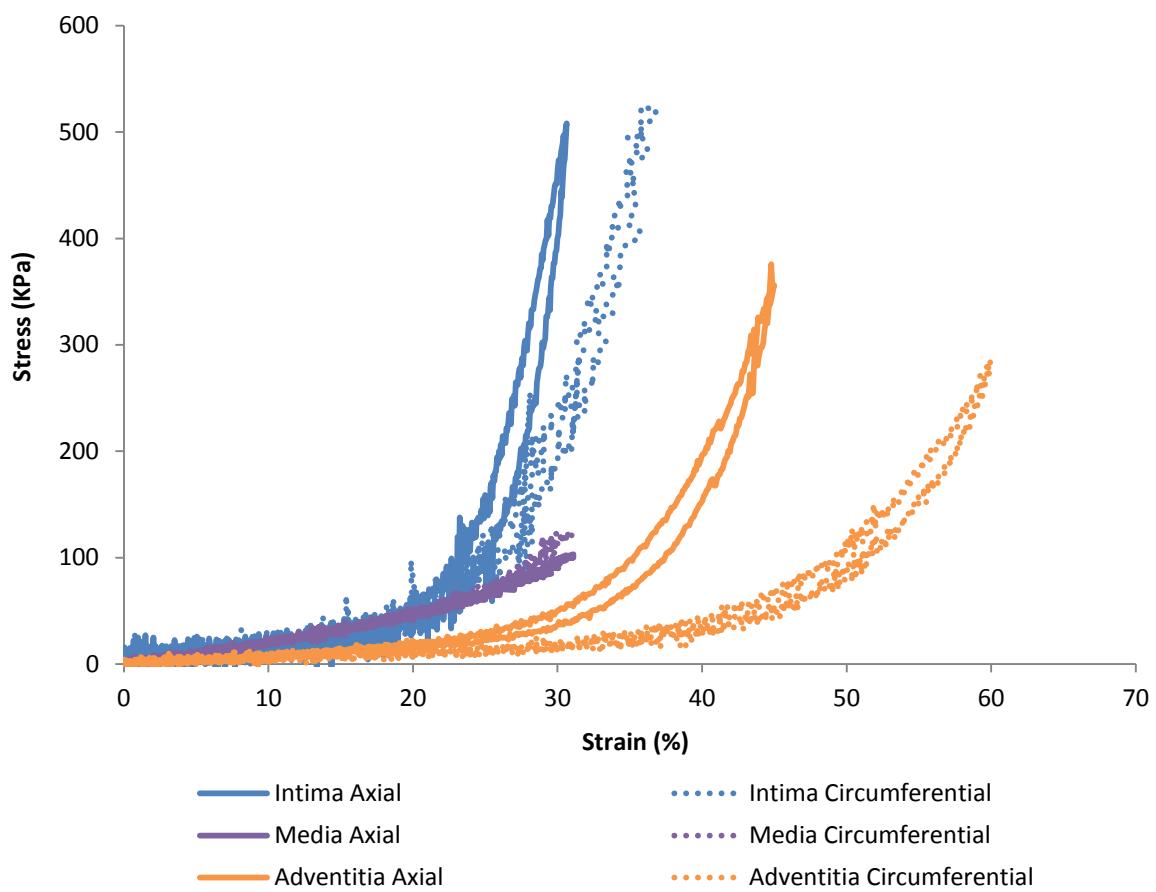
Figure 3.14: **Specimen 1's uniaxial characterisation results expressed in Engineering stress and strain.**

3.4.1.3 Pressure diameter

Pressure diameter readings were obtained from two locations on specimen 1 ABT.2. One of these was below the renal arteries, at the location at which the device would be implanted, and the other, 1.5 cm above the bifurcation (figure 3.15). Although the specimen at first appearance seemed irregular in shape as shown in figure 3.12, it tended towards a uniformly cylindrical shape when stretched to 15% and fitted to the rig.

For pressurization, branching vessels such as the renal and inferior mesenteric arteries were tied. Where pressurisation resulted in excessive leaking, an additional paper plug was inserted into the branching vessel as shown in figure 3.15. Care was taken not to affect the gauge section.

Figure 3.15: **Image of a renal artery with paper plug inserted. An adhesive was used to keep the plug in place.**

Figure 3.16 shows the pressure-diameter results obtained from location 1 and 2. As can be seen from this figure, a nonlinear pressure-diameter response was obtained, typical of soft tissue under increasing deformation.

Using equation 3.3 to calculate compliance as proposed by Langewouter *et al.* [97], compliance figures of 2.88 and 3.42 were obtained for location 1 and 2 respectively.

$$C_{Compliance} = \left(\frac{Vessel\ OD\ at\ 120\ mmHg - Vessel\ OD\ at\ 80\ mmHg}{Vessel\ OD\ at\ 120\ mmHg} \right) \times 100 \quad \textbf{(3.3)}$$
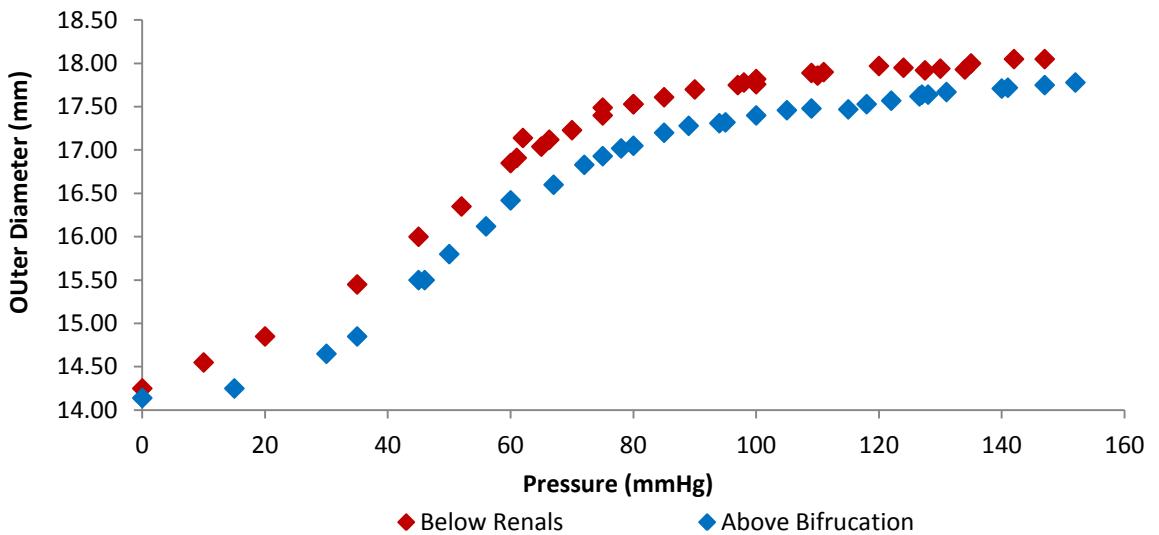
Figure 3.16: **Pressure diameter results for specimen 1. A nonlinear relationship was established, typical for that of biological tissue under increased deformation.**

3.4.1.4 Deployment simulation

For deployment, device R_21_Lutz_1.3 was chosen from table 3.1. A full set of data points were extracted which characterised the deformations at the three pressures 0, 80 and 140 mmHg, results of which is shown in figure 3.17. The process of device deployment was challenging. The single ring configuration within this particular test was highly unstable during deployment and pressurisation. Leaking became an issue at larger pressures, resulting in several attempts to obtain data points. Figure 3.17 represents a section of the specimen tested, where the baseline for the axial measurements were taken to be from the bottom fitting. Fittings induced negligible distortion, close to connection end points.

An observation made from results presented here is that there was no significant change in deformation imparted by the ring during pressurisation from 0 mmHg to 80 mmHg. This indicated that the ring deformed the vessel to diameters noted within the physiologic pressure range (80 mmHg to 120 mmHg) once implanted. Further pressurisation to 140 mmHg deformed the vessel to a cylindrical form, at which point, deformations imparted by the ring were minimal.
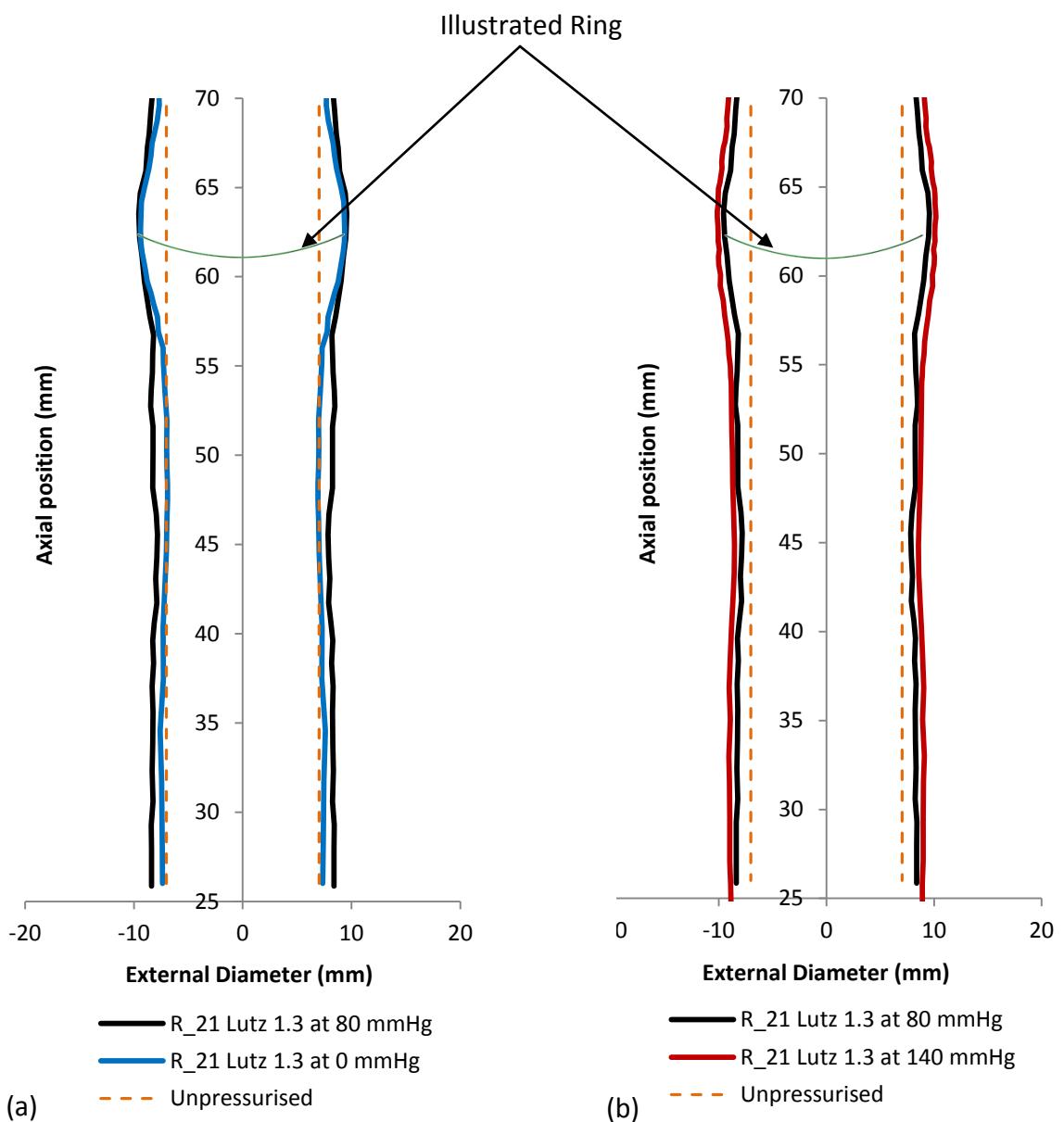

Figure 3.17: **Edge profile results for device R_21 Lutz 1.3 deployed at pressure 0, 80 and 140 mmHg.**

Figure 3.18 (b) is a plot of the peak-to-peak compliance over a range of pressures. The results shown here depict an initial, unpressurised deformation of 19.7 mm which increases gradually to 19.8 mm at 80 mmHg. Here, the diameter was seen to increase rapidly to 20.15 mm at 120 mmHg. The highest peak-to-peak deformation was measured at 20.17 mm at 130 mmHg, at which point an inflection was noticed.

The initial, unresponsive stage seen in figure 3.18 was a function of the device being the dominant deformation force. With the pressure continuing to increase, point A marks the stage where the pressure became significant and induced further deformations. The inflection point B is thought to be unique to the ring's saddle shape. With the ring deployed, the vessel takes on a non-circular form. At point B the internal pressure deformed the vessel into a cylindrical shape, reducing peak-to-peak deformations.

The results shown in figure 3.18 supports the choice of device used during the experimental work. As seen in figure 3.18 (b), point A coincides very well with diastolic pressures, whilst point B coincides well with systolic pressures. During service this property would be beneficial to the performance of the proximal ring so as not to impede hemodynamics. The small window of operation can also be seen where the two inflection points narrowly encapsulate the physiological range. This highlights the challenges faced by design engineers and the need for advanced design tools.

The peak-to-peak deformation and its variation with pressure are closely linked to the maximum strain experienced by the device and therefore the mechanism that induces fatigue *in situ*. Figure 3.18 (b) is therefore central to the design challenges that companies such as Vascutek face and as such is critical to the work herein.

Peak-to-peak deformations imparted
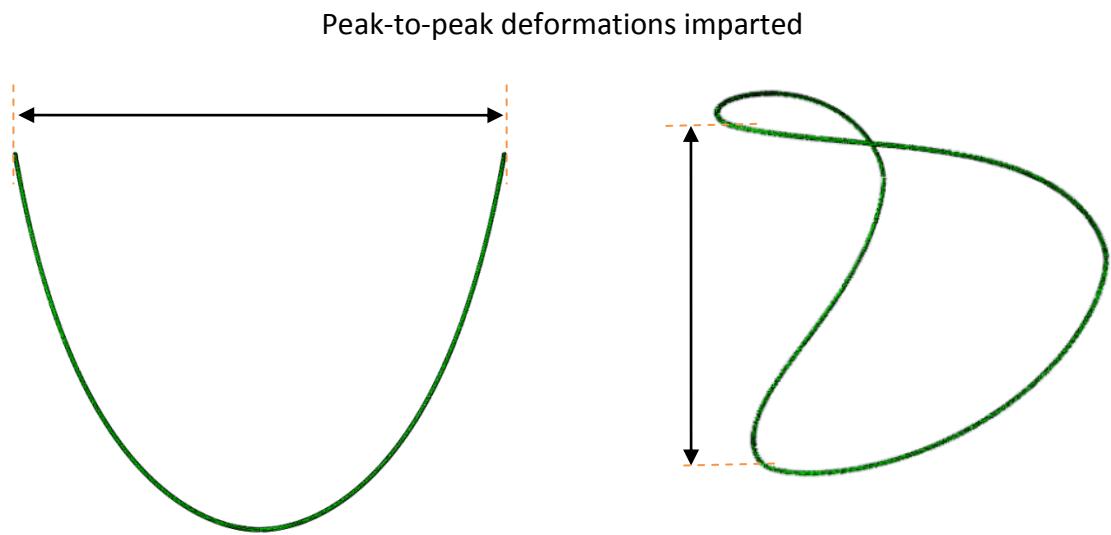
Figure 3.18 (a): **Peak-to-peak deformations coincide with the maximum deformations imparted by the ring compacted into a saddle shape.**
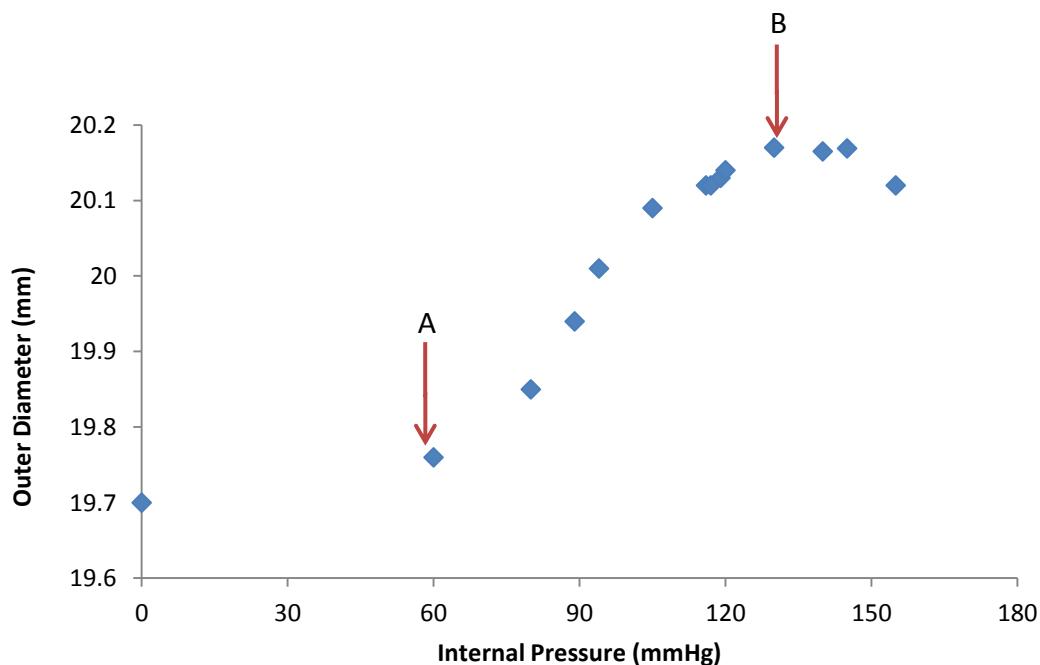

Figure 3.18 (b): **Peak-to-peak deformations over a range of pressures. Deformations were obtained for a comprehensive pressure range, extending from 0 mmHg to 158 mmHg. Inflection point B within this study was not expected and was thought to be associated with the complex interactions of the ring's unique saddle shape and the vascular wall.**

3.4.2 Specimen 2 data

Table 3.3 summarises donor 2's patient information. From a study of the patient's medical history, hypertension was seen as being most relevant to the mechanical properties of the specimen received. Synthroid, a drug often used in the treatment of hypothyroidism, was listed as a prescribed medication alongside Prilosec which is commonly used in the treatment of pyrosis. Neither of these drugs has been reported as having a significant influence on the mechanical properties of vascular tissue. Significant lipid deposits were found around the SMA and celiac trunk as shown in figure 3.19. These were removed along with excess perivascular tissue. As can be seen in figure 3.19, specimen 2 seemed discoloured on receipt, a condition thought to be associated with liver disease listed within the patient's medical records.

Table 3.3: **Specimen 2's donor information**

Age	61
Sex	Male
Race	Caucasian
Height	1.80 Meters
Weight	113 kg
Cause of Death	End-Stage Liver Disease
Medical History	Hypertension for 3 years, Hypothyroidism, Alcohol abuse for 40 years, chronic back pain, Rotator cuff surgery, knee surgery, Achilles tendon surgery, liver disease due to alcohol abuse.
Medications	Synthroid, Prilosec
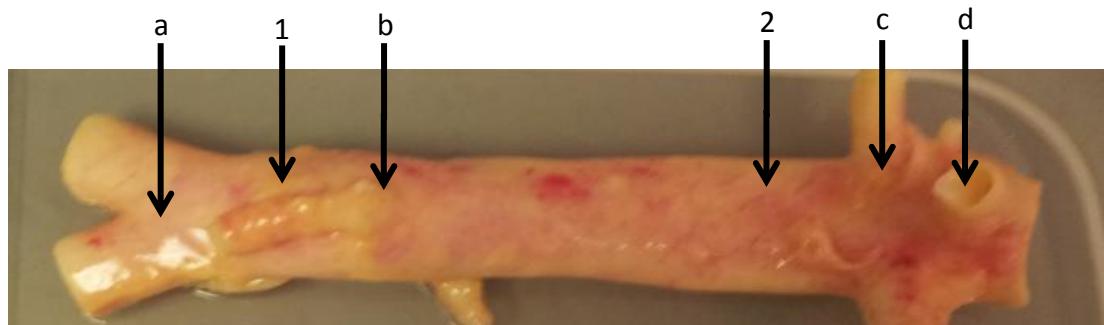
Figure 3.19: **Image of specimen 2. Aortic features were identified as follows, aortic bifurcation (a), inferior mesenteric artery (b), renal artery (c), superior mesenteric artery (d). Notations 1 and 2 point towards the locations at which pressure-diameter readings were obtained.**

3.4.2.1 Separation of layers

Layer separation followed protocol as outlined in section 3.2 of this thesis. In general the process was less problematic than found for specimen 1. The relative ease at which layers were separated was attributed to the patient's age. Although tearing of the intimal layer was still an issue, enough of the specimen could be salvaged to extract two specimens in both axial and circumferential directions.

In contrast to specimen 1, very little branching vessels were noted within the region dissected as can be seen in figure 3.20. With this, large areas of media and adventitia layers were available for characterisation.
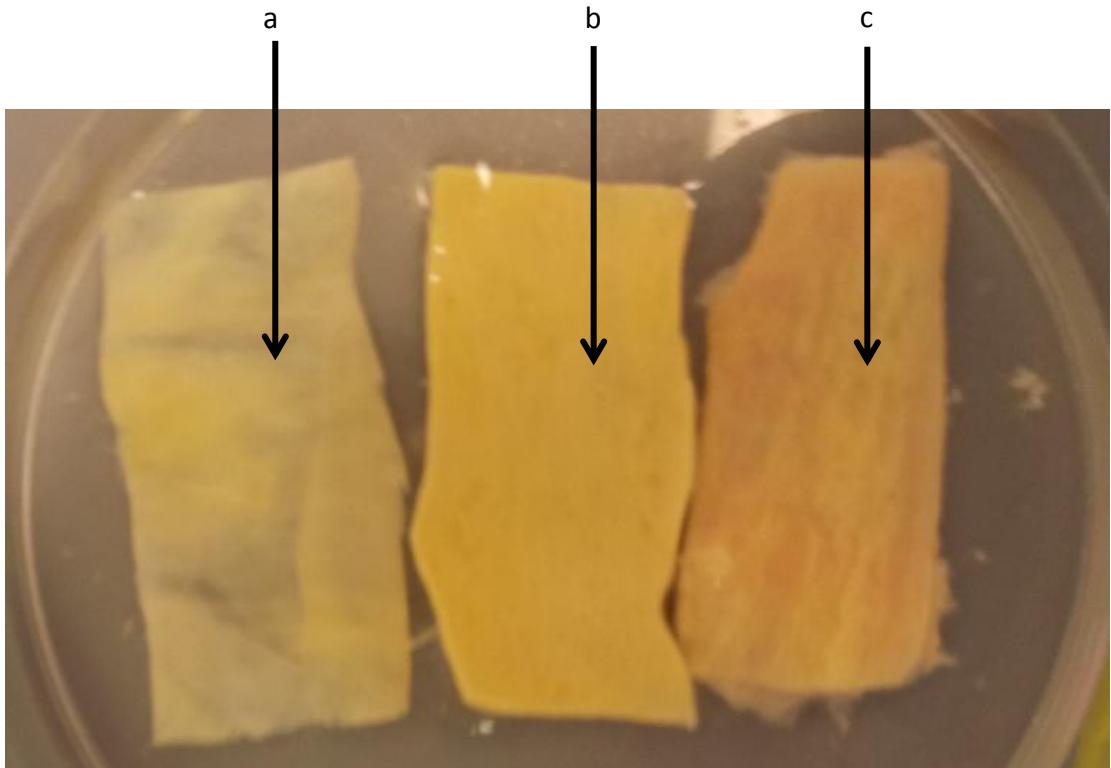
Figure 3.20: **Separated layers of specimen 2. Layers were identified as the intima (a), the media (b) and the adventitia (c). Each of the three layers was subject to yellowish discoloration attributed to end stage liver disease.**

3.4.2.2 Layer-specific results

For stress-strain specimen characterisation, two specimens per direction, per layer, were obtained, representative results of which are shown in figure 3.21. Further data produced through testing can be found in appendix 3. As can be seen from the figure, highly anisotropic trends were noticed for the intimal and adventitial layers. Although still nonlinear, the medial samples tended to behave in a more isotropic manner. Data displayed similar patterns to that obtained for specimen 1, with only results obtained for the adventitia being notably stiffer.
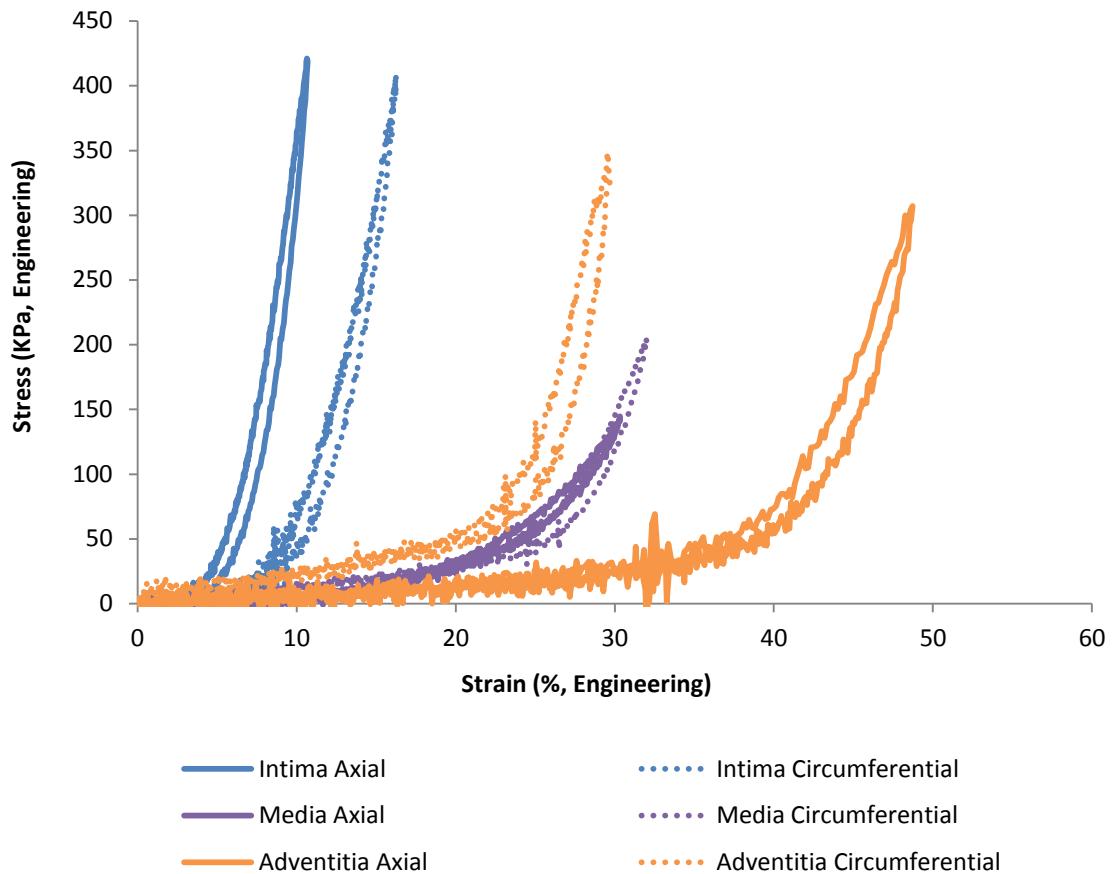
Figure 3.21: **Specimen 2's layer-specific stress-strain data.**

3.4.2.3 Pressure-diameter results

Pressure-diameter results were obtained from two locations. These locations were 1.5 cm below the renals and 1.5 cm above the aortic bifurcation. Results presented in figure 3.22 display a distinct nonlinear relationship, consistent with that of collagen recruitment theories [69], [70].

Using Langewouter's compliance calculations as per equation 3.3, a compliance value of 1.85 was calculated for the region below the renals, whilst a figure of 1.09 was obtained for the region just above the bifurcation. The relatively low compliance figures obtained were attributed to the severe calcifications noted upon further dissection of the tubular specimen (figure 3.23).
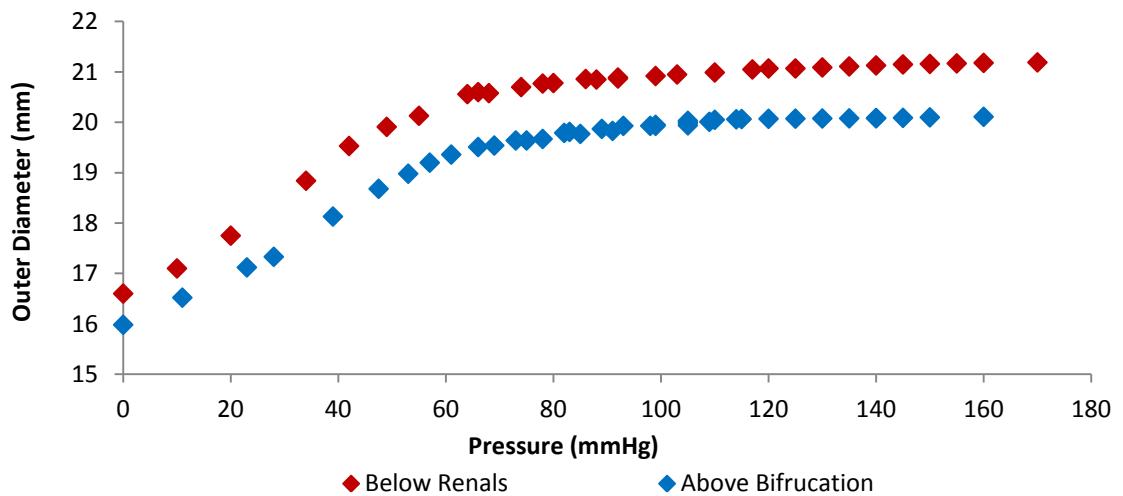

Figure 3.22: **Specimen 2's pressure diameter results**

Figure 3.23: **Specimen 2's ABT.2 section further dissected. Severe calcifications were noted upon further dissection, disease that was thought to have influenced pressure-diameter results.**

3.4.2.4 Deployment simulation

When pressurised to 100 mmHg, specimen two's diameter was measured to be 20.95 mm, 10 mm distal to the renal arteries. With the transition point of R_23.5 and R_25.5 being 21 mm, this meant that for the purposes of ideal over sizing it lay between two device sizes. For this reason both devices were deployed in turn.

Within figure 3.24, peak-to-peak results have been overlaid onto the pressure-diameter graph of the same region. It can be seen that R_25 Lutz 1.3 resulted in an initial peak-to-peak value of 21.99 mm. As this value was above the natural plateau level for the vessel at that location, pressurisation resulted in a decrease in peak-to-peak displacement. This behaviour is not reported in the literature and supports findings made through specimen 1. Results for device R_23 were more conventional which resulted in a Langewouter compliance of 0.58.
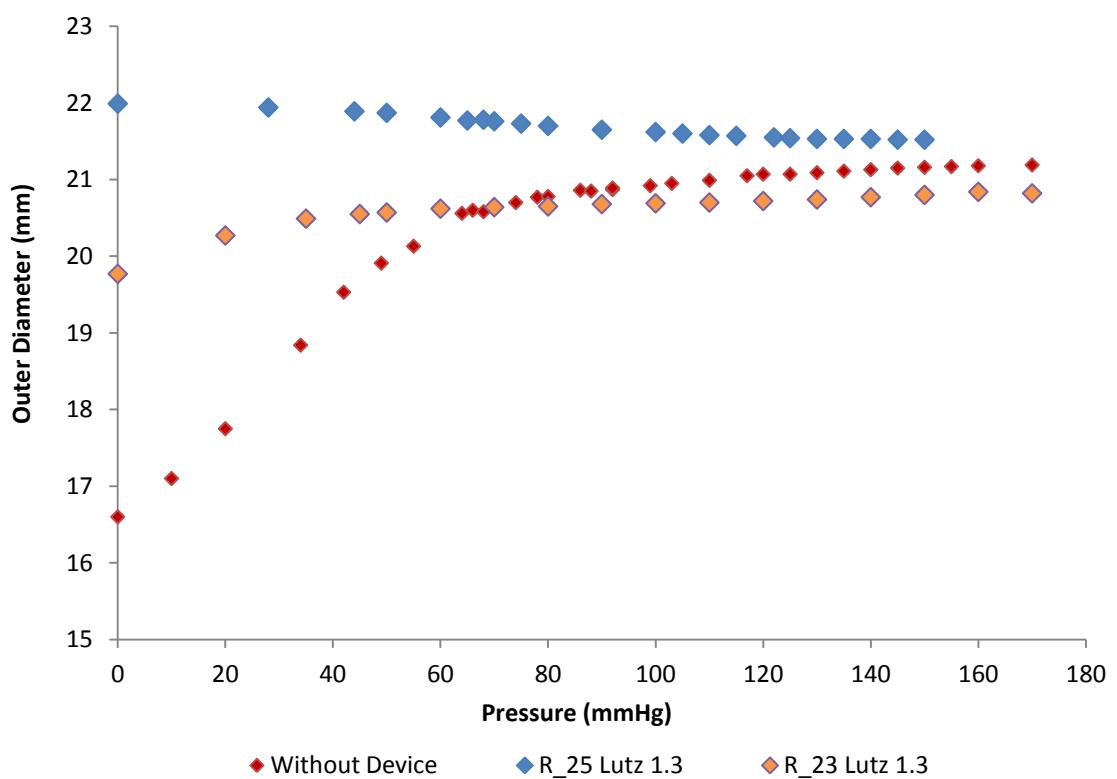

Figure 3.24: **Peak-to-peak deployment results for both R_25 Lutz 1.3 and R_23 Lutz 1.3 being deployed below the renal arteries.**

3.4.2.5 Profile readings

In general, leaking rates were less problematic than experienced for specimen 1. This meant that profile readings could be obtained for both R_23 Lutz 1.3 and R_25 Lutz 1.3 devices at a range of pressures. Results for these devices at pressures of 0 and 80 mmHg are presented in figure 3.25.

Results for R_23 Lutz 1.3 are as expected, with pressurisation of the vessel resulting in the vessel, initially only being deformed by the ring, taking on a more uniform cylindrical shape. It is worth noting that the region around the ring, and hence the ring itself, only underwent a small change in deformation during pressurisation, with the bulk of the deformation occurring proximal and distal to this region. These findings are consistent with the results shown in figure 3.24 which indicate only a 1 mm increase in diameter between the 0 to 150 mmHg pressure range tested for R_23 Luz 1.3.

Results presented within figure 3.25 (b) are more intuitive in nature. Due to the larger oversize of the device, the vessel initially deforms to a greater extent. These increased deformations are seen to extend past the region of implant. As a result of these deformations imparted by the device, the vessel experiences little further deformation during pressurisation. The deformation that does occur does so by reshaping the vessel to its cylindrical form to best accommodate pressure forces. Through this process the peak-to-peak deformation decreases, essentially causing an unintuitive negative dilation within this region. Once in its cylindrical form, further pressurisation would cause conventional dilation. Results shown in figure 3.25 are in agreement to those shown in figure 3.24.
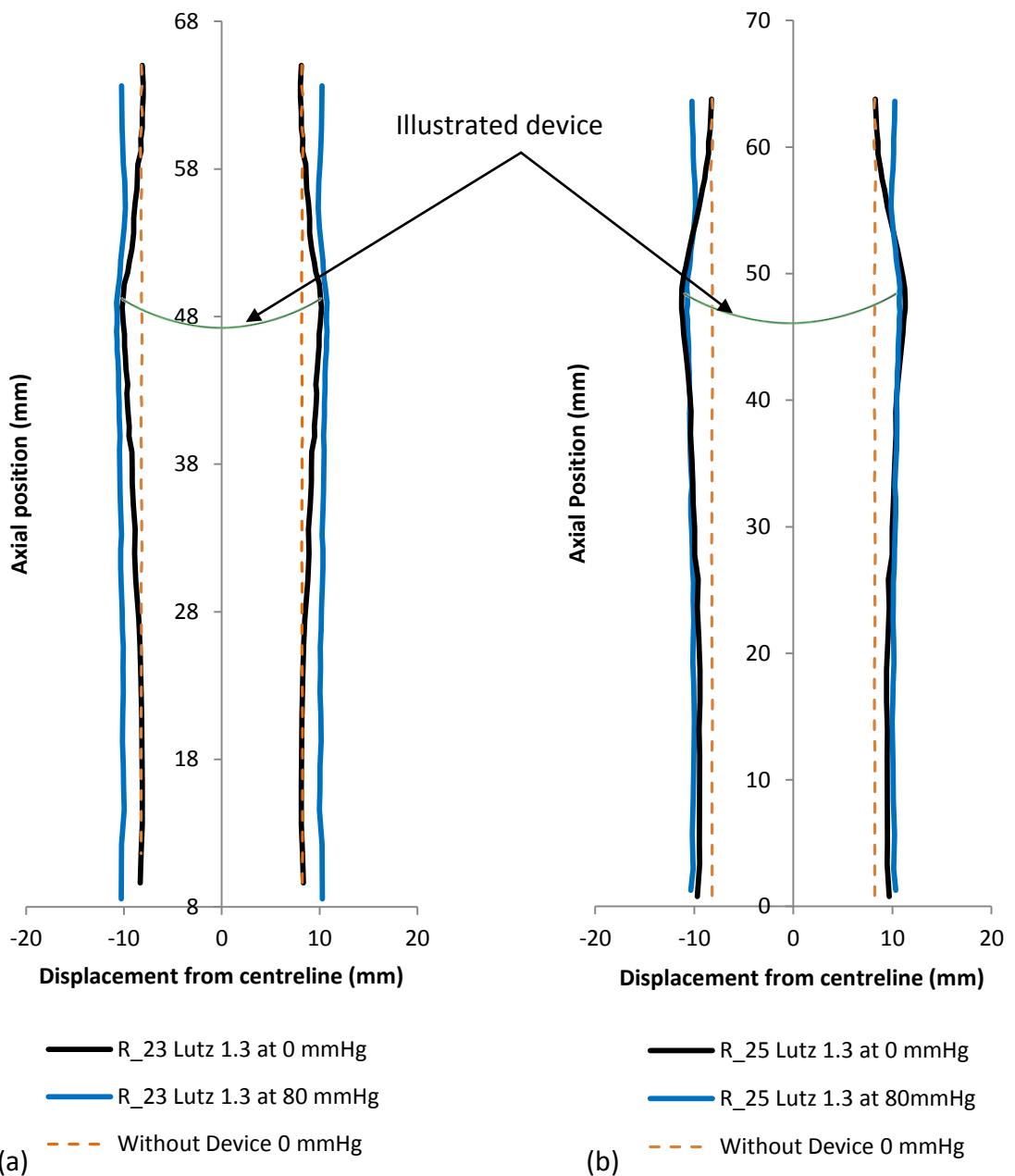
Figure 3.25: **Edge profile results for specimen 2 for device R_23 Lutz 1.3 (a) and R_ 25 Lutz 1.3 (b).**

3.4.3 Specimen 3 data

Donor information for specimen 3 is provided in table 3.4. As can be seen, the male fell within the ideal age range of 56-65 years old. Hypertension and diabetes were listed within the medical history, and from details provided, are the most likely to have an impact on the mechanical properties of vascular tissue. Figure 3.26 is an image of the vessel as received. Large lipidic deposits were noticed around the celiac trunk whilst an abnormal dilation was observed towards the aortic bifurcation. Regions below the renal arteries seemed to be in relatively good health, with no visible signs of disease.

Table 3.4: **Specimen 3's donor information.**

| Age	56
Sex	Male
Race	African American
Height	1.87 Meters
Weight	106.6 kg
Cause of Death	Pulmonary Embolism
Medical History	Corneal Transplant, diabetes, keratoconus disorder, diabetic ketoacidosis, hypertension, elevated haematocrit, mild thrombocytopenia
Medications	None
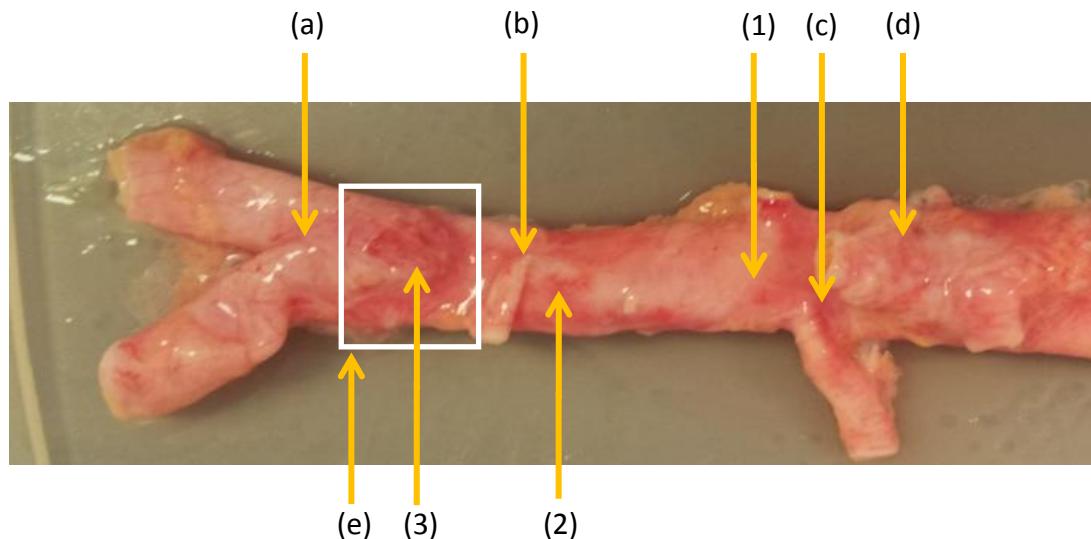
Figure 3.26: **Image of specimen 3. Arterial features were identified as the aortic bifurcation (a), the inferior mesenteric artery (b), the renal artery (c) and the superior mesenteric artery (d). The abnormal dilation (e) was noticed just above the aortic bifurcation. Notations 1, 2 and 3 point towards locations at which pressure-diameter readings were obtained.**

3.4.3.1 Specimen 3 layer separation

Layer dissection for specimen 3 was unfortunately much more problematic than for either specimens 1 or 2. Arterial layers seemed more fragile, especially the media, leading to tearing during separation. An image of the dissected layers is provided in figure 3.27, where laceration-like damage is noticeable on the medial sample. Lacerations seemed to be predominantly in the circumferential direction, perhaps pertaining to the dominant direction of collagen found in this layer.
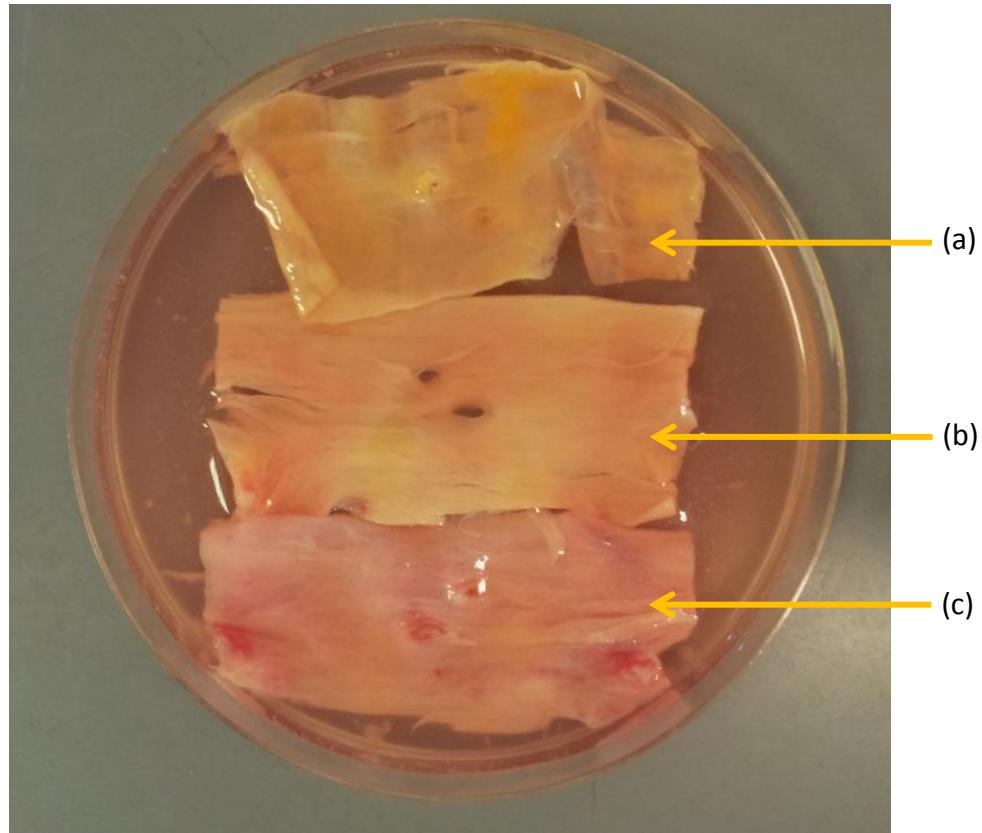

Figure 3.27: **Separated layers of specimen 3. Layers were identified as the intima (a), the media (b) and the adventitia (c). The intima again was subject to arterial disease seen within the image as discoloration. The fibrous nature can clearly be seen, with two branching vessels visible as holes within the layer.**

3.4.3.2 Layer-specific uniaxial results

Considerable difficulties were encountered in the process of characterising specimen 3's medial layer. Test specimens tended to be fragile in nature with tearing a problem at low levels of stress and strain. In spite of these issues two uniaxial samples, one axial and one circumferential, were successfully characterised. The adventitia and intima presented fewer issues and as a result, two specimens per direction were successfully characterised. Results of uniaxial tests are shown in figure 3.28.

As seen from the graph all layers, especially the adventitia, displayed highly anisotropic behaviour. Intimal layers were the least compliant, whilst the adventitial layers were the most. The medial sample of specimen 3 behaved in a more pronounced anisotropic manner than what was noticed for both specimens 1 and 2.
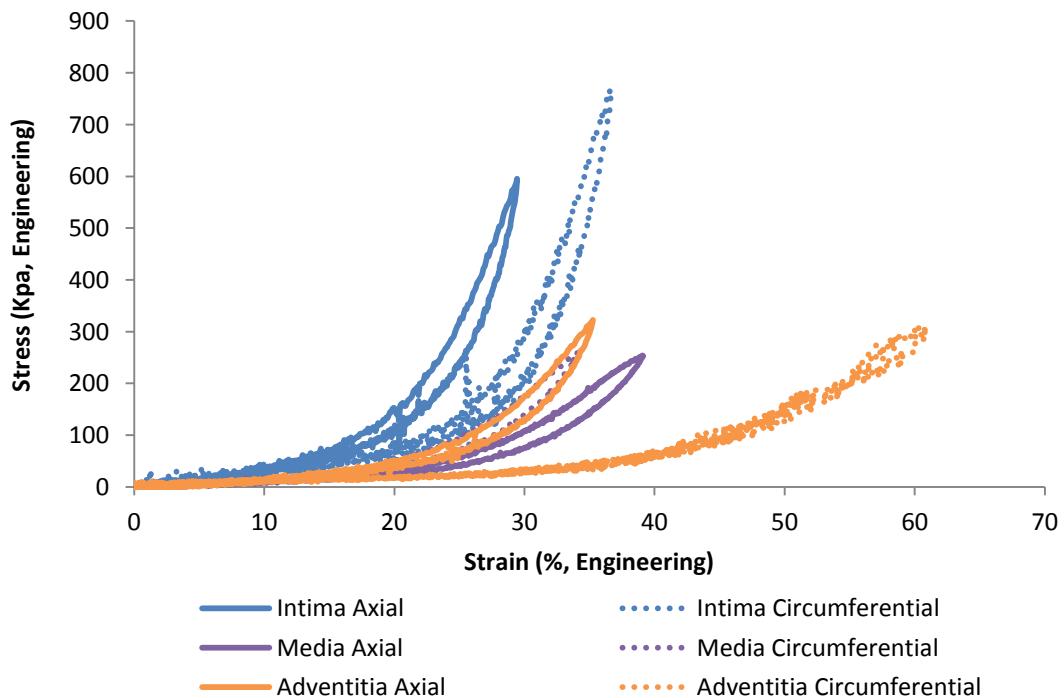

Figure 3.28: **Specimen 3's uniaxial characterisation results.**

3.4.3.3 Pressure-diameter results

Through closer inspection of specimen 3, the dilatation noticed in section 3.4.3 of this report appeared to be the early stages of a type 1 aneurysm (figure 3.29). Although not an original objective of this work, this presented the opportunity to obtain rare *in vitro* pressure-diameter data for such a region. The defined locality of the diseased tissue also meant that data collected could directly be compared against non-diseased sections. To this author's knowledge, no such data is yet available within the published literature.

After experimentation, examination of the vessel's surface revealed distinct signs of atherosclerosis. Interestingly, no thrombosistic formation was observed within the aneurysm sack, a condition often associated with aneurysm pathology [4]. With no visible signs of external damage, proteolytic degradation of elastic and collagen fibres was seen as the most likely cause of the aneurysm. Such reasoning would be supported by the fragile nature of the specimens tested.

Figure 3.30 displays the results of pressure-diameter experiments conducted. Regions below the renal arteries, away from the aneurysm sack, were the most compliant with a Langewouter compliance of 3.14. This compliance then reduced in regions towards the aneurysm, which itself had a compliance of 2.53.
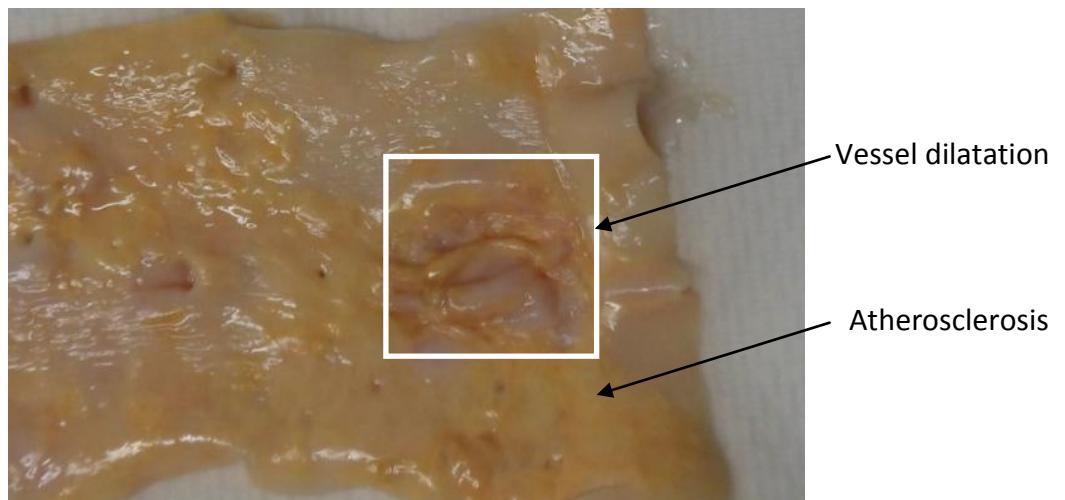

Figure 3.29: **Early stage aneurysm.**

Results presented in figure 3.30 indicate that diseased regions became non-compliant at pressures far below that of physiological diastolic pressures. The non-compliance of diseased regions is thought to be an effect of elastin degradation and collagen synthesisation. Healthier regions below the renal arteries displayed more conventional characteristics, with stiffening noted at around 100 mmHg.
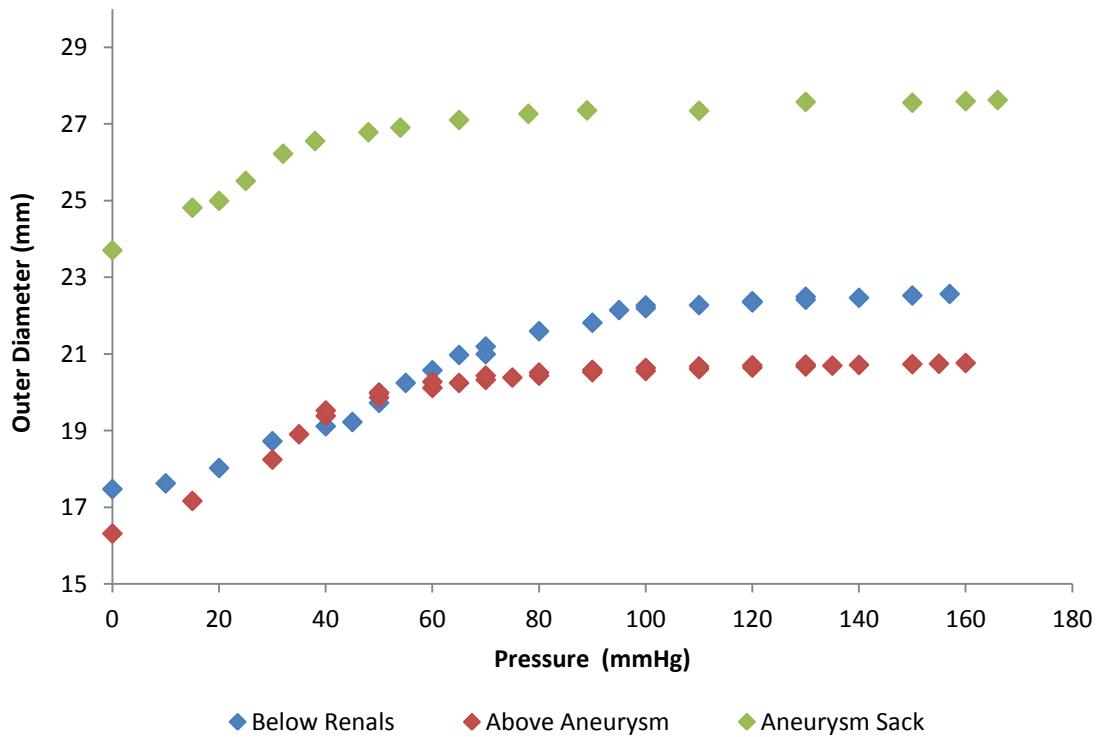

Figure 3.30: **Pressure-diameter results obtained for specimen 3.**

3.4.3.4 Specimen 3 device deployment

With a lumen diameter of 22 mm at 100 mmHg pressure, three R_25 devices of Lutz number 1.3, 0.9 and 0.5 were deployed within specimen 3. As with specimens 1 and 2, peak-to-peak deformations were compared against pressure-diameter results of the same location, the results of which are shown in figure 3.31.

As can be seen from the graph, due to the relatively high compliance of the vessel, devices of Lutz numbers 1.3 and 0.9 deformed the vessel past its natural plateau level. With pressurisation, peak-to-peak deformations of devices 1.3 and 0.9 did not tend back to the natural plateau levels. R_25 Lutz 0.5 allowed for the vessel to behave in a more natural manner, with the peak-to-peak diameters tending to the unassisted pressurisation curve at a pressure higher than 60 mmHg. With R_25 Lutz 0.5 deployed, a Langewouter compliance of 2.36 was calculated.
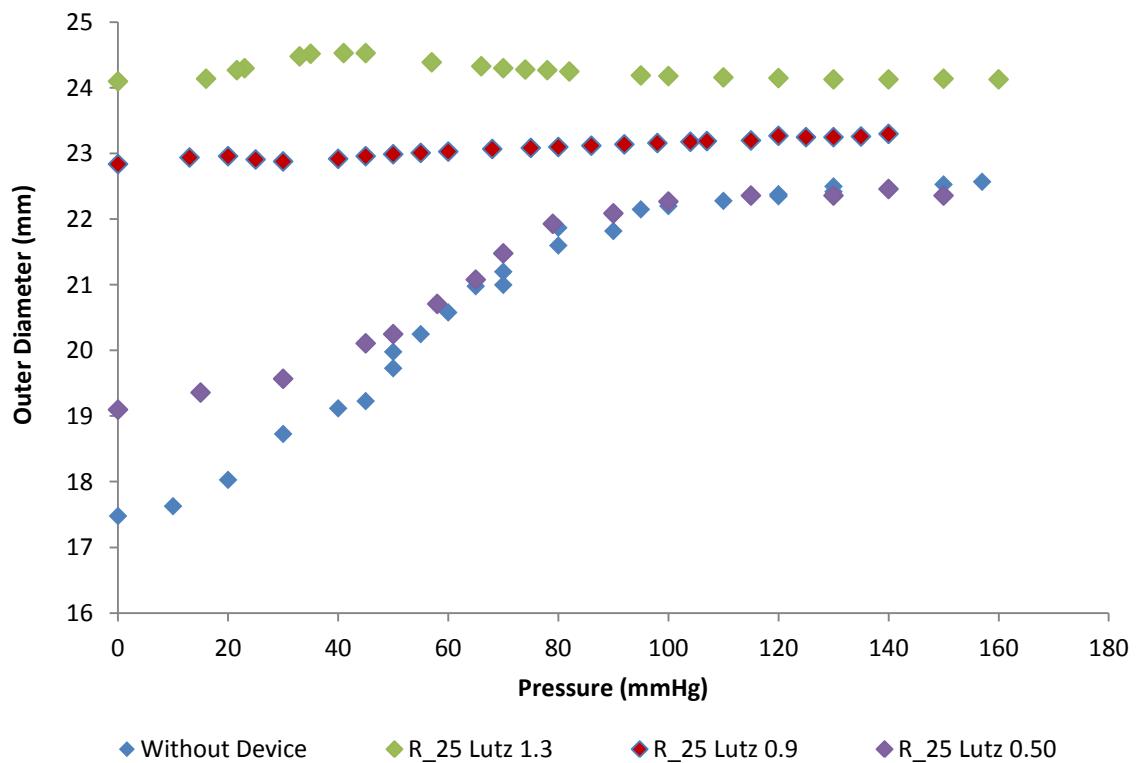

Figure 3.31: **Deployment results for three different R_25 strengths overlaid onto relevant pressure-diameter results.**

3.4.3.6 Profile readings

In figure 3.32 (a), deformation results are shown for ring devices Lutz 1.3 and 0.9 at 0 mmHg. Results indicate, as would be expected, that the stiffer device produces larger deformations around contact areas. Distal to the deployment location, the stiffer device induced a slight narrowing within the vessel. Figure 3.32 (b) displays profile edge results obtained for Lutz 1.3 at pressures of 0 mmHg and 140 mmHg. In this figure, the considerable deformation of the vessel is seen away from deployment locations. A slight decrease in peak-to-peak diameter can be noted as the vessel is pressurised to 140 mmHg and the vessel deforms to a more uniform cylindrical shape.
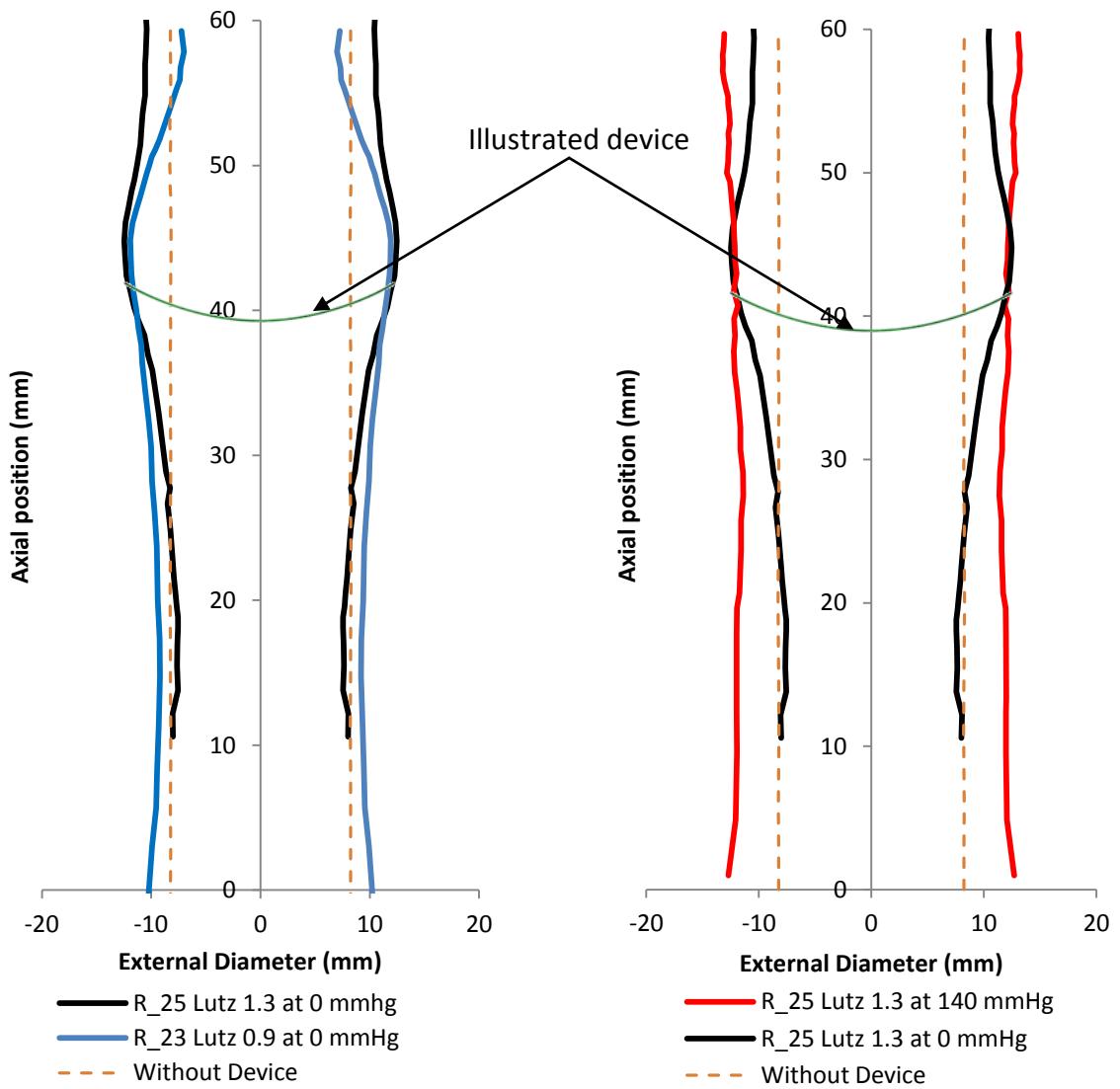

Figure 3.32: **Edge profile readings of deployment simulations.**

3.5 Vascular programme data analysis

In this section data obtained from the vascular testing programme is collated, further analysed and compared against data available from the published literature.

3.5.1 Uniaxial tensile tests comparison

As discussed in section 2.3.2.6, layer-specific abdominal data has previously been published in the form of Holzapfel parameters by Weisbecker *et al.,* [72]. An opportunity therefore exists to collate and compare published results against characterisation work conducted herein. Results of this study are shown in figure 3.33 through to 3.38 which compare uniaxial tensile results for all three layers characterised. For clarity, only the most and least stiff arterial responses from Weisbecker's study are used for comparison.

Within the study conducted by Weisbecker, specimens were obtained from the region between the renal arteries and aortic bifurcation. As specimens within this body of work were obtained from the region just proximal to the renal arteries, comparison of results shed light on the variability of the mechanical properties across the abdominal aorta. Furthermore, the comparison also provided an understanding of the effects that major branching vessels have on the properties of specimens.

Within figure 3.33 and 3.34, the comparison of intimal results are presented. Results obtained from the vascular characterisation programme largely enveloped that of data obtained from Weisbecker. A distinct pattern emerged, with arterial hardening with age clearly prevalent. The relative stiff nature of specimen 2 was thought to be related to the donors medical conditions which included hypertension. The severe discoloration of specimen 2 also suggests that alcohol abuse could have had an impact on vascular mechanics. With the health issues noted for specimen 2, and considering that a similar age range was characterised within the compared publication, results obtained from the vascular testing programme were thought to be on average more compliant. This finding is

consistent with known global trends of the increased arterial compliance towards the heart.

Figure 3.35 and 3.36 displays the comparison of medial results against Weisbecker's. As seen, results produced herein were consistent with those found in the literature, with results produced tending towards being marginally more compliant in nature. As the media is a mechanically significant layer, dominating the arterial response at low levels of deformation, this finding is significant.

Comparison between figures 3.33 and 3.35 displays the relative difference in response between the media and intima. The comparison highlights the large scatter in results obtained for the intima which displayed non-linear stiffening anywhere between 5% and 27% strain. The inconsistency of results obtained from this layer was attributed to its susceptibility to disease. As a whole, the media's response was more compliant in nature.

The comparison of adventitia results is shown in figure 3.37 and 3.38. In general, axial results seemed to be in good agreement with those found within Weisbecker's. Circumferential data for specimen 1 and 3 were outside the envelope of results obtained from Weisbecker's study, being highly elastic in nature.
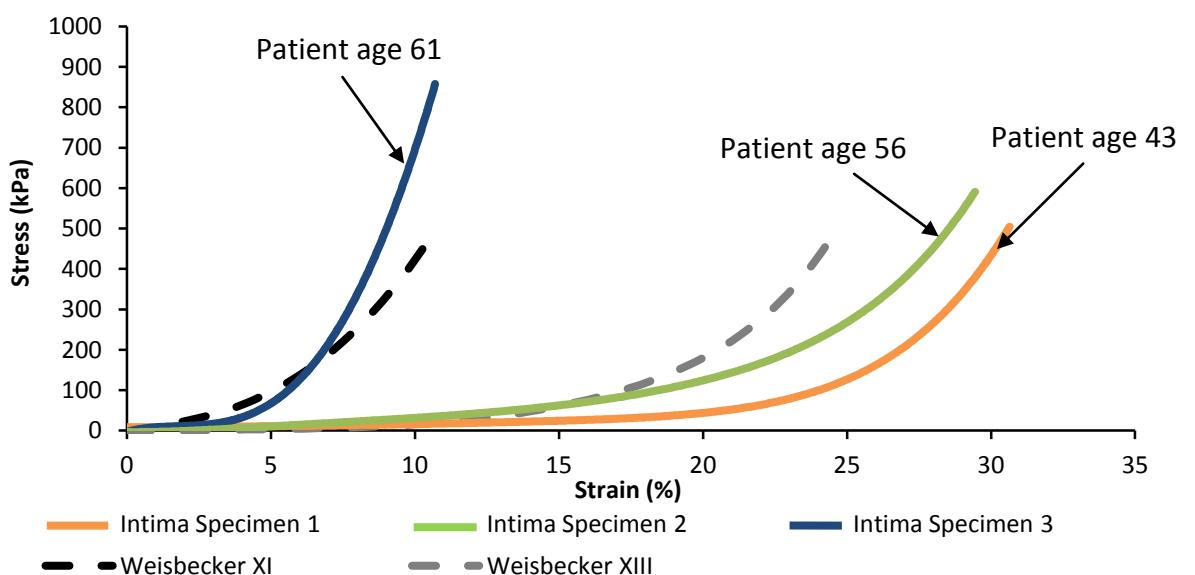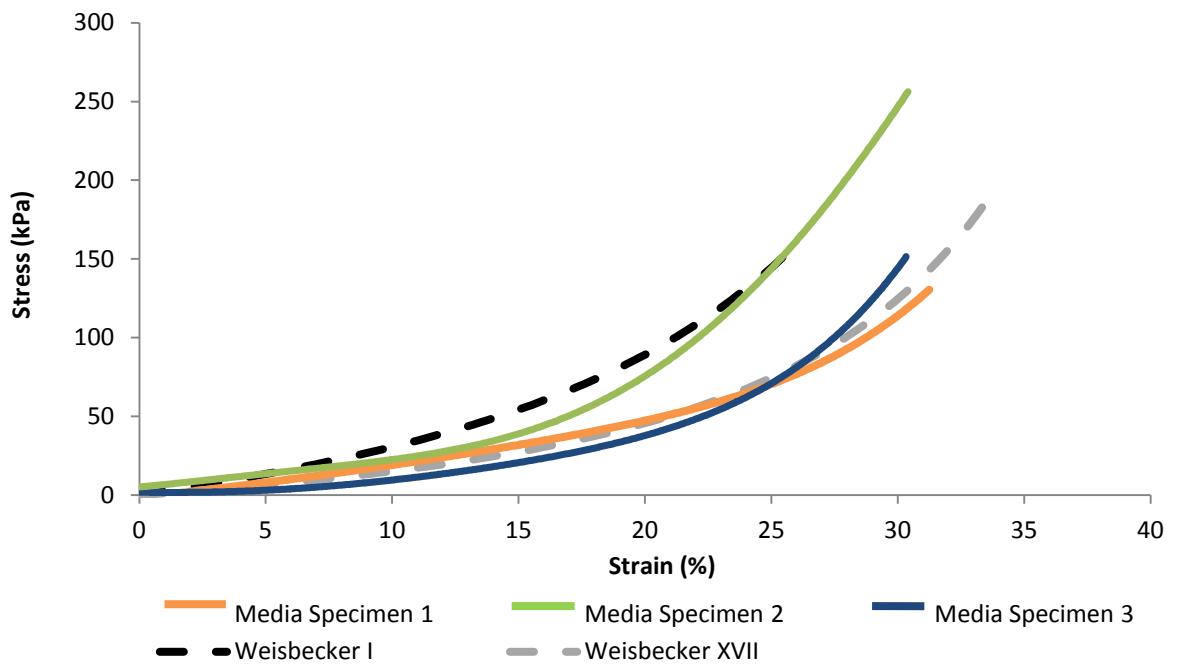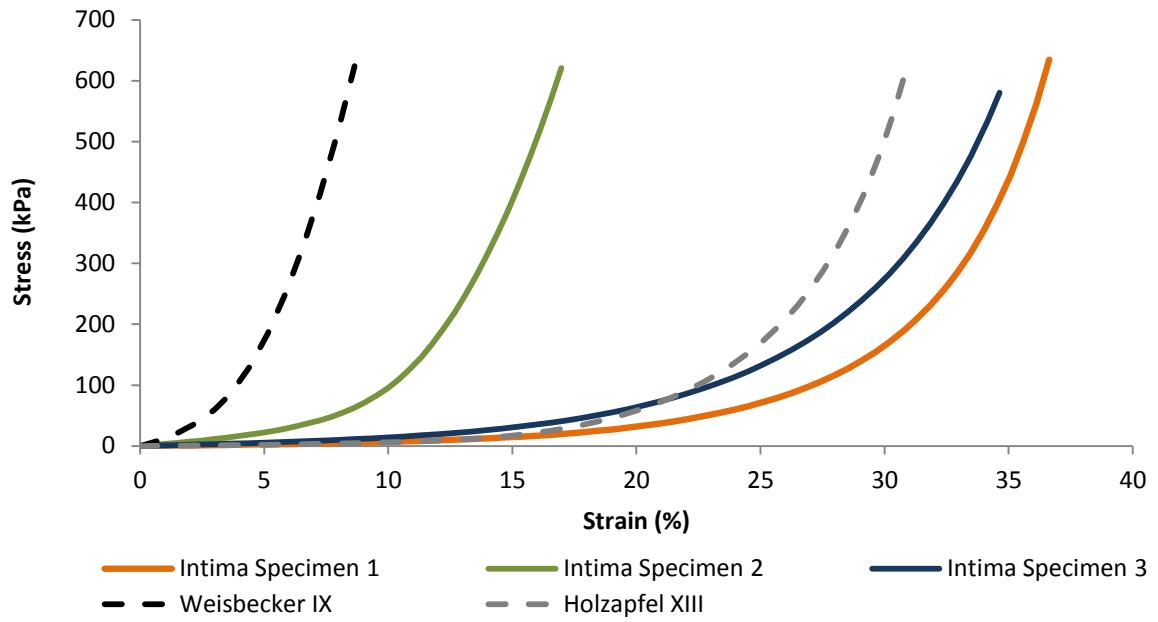

Figure 3.33: **Intima axial stress-strain results in comparison to those obtained from Weisbecker et al.,** [72]**.**

Figure 3.34: **Intima circumferential stress-strain results in comparison to those obtained from Weisbecker *et al.*,** [72].


Figure 3.35: **Medial axial stress-strain results in comparison to those obtained from Weisbecker *et al.*,** [72].
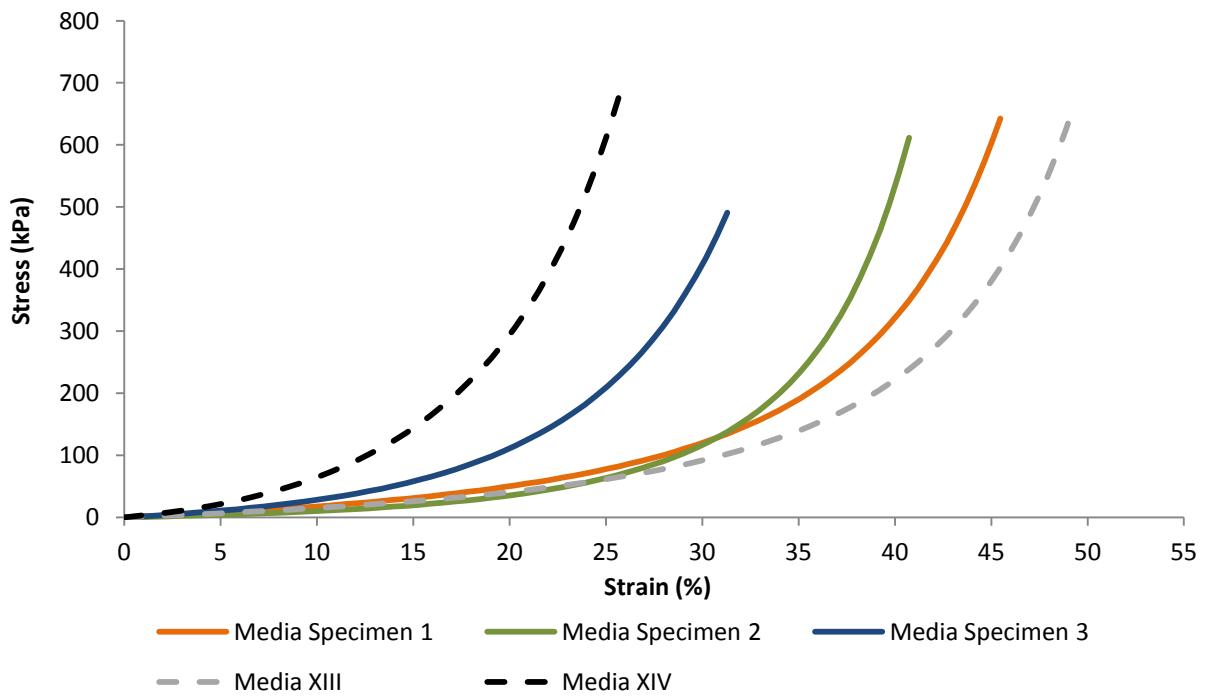
Figure 3.36: **Medial circumferential stress-strain results in comparison to those obtained from Weisbecker *et al.*, [72].**
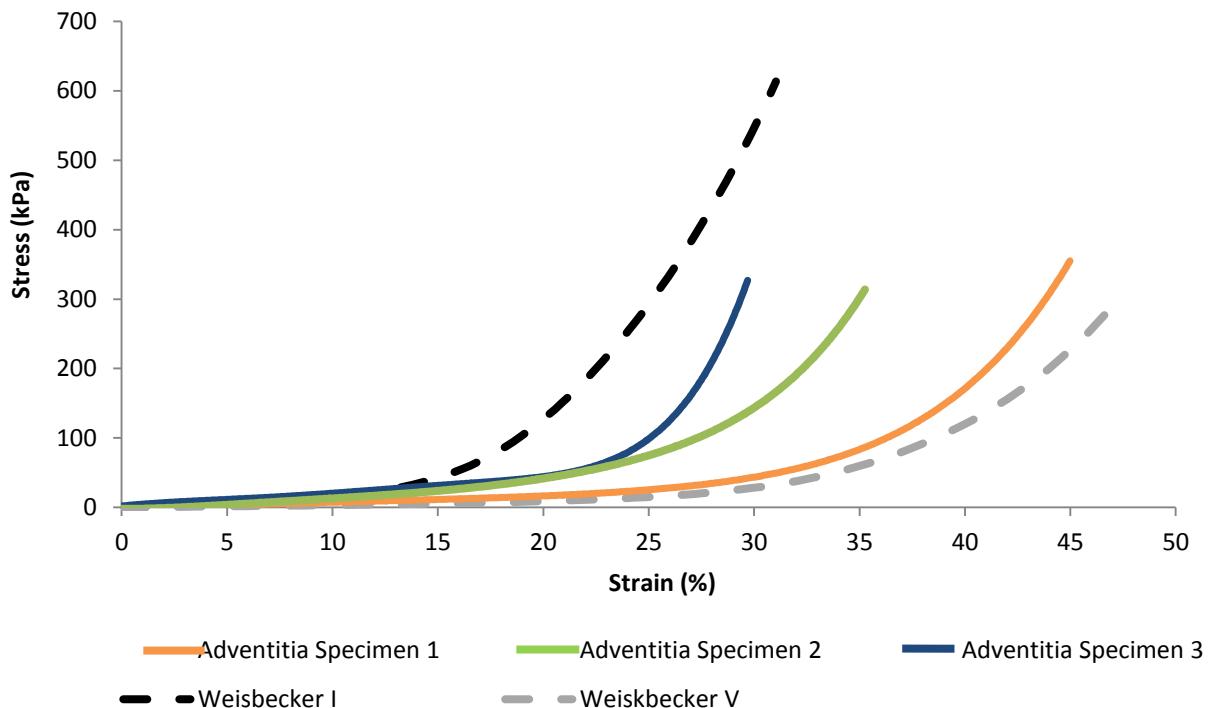

Figure 3.37: **Adventitia axial stress-strain results in comparison to those obtained from Weisbecker *et al.*, [72].**
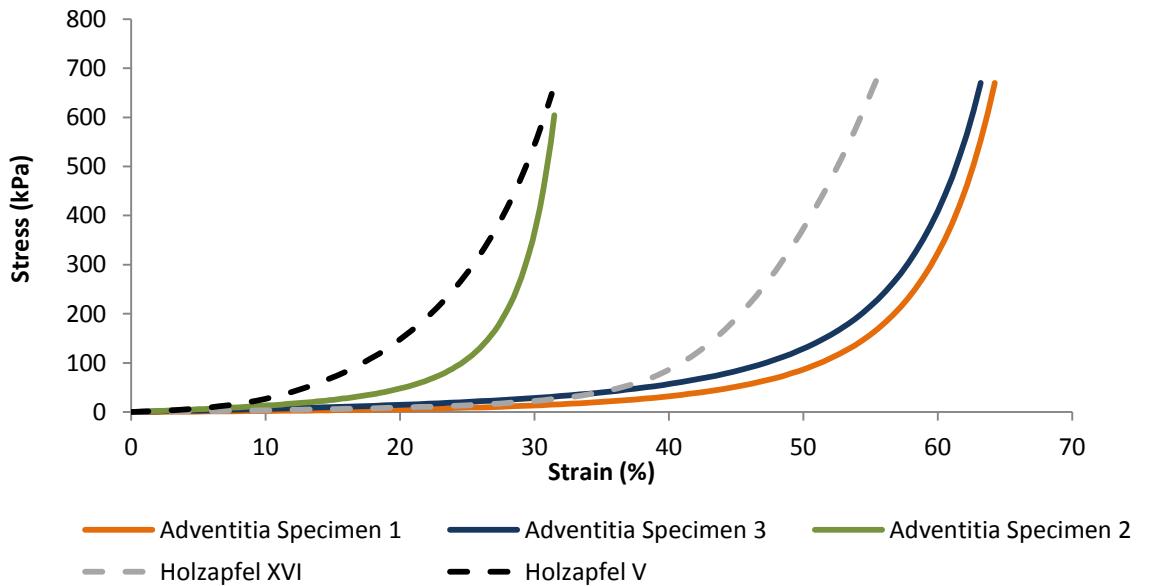
***Figure 3.38:*** **Adventitia circumferential stress-strain results in comparison to those obtained from Weisbecker *et al.*, [72].**

3.5.2 Pressure-diameter comparison

For further analysis, efforts were made to establish how representative specimens were of their individual age brackets. For this, pressure-diameter compliance data produced herein was compared against data published by Langewouter *et al.,* [97]. Within the referenced publication, pressure-diameter characteristics for 20 abdominal aortas are provided. The programme objectives were aimed at characterising the abdominal aorta within its basal state, following protocol analogous to ones adopted herein. Data within this publication is presented in the form of Langewouter's parameters (equation 3.3), a format that this project also adopted.

The comparison of data collected herein against that published by Langewouters, *et al.* is presented within figure 3.39. A global trend of a decrease in compliance with increasing age was once again established when plotting results. Using a 3rd order polynomial line of best fit within figure 3.39 for reference, specimens 1, 2 and 3 was seen to conform to trends with reasonable agreement to Langwouter's data. Specimen 1's compliance, as calculated in section 3.4.1.3, was especially seen to be

in good agreement. This correlation of biaxial data provided evidence that specimen 1 was representative of other patients of similar age.

Specimen 2's compliance, as calculated in section 3.4.2.3, generally compared low against published data. This was thought to be related to the highly inelastic results obtained for its intimal layer during uniaxial characterisation (figure 3.33 and 3.34). This finding provided evidence of the mechanical significance of the intima in older specimens. This is in contrast against many studies in which this layer is disregarded due to its relative thickness when compared to the media and adventitia.

Specimen 3's results, as calculated in section 3.4.3.3, showed the most variation. Regions characterised below the renal arteries displayed much higher levels of compliance than would be expected for specimens of that age. In contrast, the region just proximal to the aortic bifurcation displayed relatively low levels of compliance. Compliance data obtained for the aneurysm sack also fell just above that which would be expected for healthy tissue.
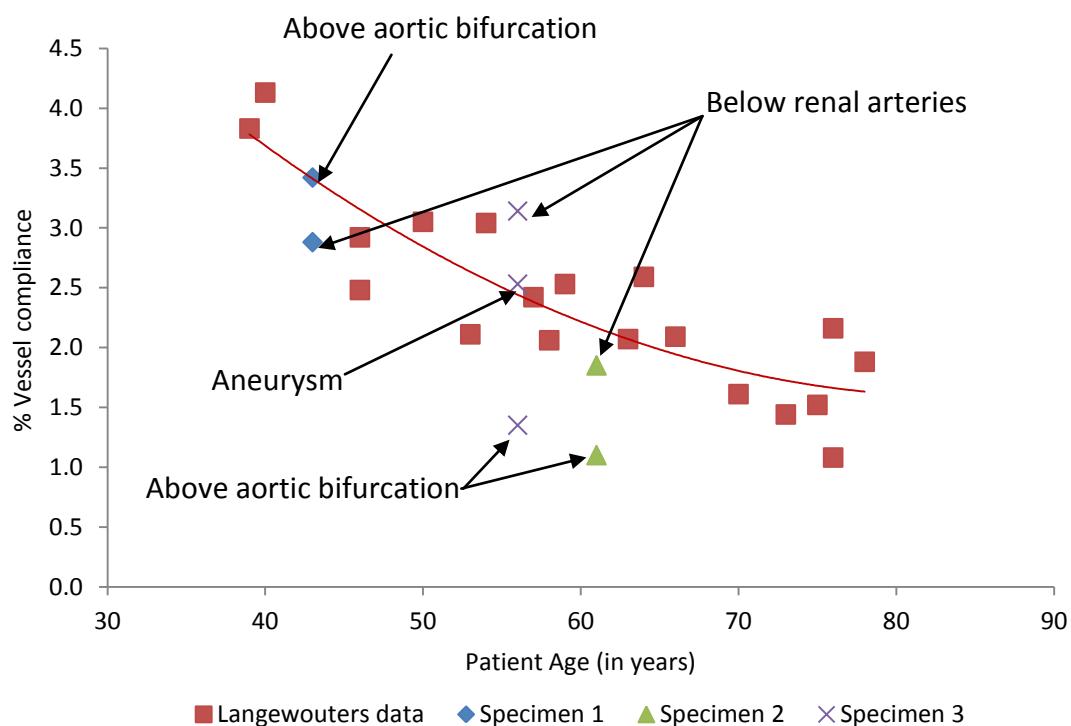

Figure 3.39: **Comparison of data collected herein as compared against data available within literature** [97] **for the abdominal aorta.**

3.6 Chapter summary

This chapter produced the comprehensive data sets required for both soft tissue material model development and FE validation. Following this, a summary of data was presented for three human cadaver specimens characterised using the developed protocol.

The work presented the first attempt at site specific characterisation across multiple specimens. With this, the data produced from this study could be used in conjunction with site unspecific studies to address a range of academic questions. Two of these questions addressed were the mechanical variability of vascular tissue in the presence of major branching vessels and the consistency of properties across the abdominal aortic region. Results shown in section 3.4.1 provided compelling evidence that, mechanically, trends of increasing elasticity towards the heart remain consistent even in the presence of arterial features. This finding is significant as it allows the use of characterisation data obtained from uniform cylindrical sections for the development of material models. These models can then be used in non-uniform, feature intense sections with a greater degree of confidence and understanding. During studies, the intima displayed the greatest variability in mechanical properties, a finding ascribed to the susceptibility of this layer to arterial disease. The difficulties associated with the separation of this layer from the media are also thought to be a factor.

To this author's knowledge, no single publication exists in which specimens were subjected to comprehensive uniaxial layer-specific, biaxial and non-uniform out of plane characterisation. As comprehensive data sets are crucial for the adequate FE modelling of arterial tissue, the data sets produced herein were seen as a much needed development within the academic field. By further combining the data sets produced with data available within literature (Weisbecker *et al.*, [72]) links were developed between previously unconnected studies. Through collating data steps have also been taken towards creating statistically significant data sets from which

averaged properties can be drawn. Generalised properties are essential if FE modelling is to be adopted into the heart of endovascular device design.

Device deployment simulation data presented within this chapter provides a new insight into the complexities involved in device/artery interactions. Complex interactions captured experimentally provide an excellent benchmark for future FE model validation activities.

In addition to meeting the main objectives of the vascular testing programme, rare, early stage type-1 aneurysm pressure-inflation data was obtained. In combination with the characterisation data collected for surrounding non-diseased tissue, the data collected provides unique information on aneurysm pathology. Along the path of completing the programme a vascular testing capability was established at the University of Strathclyde. Protocol required for the testing of arteries was developed and recorded through extensive experimentation. With the capability set and methods recorded, efforts within this body of work will aid future studies.

4 Integrated modelling framework development

Much of the difficulties associated with creating accurate device-artery simulations, stem from the asymmetric, nonlinear material models involved. With the Anaconda device there is also then the added complexity of contact interactions under large deformations. As a result of these challenges, although previous attempts had been made [24], a FE design tool had yet to be created which could effectively be used to study the interactions between the Anaconda's proximal ring and the arterial wall.

This chapter provides details on the steps taken within this project to readdress these challenges. The difficulties associated with the FE modelling of device/artery interactions are presented, and modelling assumptions adopted within the current work are clarified. The steps taken within this project to address issues encountered by previous authors are also discussed, before further novel modelling developments are presented.

The entire framework was constructed using the high-level, object oriented scripting language, Python 3.2. The scripts produced during this project will not be presented within this chapter. Instead, concise flow diagrams will be used to convey methodology whilst the scripts can be found in Appendix 6.

As an independent scripting language, Python includes built-in functionality to deal with lists, tuples and dictionaries. The use of Python meant that built-in mathematics modules could be utilised, simplifying the process of parameterising. Through this, algorithms could be developed for the automatic application of boundary conditions. With a built-in Python dictionary within Abaqus, scripts produced could also directly be read into the FE platform as input files. The choice of using Abaqus 6.11 as the FE platform was primarily based on the availability of bespoke material models for both Nitinol and arterial tissue, as built-in user sub-routines [48].

4.1 Finite element challenges and simplifications

4.1.1 The Anaconda device

The device as seen in figure 4.1 is relatively intricate. Modelling of the complete structure within FEA, although possible, would result in excessively long solutions times for even the simplest loading conditions. As most of the body only acts as a conduit for blood flow, such a model would also provide large amounts of trivial data. Modelling of the complete device was therefore deemed excessive and focus was placed on the proximal ring of the device.

The proximal ring dictates much of its performance. It plays a key role in the device's sealing capabilities and is also its primary form of anchorage. With this, and the critical nature of the oversize property introduced in chapter 1, a number of academic questions could be posed and answered by the FE modelling of its interactions with the vessel wall. Primary of these questions were the strain the proximal ring experienced *in situ* and the force exerted by the ring onto the arterial wall once implanted.

As the polyester fabric onto which the device is sutured has been shown to be mechanically insignificant [24], it was omitted from modelling efforts. This vastly simplifies modelling efforts with negligible impact on ring stiffness as demonstrated in the referenced study.
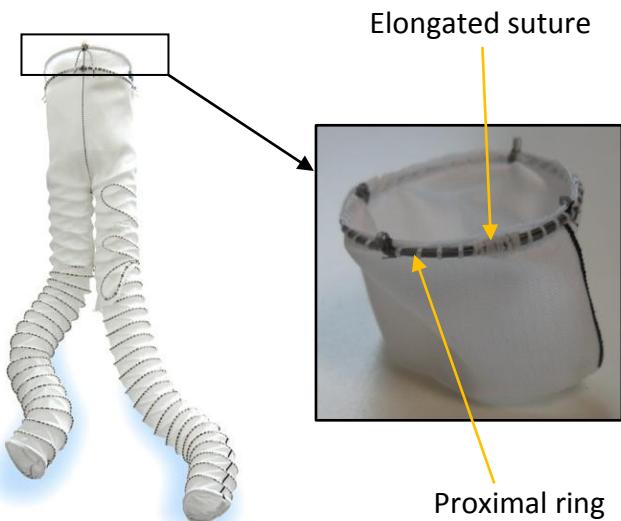

Figure 4.1: **Location and nature of the proximal ring.**

The proximal ring of the device is made from a single straight drawn Nitinol wire (OD of 0.18 to 0.24 mm), which is coiled between seven to fourteen times to form the ring. The two ends of the wire strand are crimped and contained within an elongated suture which can be seen in figure 4.1. Once coiled, the wire bundle can take a number of different configurations, with stable configurations for a 12 turn bundle illustrated in figure 4.2 [24]. During deformation these turns interact with each other, presenting complex FE contact modelling difficulties. To address these difficulties, a simplification has previously been proposed in which the ring bundle is replaced by a single, thicker ring with identical stiffness properties [24], a method referred to as the "Equivalent-I" approach. This approach assumes that wire turns behave independently and hence, the second moment of area of the entire ring bundle is simply the second moment of area of an individual wire turn multiplied by number of turns within the bundle. When attempting to capture the stiffness characteristics of the proximal ring, the wire bundle can hence through this method be replaced by a single thicker wire of equivalent second moment of area. Although seen as significant, this Equivalent-I ring-modelling simplification was adopted during initial framework development. Novel bundle modelling methods are later proposed in section 6.2.

As the proximal ring is formed from straight drawn wire, ring bundles are in a state of constant strain once sutured onto the polyester fabric. This property is referred to as the "pre-strain" of ring bundles and has a significant influence on the behaviour of the device. Capturing pre-strain effectively was a major challenge within the present study.
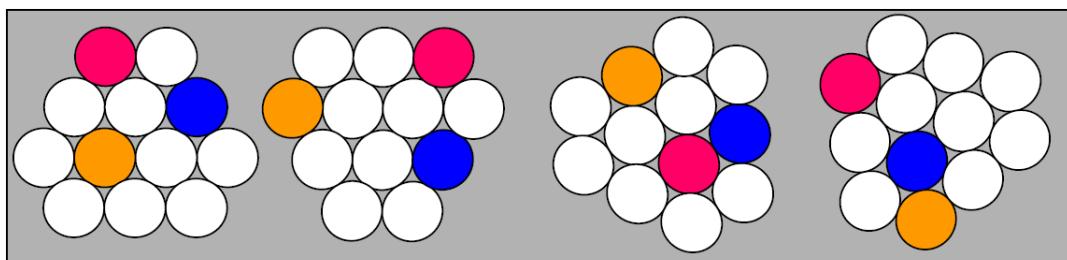

Figure 4.2: **Stable turn configurations are shown for a 12 turn wire bundle. Coloured turns demonstrate the varied positions three consecutive turns can assume around the bundle.**

4.1.2 Vessel challenges and simplifications

Various simplifications and assumptions were required to make the FE study of device/artery interactions feasible. As the most prominent simplification, the vessel was modelled in free space, meaning that interactions between the aorta and surrounding organs were omitted from study. This simplification is standard within many Finite Element stent studies, and is the only realistic option with current computing capabilities.

From chapter 2, it can be seen that significant effort was made to introduce a representative vascular model. It should be noted, however, that even the most sophisticated arterial constitutive models currently available are still, for the most part, phenomenological.

Within this project, as in most preceding studies, the artery was assumed to be uniform and cylindrical in shape. Furthermore, branch vessels and other irregular arterial features were omitted from modelling efforts. This simplification stemmed from the considerable patient-to-patient variations which exist.

Following from the conditions under which vascular tissue was characterised in chapter 2, all tissue was modelled within its basal condition. This meant that the active muscular response was omitted from modelling efforts. This simplification was deemed suitable with reference to section 2.3.6, where it was shown that such a modelling approach would be appropriate for highly elastic arteries.

For material model development, characterisation data from non-diseased tissue was used. This assumption was generally consistent with medical procedures during which healthy tissue is identified and in which the device is subsequently anchored.

4.2 Integrated modelling framework development approach

In section 2.4 of this thesis, relevant studies to the one conducted herein were reviewed. Of particular interest was a study conducted by McCummiskey [24], which had similar objectives to this project. Although a valued academic contribution, a number of issues were encountered regarding robustness, computational expense and accuracy.

The approach taken within this project was to initially follow the work conducted by McCummiskey, borrowing from the approach established and addressing core issues encountered. Once these issues were addressed, further work focussed on the introduction of novel modelling techniques and the implementation of a bespoke arterial model.

For structure, the model developed will be presented per simulation phase as follows:

1. Forming of the proximal ring from straight drawn wire
2. Compressing the device into the sheath
3. Delivery of the device within the vessel
4. Deploying the device

The modelling methods adopted will be compared against previous attempts, highlighting progress achieved by this study.

4.2.1 Ring forming from wire in straight drawn condition

There were several methods by which the pre-strain within the ring could be obtained, with the use of thermal gradients being the most common within the existing literature. Through this method, thermal expansion and contraction is used to replicate strain states. For this particular study however, Nitinol's distinct temperature dependence made the use of thermal gradients inappropriate. Although Nitinol's mechanical properties could be made to be temperature independent within the Aurichio material sub-routine, such a modelling step would have to come with the reassurance that future iterations of the framework would

not want to take thermal effects into account. Without these reassurances, the simulation of a displacement-based method was favoured within this project.

Although a displacement method was chosen, care was taken to avoid complex contact conditions. Instead, a parametric algorithm was favoured that could directly enforce displacement vectors on nodes.

After adopting a quarter symmetric modelling approach, a process was developed whereby the straight drawn wire was slowly displaced into a semi-circular shape. This was at first achieved by employing incremental displacements on nodes, which was made to coincide with the centreline of the wire. By calculating the theoretical final position of each centreline node, displacement vectors could be specified and the wire made to converge onto the semi-circular shape. Although this process showed promise, the over-constrained nature of the employed boundary conditions led to robustness issues. Another concern was that shear effects resulted in planar sections of the wire not being normal to the axis of rotation. To compensate for this effect, an additional load step was incorporated to ensure the correct orientation of the wire ends. Within this additional load step, final nodal positions of the two faces were corrected using planar surface constraints. As seen in figure 4.3, this method yielded exceptionally good results with the additional load step ensuring a uniform stress-strain distribution across the entire arc. The FE analysis as shown in figure 4.3 used C3D20R elements to represent a 24 mm OD proximal ring, with wire thickness of 0.18 mm. Validation procedures are presented in chapter 5.
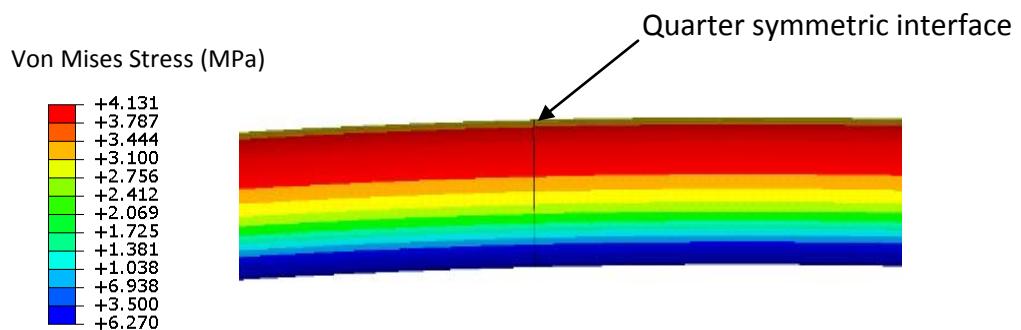

Figure 4.3: **Stress contours seen at the quarter symmetric interface.**

With it shown that a uniform stress-strain distribution could be achieved using displacement techniques, further work regarding pre-strain modelling focused on the reduction of the computational expense involved with the pre-strain phase. For this purpose further development focused on the removal of excessive boundary conditions.

A technique was developed by which wire faces were made to be perpendicular with the xz and yz planes. Using this condition alone as the system constraints, as shown in figure 4.4, the wire would tend to a perfect arc. This condition set was also consistent with the quarter symmetry model approach. By making the conditions a function of nodal positions after mesh generation, the script was made to be fully parametric. The technique worked exceptionally well and as such was incorporated into the final framework.
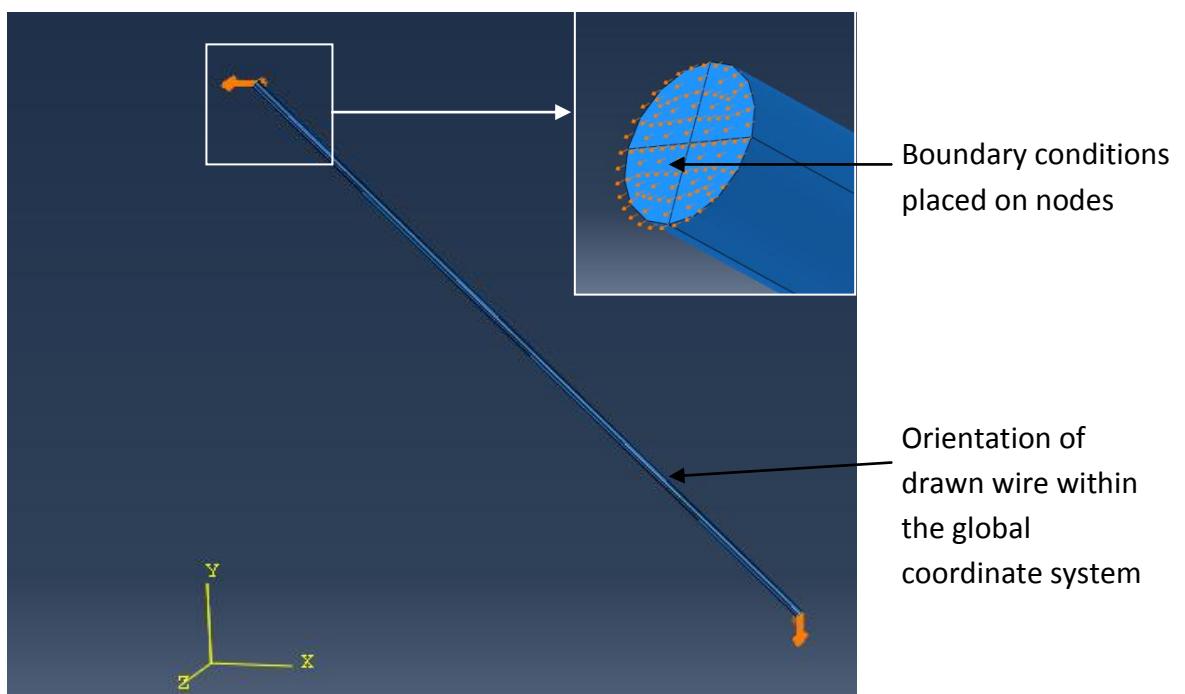

Figure 4.4: **Positioning of the straight drawn wire within the global coordinate system with boundary conditions applied. Boundary conditions were set to constrain wire faces towards the XZ and YZ planes as indicated.**

4.2.2 Compaction of wire

In practice the Anaconda is compacted into a sheath by pulling it through a conical device into a highly compacted saddle shape. Once in the sheath, it is delivered directly into the patient via minimally invasive surgery. As an emphasis was placed within this study on capturing all major loading events, modelling efforts were made to represent this phase of the device's lifecycle.

In previous studies [24], partial compaction of the ring was achieved through a series of displacement boundary conditions placed on the wire's neutral axis. Concerns over this method were raised during this study when it was found that the wire twists around its centreline during compaction.

In this study, to allow for the wire to freely rotate around its centreline, displacement boundary conditions used to compact the wire were placed on a single central node within each wire face (as indicated by the white arrow in figure 4.5). Although placing a displacement boundary condition on a single node could be regarded as poor FE modelling practice (as this has the potential for creating unwanted stress concentrations), the method yielded physically intuitive results as presented in figure 4.5. The FE analysis as shown in figure 4.5 used C3D20R elements to represent a 24.0 mm OD proximal ring with a wire thickness of 0.18 mm. A mesh convergence study is shown in figure 4.6. Recognising that analyses are only conducted up to 20% oversize, results indicated that, increasing the through thickness mesh density above twelve elements yielded little change in results.
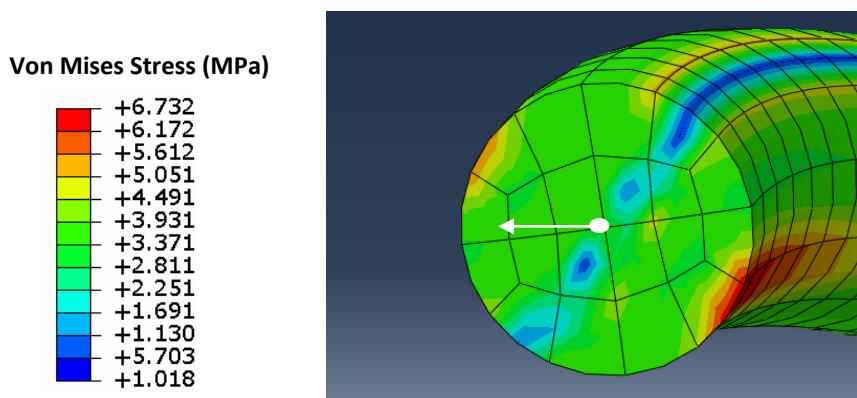

Figure 4.5: **Through thickness stress distribution of the wire compacted down to 65% oversize.**
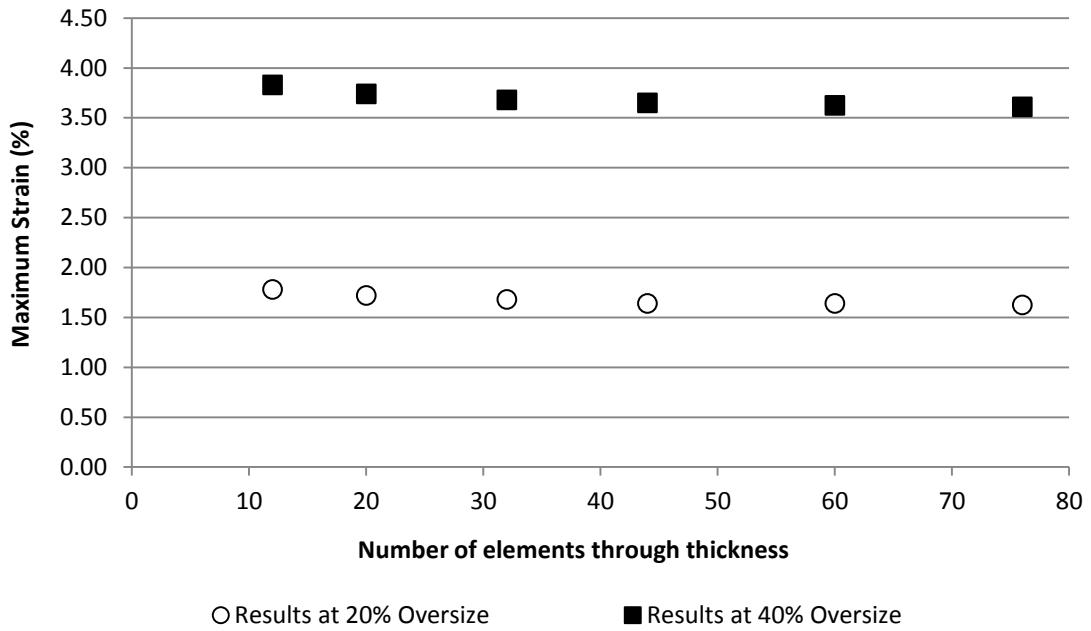
Figure 4.6: **Convergence on results with increased mesh density for a R_28 device.**

4.2.3 Delivery of system

In an attempt to reduce computational cost, care was taken not to include any load steps which could be deemed unnecessary. For this reason, the proximal ring was compacted in position at its delivery site, removing the need to manipulate the ring into position once compacted, as was previously done [24].

To achieve this, contact conditions were eliminated during the initial stages of the simulation. With this, the wire would simply form through the vessel wall as seen in figure 4.7. In position, the proximal ring could be released at which point contact conditions were invoked, initiating interactions between the artery and device.

Although physically unintuitive, this modelling method has no influence on the final FE simulation results.
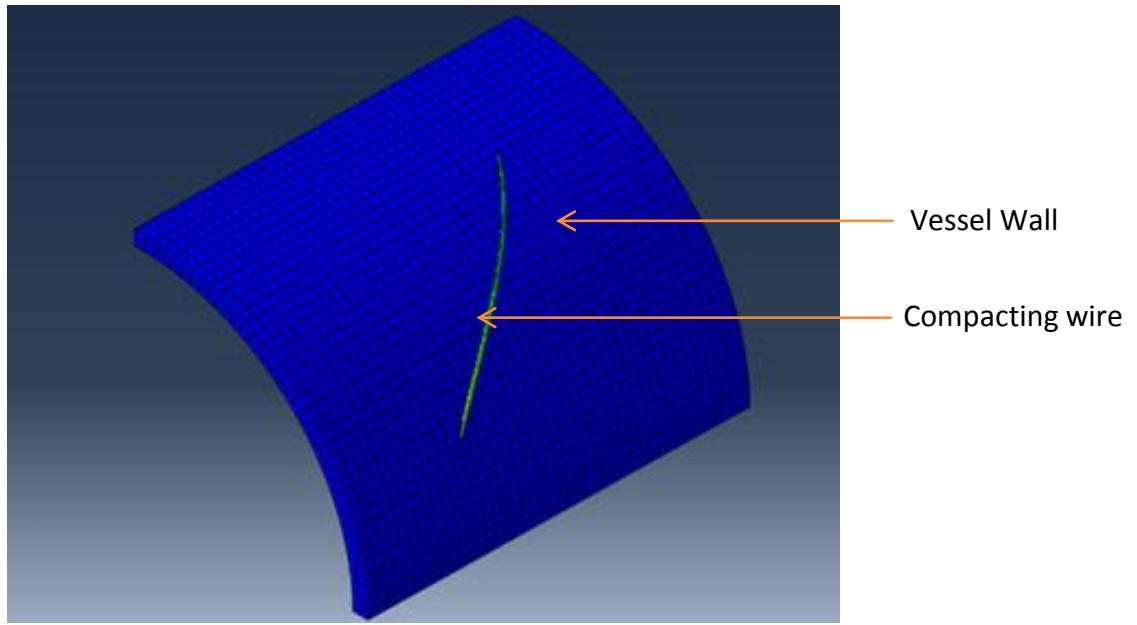
Figure 4.7: **Compaction phase of the wire. With no delivery phase the wire was modelled already in position. The ring was then formed and compacted through the vessel wall. Once compacted, boundary definitions were invoked and the device deployed within the vessel.**

4.3 Further developments

Section 4.2 summarised the initial development of the python script framework that could be used to study device-artery interactions. The approach taken within this thesis to build upon previous projects led to a stable, computationally efficient baseline, to which further developments could be introduced. Further developments fell into two categories: the introduction of a beam element model; and the introduction of a more representative arterial model.

4.3.1 Introduction of a beam element proximal ring model

Initial development of the framework utilised C3D20 continuum elements for proximal ring representation. Although these elements produced detailed through thickness results, they were relatively computationally expensive when compared against beam elements (Abaqus B32H [48]). For this reason, an additional script was introduced (Appendix 6.3), which could be used to replace the C3D20 elements with B32H elements at any point during the pre-processing phase. The beam element model was redeveloped using the modelling principles as established in its

continuum counterpart. With this, boundary conditions during the forming phase forced wire ends to become perpendicular to the XZ and YZ planes as illustrated in figure 4.9. Compaction and deployment were done through boundary conditions equivalent to that of the continuum representation, displacing the wire ends along the Z axis with displacement boundary conditions.

Beam element theory rests on a number of simplifications and assumptions. These assumptions have in the past been based upon slender beam assumptions. As a result, they have in the past been limited in their ability to account for large bending deformations. New technology that allows for large out of plane deformations and nonlinear shear, such as the Timoshenko formulation, was used in this study. Validation of the beam element approach to this particular application is shown in chapter 5 of this thesis. Mesh convergence studies indicated that increasing the beam element density below 0.35 mm, yielded no significant change in results for both the 20% and 40% oversize conditions (figure 4.8). The beam element script was produced as an add-on, which meant that it sat as an additional script that could be used during pre-processing. The script worked by editing the model assembly, replacing the continuum representation with the beam element approach. Through the use of beam elements a significant reduction in computational expense was achieved. The development of a beam element representation was a valuable contribution to the framework and a precursor to the development of the multi-turn proximal ring model.
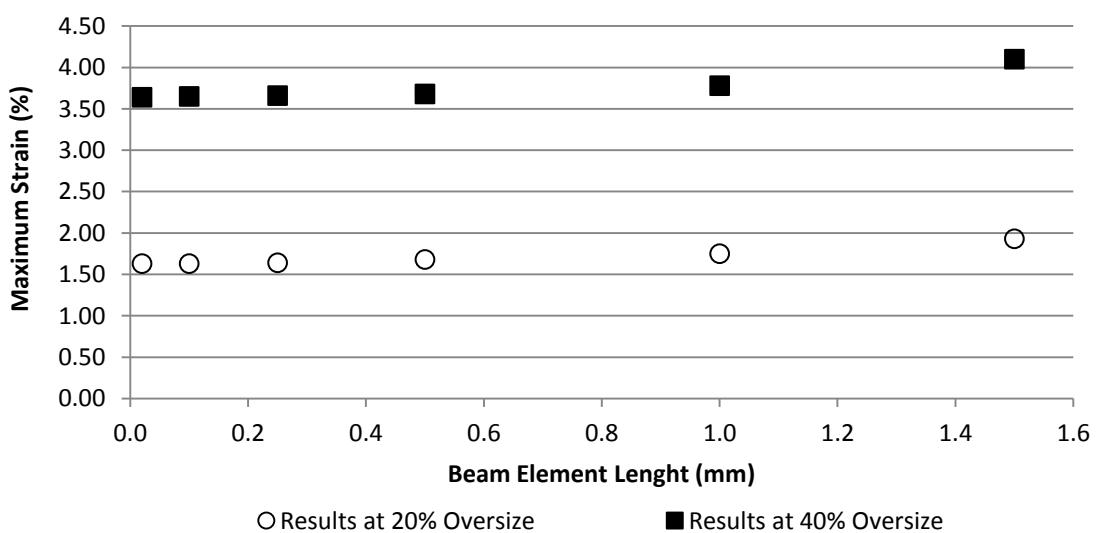
Figure 4.8: **Convergence on results with increased mesh density for a R_28 device**
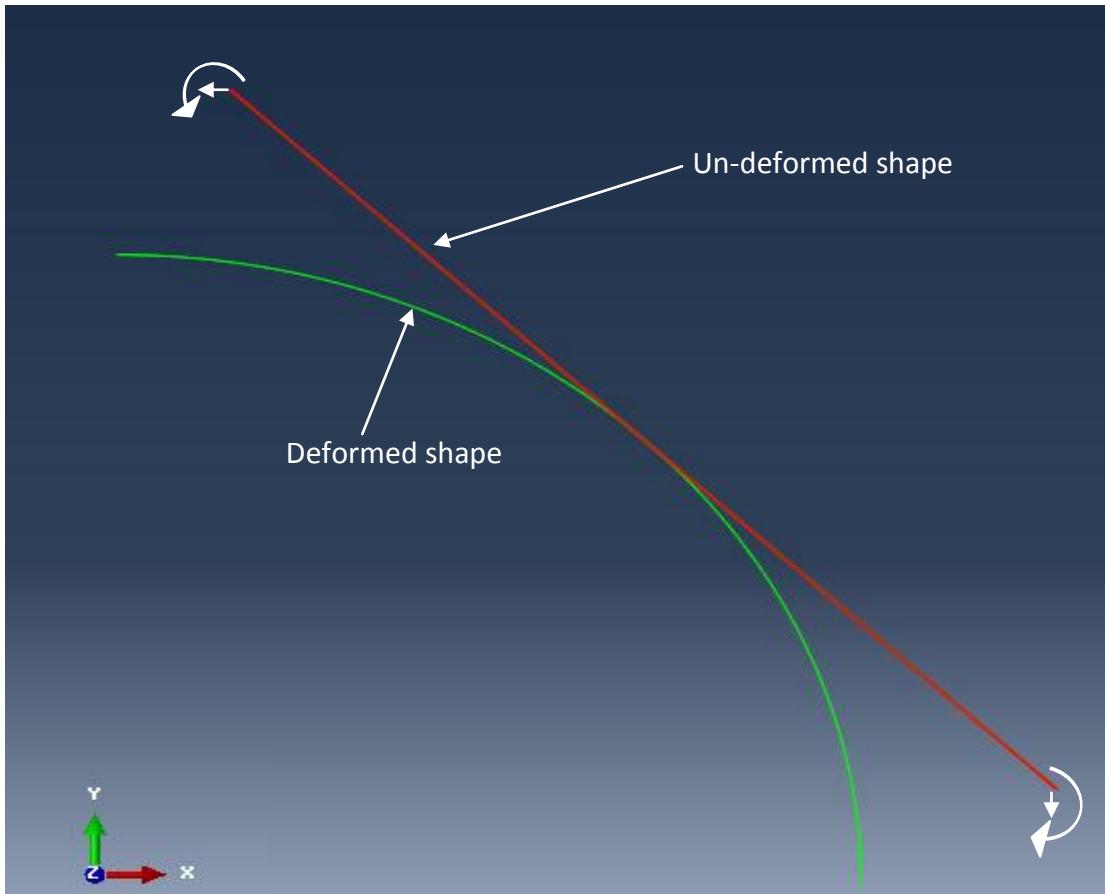
Figure 4.9: **Illustration of beam element ring formation.**

4.3.2 Vessel modelling

Previous attempts at capturing device/artery interactions have included severely compromised arterial models as discussed in section 2.3. To this extent, the incorporation of a comprehensive arterial model into the integrated modelling framework was seen as one of this project's biggest contributions. A considerable amount of effort was therefore invested in the development of a credible vascular representation.

This section will first outline the finite element modelling approach adopted for the representation of the artery. An overview of the python script produced for the arterial model's incorporation into the framework, will also be presented. Once the modelling methods are outlined, the procedures used to obtain artery material parameters will be clarified. Validation studies for any of the derived models work, is discussed in chapter 5.

4.3.2.1 Development of the arterial model

Development of a vessel model followed the simplifications and assumptions outlined in section 4.1.2 of this report. With this, the arterial wall was modelled as a quarter cylindrical vessel.

The media and adventitia were meshed using quadratic, hexahedral elements with hybrid and reduced integration formulations (Abaqus reference: C3D20RH). The use of quadratic elements was needed to cope with large deformations, whilst the hybrid formulation was required for the incompressible material involved. Laminated shell and other idealised forms of representation were not considered during this work. This was because such forms of representation are not validated in Abaqus 6.11 documentation for use when employing Holzapfel's formulation [48]. Idealised forms of representations are however appropriate for other Hyperelastic formulations, such as the Fung Model, and exploration of their use, are therefore suggested as a recommendation for further work in section 7.3.

During ring deployment, the use of quadratic hexahedral elements resulted in robustness issues during contact initiation. Furthermore, once contact had been established, element distortion was problematic. To address these issues, the intima was modelled using linear tetrahedral elements with a hybrid formulation (C3D4H). This approach vastly improved the robustness of simulations and reduced their computational cost.

As C3D4H elements had the potential of over-predicting stiffness due to bend locking, their use within the framework was explored through mesh studies presented in figures 4.10 and 4.11. Within these figures, stress and stiffness results from two otherwise identical vessels are compared (OD of 28.00 mm and thickness of 1.43 mm with Abaqus Holzapfel parameters < .01, 0.0, 0.22, 13.42, 0.135 >). Figure 4.10 demonstrates that similar stress distributions were obtained when using tetrahedral opposed to hexahedral elements, with agreement of maximum Von Mises stresses within 2.1%. This agreement came despite the discontinuity of using linear and non-linear elements, as Abaqus 6.11 automatically reduced the non-

linear hexahedral boundary edge to be linear. Figure 4.11 displays pressure-diameter results, demonstrating that near identical stiffness characteristics were obtained through both approaches. Within this graph, a comparison is also made against a vessel model using an increased mesh density of eight C3D20RH elements through thickness. This comparison indicates that mesh convergence had been reached for the vessel with the combination of tetrahedral and hexahedral elements shown in figure 4.10.
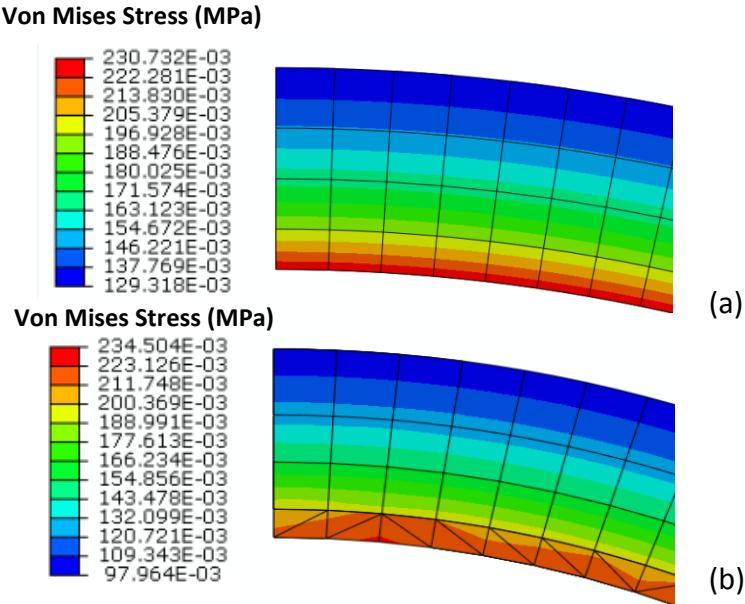

Figure 4.10: Stress distributions for arterial vessels where the intima is modelled using hexagonal (a) and tetrahedral elements (b) in a 220 mmHg pressurised simulation.
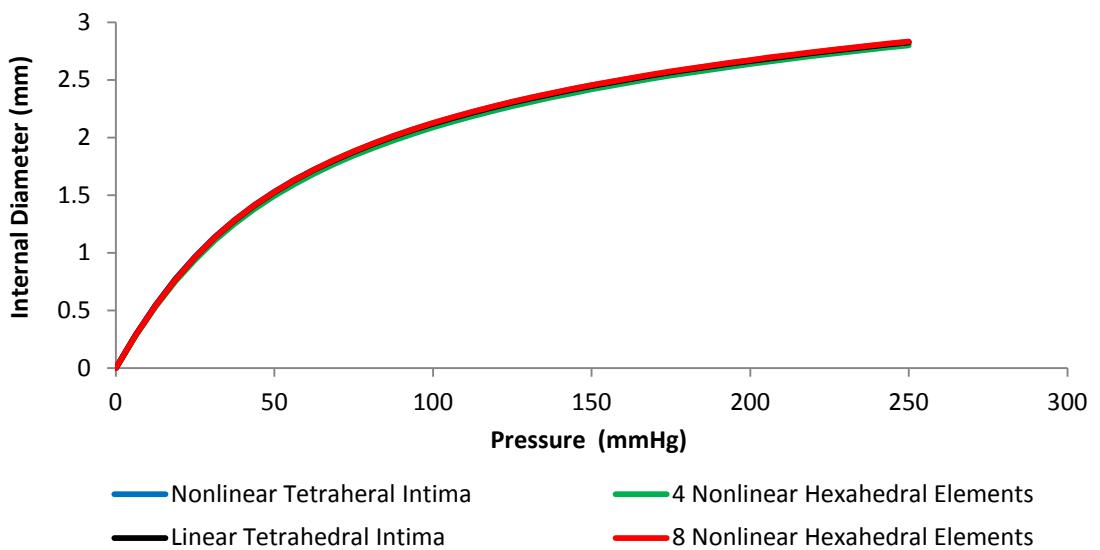

Figure 4.11: Pressure-Diameter results of vessel using various mesh representations.

Figure 4.12 (c) displays the boundary set employed. Standard symmetric conditions were set on marked surfaces whilst an axial boundary condition was used to simulate *in situ* stretches (10-15%). As seen from the image, internal pressure was directly applied to the inner surface of the vessel wall.

Cartesian material orientations were assigned per element, with a projection parallel with the axis of the vessel, a projection tangential to the circumference of the vessel, and a 3rd projection perpendicular to vessel's central axis. The model as shown in figure 4.12 was parameterised and scripted within Python (Appendix 6.4). Within the script a choice of material models is provided for users. The material models ranged from near rigid condition, linear elastic models to the Holzapfel arterial material model. Material parameters used to particularise the linear elastic model were user-defined per simulation run whilst the Holzapfel parameters are derived in section 4.3.2.2 from data presented in chapter 5.
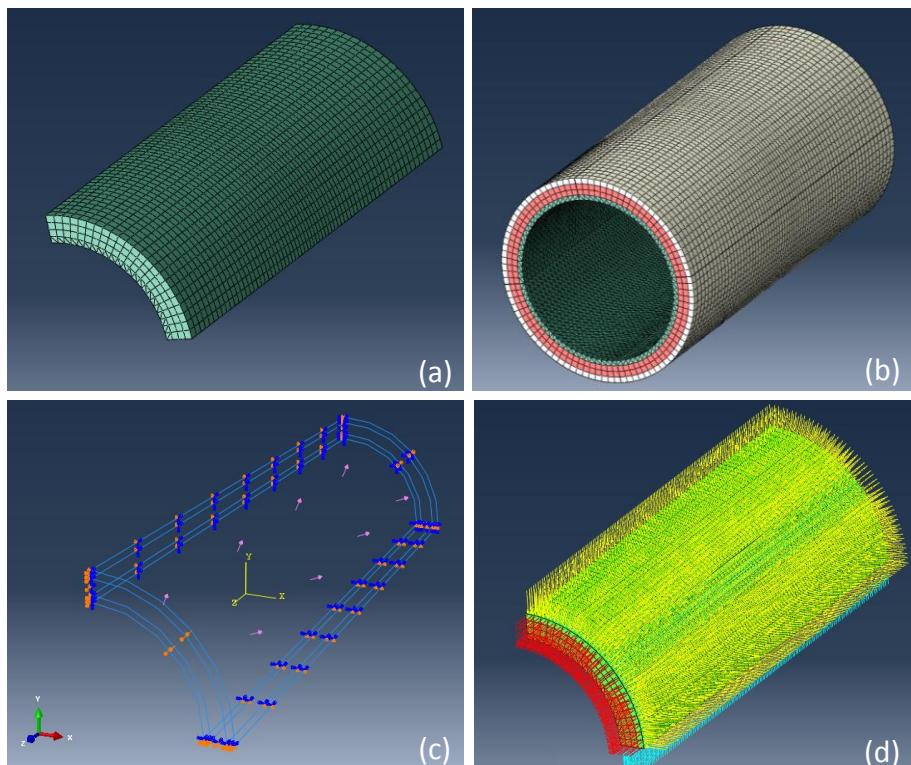
*Figure 4.12:* **Quarter symmetrical representation of the arterial wall. The vessel wall is comprised of a basic cylindrical shape (a). This cylinder was sectioned into three discrete regions to form 3 arterial layers (b). Boundary conditions were placed as required to apply axial stretches and internal pressures (c). Material orientations were then applied, as required for soft tissue modelling (d).**

4.3.2.2 Arterial material model development

Embedded within the Holzpafel [89] constitutive model are five material parameters which fit it to a given data set . A host of different methods can be used for the derivation of these parameters. The method best suited is largely dependent on the experimental data sets available. Herein, as would be the case in many cases within industries, uniaxial material data was available.

Holzapfel [67] proposed an approach which could be used for the determination of parameters from uniaxial data sets. An outline of this approach will be presented within this section. Following this, the approach will be applied to the data sets produced through the vascular testing programme. It should be noted that modern FE suites, such as Abaqus 6.11-2, have built-in curve fitting applications, resulting parameters of which are provided in table 4.2. These applications disguise the underlying assumptions of constitutive relations and a very limited number can fit anisotropic hyper-elastic data sets. For these reasons, both methods were used within this study.

For further details on the mathematical derivations interested readers can refer to [98], [73] and [90].

Outline of the approach

Uniaxial data is often not sufficient to determine multi-dimensional models. The reason is that these experiments do not cover the same strain domain as might be explored during simulation. As a result of fitting multi-dimensional models to uniaxial data, convergence issues could be encountered. Ideally then the free energy function as introduced in section 2.2.6 should be fitted against biaxial data. This was however not possible with current University of Strathclyde capabilities, a complication experienced by many end users within industry.

With these issues noted, Holzapfel [67] suggests a technique whereby physical and structural related constraints are imposed on the free energy function in such a way that it can be fitted against uniaxial data. Using additional data from histology examinations, further constraints are placed on parameters so that, in addition to

providing satisfactory uniaxial results, parameters also provide adequate multi-axial convergence.

To follow this approach by Holzapfel, the free energy function is modified for uniaxial test conditions. Partial derivatives of the function are then taken with respect to the in-plane strain directions (E_{33} is assumed to be zero), giving components of Piola-Kirchhoff stress tensor. If strain values are taken from the experimental tests, analytically calculated stress values can then be compared against those predicted by the modified function. Using this comparison, through a least square analysis optimization technique, the energy function can be fitted against the data sets and the material parameters extracted.

Derivation of parameters

Recalling the basic expression for the free energy first presented in section 2.3.10.2, it was shown that the total helmholtz free energy (Ψ) can be expressed in terms of its isotropic (Ψ_{iso}) and orthotropic (Ψ_{ortho}) free energy contributions as stated in equation 4.1.

$$\boldsymbol{\Psi = \Psi_{iso} + \Psi_{Ortho}}$$

(4.1)

This general expression can be particularised through an appreciation of the test setup used within the vascular testing programme. During the vascular testing programme two rectangular strips were harvested per arterial layer, one aligned in the axial (x^1) direction of the aorta and the other in the circumferential direction (x^2). As with the test setup, the Green-Lagrange strain tensor (E_{11} and E_{22}) are components of strain that were directly supplied by the Video Extensometer. From the Green-Lagrange strain tensor, the Piola-Kirchoff stress tensor could be deduced of which the transverse components are near zero (with reference to the tensile axis). This provides the first of the constraints which can be placed on the associated strain-energy function as analytically, the experimental paths must cross in a location at which the transverse components of the second Piola-Kirchoff tensor vanish. Applying this kinematic constraint to equation 4.1 and

assuming incompressibility it can be shown that the isotropic and orthotropic components can in turn be expressed as:

$$\Psi_{iso} = \frac{\mu}{2}\{2(E_{11} + E_{22}) + [(2E_{11} + 1)(2E_{22} + 1)]^{-1} - 1\} \qquad \textbf{(4.2)}$$

$$\Psi_{Ortho} = C[\exp(c_{11}E^2{}_{11} + c_{12}E_{11}E_{22} + c_{22}E^2{}_{22}) - 1] \qquad \textbf{(4.3)}$$

In the above expressions $\mu, C, c_{11}, c_{12}, c_{22}$ are parameters that fully define the material's behaviour. It is these parameters which the data fitting process aims to retrieve.

In order to derive meaningful parameters, another constraint can be introduced whereby the parameters chosen must be such that the second derivative of the strain energy function with respect to E_{11} and E_{22}, is positive. This ensures that contours of constant strain energy values are convex when projected onto a E_{11}, E_{22} plane. The property of "convexity" is an important attribute required for numerical solver implementation [99] .

This property of local convexity can be achieved when the exponential term in equation 4.3 is set to a constant value, as shown below in equation 4.4.

$$\text{Const} = c_{11}E^2{}_{11} + c_{12}E_{11}E_{22} + c_{22}E^2{}_{22} \qquad \textbf{(4.4)}$$

Equation 4.4 is in a quadratic form and as such can be rewritten in matrix form with eigenvalues γ_1, γ_2 of the Hessian matrix as shown in equation 4.5

$$\gamma_{1,2} = \frac{1}{2}\left[c_{11} + c_{22} \pm \sqrt{c_{12} + (c_{11} - c_{22})^2}\right] \qquad \textbf{(4.5)}$$

If the requirement exists that the Hessian matrix is positive definite, as it is for implementation into FE [99], then the inequality of equation 4.6 can be assumed.

$$4c_{11}c_{22} - c_{12}{}^2 > 0 \qquad \textbf{(4.6)}$$

This inequality dictates that both c_{11} and c_{22} are either positive or negative. For results to make physical sense however both these parameters must be positive [89].

Study into parameter c_{12} reveals another constraint. For all stress components to be positive during biaxial extension and negative for biaxial compression, parameter c_{12} must be positive. Holzapfel also further relates parameter c_{12} to mean collagen orientations through an appreciation of its relationship with the slope eigenvector.

Constraints to be imposed onto any parameters derived using this approach could be summarised as shown through equations 4.7 and 4.8

$$\mu > 0, C > 0, c_{11} > 0, c_{12} > 0, c_{22}, > 0 \qquad \text{(4.7)}$$

$$4c_{11}c_{22} - c_{12}{}^2 > 0 \qquad \text{(4.8)}$$

The total strain energy is based on two terms referring in part to orthotropic and isotropic contributions. The inequality constraints that are discussed within this section only relate to the orthotropic component. With this, the shear type parameter μ is yet to be addressed. In accordance with an assumption adopted by previous studies [100], this thesis assumed that the isotropic contributions dominate the initial linear elastic response noted during tensile testing. With this assumption, the parameter μ can be fitted independently using a truncated stress-strain curve. In this study, parameter μ was fitted against these truncated sets using a damped-least square method. The method is a well established method for curve fitting problems [101].

Fitting results

Curve fitting procedures outlined by Holzapfel [67] were completed within Microsoft Excel 2010. Results obtained by following this process are shown in table 4.1 for all specimens, with the accuracy of fits displayed through the coefficient of determination "R^2" .

To illustrate the effectiveness of these parameters, figures 4.13 through to 4.18 are presented which demonstrate the ability of the constitutive model, and the parameters derived, to replicate experimental data. Within these figures relevant experimental results are compared against the constitutive model's predictions which are presented per isotropic and orthotropic contribution. Doing so reveals

the inner workings of the model and the relative dominance between elastin and collagen during mechanical straining.

Table 4.1: **Summation of material parameters obtained through following curve fitting procedures outlined in section 4.3.2.2.**

		c_{11}	c_{12}	c_{22}	C	μ	R^2
Specimen 1	Intima	10.46	8.66	14.5	.0004	.0090	0.96
	Media	6.72	7.76	5.03	.0047	.0095	0.93
	Adventitia	5.34	3.76	6.91	.0028	.0019	0.91
Specimen 2	Intima	8.45	8.24	7.14	.0046	.0084	0.97
	Media	6.14	7.42	5.34	.0042	.0094	0.92
	Adventitia	6.71	4.42	5.01	.0037	.0084	0.91
Specimen 3	Intima	8.21	7.94	7.43	.0042	.0089	0.93
	Media	6.14	7.21	5.24	.0041	.0084	0.96
	Adventitia	3.12	3.42	6.18	.0031	.0023	0.98

Table 4.2: **Summation of material parameters obtained through following curve fitting procedures in Abaqus 6.11** [48]**. Validation of these parameters are presented in chapter 5.**

		k	k1	k2	φ	μ	R^2
Specimen 1	Intima	0.140	0.389	27.25	47.1	0.006	0.91
	Media	0.120	0.145	5.58	44.2	0.091	0.93
	Adventitia	0.142	0.046	4.68	51.7	0.003	0.92
Specimen 2	Intima	0.228	35.42	10.62	49.1	0.025	0.93
	Media	0.135	0.220	13.42	45.8	0.010	0.89
	Adventitia	0.080	0.035	28.41	52.9	0.012	0.91
Specimen 3	Intima	0.170	0.728	20.94	47.6	0.014	0.93
	Media	0.009	0.219	8.77	42.9	0.010	0.94
	Adventitia	0.210	0.110	7.40	59.6	0.001	0.93
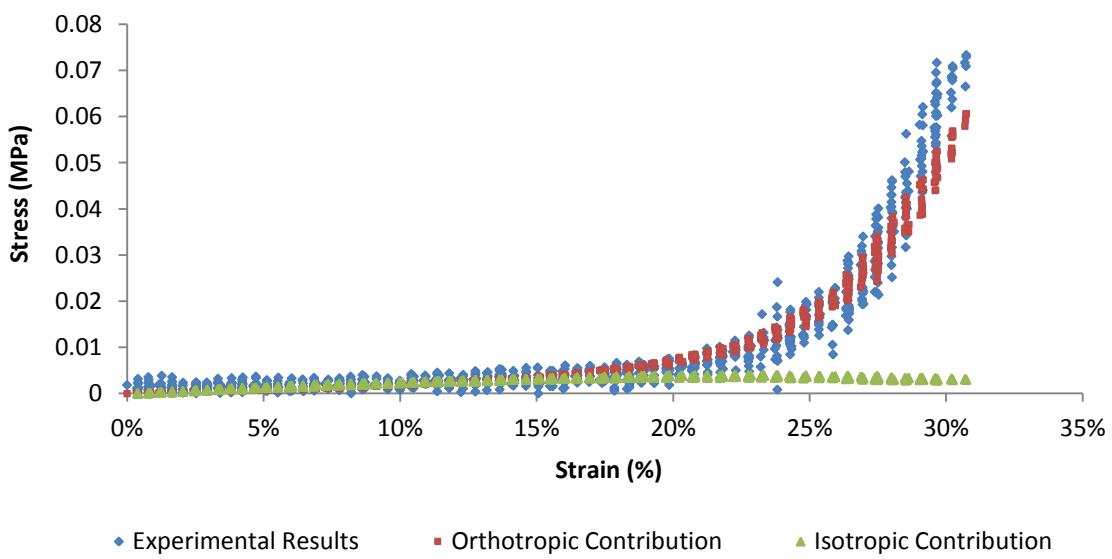
Figure 4.13: **Fitting results for specimen 1's axial intimal data.**
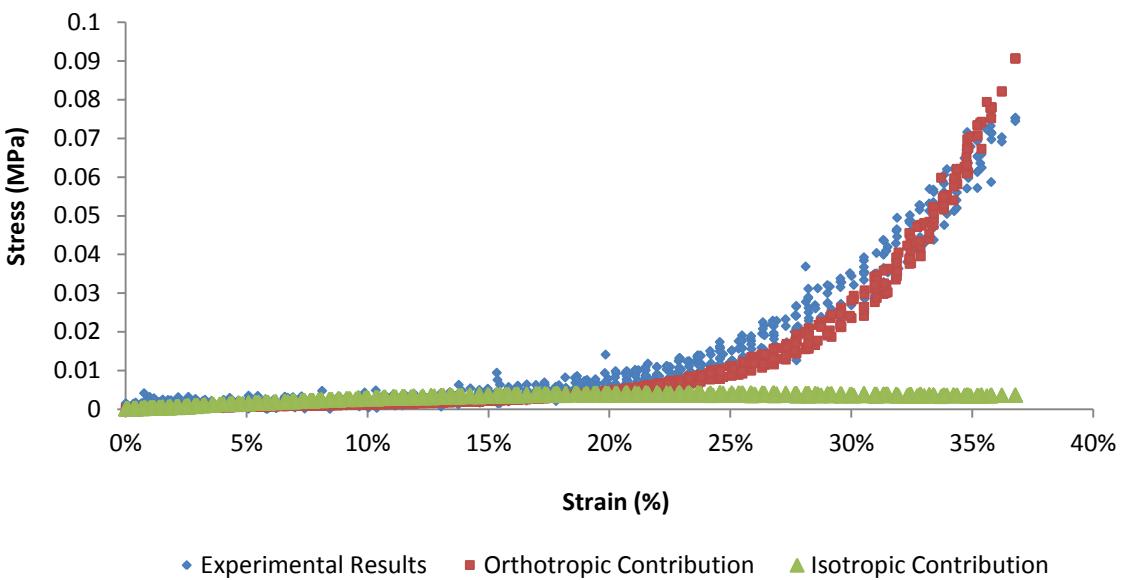
Figure 4.14: **Fitting results for specimen 1's circumferential intimal data.**
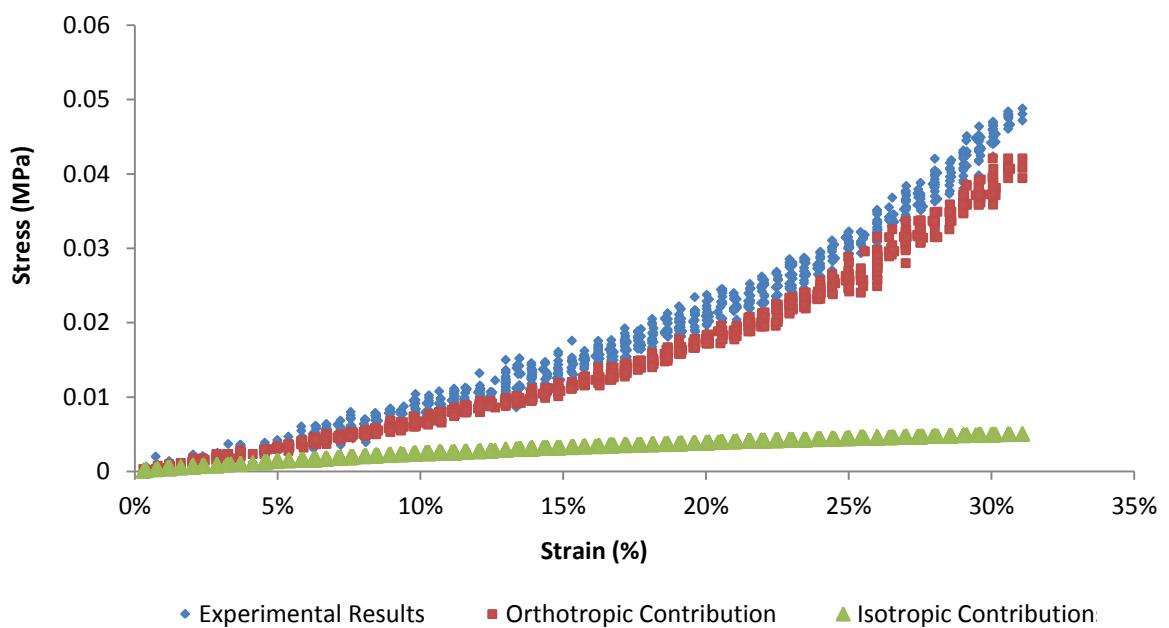
Figure 4.15: Fittings results for specimen 1's axial medial data.
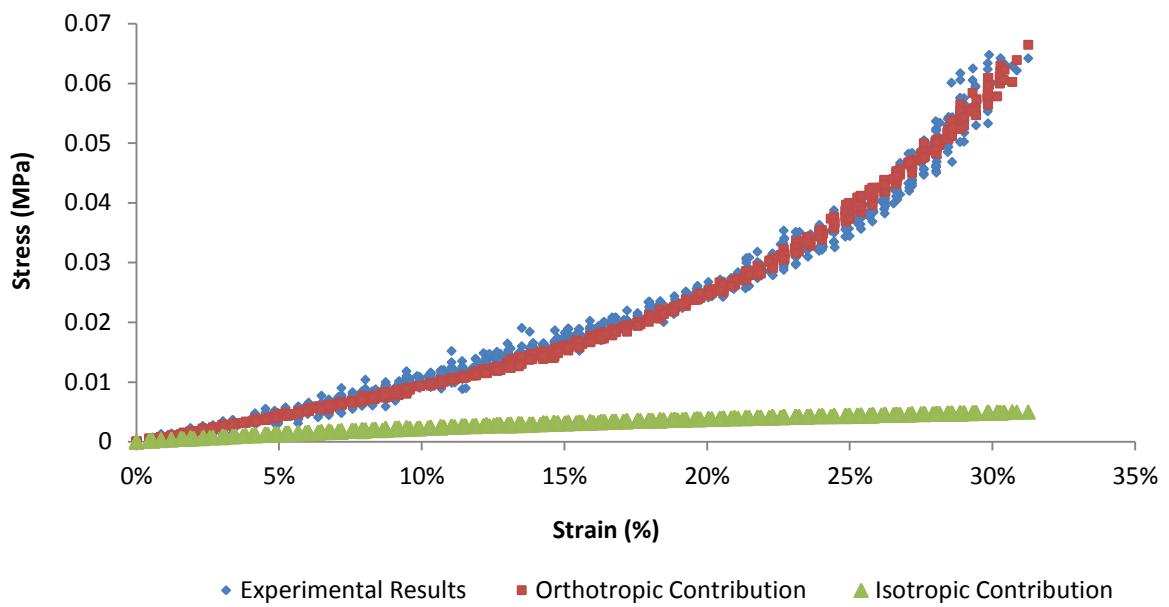
Figure 4.16: **Fitting results for specimen 1's circumferential medial data.**
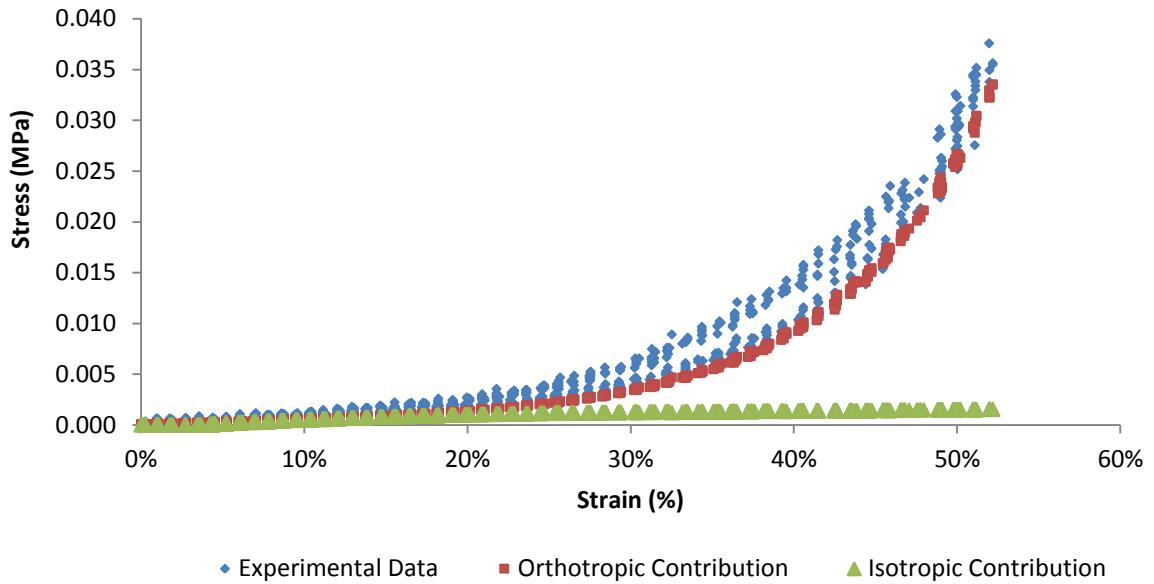
*Figure 4.17:* **Fitting results for specimen 1's axial adventitia data.**
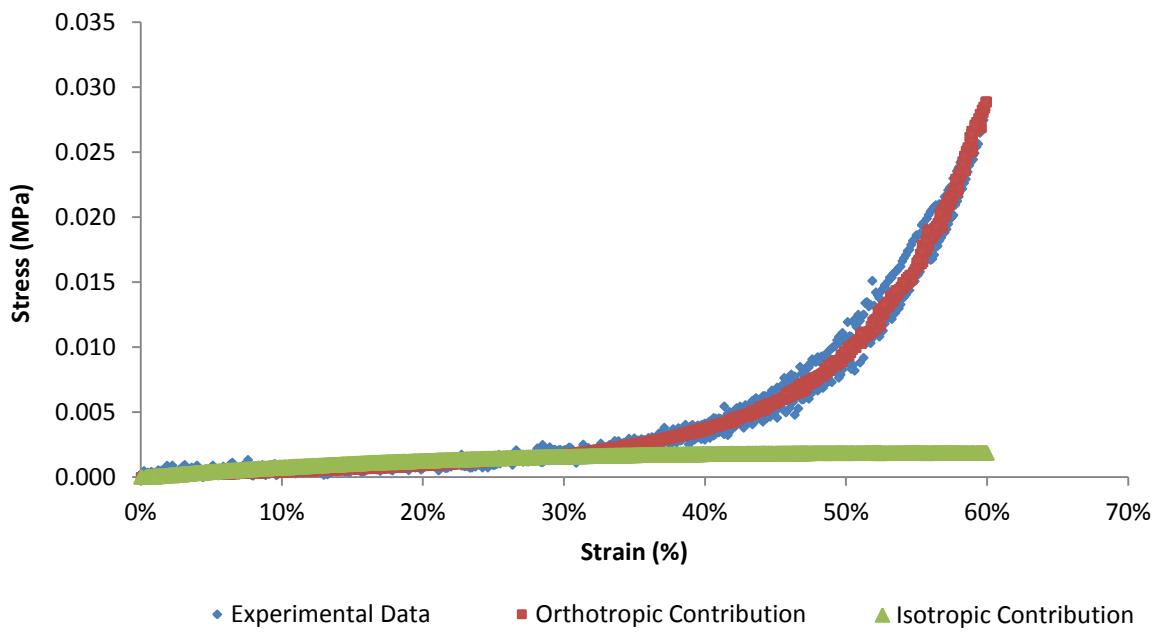
Figure 4.18: **Fitting results for specimen 1's circumferential adventitia data.**

4.3.3 Auricchio Nitinol material model

In this study, the Auricchio Nitinol material model was implemented as a built in user-subroutine [48]. The model requires 15 parameters to be particularised to a given data set. These parameters are deduced through a straightforward process during which key stages of the material's stress-strain response are used as parameter inputs. For further information regarding this method, and for the physical meaning of parameters, please refer to appendix 4. The Nitinol wire used within the Anaconda device is supplied by Fort Wayne Metals. The alloy specification is categorised under the product name "Nitinol#1 Super-Elastic Straight Annealed". The alloy supplied has an etched (oxide free) surface finish.

Uniaxial stress-strain results obtained from the supplier for this material are shown in figure 4.19. Through following the procedure outlined in appendix 4, 15 parameters were picked from this response, as shown in table 4.3. These parameters were implemented within the endovascular device model, resulting in a replication of the stress-strain curve as shown in figure 4.14. A representative tensile response were obtained whilst a less accurate compressive response was noticed. This is an inherent limitation of the Auricchio constitutive model, the accuracy of which is further explored in chapter 5 of this thesis. Further studies regarding the accuracy of the Aurrichio model can be found within the literature [24].

Parameter:	E_A	v_A	E_M	v_M	ε^L	$\left(\frac{\partial \sigma}{\partial T}\right)_L$	σ^S_L	σ^E_L
Units:	MPa	-	MPa	-	-	MPaT^{-1}	MPa	MPa
Value:	65800.0	0.435	65800.0	0.435	0.0538	5.74	637	657

Parameter	T_0	$\left(\frac{\partial \sigma}{\partial T}\right)_U$	σ^S_U	σ^E_U	σ^S_{CL}	ε^L_V	N_A
Units:	^{o}C	MPaT^{-1}	MPa	MPa	MPa	-	-
Value:	0	6.99	327	307	853	0.0538	0

*Table 4.3:* **Parameters deduced from provided stress-strain results.**
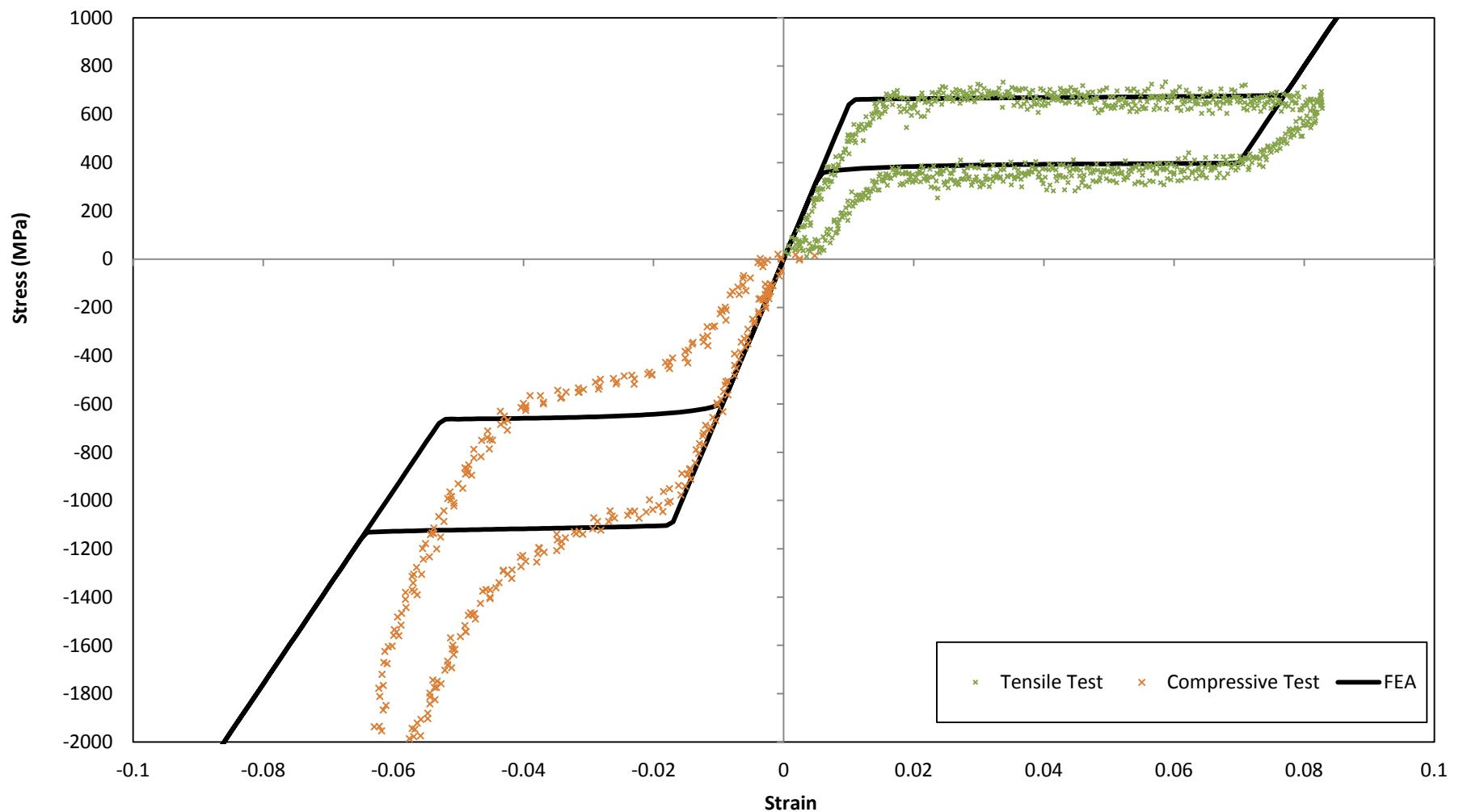
Figure 4.19: **Uniaxial stress-strain results for a 1 mm diameter Nitinol specimen undergoing tension and compression at 37⁰C. Best fit results using the Auricchio material model are shown, driven by parameters provided in table 4.3**

4.4 The python script framework

Sections 4.2 and 4.3 discussed the development of individual constituents required to simulate device-artery interactions. Once constituents were developed, they were integrated into a viable design structure, which took the form of a framework of python scripts.

4.4.1 Script outlay modelling methodology

To create a simulation using the framework, a user would simply import a sequence of scripts into Abaqus which would then automatically generate an FE study. A number of scripts were available, all of which could be combined in manner of ways to create a variety of studies. The parameters of these studies could be adjusted within the scripts to edit model geometry, whilst load conditions could be adjusted within Abaqus as per study requirement.

Each script represented a unique element of the framework, be it a geometric feature or load step. By adopting this modular approach the framework was kept open for future development as each element could easily be replaced with an updated version. With this it should be clear that the framework was developed with usability in mind, a starting point on top of which future iterations could easily be built. Such an approach was key if the framework was to be viable for both academic and industrial application.

4.4.2 Script framework overview

The framework was structured into a user-friendly tier structure as presented in figure 4.20. Within each one of these tiers a number of scripts existed. An approach was outlined by which an end user would move from tier to tier, selecting scripts around which to build a specific study. Each tier represented a crucial modelling step, outlined as follows:

Tier 1. *Study is named and global parameters are set (Appendix 6.1).*

    a. A single script held all the core parameters required to construct the device-artery model. This included geometric properties for the vessel and proximal ring. For most basic studies the parameter file was the only script that required input from the end user.

Tier 2. *The proximal ring is modelled within Abaqus.*

a. Running the Beam Element script 1 resulted in a beam element (B32H) representation of the Nitinol proximal Ring. A simplified symmetric representation of the tension/compression curve was induced using this script (Appendix 6.3).

b. Beam Element script 2 (B32H) evoked an asymmetric representation of Nitinol (Appendix 6.3).

c. Continuum script 1, which resulted in continuum elements C3D8R being used for ring representation. Using this script, a symmetric Nitinol material model was evoked (Appendix 6.2).

d. Continuum script 2 used quadratic C3D20R elements for ring modelling purposes (with reduced integration). The script also induced an asymmetric Nitinol material description (Appendix 6.2).

Tier 3. *Artery vessel representation is modelled.*

a. The use of Vessel 1 script resulted in a single layered arterial model. The script could be used for a rigid material representation of the artery using linear C3D8R elements (Appendix 6.5).

b. Vessel 2 resulted in a semi-compliant representation of the artery. The script created a three layered arterial model, using a user defined elastic response (per simulation). This model was not validated within this work (Appendix 6.4).

c. The use of Vessel 3 resulted in the most comprehensive arterial model put forward herein. The script modelled a three layered artery using the Holzapfel material model representation. Through the use of this script the media and adventitia was modelled using C3D20H elements, which are continuum based. The intima was modelled using linear tetrahedral elements with hybrid formulation C3D4H (Appendix 6.4).

Tier 4. *Load steps are created; boundary conditions are calculated and applied (Appendix 6.6).*

    a. The Beam Element script within this tier defined all boundary conditions required to form the proximal ring from the straight drawn condition when using a B32H representation.

    b. The Continuum Element script set established all conditions required for the proximal ring when using a C3D8R/C3D20R representation.

Tier 5. *Boundary conditions required for ring compaction are calculated and applied (Appendix 6.7).*

    a. A single script was used for all configurations.

Tier 6. *Contact conditions and properties are defined. Load steps used to simulate deployment are created and appropriate boundary conditions are edited (Appendix 6.8).*

    a. A single script was required as the contact properties remain identical across model variations.

Tier 7. *Scripts were written to facilitate additional pre and post-processing features. Although a number were written, three that will be used at a later stage in this thesis will be outlined here.*

    a. An additional script was written which employed a stabilizing boundary condition on the centre point of the straight drawn wire. The condition is rigid constraint in the Z axis of the global coordinate system. The condition was used to avoid rigid body movement during ring deployment into a rigid arterial vessel with frictionless contact (Appendix 6.9).

    b. An additional script was written which would retrieve the stress-strain history for a single element over a user specified number of load steps (Appendix 6.10).

    c. A script was written which could extract the stress distribution along the length of the wire from the Abaqus's results database (.odb) (Appendix 6.10).
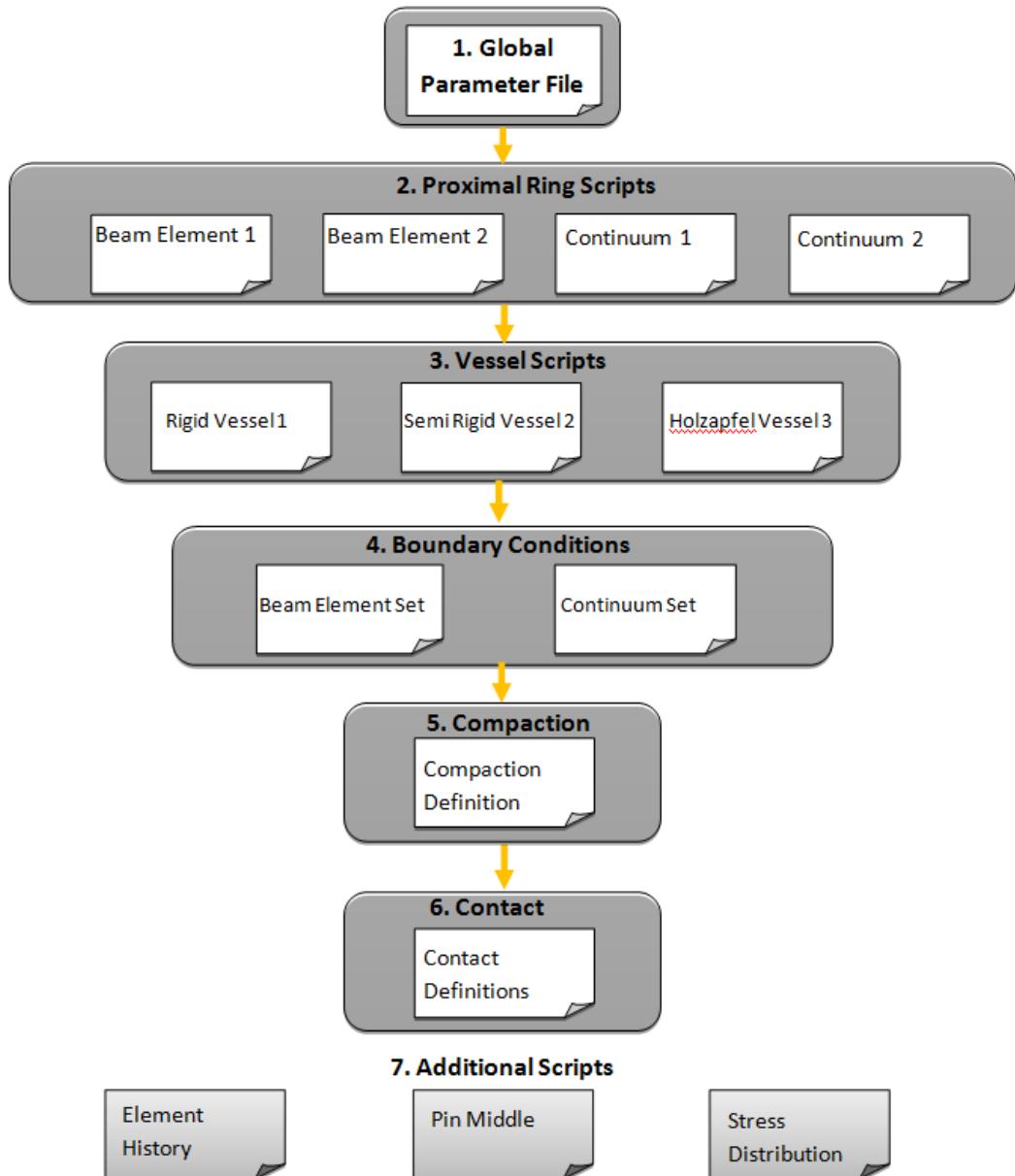
Figure 4.20: **Structure of framework developed. Scripts were structured in a hierarchical tier format, simplifying use.**

4.4.3 Typical simulation overview

Figures 4.21 and 4.22 displays an Abaqus FE model generated by the integrated modelling framework. Within these figures, key simulation phases are shown being ring formation, compaction and subsequent deployment.

Ring Forming
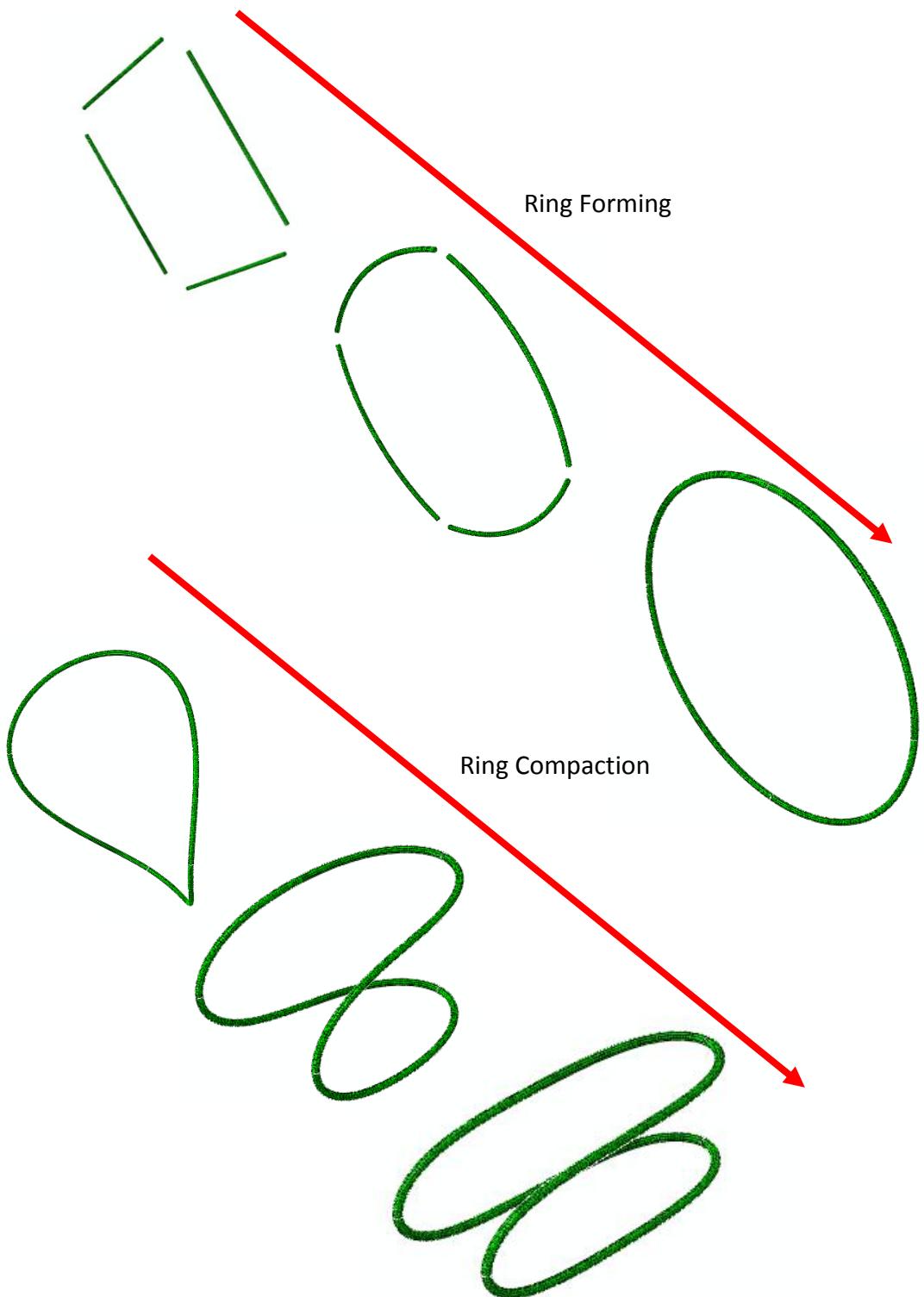
Ring Compaction

Figure 4.21: **Formation and compaction of the proximal ring.**

Stretches are employed

Ring is deployed
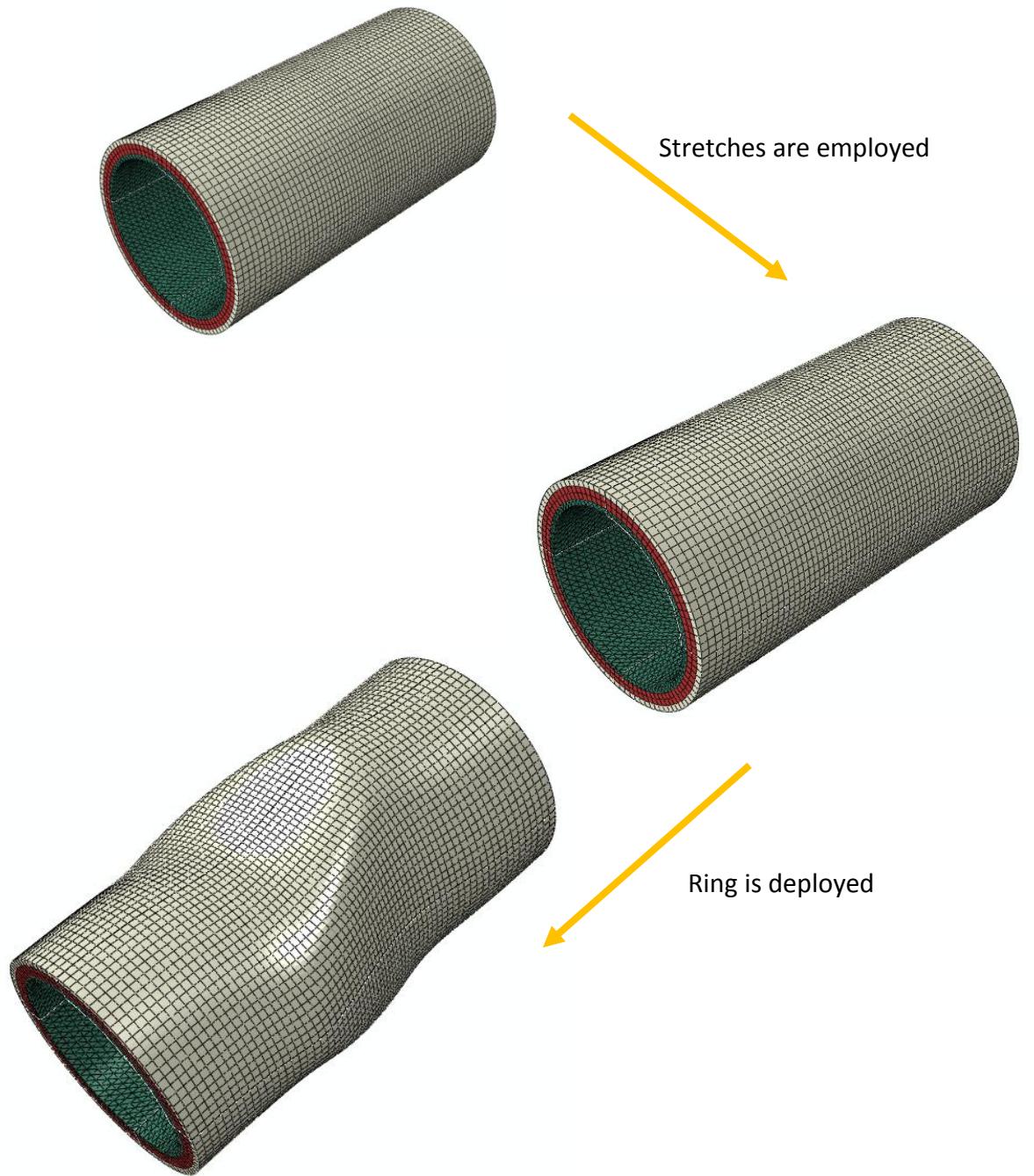
Figure 4.22: **Image sequence displays the main simulation phases associated with the vessel. These are comprised of the application of user-defined pre-stretches, deployment of the compacted proximal ring and the cycling of internal pressures.**

In an attempt to further illustrate the robustness and usability of the framework created, an Abaqus solution summary is presented in figure 4.23. As can be seen, a simulation as illustrated by figures 4.21 and 4.22 could be completed within 31 minutes using a standard desktop computer (appendix 1). This is in sharp contrast to previous studies where analogous simulations took in excess of 6 hours [24]. Running the most comprehensive artery-vessel interaction model, being an asymmetric Nitinol model and Holzapfel arterial model, took approximately 130 minutes.

Input warning messages as seen in figure 4.23 were generated as the two parts, the vessel and proximal ring, were unconnected during the first two stages of the simulation. The further 23 error messages can be seen, generated due to failed convergence iterations during contact initiation. These errors had no effect on overall accuracy of the simulation.

```
ANALYSIS SUMMARY:
TOTAL OF      107  INCREMENTS
            13  CUTBACKS IN AUTOMATIC INCREMENTATION
           368  ITERATIONS INCLUDING CONTACT ITERATIONS IF PRESENT
           368  PASSES THROUGH THE EQUATION SOLVER OF WHICH
           368  INVOLVE MATRIX DECOMPOSITION, INCLUDING
             0  DECOMPOSITION(S) OF THE MASS MATRIX
             1  REORDERING OF EQUATIONS TO MINIMIZE WAVEFRONT
             0  ADDITIONAL RESIDUAL EVALUATIONS FOR LINE SEARCHES
             0  ADDITIONAL OPERATOR EVALUATIONS FOR LINE SEARCHES
             2  WARNING MESSAGES DURING USER INPUT PROCESSING
            23  WARNING MESSAGES DURING ANALYSIS
             0  ANALYSIS WARNINGS ARE NUMERICAL PROBLEM MESSAGES

  JOB TIME SUMMARY
   USER TIME (SEC)    =  3797.7
   SYSTEM TIME (SEC)   =  68.400
   TOTAL CPU TIME (SEC) =  3782.6
   WALLCLOCK TIME (SEC) =     1817
```

Figure 4.23   **Abaqus Analysis Summary produced at the end of a simulation using an Asymmetric Nitinol model and semi-compliant arterial model.**

4.5 Chapter summary

This chapter detailed the development of the integrated modelling framework. Work conducted within this chapter stands as a continuation from a previous study [24], in which advanced constitutive models were used to study the interactions between the Anaconda and a pseudo-arterial model. The work herein addressed limitations noted within the referenced study, focusing on the introduction of an accurate arterial model. Care was taken to ensure that simulations remained computationally efficient and robust, ensuring that the framework could feasibly be used as an industrial tool to study the interactions between endovascular devices and the arterial wall.

Key to the successful development of the integrated modelling framework was the modular approach adapted. Through this approach, the framework allowed for incremental advances, simplifying the development process. The framework as presented, is seen as an excellent base upon which future design tools can be based. All python scripts produced during this study can be found with annotations in Appendix 6.

Towards the overall objective of this research project, the development of the framework allowed for an assessment to be made on whether advanced hyper-elastic and super-elastic constitutive models could be used under complex contact and loading conditions to simulate the deployment of endovascular devices. Through the results presented, it was shown that such simulations are indeed feasible, with accuracies as defined in chapter 5.

5 Validation

Within this chapter the accuracy of FE simulations is quantified through a series of verification and validation steps. These steps are presented per simulation phase, addressing each of the load steps associated with a ring deployment simulation.

By presenting these validation steps the limitations of the framework developed in chapter 4 are identified. With the boundaries of the device-artery simulation defined, light is shed on the applicability of FE technologies in the proposed context, answering several academic questions that were set out to address.

5.1 Standard device-artery model

The integrated modelling framework was developed around a concept of flexibility to allow for a range of different device-artery interaction studies to be conducted. For this reason aspects of mesh density, element type and material representation were kept as user inputs, to be defined for each specific study. This complicated the process of validation as a large number of model combinations were possible. Within this section this complication is addressed by defining a standard device-artery model with which all validation studies were completed. Boundary conditions, as introduced in chapter 4, were consistent over all device-artery simulations and as such only geometric and mesh properties are discussed.

5.1.1 Continuum wire model

Four quadratic continuum elements (C3D20R) were used through the wire depth (figure 5.1). Each element incorporated 20 nodal points and reduced integration points. A seeding policy of 0.05 mm was employed along the length of the wire. This seeding approach resulted in 5340 elements per quarter symmetric representation. Unless otherwise stated within any validation study presented within this thesis, an asymmetric Nitinol material definition as introduced in table 4.3 was used. The Equivalent-I modelling approach, as discussed in section 4.1.1, was utilised for all studies (wire diameter 0.18 mm) with a ring diameter of 34 mm.
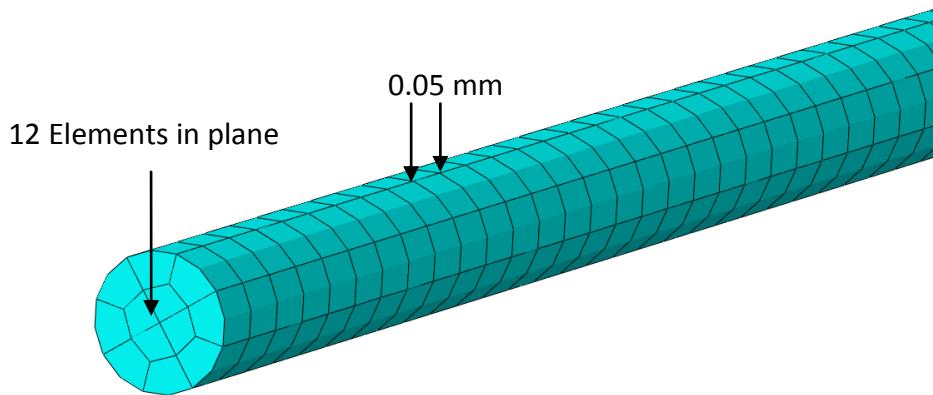
Figure 5.1: **Element mesh used for continuum representations.**

5.1.2 Beam wire model

A beam element representation of the wire is shown in figure 5.2. A double bias seeding policy was adopted, with elements decreasing from 0.2 mm to 0.02 mm in size towards quarter symmetric interfaces. This seeding policy was used to insure bending deformations did not violate slender beam theory assumptions at the peaks and troughs created by the ring's saddle shape. The elements used were quadratic in nature (B32H) with seven section points through thickness. Unless otherwise stated, an asymmetric Nitinol material definition was used with parameters as stated in table 4.3.

5.1.3 Vessel representation

Two different element types were used for vessel representation. The intima was represented through linear tetrahedral elements (C3D4H), which vastly improved contact initiation (Figure 5.3). The media and adventitia were represented through standard quadratic hexahedral elements (C3D20R). A seed size of 0.35 mm was utilised resulting in 30 000 elements per quarter symmetric representation (based on a unpressurised vessel diameter of 25 mm outside diameter and 1.55 mm wall thickness). The Holzapfel hyper-elastic material definition was used in all simulations, with parameters defined per study. All tetrahedral elements were based on a hybrid formulation [48] to accommodate incompressibility assumptions made with the Holzapfel material formulation.

133

Double bias seeding policy ranging
from 0.20 mm to 0.02 mm
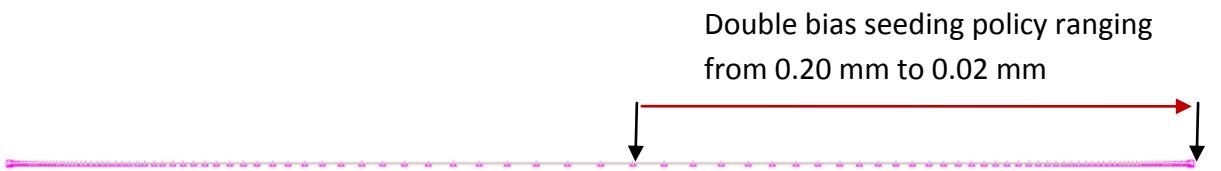
Figure 5.2: **Element mesh used for beam representations.**

0.35 mm

Adventitia
Media
Intima

Quadratic Hexahedral Elements

Linear Tetrahedral Elements
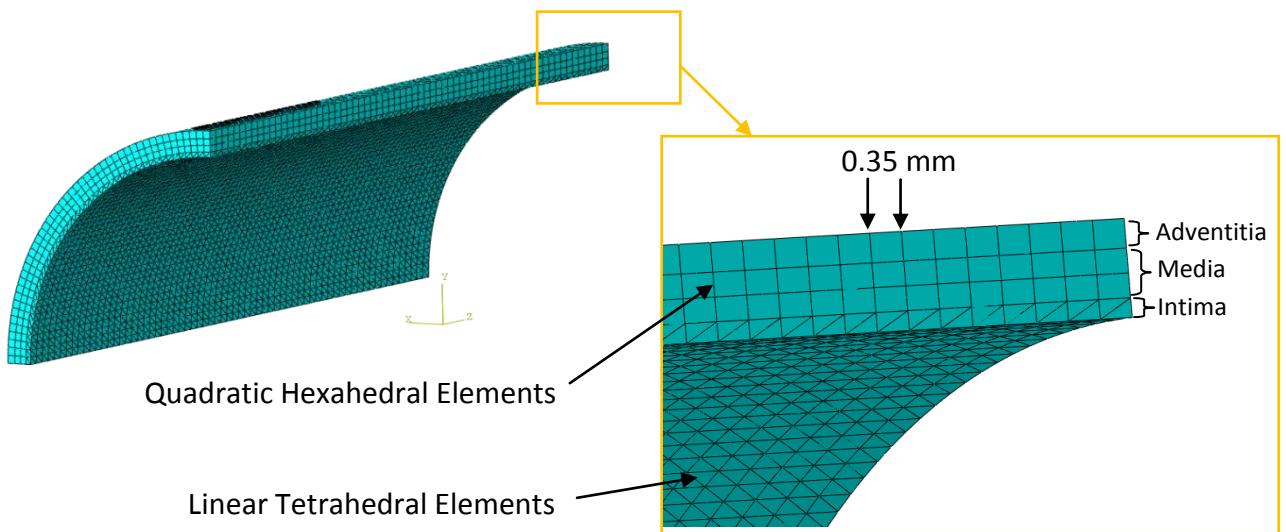
Figure 5.3: **Element mesh used for vessel representations. Four elements were used through the thickness of each artery, with section definitions as shown.**

5.2 Ring forming verification

In practice the proximal ring is manufactured from straight drawn wire which is coiled several times to form a ring. Once this ring is formed, it is incorporated into the Anaconda device which effectively locks it into a state of constant strain. These "pre-strains" are essential to the mechanical performance of the device and as such had to be captured within FE modelling activities.

To capture pre-strains within the FE wire model a novel boundary set was developed as detailed in section 4.2. These boundary conditions are validated here through the comparison of FE results against analytical methods. This method of validation was made possible as it can be shown that the proximal ring remains within the linear-elastic material regime during the pre-straining load step.

Table 5.1 displays this comparison between Von Mises stresses as calculated by Abaqus with those obtained using equation 5.1, where E is the first elastic modulus, R the radius of curvature and γ is the perpendicular distance to neutral axis. The table displays the results obtained for ring configurations which envelopes Anaconda devices manufactured by Terumo Vascutek. As can be seen from the results, the FE modelling methods adopted compared well against analytical calculations.

$$\sigma = \left(\frac{E}{R}\right)\gamma$$

(5.1)

Wire Diameter (mm)	Ring Diameter (mm)	Analytical (MPa)	Finite Element Continuum Results		Finite Element Beam Results	
			MPa	Difference %	MPa	Difference %
0.16	36.5	288.43	299.30	3.70%	288.80	0.12%
0.22	36.5	396.60	409.84	3.20%	397.04	0.10%
0.26	36.5	468.71	484.67	3.30%	468.98	0.05%
0.18	34.0	348.35	361.70	3.80%	348.63	0.05%
0.18	26.0	475.10	455.53	4.29%	475.80	0.10%
0.18	18.0	658.09	694.70	5.20%	658.50	0.07%

Table 5.1: **Comparison between results obtained through Finite Element Analysis with those calculated through analytical methods.**

5.3 Stress distribution comparisons

The computational savings brought forward by beam elements make multi-turn bundle modelling a potentially viable option. The development of a multi-turn bundle model would remove the need for methods such as the Equivalent-I approach adopted herein. Beam elements (Abaqus B32H) are, however, based on a series of slender beam assumptions [48] and care must be taken when using them under conditions of large scale, out-of-plane, deformation.

To demonstrate that beam element assumptions are not violated during device-artery simulations a study was conducted. This study compared results obtained between beam and continuum element ring representations at different stages of a deployment simulation. Through agreement of results, it could be shown that beam element assumptions held true. In the process of completing this study, an additional post-processing script was introduced into the framework. This script, made available in Appendix 6.10, could sample the highest recorded value of a chosen variable along the length of both solid and wire representations as shown in figure 5.4.

For comparison, identical simulations were constructed using beam and continuum representations and the final results were compared. The results are shown in figure 5.4 through to 5.6 and were obtained for a single 36.5 mm diameter ring (0.22 mm wire diameter) being formed, compacted and deployed. In both cases the ring was compacted into a sheath-like diameter (ID 9 mm) and deployed into a rigid vessel of ID 30 mm (15% oversize).

Figure 5.4 displays the Von Mises Stress distribution along the length of the wire, at the end of the ring forming stage. As can be seen, results obtained from both representations compared well with a maximum divergence of 4.02 % noted at any one location. The results also compared well against the analytical solution of 396 MPa, following trends witnessed in table 5.1.

Elevated regions of stress towards the quarter symmetric boundaries for the continuum (solid) representation (figure 5.4 a.2) were noted within the results. These elevated results were imparted by the boundary conditions required to induce quarter symmetry conditions.
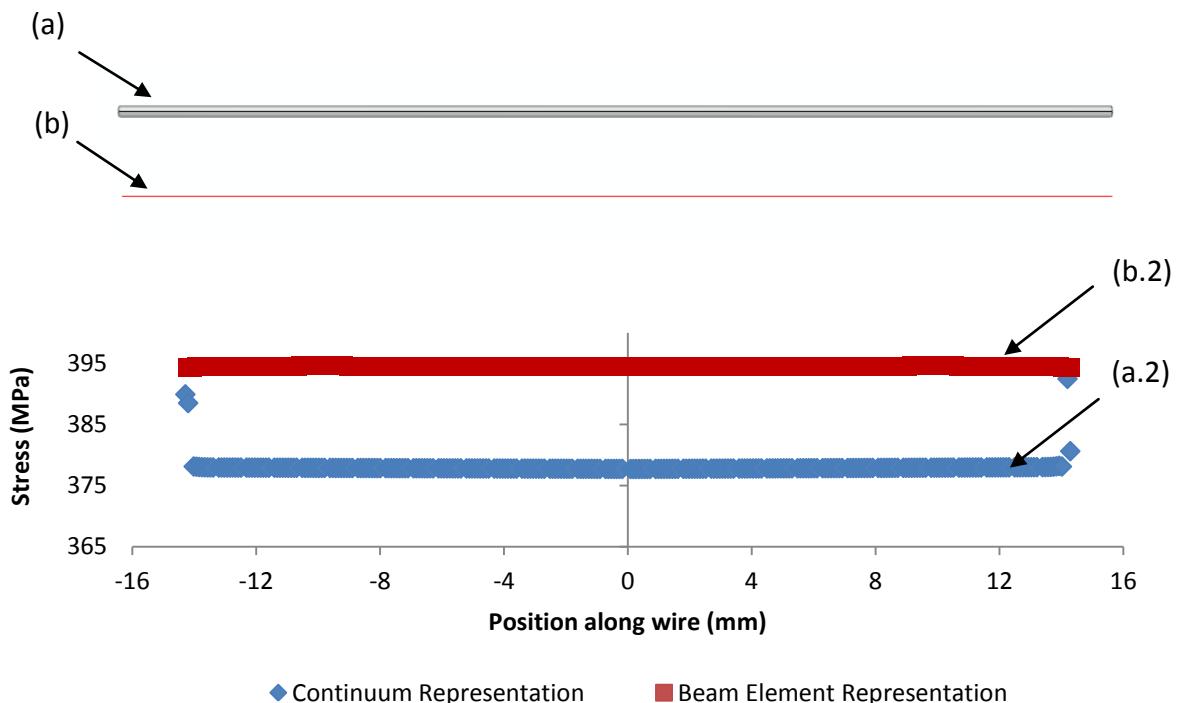

Figure 5.4: **Continuum (a) and beam representations (b) for an R_36.5 ring in straight drawn condition. Below, a.2 and b.2, presents the stress distributions along the length of the wire obtained for the wire and the end of the ring forming stage.**

Figure 5.5, presents results achieved at the end of pseudo compaction. As can be seen from the graph, results were again in good agreement. Although the nodes subject to boundary conditions were removed from post-processing, elevated regions were noticed for the beam representation, as is indicated within the graph. These effects tended to increase with increasing levels of compaction, eluding to a breakdown of beam theory assumptions under high sheath-like compaction levels (above a 75% reduction in ring diameter).
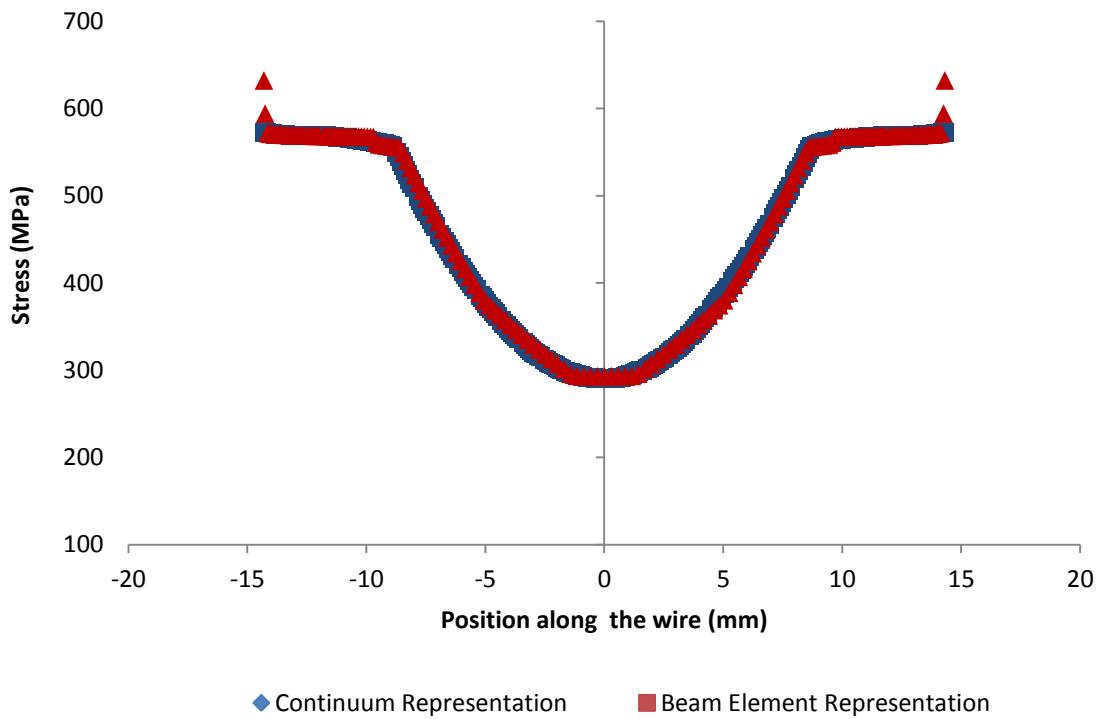
Figure 5.5: **Stress distribution along the length of the wire at the end of 75% compaction. Under these conditions a good correlation between continuum and beam element results was found.**

Finally, figure 5.6 displays stress distributions along the ring once deployed. As can be seen from this graph, increased divergence was noted between the two representations at this stage. The reasons for this divergence were thought to be associated with Nitinol's hysteretic behaviour and the way this was dealt within the element formulation.
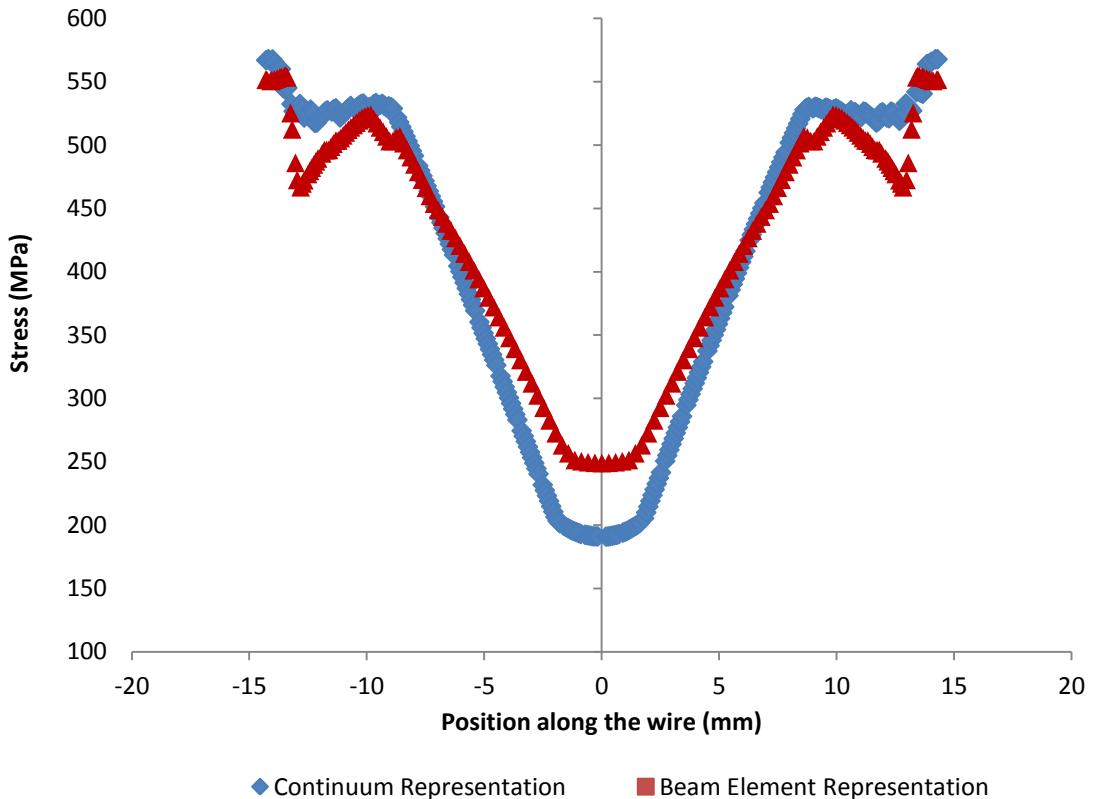
Figure 5.6: **Stress distribution once deployed into a 15% oversized vessel. A divergence in results was noticed between the two representations under load history conditions.**

5.4 Equivalent-I approach assessment

In chapter 4 a method, referred to as the Equivalent-I approach, was adopted from a previous study [24] for the finite element modelling of the Anaconda's proximal ring. The method removed the need for multi-turn bundle modelling by using a single turn of equivalent stiffness.

Within this study, this approach was reassessed after limitations were identified by Mr David Bow, Knowledge Exchange Partner to this project. The limitations surrounded the linear theory on which this approach was based and the conflicting nonlinearity of Nitinol. A reassessment was also further justified as this approach was originally validated using experimental results from un-sutured rings. This followed from assumptions made that the ring sutures and graft fabric did not affect bundle stiffness.

For this assessment sutured rings as used in the in the vascular testing programme (table 3.1) were commissioned through Vascutek. Once obtained, each ring's stiffness was characterised through pseudo compactions within a Tinius Olsen Tensile machine, as shown in figure 5.7. This experiment was then modelled within the Finite Element environment allowing force/displacement results to be compared (figure 5.8).
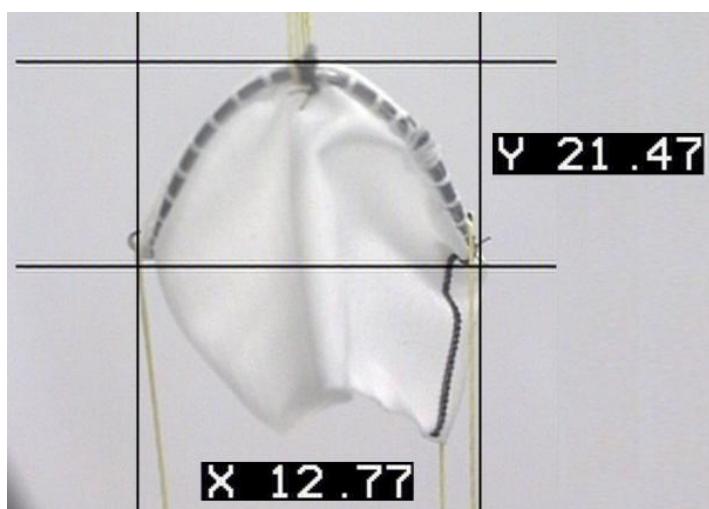
Figure 5.7: **Ring fitted into a uniaxial tensile machine being compacted into the saddle shape.**
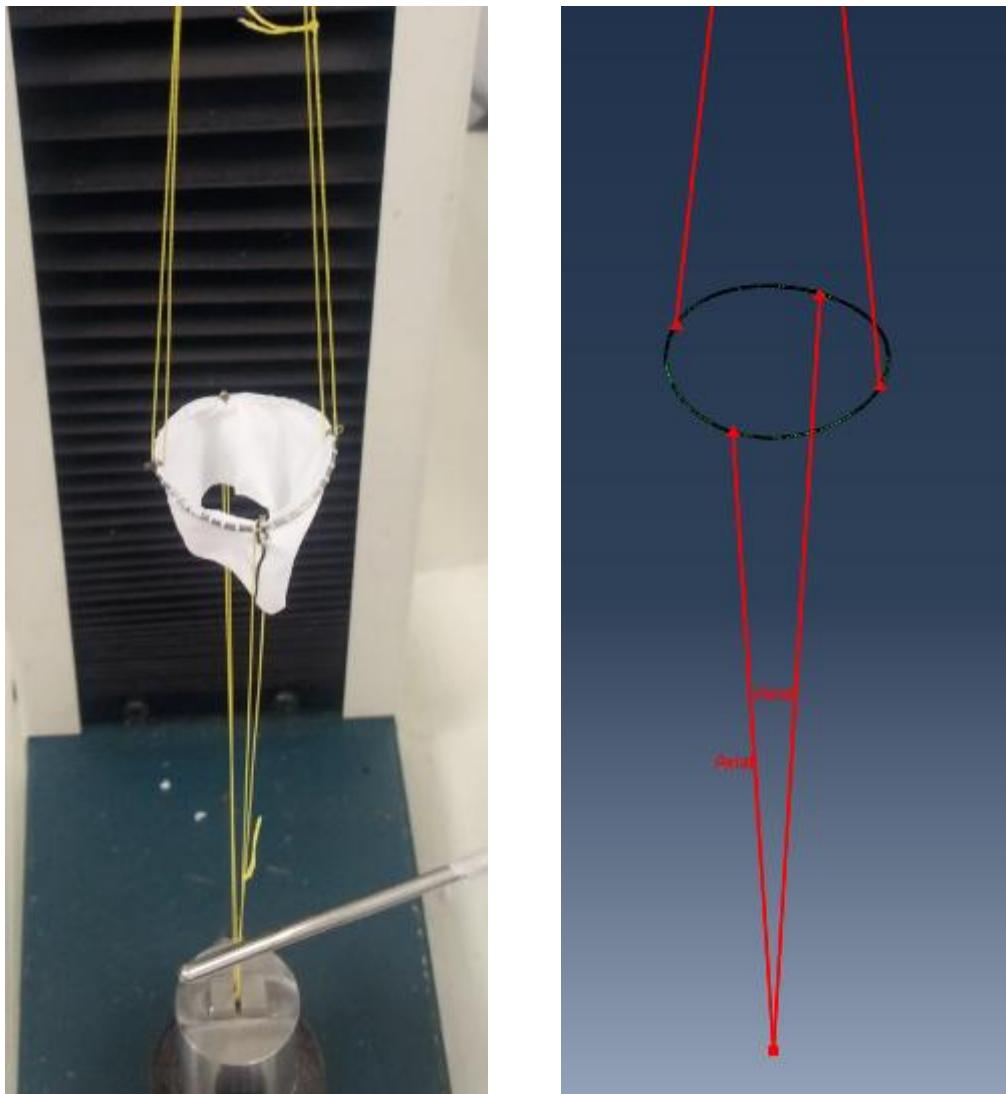
Figure 5.8: **Experimental setup and FE representation. Each ring was fitted to the rig using high tensile strength line which was modelled in FE simulations as near inelastic. The proximal ring was modelled according to the standard model presented in section 5.1.1.**

The testing rig used was fitted with an environmental chamber set to $37^{o}C$. Each ring, once fitted, was allowed to equilibrate for 20 minutes. Twenty training cycles at a rate of 3 mm/min were performed before characterisation took place. Three rings were characterised during the testing programme (R_21, R_25 and R_34) all of which were made in an identical manner to the rings stipulated in table 3.1. Trends were consistent and as such comparisons between two of these devices, R_34 Lutz 1.3 and R_25 Lutz 1.3.

For comparison with experimental results, FE results using the Equivalent-I method were produced alongside a FE bundle model approximation. Bundle approximation results were produced by multiplying force results obtained from simulating the

compaction of a single wire turn by the number of turns within a ring bundle. These results could be used to fully define the appropriateness of the Equivalent-I approach and gauge the merits of full bundle modelling.

Figures 5.9 and 5.10 present the comparisons. What is clear from these graphs is that the Equivalent-I approach diverges from experimental results with increasing levels of compaction. This is consistent with the limitations noted within the method which conflicts with material and geometric stiffness nonlinearities induced through increased compaction. To clarify the impact this divergence will have on the accuracy of simulation, red markers are included into figures 5.9 and 5.10 which indicate the operating range of rings (10 - 20% oversize). These markers were produced through considering, FE produced, ring displacement-compaction graphs as presented in figures 5.11 and 5.12, which correlates the level of axial compaction (figure 5.8) against diameter decrease (oversize).

Although significant divergence is shown in figure 5.9 and 5.10, it should be emphasised that these lines are based on the 10-20% deployment range. As the arterial vessel is compliant, the ring will deform the vessel, resulting in a lower oversize. This can be seen in experimental data shown in figures 3.18, 3.24 and 3.30 where the true operating oversize for devices deployed within the vascular testing programme range from as low as 6% to a maximum of 14%. Deficiencies within the Equivalent-I approach remain significant however and should be accounted for in situations where operational oversize is significant (>16%).

The comparison between experimental and "bundle approximation" results supports previous findings whereby the effects of material sutures have a negligible effect on ring stiffness. These conclusions could be drawn from the results which suggest that each turn adds an independent contribution to overall ring stiffness. Results as shown in figures 5.9 and 5.10 also further eludes to the benefits of full bundle modelling, indicating a close match to experimental results.
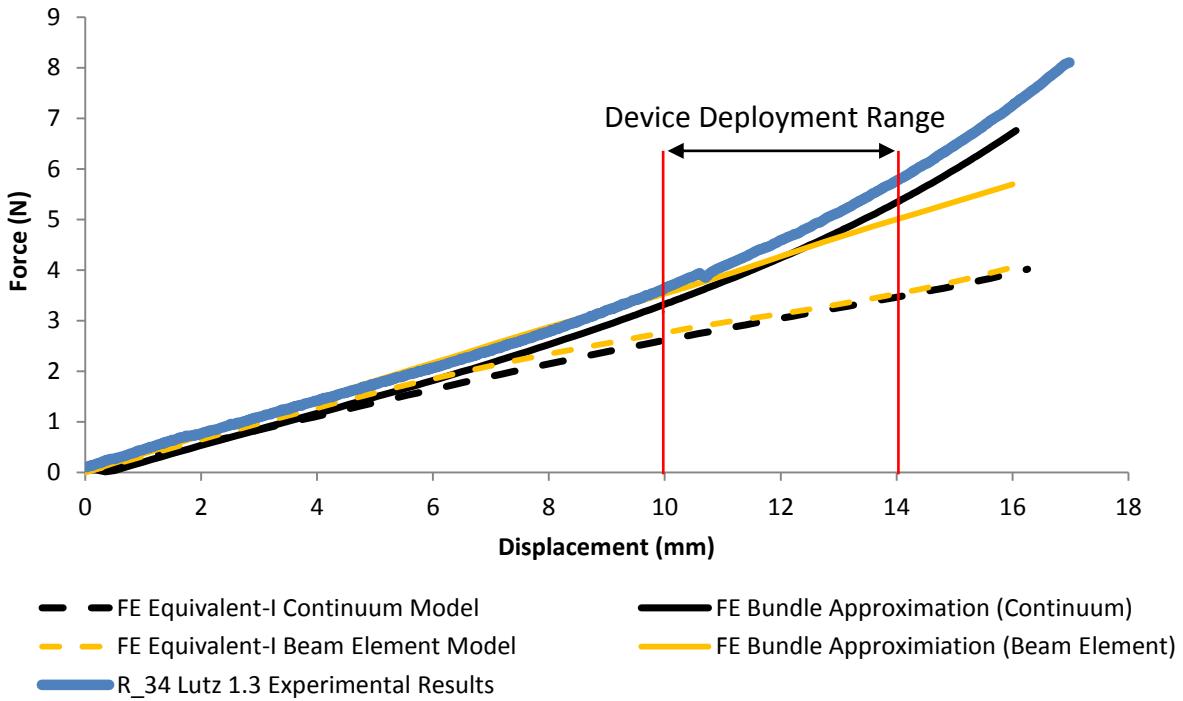
Figure 5.9: **Comparison between experimental results obtained for R_34 Lutz 1.3 and FE approximations. Continuum bundle modelling was found to provide the closest comparison to experimental results. The equivalent I approach was shown to diverge under increasing levels of strain.**
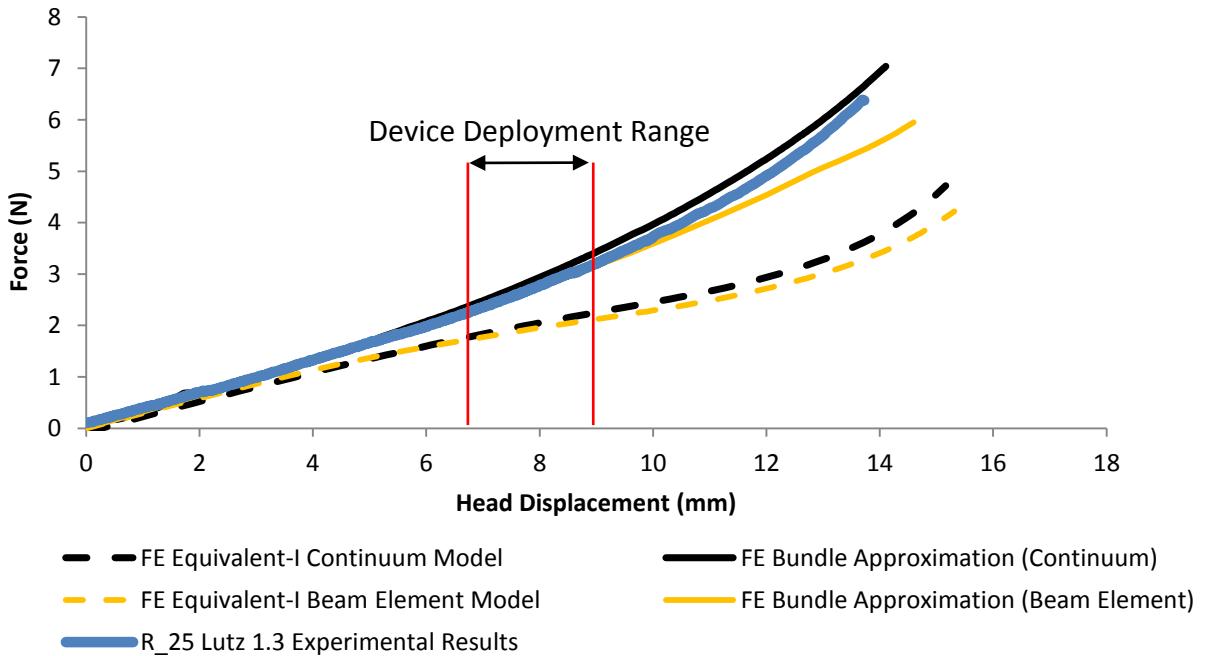
Figure 5.10: **Comparison between experimental results obtained for R_25 Lutz 1.3 and FE approximations. Similar trends were noticed to that obtained for R_34.**
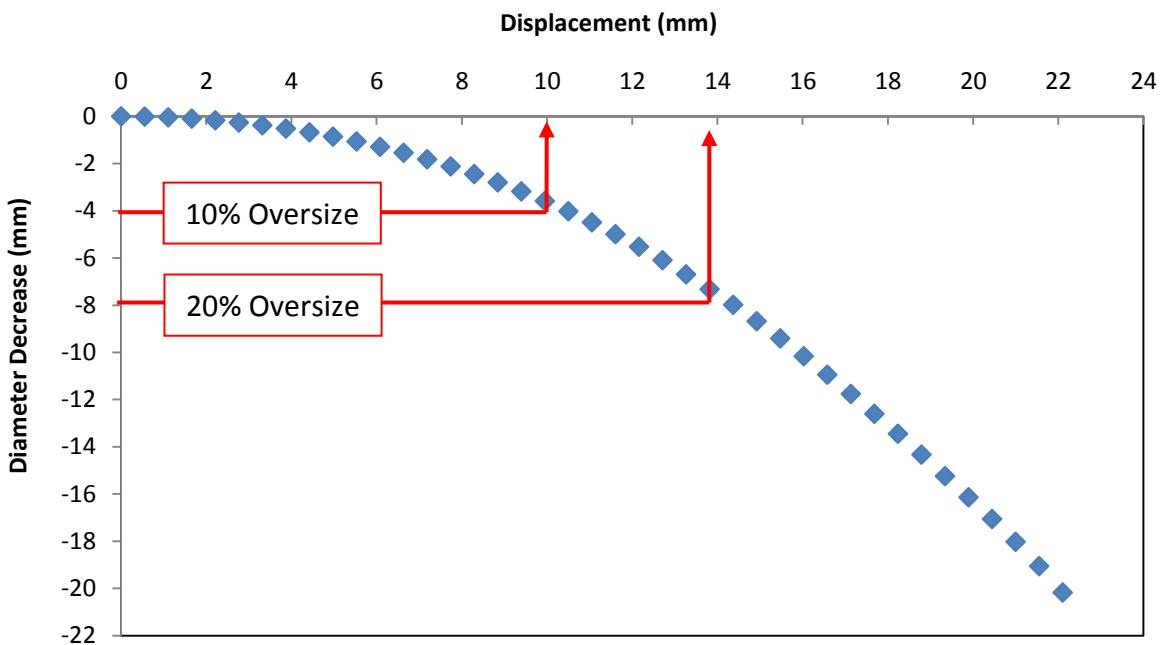
Figure 5.11: **Relationship between axial displacement and the decrease in diameter for the R_34 Lutz 1.3 device. Red lines indicate the diameters which are associated with the 10 - 20% oversize operation range (Approximately 10 to 13.96 mm compaction displacements).**
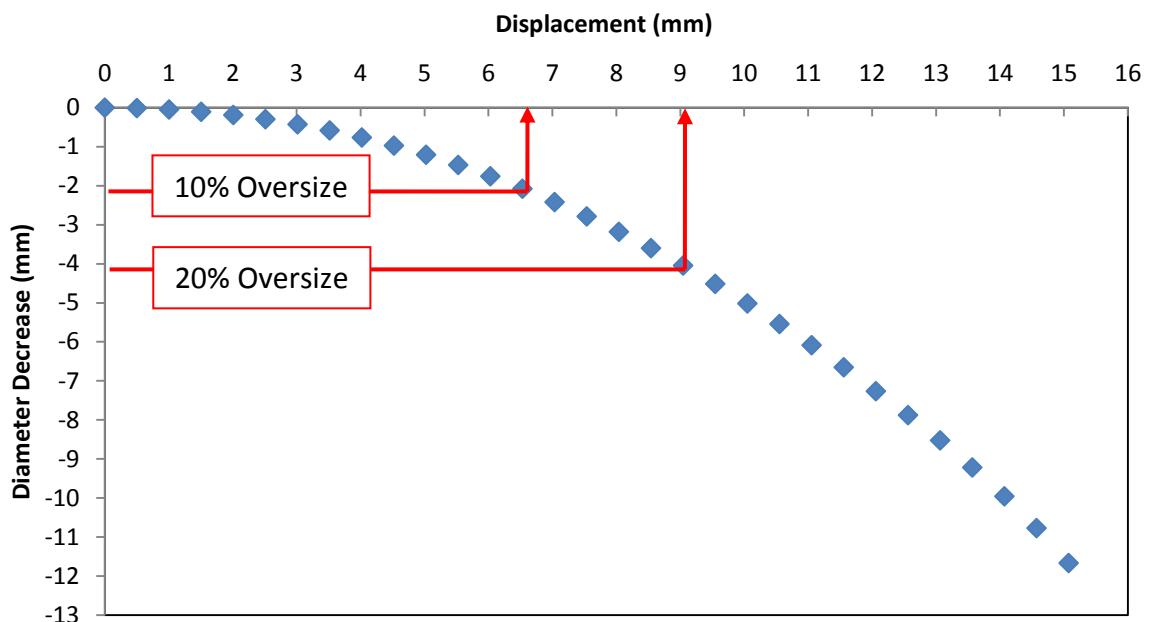
Figure 5.12: **FE determined relationship between axial displacement and the decrease in diameter for the R_25 Lutz 1.3 device. Red lines indicate the diameters which are associated with the 10 - 20% oversize operation range (Approximately 6.7 to 9.04 mm compaction displacements).**

144

5.5 Material model validation

In section 4.4.2.2 of this thesis, Holzapfel material parameters were derived for the three abdominal specimens characterised. These parameters were derived through marcos developed within Microsoft Excel. This section demonstrates that when incorporated into a FE software suite, these parameters are able to replicate the uniaxial experimental data collected during the vascular testing program.

For this validation exercise uniaxial specimens were modelled within Abaqus 6.11. FE models incorporating non-linear C3D20 elements, were fully fixed at the base and subject to a displacement boundary condition as shown in figure 5.13. Each specimen modelled was assigned the derived material parameters before being subjected to a uniaxial stretch. Through this, the resulting stress-strain results response could be compared against experimental data.

Figure 5.14, 5.15 and 5.16 displays results from this study. As can be seen in these figures, the predicted material's response compared well against experimental data. The biggest error was noted within Specimen 2's intimal response which was attributed to the highly anisotropic nature of this layer's axial and circumferential orientations.

Furthermore, little is published on the ability of the Holzapfel's constitutive model to fit different types of tissue response. In this study, it was noted that the model had limited ability to fit two data sets, which were initially isotropic, but which then experienced increasing anisotropy with increasing strain (for example, the intima response of specimen two as shown in figure 5.15). Although not perceived to be of major concern to this study, this could become a source of significant error when dealing with patient specific data sets.
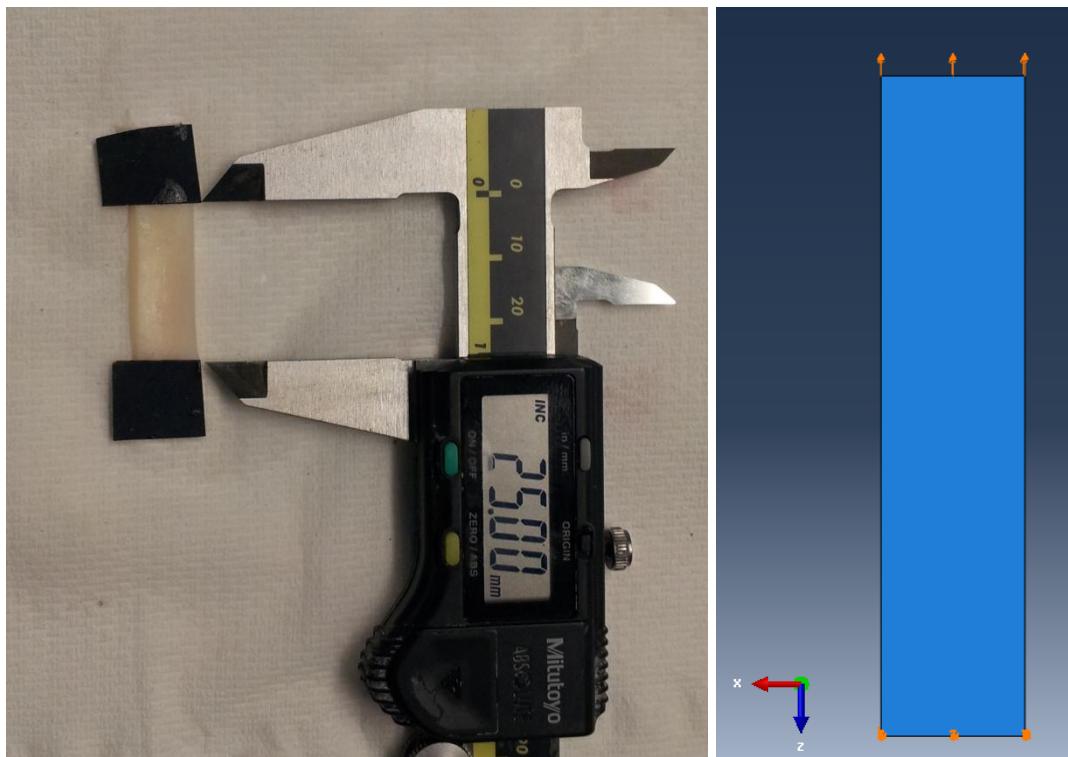
Figure 5.13: **Arterial specimen (left) and representative FE model (right).**
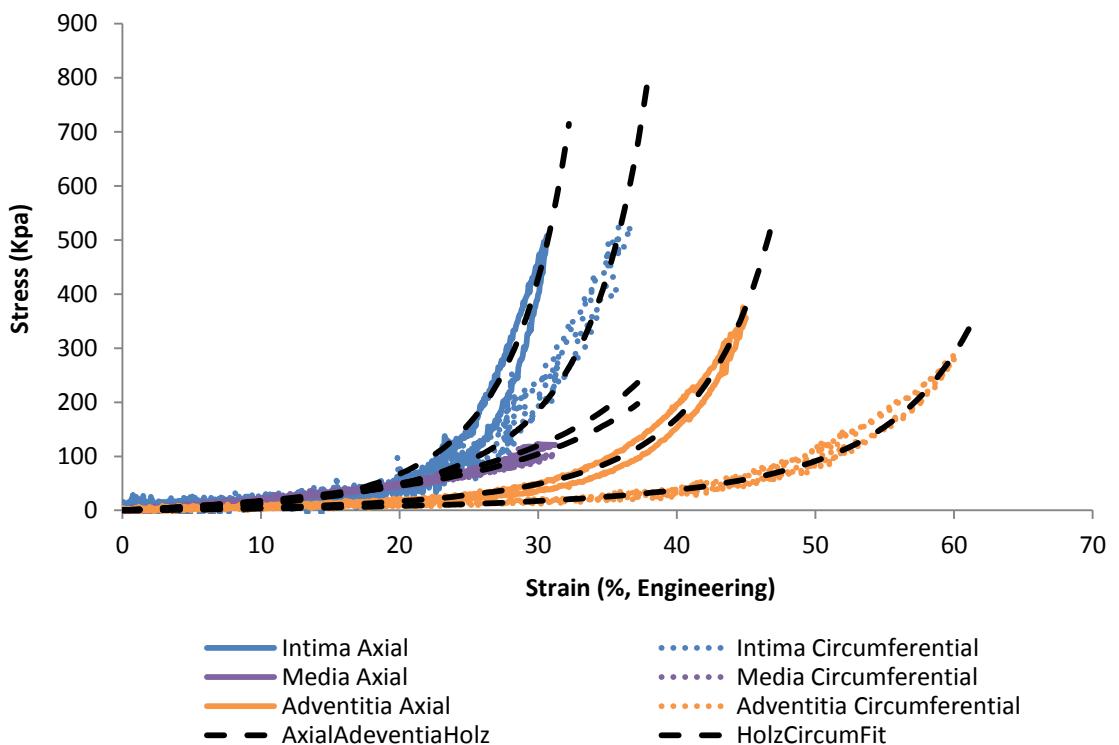
Figure 5.14: **Fitting results for specimen 1. Coloured lines represent experimental data whilst black segmented lines represent relevant FE Results. Good agreement was achieved, with the largest divergence noted within the specimen's intimal response.**
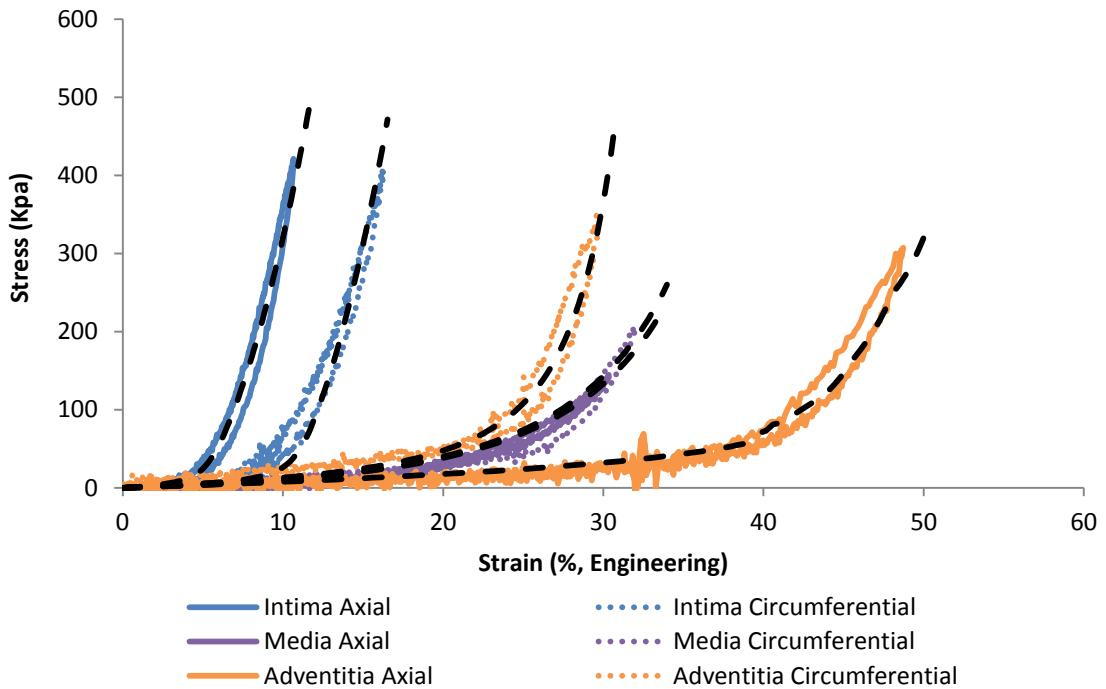
Figure 5.15: **Fitting results for specimen 2. Coloured lines represent experimental data whilst black segmented lines represent relevant FE Results. Strongly anisotropic results, especially the Intima and Adventitia, resulted in less well fitting FE curves.**
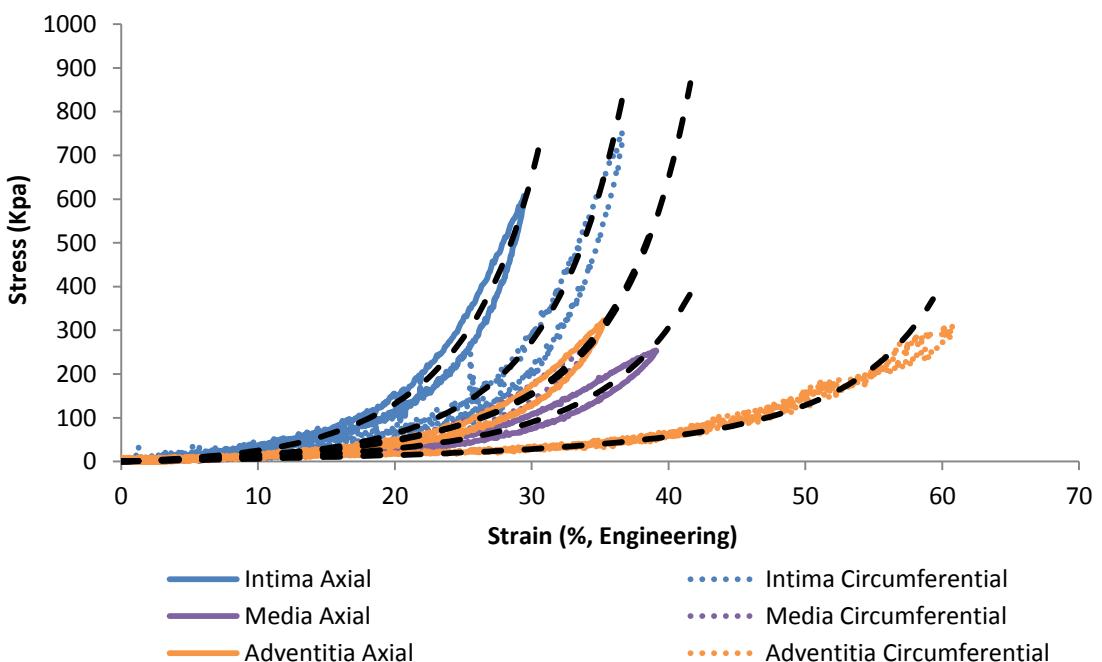
Figure 5.16: **Fitting results for specimen 3. Coloured lines represent experimental data whilst black segmented lines represent relevant FE Results. As can be seen from the graph, the constitutive model used was able to replicate the anisotropic nature of the specimens tested. FE divergence from experimental results was noted for the adventitia circumferential results at large levels of strain (above 54%).**

5.5.1 Pressure-diameter comparisons

For further arterial model validation the parameters derived in section 4.4.2 were assessed according to their ability to replicate biaxial deformations. For this purpose, the three specimens characterised within the vascular testing programme were modelled within Abaqus 6.11 using the FE framework created and data collected. The FE modelling methodology was identical to the Standard Model presented in section 5.1, with only relevant material parameters and geometry changes introduced per simulation. Each specimen was modelled using the average diameter as calculated during characterisation at 15% axial stretch. Once modelled, each tubular model was subjected to a 0-160 mmHg pressure range. Pressure/deformation results were then added to local unpressurised readings for comparison with FE results.

Due to its young age, specimen 1's intima was thin in nature. In addition to this, its thickness varied dramatically across the section obtained, with localised regions being too thin to be reliably measured with a vernier caliper, as can be observed in figure 3.13. As a result, although samples could be obtained for uniaxial characterisation, overall, as an arterial layer, it was judged to provide an inconsistent and generally insignificant mechanical contribution to the vessel. As a result of this, the layer was omitted from arterial wall modelling activities. Not to deviate from the Standard model, the vessel was still modelled using three layers, using two to represent the media. Figure 5.17 displays the comparison between FE and experimental results for specimen 1's pressurisation. Considering the considerable difficulties involved with arterial modelling, figure 5.17 is seen as a reasonable replication of experimental results.

Due to the more substantial nature of specimen 2's intimal layer, it was included into the vessel model. Once the tubular specimen was modelled, pressure/diameter FE results were compared against experimental results. Figure 5.18 displays the results of this comparison, revealing a fairly accurate fit. In general, the results seem to converge at higher pressures, with only pressure/diameter data at the inflection point not agreeing. As with specimen 1, FE simulations generally under predicted the elasticity of arterial tissue.

Figure 5.19 displays comparison results obtained for specimen 3. FE results fitted well against pressure/diameter data obtained just below the Inferior Mesenteric Artery (IMA). A less reasonable fit was obtained for the more elastic response noted below the renal arteries. As both locations had approximately the same initial unpressured diameter, local mechanical variability was thought to have influenced these findings.

With reference to section 2.3.6, it has noted that arteries are subject to complex *in situ* residual stresses. These are generally thought to exist in order to homogenise physiological pressures, although their influence on vascular mechanics is yet to be fully understood and quantified. Due to the ambiguity which exists around these *in situ* stresses, and the substantial added computational difficulties these would introduce into a FEA, they were omitted from the integrated modelling framework design created in chapter 4. Figures 5.17 through to 5.19 however display a constant under prediction of vascular compliance by the Finite Element approach. This is thought to be a consequence of this omission of *in situ* stresses, and alluding to their significance.
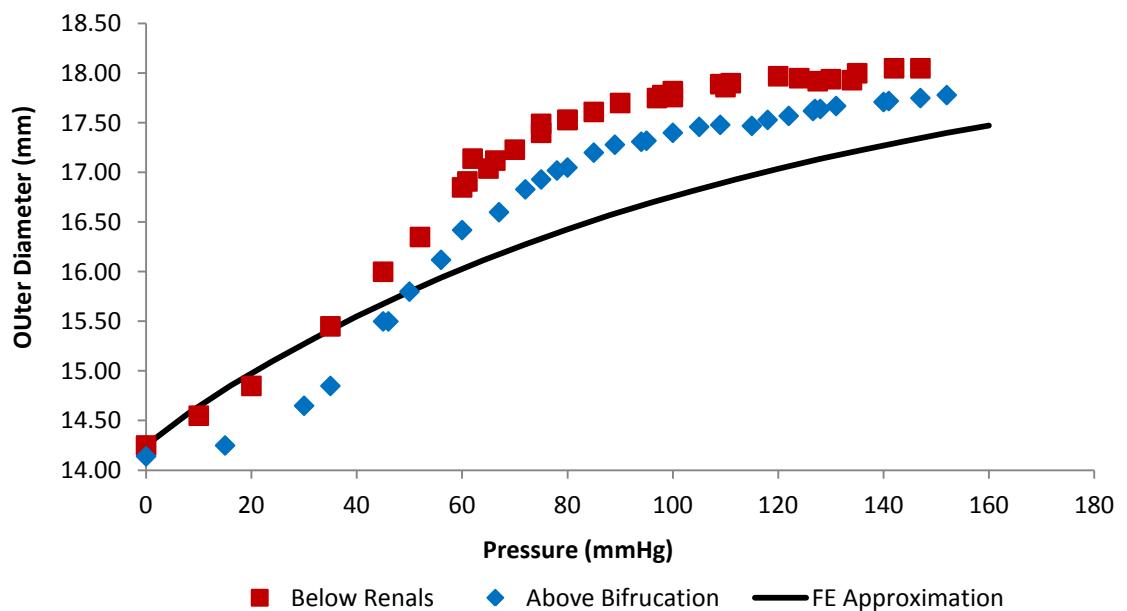
Figure 5.17: **Finite Element replication of Specimen 1's pressure/diameter data. As the unpressurised diameter for both the "Below Renals" and "Above Bifurcation" regions were 14.25 mm, only one FE approximation for both data sets is provided.**
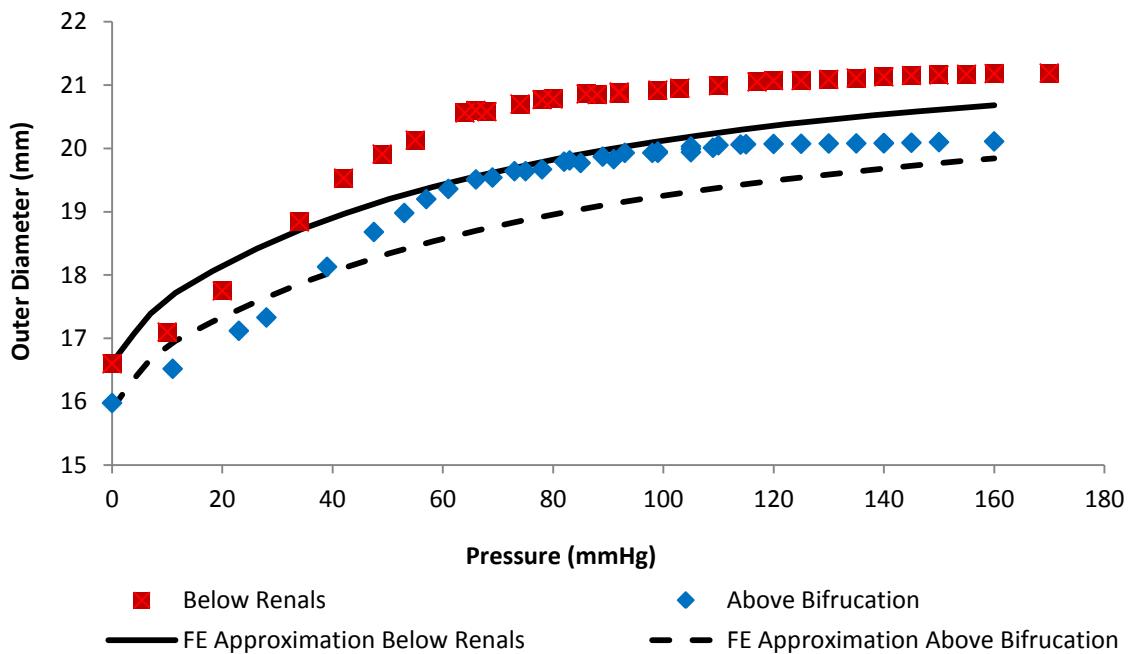
Figure 5.18: **Finite Element replication of Specimen 2's pressure/diameter data. For this simulation the average diameter of specimen 2 was used to model the vessel in FE. Subsequent pressure/diameter results were added to local "Below Renal" and "Above Bifurcation" diameters to produce results presented in the graft.**
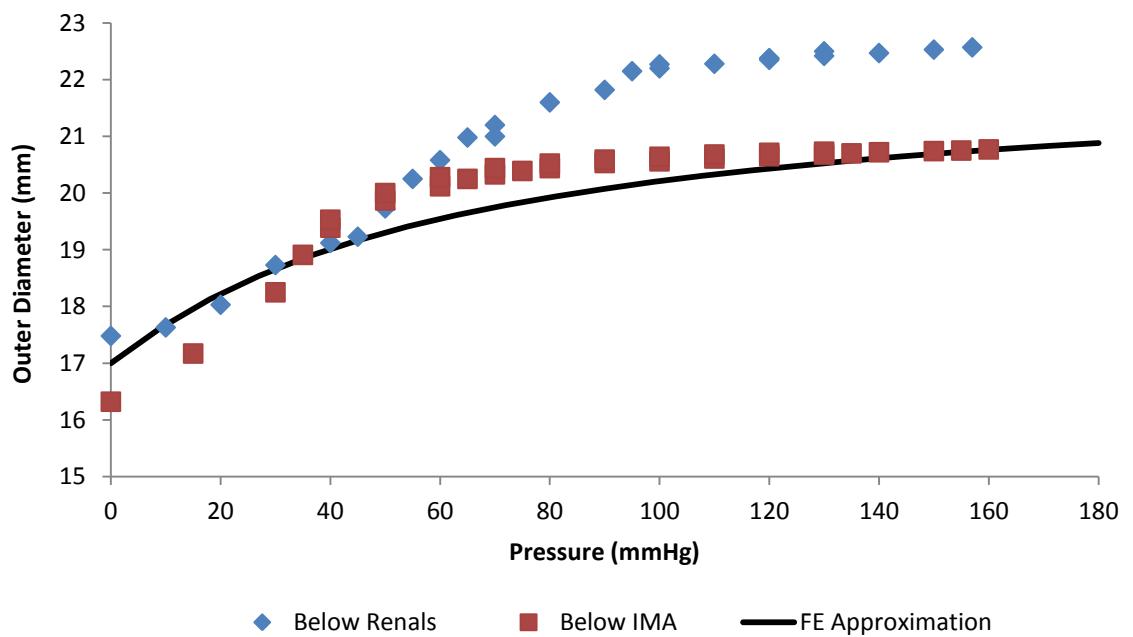

Figure 5.19: **Finite Element replication of Specimen 3's pressure/diameter data. For this simulation the average diameter of specimen 2 was used to model the vessel in FE. Results obtained for the simulation is shown in the graft.**

150

5.5.2 Device- artery profile comparisons

To further support validation studies, device deployment simulations were modelled within FE (as per the standard model presented in section 5.1). FE deployment simulations were then compared against data collated during the vascular testing programme. Through this study, this framework's ability to replicate complex device/artery interactions could be assessed.

For comparison, deformation profiles obtained during device deployment experiments were compared against Finite Element predictions. During this study, focus was placed on the peak deformations imparted by the device upon contact. Focus was placed on these locations as these deformations most directly relates to the deformation state of the proximal ring. Within the comparisons presented, two characteristic internal pressure of 0 mmHg and 120 mmHg are shown for discussion. The largest discrepancy between FE predicted and experimental data is also highlighted.

Figure 5.20 displays the comparison between FE predictions and experimental results for specimen 1. As can be seen from the image, finite element predictions followed similar patterns measured during deployment simulations. A maximum discrepancy of 26.84% was measured between FE and experimental results.

Figure 5.21 displays the results obtained for a comparison between specimen 2's experimental results and FE simulations. As for specimen 1, a general under prediction of deformations was noted, with a maximum discrepancy of 32.23% being measured. With reference to figure 3.23, it should be noted that these results would be influenced by the considerable sections of calcification noted within specimens. Broadly speaking, FE was however able to capture deformation trends as obtained through experiment.

Figure 5.22 displays results obtained for the comparison between FE and experimental results for Specimen 3. In general good results were achieved with peak-to-peak errors of less than 5% being measured. In addition, FE still generally under predicted deformations with a maximum divergence of 13.02% measured. Complex interactions were also captured through FE, where peak-to-peak

deformations imparted by the device were less pronounced at higher pressures. To the author's knowledge, these idiosyncrasies associated with the proximal ring's interactions with the vascular have not yet been documented. With these interactions captured within FE, reassurance is given that experimental results were indeed a function of mechanical interactions rather than errors induced by the *in vitro* study. Further, with interactions captured in FE, an excellent platform for further investigation is presented.
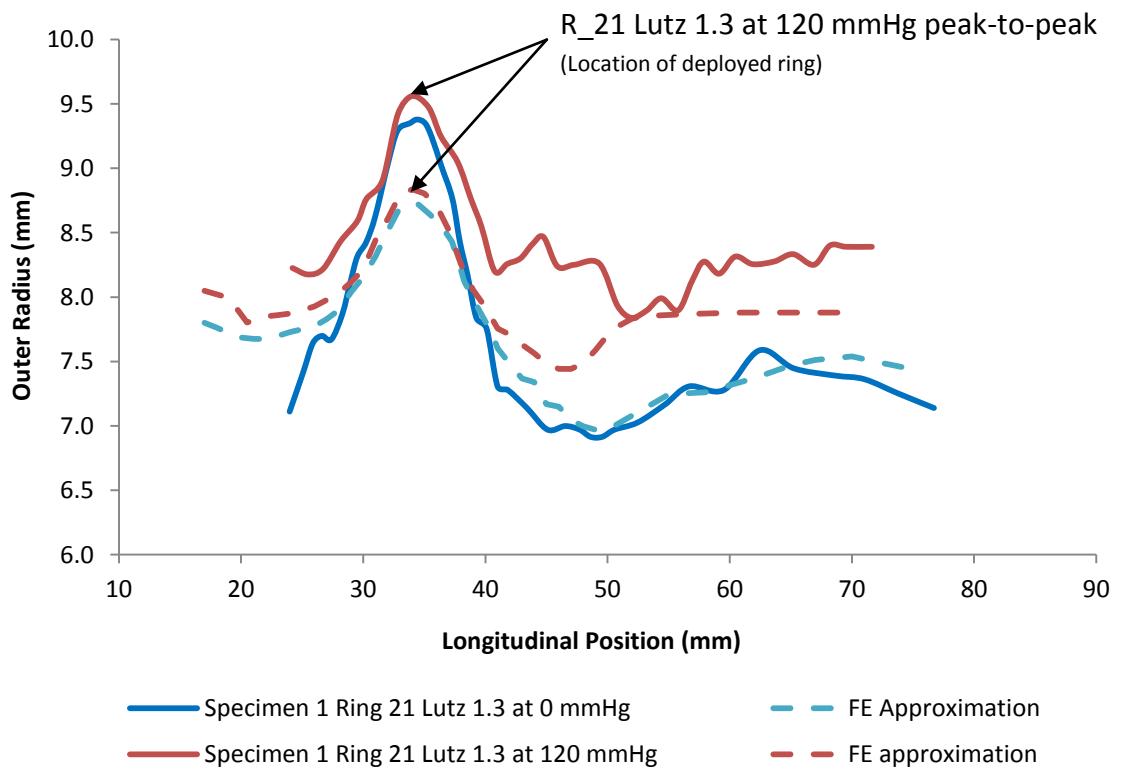
Figure 5.20: **Comparison between deployment profiles produced in section 3.4 against FE predictions.**
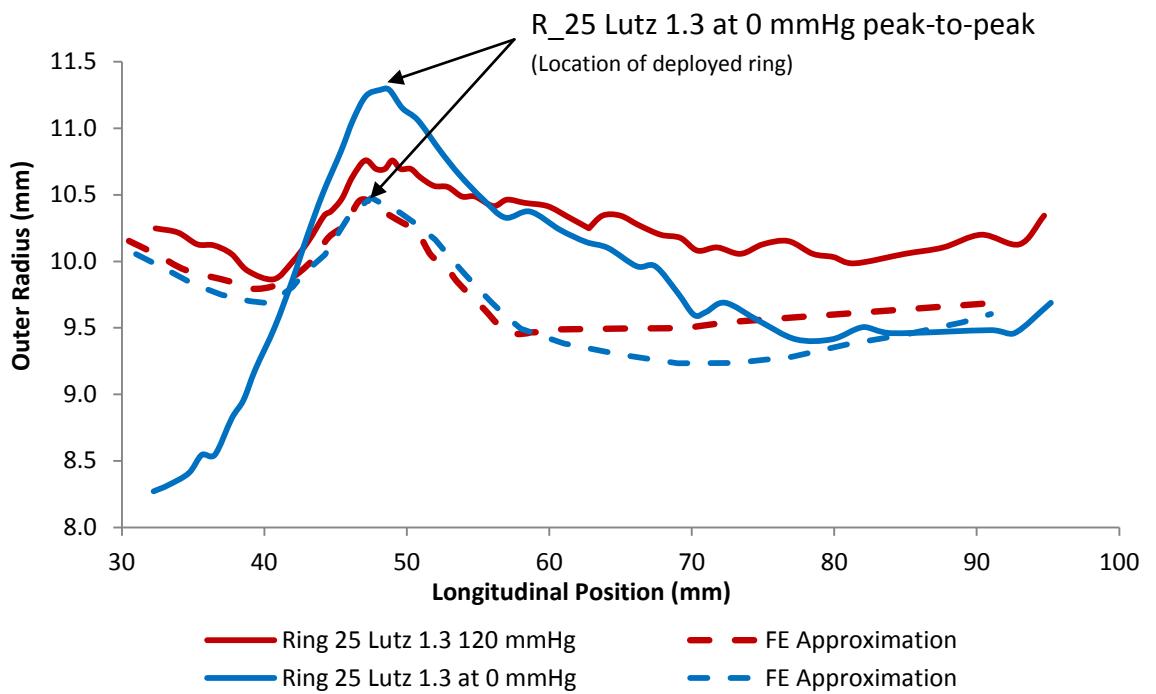
Figure 5.21: **Comparison between deployment profiles produced in section 3.4 against FE predictions.**
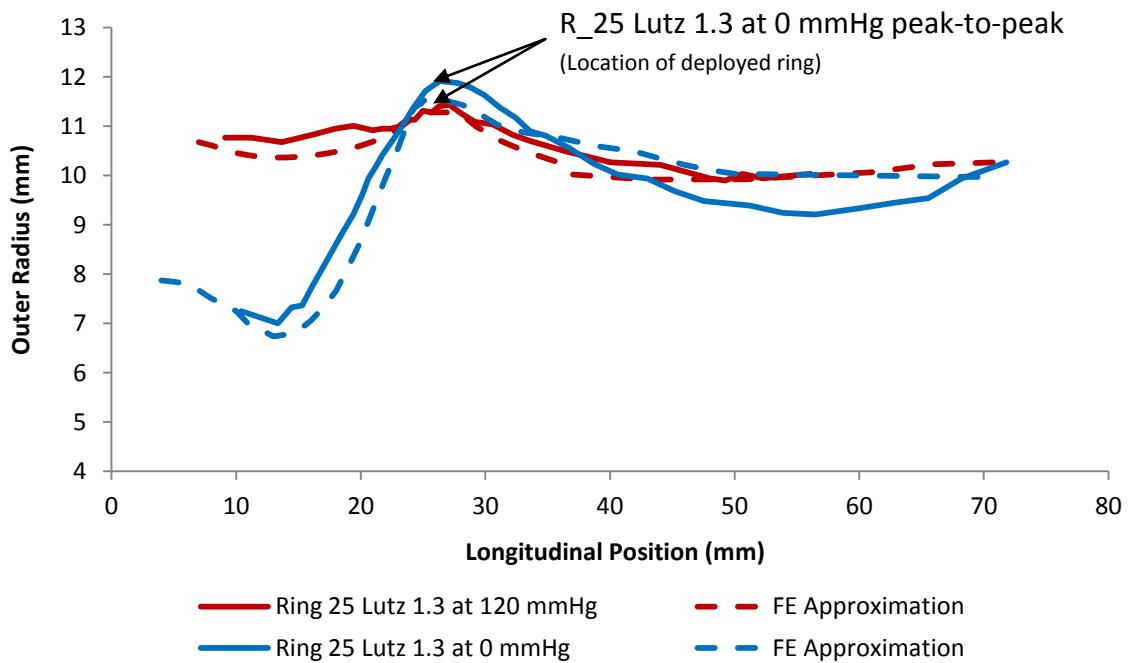
Figure 5.22: **Comparison between deployment profiles produced in section 3.4 against FE predictions.**

The difference is thought to exist as a function of the under prediction of vascular compliance, as shown in the biaxial comparison and the deficiencies noted with the Equivalent-I approach.

5.6 Strain accuracy prediction

In section 5.5.2, it was shown that FE simulations and experimental results were within 32.0% agreement. To relate this finding to the accuracy of FE strain predictions produced through the integrated modelling framework, figure 5.23 is presented which correlates the oversize of the proximal ring against the peak strain it experiences. For discussion, only enveloping design solutions of the Anaconda are presented within this graph. It is also acknowledged that the ring/lumen oversize ratio never exceeds 20%, as per Vascutek clinical protocol.

As the device is released into the lumen, contact is made with the arterial wall and deformation takes place. During this deployment, the ring/lumen oversize ratio decrease from 20% as the vessel deforms. Recognising that the ring can only deform the vessel down to 0.0% oversize, it is clear that the 20% to 0% oversize range provides an operating envelope for all devices once deployed. Furthermore, as seen in figure 5.23, ring configuration 1, provides the highest strain to ring oversize relationship, the equation of which is shown below in equation 5.2 (3rd order polynomial of best fit).

$$f(RO) = \varepsilon \ = \ 5.173 \ (RO)^3 - \ 1.1315 \ (RO)^2 + \ 0.1073 (RO) + 0.0077 \qquad \textbf{(5.2)}$$
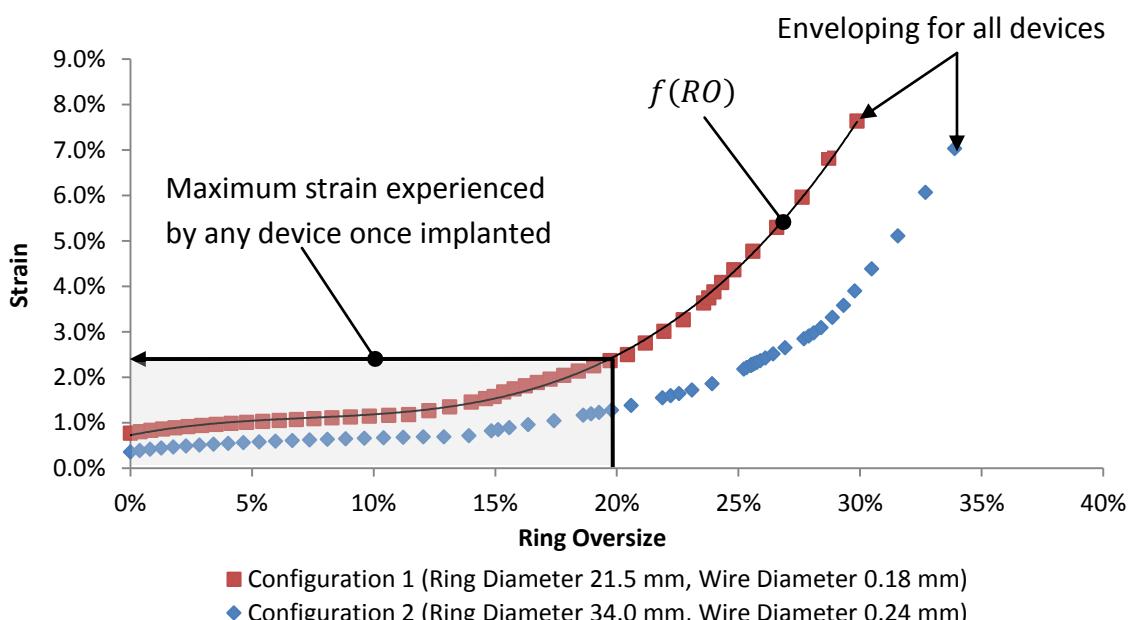
Figure 5.23: **FE results depicting the relationship between oversize and maximum strain experienced by the proximal ring for two enveloping design solutions.**

As the framework has been shown to under predict deformations by 32%, the largest possible error in strain prediction will occur when a ring experiences the largest possible change in deformation (20% to 0%, once implanted). In this case of ring configuration 1, the vessel would have experienced a diameter expansion of approximately 4.3 mm as shown in equation 5.3.

$$21.5 \times 20\% = 4.3 \, mm$$

(5.3)

For this expansion, in the worst case, the framework will under predict deformations by 32%, resulting in an under prediction of expansion by 1.376 mm. This would result in a final equilibrium position of not 0% oversize, but 6.4% oversize conditions as demonstrated in equation 5.4.

$$1 - (21.5 - 1.376) \div 21.5 = 6.4\%$$ **(5.4)**

Using equation 5.2, the FE predicted strain at 6.4% oversize can be estimated as shown in equation 5.5.

$$\varepsilon = 5.173 \, (0.064)^3 - 1.1315 \, (0.064)^2 + 0.1073(0.064) + 0.0077 = 0.0113$$ **(5.5)**

This value of 1.13% strain, can then be compared against the maximum strain the ring should have experienced, if allowed to expand into its planar state, as calculated in equation 5.6.

$$\varepsilon = 5.173 \, (0.0)^3 - 1.1315 \, (0.0)^2 + 0.1073(0.0) + 0.077 = 0.0077$$ **(5.6)**

Based on a 32% underproduction of deformation, results from equation 5.5 and 5.6, indicate that a maximum strain discrepancy approximately 0.36% can be expected. If the framework was used to calculate the strains at both systolic and diastolic pressures, allowances for a $\Delta\varepsilon$ error of twice this value, 0.72% should be made. These results are very reasonable considering the conservative approach of the calculation.

5.7 Chapter summary

This chapter addressed questions regarding the accuracy of the framework created in chapter 4. Results presented herein should be reflected against the complex nature of the materials involved, limitations in the constitutive models available and the complexities associated with the experimental studies conducted.

Within section 5.2, analytical methods were used to demonstrate that the method developed to incorporate proximal ring pre-strains were fit for purpose. Further validation activities surrounding the proximal ring highlighted limitations regarding the Equivalent-I approach adopted from a previous study [24]. These limitations were contrasted against alternative methods of bundle modelling, providing support for future work recommendations made in chapter 7 of this thesis.

In general, it was shown that material parameters derived in chapter 4 could replicate experimental stress/strain results. However, when incorporated into the framework, a trend of under predicting biaxial pressure/inflation experimental has been shown. This is thought to be a function of the omission of *in situ* stresses, a consequence of modelling the artery within a zero strain state. As the inclusion of these residual stresses falls outside of the time limits associated with this project it is hoped that future development of this framework could investigate the implementation of these. Further complicating the comparison between biaxial FE and experimental data was the uniformity of the FE models created in contrast to the feature intense true nature of biological tissue.

In spite of the considerable challenges faced within this project, an agreement of within 32% between Finite Element and experimental displacement results has been shown within this chapter. Moreover, with the focus on reducing computational expense within chapter 3, it has been shown that such an agreement can be reached with a computational tool which could feasibility be used within the industry. When accessing strain prediction accuracies, it was shown that a discrepancy of up to 0.36% can be expected under extreme conditions. Clearly, such a discrepancy in strain prediction is significant. As a result, caution should be applied when interpreting FE results under conditions of large oversize.

Although further progress within constitutive theory and FE modelling is clearly still needed, the ambitious nature of FE modelling attempted herein should be kept in mind. In addition to this, it was demonstrated that complex device/arterial interactions could be captured within Finite Element Analysis, clearly demonstrating the worth of the integrated modelling framework developed.

With regard to the overall objectives of this study, a thorough assessment of the accuracies associated with current technologies within proposed context has been completed. This assessment was required in order to further encourage the industrial adoption of FE technologies and modelling techniques.

6 Towards a design tool: further studies

This chapter presents studies conducted to conclude the current thesis. Some of these studies are presented to provide an improved understanding of the integrated modelling framework's constituents, whilst others provide guidance on further work recommendations.

Within section 6.1 a study conducted into the Load Path Dependency (LPD) effects of Nitinol will be presented. The effects of this material property were first indirectly noted by McCummiskey [24] and ambiguity still exists regarding its implications for design. FE studies and experimental results will be presented prior to the Anaconda device design implications being clarified.

In section 6.2, two FE modelling techniques are introduced. The first of these addresses the limitations noted within the Equivalent-I approach in chapter 5. The technique used a combined beam and continuum approach to replicate bundle stiffness. The second technique introduced is a modelling approach devised to more accurately capture Nitinol's asymmetric material complexities. Methods will be outlined and preliminary results discussed.

The chapter will conclude by assessing the framework's suitability for use in product design. Within this section a generalised abdominal aorta material model will be presented. The method by which this generalised model was developed is discussed and its limitations clarified. Results from these studies shed light on the applicability of the framework in the proposed context, thereby fulfilling the final objective this study set out to achieve.

6.1 Nitinol's load path dependency effects

Previous work by McCummiskey [24] suggest that the magnitude of the maximum strain experienced by the wire bundles during deformation, as calculated by FE, can be presented in a non-dimensionalised form (equation 6.1 to 6.3). In this way, the results from different bundle diameters, wire diameters and elastic modulus can be represented through a single curve.

When this curve was first produced, as shown in figure 6.1 [24], data points were subject to an unexpected degree of scatter. For the current project, possible load path dependency effects were suggested as a key contributor to the anomalies noted.
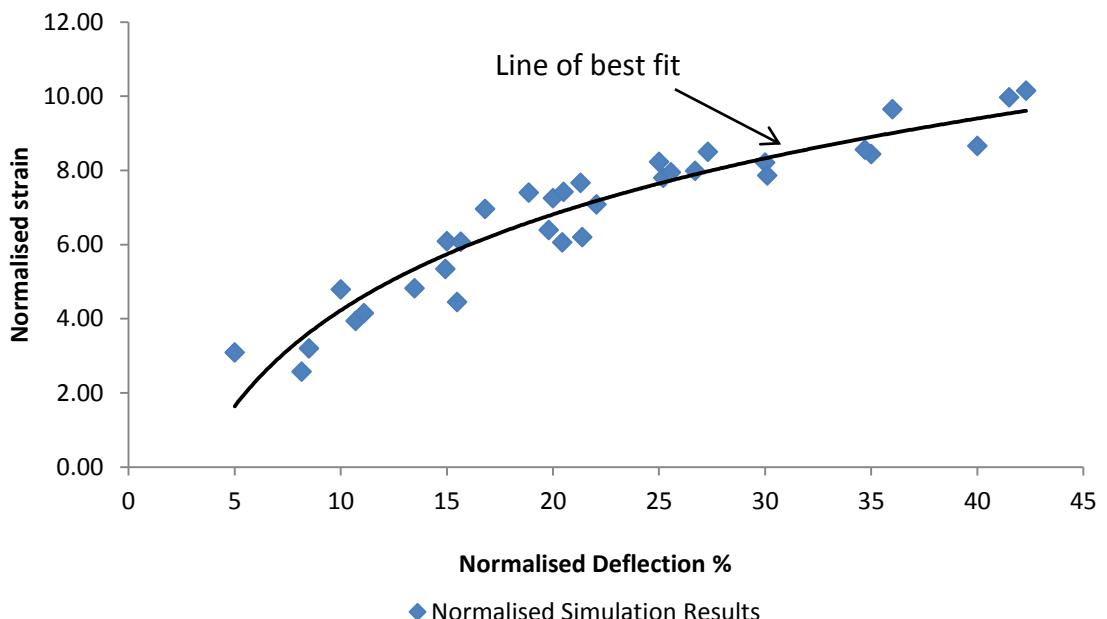
Figure 6.1: **Proximal ring normalised strain and deflection relationship.**

Figure 6.1 depicts the non-dimensional relationship between the level of compaction and the maximum strain experienced by the proximal ring. Since its development in 2008 it has been incorporated into Vascutek's design methodology to simplify fatigue life calculations.

159

Each data point in figure 6.2 represents a single simulation in which a ring was compacted and released into a rigid vessel. During the development of data points, the level of compaction and vessel size were kept identical while the ring sizes were varied according to dimensions used for Anaconda devices.

For each simulation the process of normalisation followed a number of steps. First, the normalised strain was calculated using equation 6.1

$$\varepsilon_{normalised} = \frac{\varepsilon_{max}}{\varepsilon_0}$$
(6.1)

where ε_{max} is the maximum strain experienced by the proximal ring and ε_0 is the strain within a planar un-compacted ring as expressed in equation 6.2.

$$\varepsilon_0 = \frac{d_{wire}}{D_{pr}}$$
(6.2)

Within equation 6.2 d_{wire} is the diameter of the wire and D_{pr} is the diameter of the planar ring. The normalised deflection was calculated using equation 6.3, where D_{dr} is the "diameter" of the deformed ring.

$$\delta = \frac{D_{pr} - D_{dr}}{D_{pr}}$$
(6.3)

At the time of the graph's development, the scatter in data points around the curve of best fit was attributed to the varying ratio of the ring size to compaction level. For this to be true, a relationship had to exist between the "load history" of the ring and its final stress/strain state. Such a relationship has not been addressed in the literature to any extent. Furthermore, due to a lack of understanding of Nitinol's load path dependency, ambiguity exists concerning the implications that this effect might have for the design of endovascular devices.

To investigate the potential LPD effects in the context of this research project, a preliminary study was initiated. For this, the framework was used to repeat three simulations conducted to create figure 6.2. For this three rings, R_28, R_32 and R_34, were modelled using the Equivalent-I approach and subjected to a deployment simulation. Deployment simulations were repeated several times,

varying the level of compaction incrementally between 9 and 24 mm. The standard model as introduced in section 5.1 was used for this study, substituting the Holzapfel material artery model for a rigid vessel representation.

Figure 6.2 depicts the result of this exercise overlaid onto the original graph.
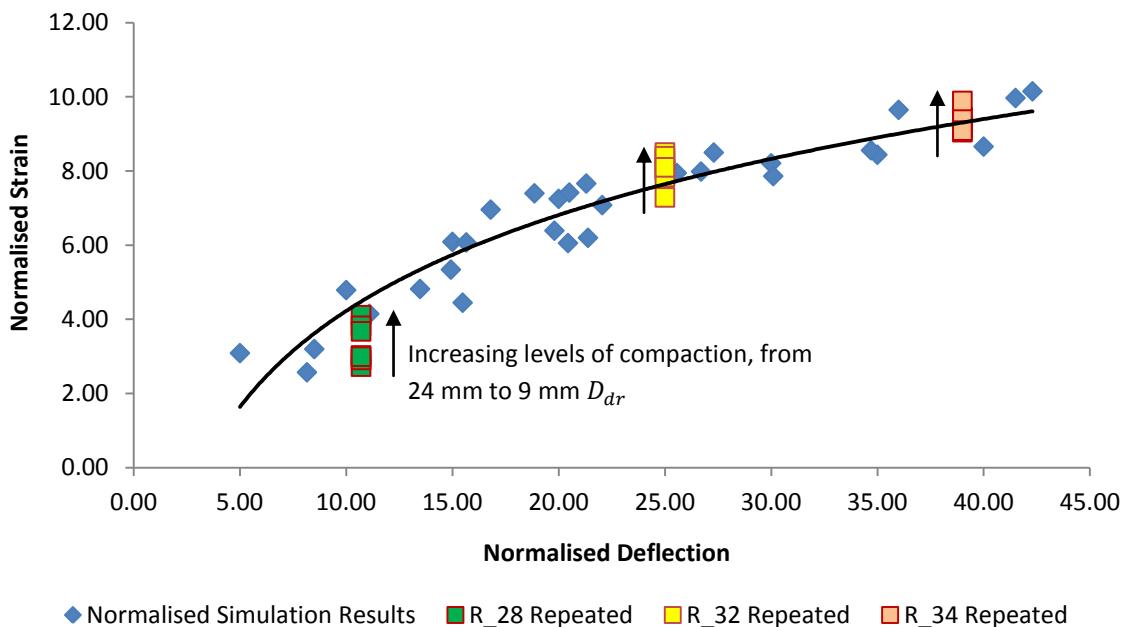
Figure 6.2: **Proximal ring normalised strain and deflection relationship.**

From figure 6.2, it is clear that a relationship of increased maximum strain within increasing levels of compaction exists. With this relationship confirmed, each of the original data points (Normalised Simulation results, figure 6.2) represents one of a scatter which can be achieved by varying the level of compaction.

It is important to note that the effects evident in figure 6.2 were not due to permanent deformation. Within the conducted simulations, none of the rings underwent plasticity as deformations remained within the boundaries of super-elasticity. The effect noticed in figure 6.2 was due to an internal mechanism of Nitinol elasticity as captured within the Auricchio constitutive model.

With Nitinol LPD effects captured within Auricchio constitutive model, further investigations were warranted to clarify its potential effect on ring behaviour. LPD effects as referred to within the current context can also be clarified as follows:

161

"The tendency for Nitinol's state variables, operating within the realm of super-elasticity, to be load path dependant when subjected to a cyclic loading regime"

Further investigations focussed on the following questions:

- Can LPD effects be isolated and studied under a simple bending regime?
- Can LPD effects be captured experimentally and how would the results be correlated to FE studies?
- What is the impact of LPD effects on design for the Anaconda device?

Before any studies were conducted, a thorough literature review was completed. Key outcomes of this review are published in section 1.3 of this thesis. Evident from the literature review was a lack of consideration for LPD effects. As a by-product that extends from the more fundamental hysteresis and super-elastic mechanisms, this behaviour trait seemed unaddressed by leading researchers working within the field of Nitinol characterisation.

6.1.1 Simplified load path dependency FEA study

To capture load path dependency effects, a cantilever beam was modelled within the FE code ANSYS 12.1 and subjected to the following load regime: Initially the beam was deflected at its free end to a displaced position (D) (figure 6.3). From this position the beam was further displaced by varying magnitude (ΔD), and then allowed to return to the initial displacement (D). The object of the study was to establish a relationship between the cycle amplitude (ΔD) and the final stress and strain state of the beam.
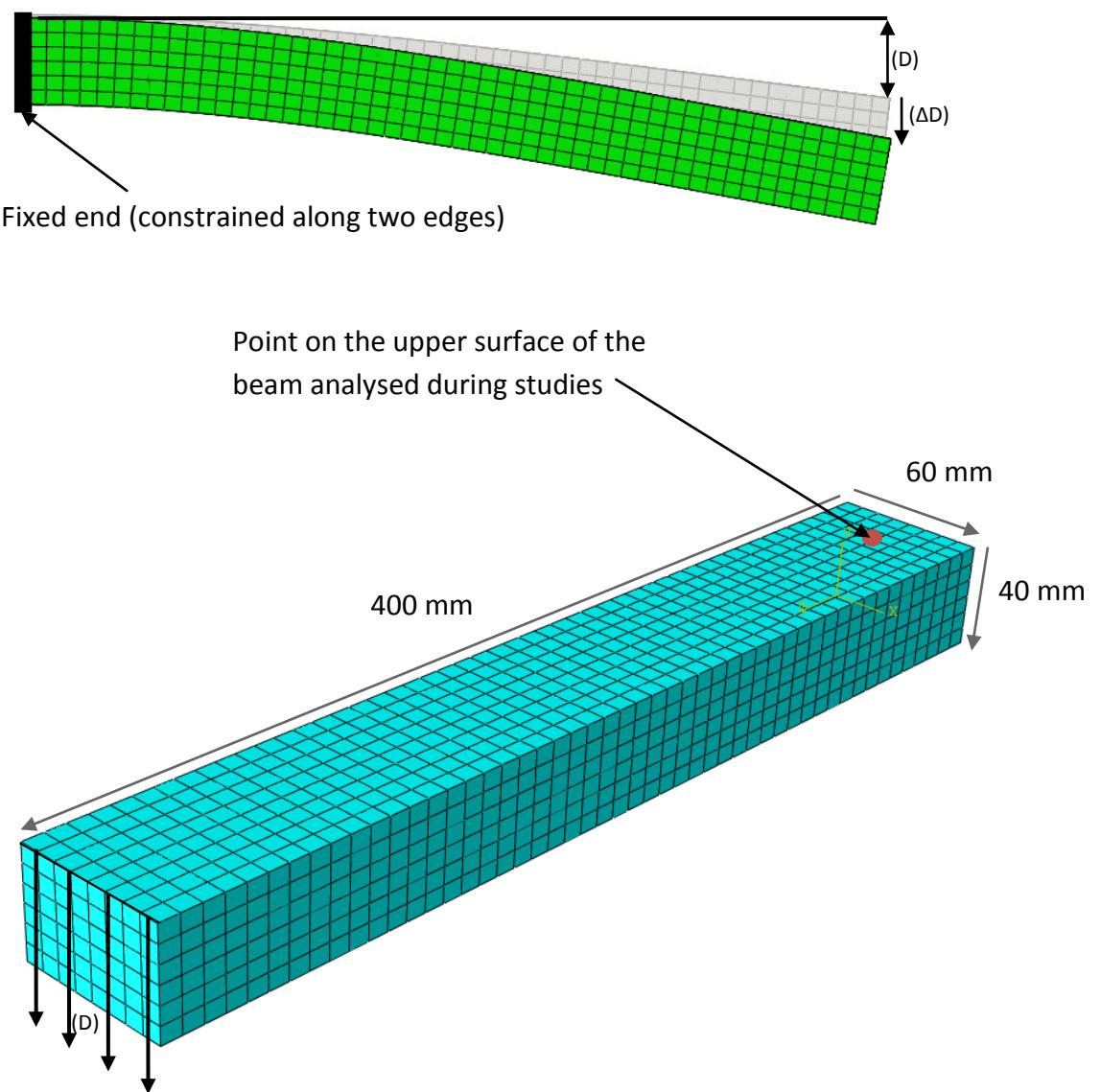
Figure 6.3: **Beam model used to study LPD effects within a simplified case study.**

Results discussed in this thesis are those obtained when tracking the stress-strain behaviour of a single node at the base of the beam. The node selected was on the upper surface of the beam, offset from the elements subjected to boundary conditions (as illustrated in figure 6.3).

Figure 6.4 shows the computational results achieved after cycling with a residual deflection (D) of 30 mm. As seen in figure 6.4, with increased amplitude, there was an increase in final strain value (Logarithmic) and an overall reduction in value of Von Mises stress. A pattern was noted where an increase in amplitude (ΔD) resulted in a convergence towards a stable final stress-strain state. It was also noted, however, that prior to complete convergence, the element tracked would enter the second marternsitic elastic modulus, which incurred plasticity, and as such remains outside the operation range of most medical devices.

By tracking this node through a simple loading regime, load history effects can clearly be seen and defined. Each of the six loading cases presented in figure 6.4 were subject to identical final boundary conditions, yet a variation of up to 33% in stress values were observed. This illustrates the significant variation in results that can be achieved dependant simply on past loading events.

Results shown here emphasise the importance of modelling the entire loading regime. This applies directly to the current context, where the entire compaction regime must be simulated in order to establish the ring's stress/strain states once deployed. Future iterations of the integrated modelling framework may even wish to take into account additional loading events associated with the delivery method. A clear line of further inquiry is also established as the long term cyclic behaviour of LPD effects are still poorly understood.
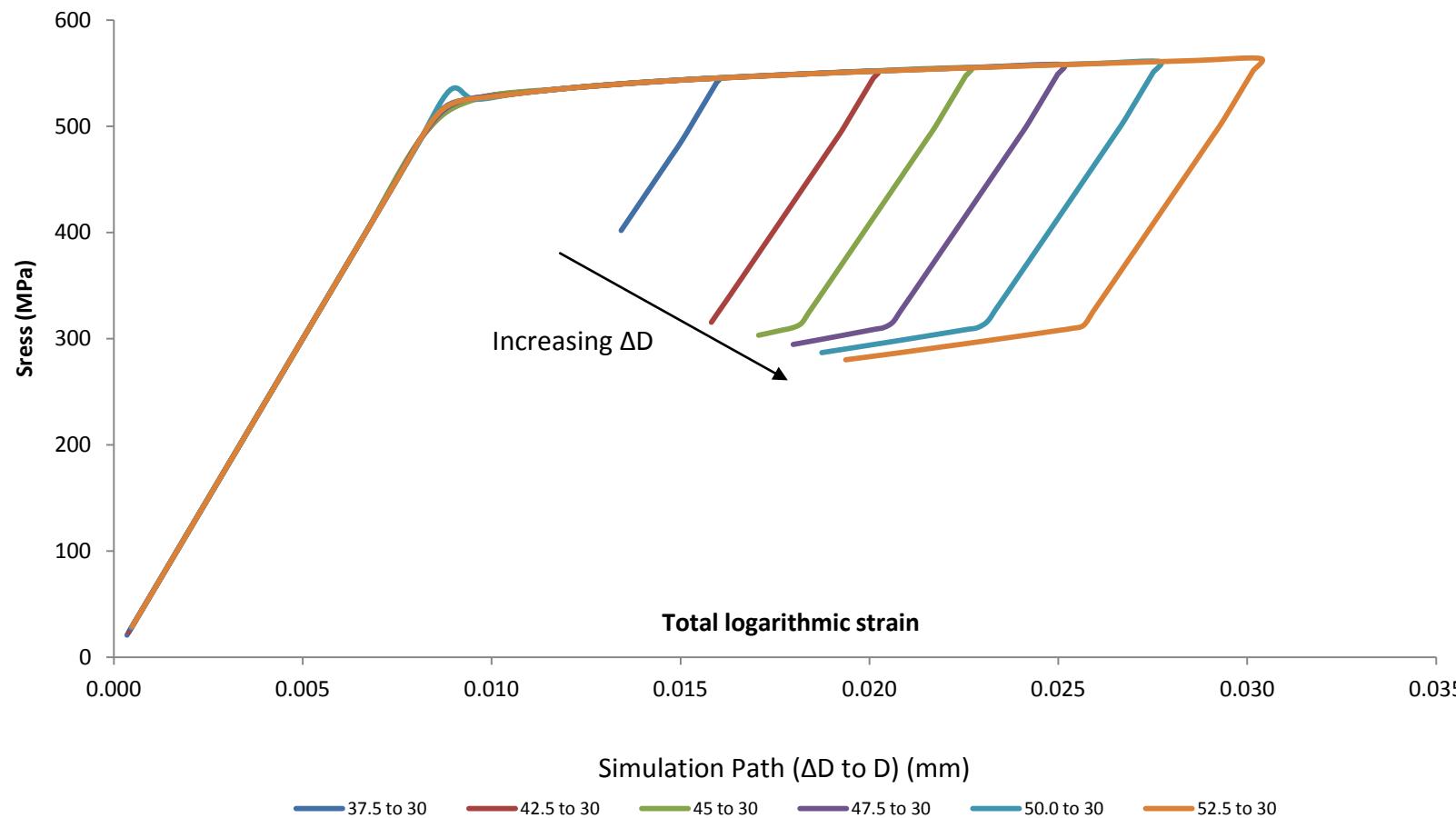
Figure 6.4: Stress-strain measurements were taken as the maximum Von Mises stress and total mechanical strain at the root location of the beam (outer fibre).

6.1.2 Load history within Nitinol specimen's

With the effects of Nitinol's load history as captured in FE clarified, further work was aimed at capturing the effects within an experimental study. For this three proximal rings were commissioned and manufactured to an identical standard to that used for the Anaconda device (R_21, R_25 and R_34, as stipulated in table 3.1). The objective of the study was to determine whether LPD effects could be noted within the proximal ring through simple uniaxial, compaction like cycles.

For this study, each ring device was in turn tethered to an uniaxial tensile machine as seen in figure 6.5. An identical test setup was used for stiffness characterisation in chapter 5, section 3.4. Once equilibrated to 37^0C, and 20 training cycles had been completed, the ring was subjected to a testing regime similar to that used for the cantilever beam in section 6.1.1. A residual displacement was established (D) from which the ring was displaced to distance ΔD and allowed to return to D. A range of these cycles were completed throughout which the crosshead displacement of actuators were recorded, alongside the force (N) required to compact the ring into the saddle shape.
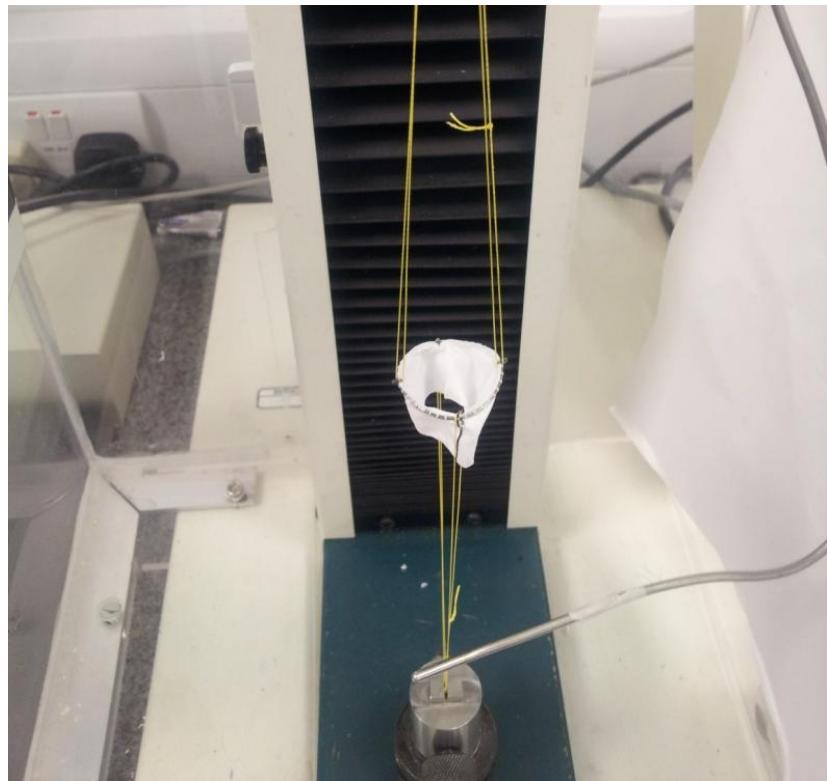
Figure 6.5: **R_34 Proximal ring attached with flyline to a uniaxial tensile rig.**

The force exerted by the ring (N), once returned to residual displacement (D) from displacement (ΔD), is shown in figure 6.6 and 6.7. Load path dependency within specimens was clearly observed. A trend was displayed in which an increase in deflection amplitude ΔD led to a decrease in the final load exerted by the compacted ring (N). This indicated a decrease in final energy potential with increasing levels of strain amplitude ΔD.

Results shown here support the findings made in section 6.1.1 and potentially highlights further design considerations for the Anaconda device. As ring stiffness can be correlated to the sealing properties of the Anaconda device, LPD effects can not only have an effect on the fatigue life of the device but also sealing properties of the device once deployed. Further investigations will, however, be required to confirm these findings, and a relationship between compaction stiffness and radial force also needs to be clearly defined.

Figure 6.8 shows the results obtained when experimental work was repeated within the Finite Element environment, using the Equivalent-I approach (section 5.1). Results indicate that FE captured load history effects in a similar manner to that obtained through experimental methods, with plateauing of results occurring at higher ΔD values.
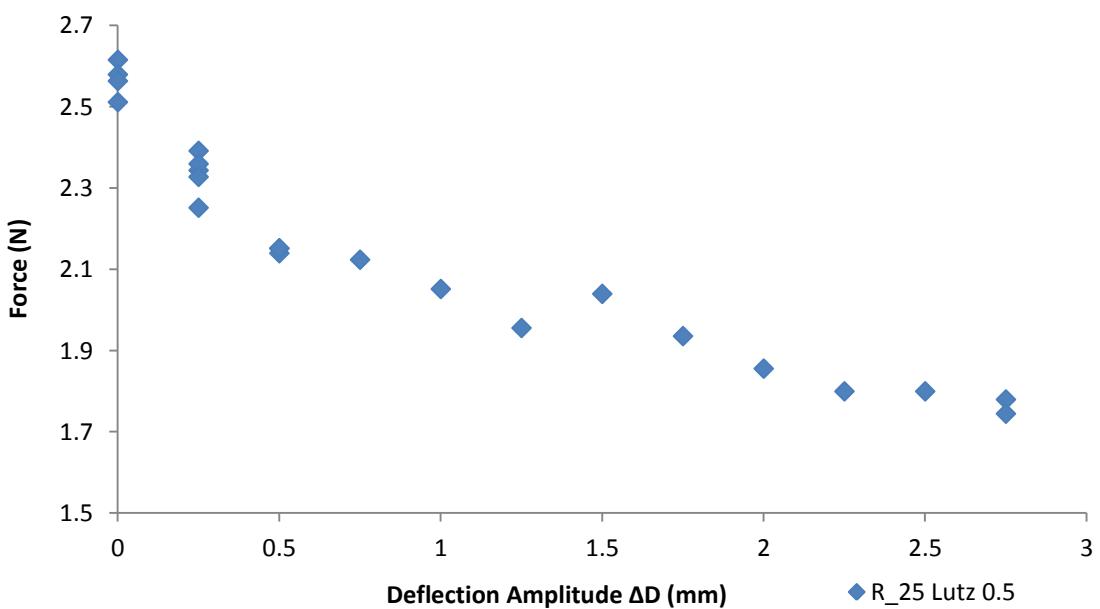
Figure 6.6: R_25 Lutz 0.5 results, where residual deflection D was 11.00 mm.
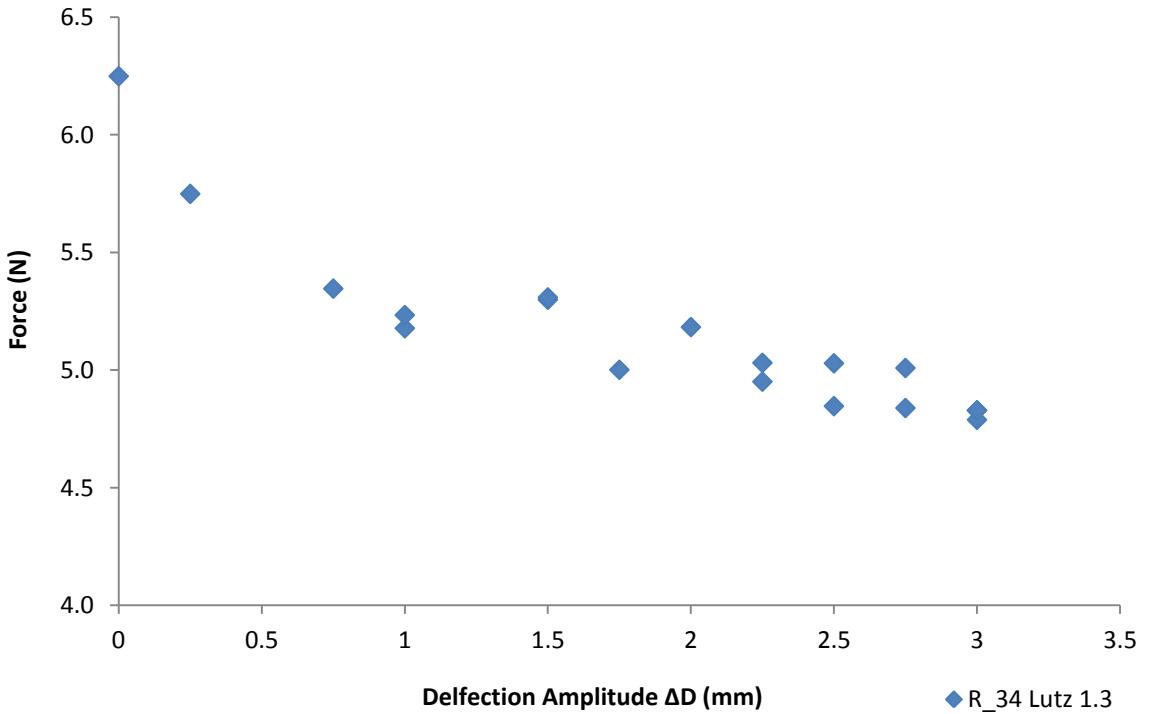
Figure 6.7: **R_34 Lutz 1.3 results, where residual deflection D was 14.25 mm.**
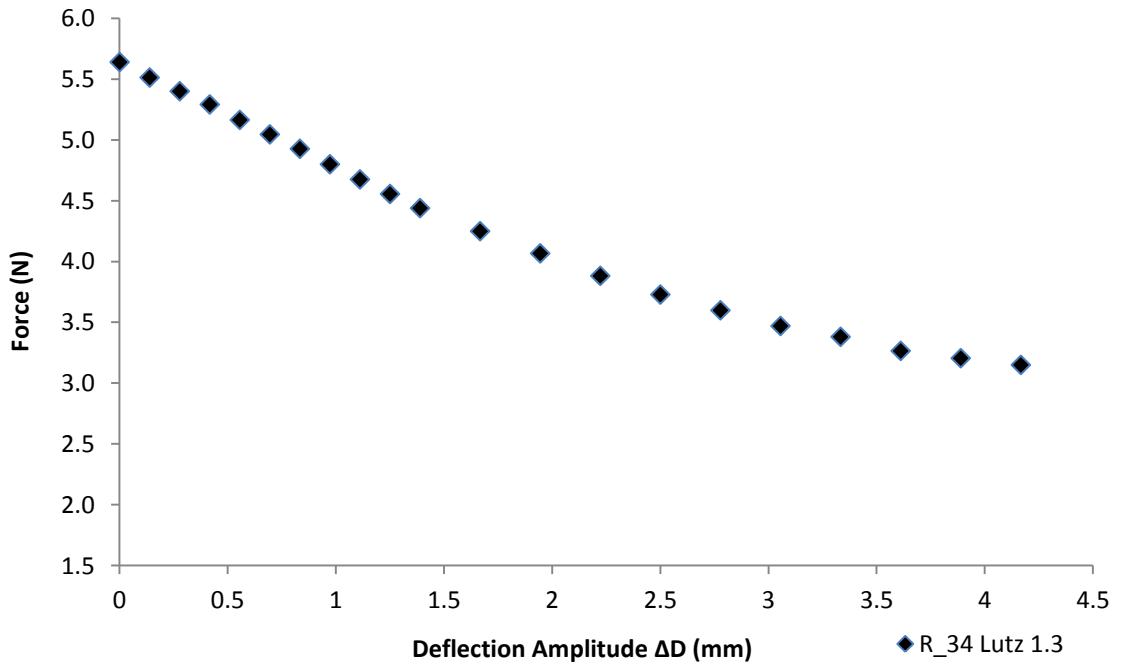
Figure 6.8: **R_34 Lutz 1.3 simulation results. Compared to figure 6.5 and 6.6, results indicate that FEA were capable of replicating LPD effects measured during experimental work. A slight under-prediction of force results by FEA was also noticeable (further investigated in section 6.2).**

6.2 Multi-turn model

In section 4.2.3, issues were noted regarding the Equivalent-I approach adopted from a previous study. It was shown that a violation of the assumptions on which the approach is based caused a divergence from experimental results at high levels of strain. To address these issues, a new method was proposed in the present study to simplify the modelling of Nitinol wire bundles. The method was based on results displayed in figures 5.9 and 5.10 where it is shown that the beam element approach can capture the stiffness properties of individual wires within a bundle.

The method proposed begins with the modelling of a single continuum wire turn. On the centreline of this continuum turn, a number of beam element wires are modelled so that the total number of wires is equal to that of the proximal ring simulated. To remove the need for complex wire interaction modelling, individual wire turns are pinned together at several locations. As incorporated into the framework, these locations were at centreline positions, where quarter symmetry boundaries exists, as well as midway between (as illustrated in figure 6.9). To further simplify the method and reduce computational cost, pins were introduced only once individual wires were compacted as shown in figure 6.10.

Using this method detailed state variables values can be read from the single continuum representation whilst bundle stiffness properties were obtained through computationally less expensive beam elements. For convenience, and to adhere to naming conventions used later in this thesis, the approach was referred to as the Bi-Element approach. To illustrate the effectiveness of the Bi-Element approach figure 6.11 is presented here, which shows that, the Bi-Element approach was used to extend a study first presented in section 5.4. The graph shows the reaction force required to compact the proximal ring, as estimated by two opposing FE approaches, compared against experimental results. As can clearly be seen, a marked improvement in accuracy was achieved through using the Bi-Element model. This improvement is achieved through a relatively small increase in computational costs and a decrease in numerical stability.
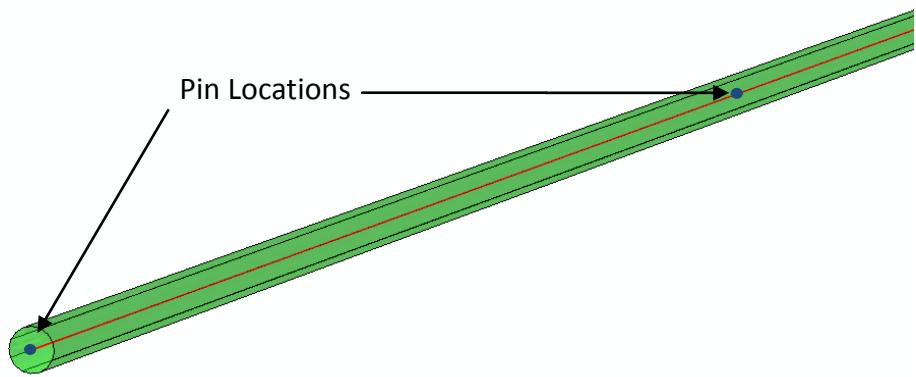
Figure 6.9: **Bi-Element wire bundle modelling method. This image displays the initial geometric layout of brick (green) and beam elements (red). As seen, all wire turns share a common centreline with no contact simulated. Wire turns are pinned at quarter symmetric boundaries, as shown.**
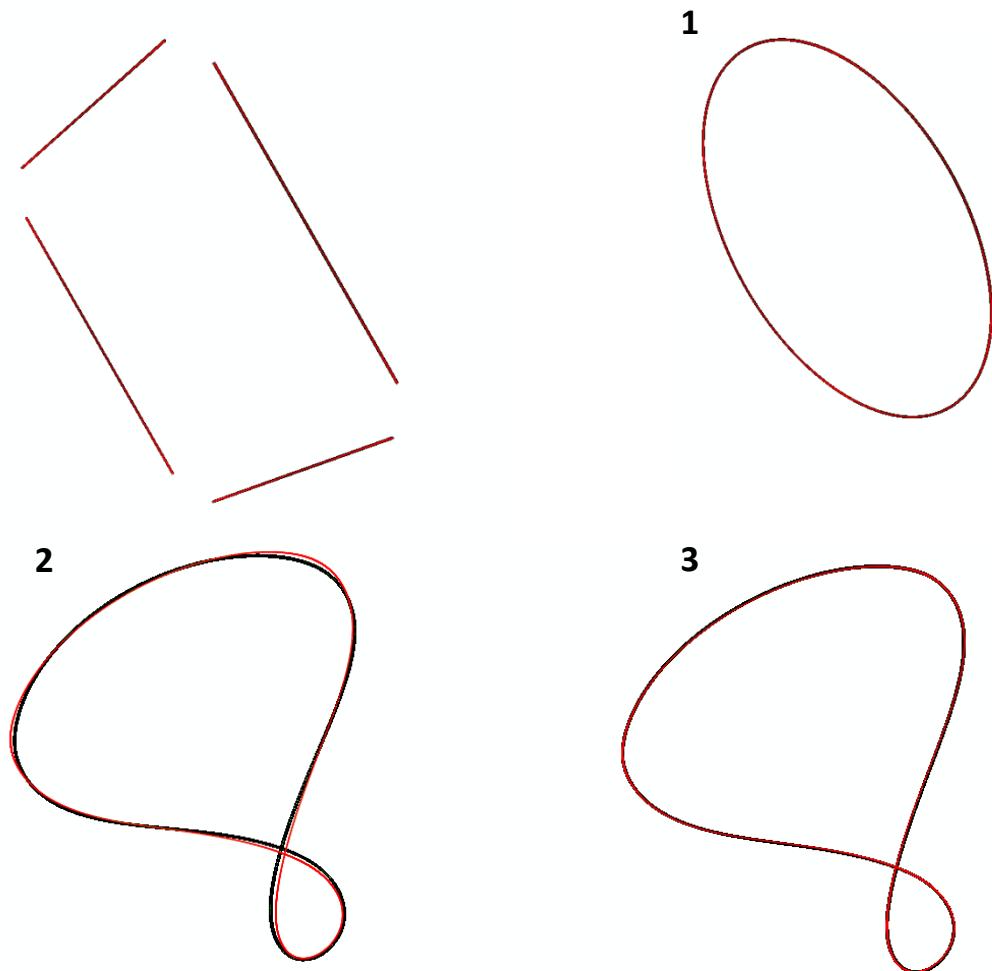
Figure 6.10: **Bundle model formation through three steps. First multiple rings are formed from the straight drawn condition (1). Once drawn, individual rings are compacted into the saddle shape (2). An additional step is then introduced, during which the individual turns are joined to form the combined bundle model (3).**
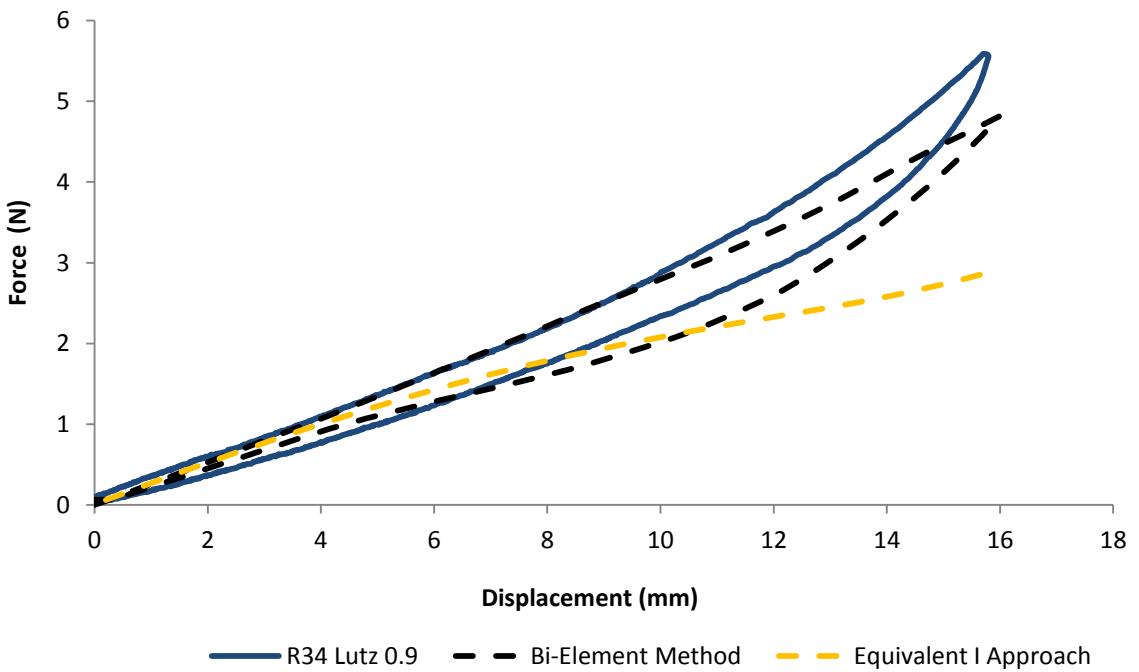
Figure 6.11: **The Bi-Element approach compared against experimental data and Equivalent-I approach.**

As shown in figure 6.11, the Bi-Element method closely approximated experimental results. A divergence is noted at higher compactions which are attributed to the dominance of the beam element approach within the method. As this divergence is mainly out of the operation window of the proximal ring once deployed the approach still holds merit.

6.3 The Bi-Material model approach

Nitinol compression/tension asymmetry is a well-documented phenomenon, often linked to the increase in transformation energy required to cause the onset of super-elastic mechanisms when under compression. This asymmetry poses significant challenges for FE constitutive modelling.

In its current form, the Abaqus 6.11 built-in Nitinol constitutive model provides users with the option of modelling the asymmetry by specifying a single parameter around which the built in algorithms automatically estimate the material's behaviour during compression. This approach provides little customisation and can lead to a significantly comprised material definition. Alongside these difficulties is the additional numerical burden that an asymmetric material model brings, which can lead to excessively long solution times and severe convergence instabilities. These instabilities can make the use of an asymmetric model unfeasible, especially

if other forms of nonlinearity or complex contact conditions are involved. In these situations, users may be forced to return to a symmetric model, which can further lead to a compromised model.

In this section, an approach is proposed for addressing these issues until such times where improved constitutive models can be presented. The approach is based around the Auricchio Nitinol constitutive model and is subject to two conditions: (1) no single element enters the transformation state in both compression and tension; (2) the first elastic modulus for compression and tension are identical.

The above approach consists of introducing an additional symmetric Nitinol material model that is optimised for capturing the compressive behaviour of the specimen as illustrated in figure 6.12. The material definition is then assigned to relevant elements, resulting in a single part consisting of two symmetrical material models. Through this, as shown in figure 6.12, an improved compressive stress-strain curve fit over a purely asymmetrical model can be achieved. This, in theory, can dramatically improve the accuracy of Nitinol FE representation, overcoming current constitutive model limitations. The more asymmetric and irregular the compressive response is, the more significant the potential advantages are of the method proposed in this thesis.

For ease of reference, throughout this section, the method will be referred to as the "Bi-Material Method". To assess the merits of the approach outlined, a thorough FE study was completed. To convey the major findings of this investigation, two case studies are presented here. The first of these is that of a Nitinol beam in bending whilst the second is the direct application to the proximal ring.
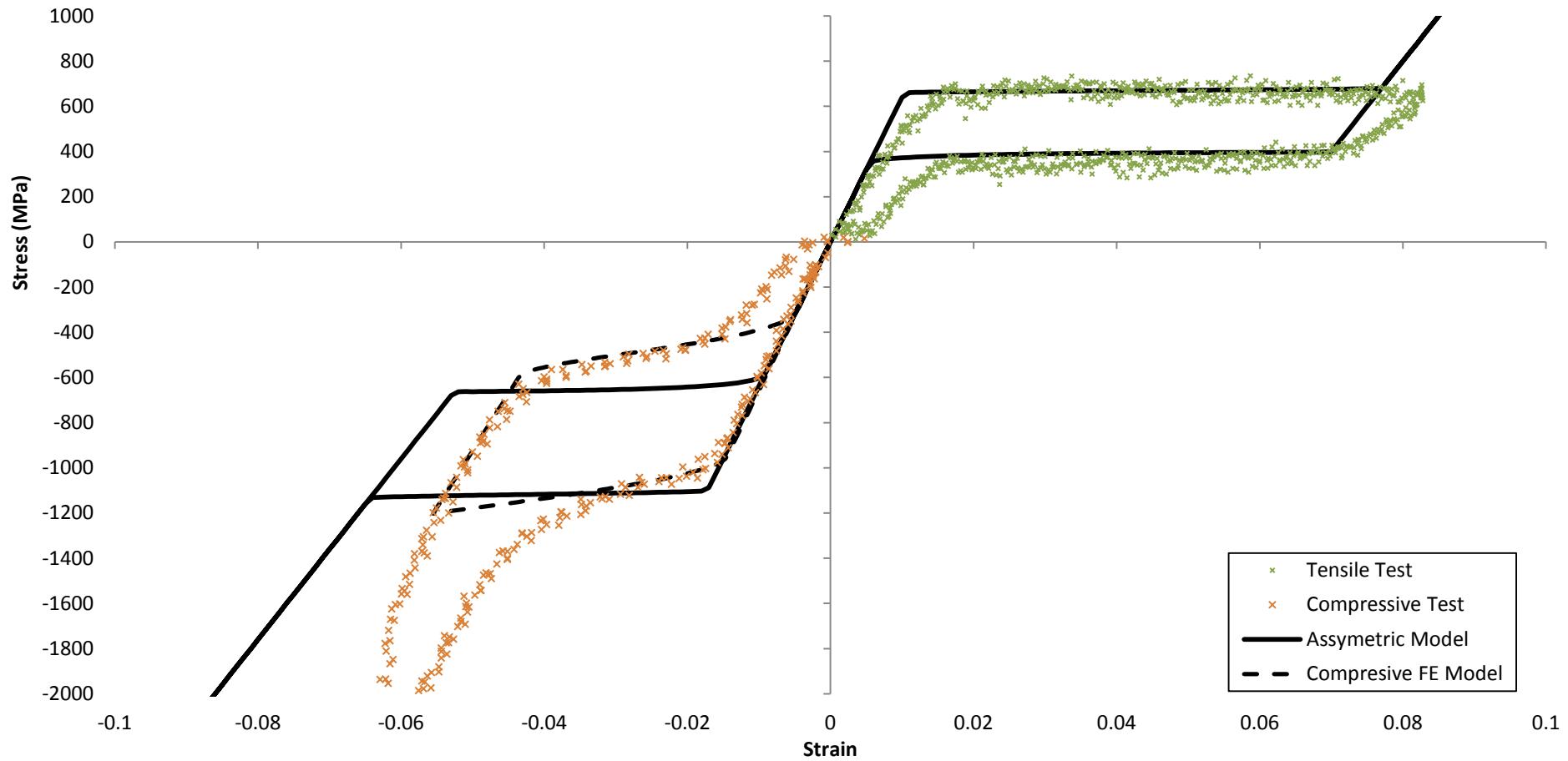
Figure 6.12: Using the Bi-Material modelling technique, elements that are judged to enter the compressive regime within an analysis are assigned an alternative Nitinol model. This alternative model's tensile behaviour is manipulated in such a way that when it is set to be symmetric, it is optimised to capture compressive behaviour. The potential benefit of this approach can be clearly distinguished from the graph.

6.3.1 Bi-Material model development

In total, three Nitinol material models were used for this study as shown in table 6.1. The two symmetrical models were manually developed and optimised for capturing the tensile and compressive behaviour of the asymmetric model, as shown in figure 6.13.

Table 6.1: **Material models used during Bi-Material model development.**

Parameter	Units	Asymmetric Model	Symmetrical (Tension)	Symmetrical (compression)
E_A	MPa	65800.0	65800.0	65800.0
v_A	-	0.435	0.435	0.435
E_M	MPa	65800.0	65800.0	65800.0
v_M	-	0.435	0.435	.435
ε^L	-	0.0538	0.0538	.04017
$\left(\dfrac{\delta\sigma}{\delta T}\right)_L$	MPaT^{-1}	5.74	5.74	5.74
σ^S_L	MPa	637	637	853
σ^E_L	MPa	657	657	879
T_0	^{o}C	0	0	0.0
$\left(\dfrac{\delta\sigma}{\delta T}\right)_U$	MPaT^{-1}	6.99	6.99	6.99
σ^S_U	MPa	327	327	437
σ^E_U	MPa	307	307	412
σ^S_{CL}	MPa	853	0.0	0.0
ε^L_V	-	0.0538	0.0538	0.04017
N_A	-	0.0	0.0	0.0
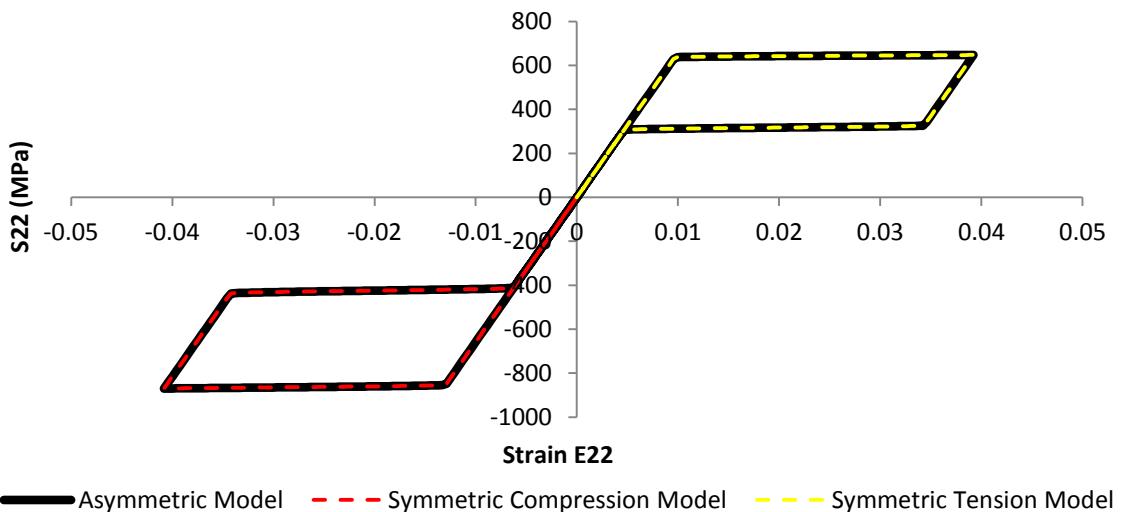
Figure 6.13: **The two symmetric models developed for this study, overlaid on top of the asymmetric model conventionally used to represent Nitinol.**

6.3.1.1 Case study one: Beam under bending

The first case study presented here to illustrate the feasibility of the approach utilised the cantilever beam introduced in section 6.1.1. The cantilever beam was subjected to a loading regime which included a vertical displacement (D) of 20 mm, a further displacement of 40 mm (ΔD), before being returned to the residual displacement (D). The analysis was repeated 3 times, each time using an alternative material as follows:

1. Through the use of the complete asymmetric model as defined in table 6.1.

2. Through the use of the Bi-Material approach.

3. Using a single symmetric model as defined in table 6.1.

As the two symmetric models used in the Bi-Material approach was developed around the asymmetric model, the results from these two simulation methods can be directly compared against one other. Differences in results can provide insight into the suitability of the Bi-Material approach. For further comparison, an analysis was completed using a single symmetric model based on the tensile definition.

Table 6.2 displays the Von Mises results obtained from this study. Results displayed within the table are with reference to results obtained using the asymmetric model. Differences were calculated on a node-to-node basis and are displayed in the table in percentage form.

Table 6.2: **A node-for-node comparison of Von Mises stresses against those obtained when using an asymmetric model. Results are given per analysis step.**

Symmetric Model					
Step-20 (D)		**Step-40 (ΔD)**		**Step-20 (D)**	
Maximum difference	Average difference	Max difference	Average difference	Max difference	Average difference
0.0%	0.00%	61%	4.11%	75.07%	4.13%
Bi-Material Method					
Step-20 (D)		**Step-40 (ΔD)**		**Step-20 (D)**	
Max difference	Average difference	Max difference	Average difference	Max difference	Average difference
0.0%	0.00%	11%	0.000297%	13%	-0.012%

Case study one results discussion

The aim of this study was to assess the use of modelling methods to address Nitinol asymmetry, thereby relinquishing the need for capturing asymmetry within the material definition. Such an approach can lead to significant improvements the robustness of computational models and reduce computational expense.

The Bi-Material approach is based on an understanding of the Auricchio Nitinol constitutive model incorporated into Abaqus 6.11.2. The constitutive model simplifies a variety of material characteristics, one of which is an identical first elastic modulus for both compression and tension. With this simplification, the response is always symmetric up to the point where the super-elastic mechanisms are encountered. This implies that a symmetrical material definition can capture the behaviour at any point in a model in a similar manner to an asymmetrical model, as long as said symmetrical model is optimised for capturing the super-elastic state that the associated element will enter. This assumption breaks down if any one element enters both the super-elastic compression and tension states.

Table 6.2 shows that all three methods captured the initial Step-20 in an identical manner. This was simply due to the material remaining within the elastic regime during this load step. During Step-40 and Step-20, large differences were primarily observed within elements containing additional boundary conditions. A divergence of results was also noted at material definition boundaries, signalling the potential onset of numerical instabilities.

It should be noted that the Bi-Material method will never yield identical results to an asymmetric model when capturing effects under compression in the transformed state. The reason for this lies with the host of automatically derived parameters over which the Abaqus.cae user has no direct control (such as the volumetric expansion and contraction coefficients associated with changing microstructures). As the user has no control over these parameters, they cannot be optimised during material model development. During case study 1, this in part lead to the differences noted.

In spite of some notable differences in results obtained between the Bi-Material and asymmetric approaches, averaged errors, as noted in table 6.2 remained small. This, combined with an analysis of reaction forces during simulations indicated that both approaches captured beam stiffness in a similar manner.

6.3.1.2 Case study two: application to the Anaconda device

Case study two considered the application of the Bi-Material model approach to the Anaconda's proximal ring, which was identified as meeting the requirements for Bi-Material implementation.

For this study, the ring-forming and compaction stages were simulated using identical representations to case study one, those being: (1) a complete asymmetric model; (2) the Bi-Material approach and; (3) a single symmetric representation (symmetric tension as defined in table 6.1).

By comparing the results obtained through these methods an assessment could be made of the suitability of the approach in the current context. A comparison between von Mises stresses, expressed as a percentage difference to that obtained through the asymmetric approach is shown in table 6.3.

Table 6.3: **A node-to-node comparison of alternative methods against Von Mises stresses obtained when using an asymmetric model. Although accentuated, patterns remained broadly the same as those noticed for case study 1.**

Symmetric Model			
Ring forming phase		**Compaction phase**	
Maximum difference	Average difference	Maximum difference	Average difference
0%	0%	368%	3.87%
Bi-Material Method			
Ring forming phase		**Compaction phase**	
Maximum difference	Average difference	Maximum difference	Average difference
0%	0%	96%	6.44%

Case study 2 results discussion

From table 6.3 shows that results from phase 1 remained identical between the various forms of representation. This finding was in line with expectations as the ring remained within the linear elastic regime during this phase.

In subsequent phases, results were seen to diverge. This divergence increased through the compaction phase and resulted in significant differences found for peak levels of strain. Although these differences were dramatic at first glance, they were consistent with trends noted in case study 1 (table 6.2) and less severe with an understanding of proximal ring kinematics.

The ring forming kinematics referred to here is the level of twist that the ring experienced during compaction. Analysis indicated that this level of twist was different for each of the simulations conducted within this study. This resulted in a slightly altered stress distribution across the ring, producing inflated node-for-node discrepancies as recorded in table 6.3.

Major contributors to the degree of twist the wire experienced is coefficients such the volumetric expansion/contraction of austenite and martensite. As these coefficients are not user inputs, and automatically calculated by predefined constitutive relations, they cannot be optimised within the symmetric material definitions. It was hence, in part, the relative difference in expansion/contraction coefficients between simulations conducted within this study that affected ring kinematics and as a result, altered stress distributions.

Analysis of the results obtained for the Highest Recorded Values in table 6.3 indicated that these differences were largely related to the formation of singularities. These singularities formed at dissimilar material boundary edges, and were amplified at regions where boundary conditions existed.

It is clear from the results presented in this thesis that the Bi-Material approach cannot be implemented without significant case specific analysis. The benefits of

additional control over Nitinol's compressive definition must be considered against stability complications and the development of irregular stress concentrations.

6.4 Formation of a generalised arterial model parameter set

For future development of a product design tool a single generalised material definition has can be proposed. This is not a trivial task, however, considering the variability of arterial tissue and the limited number of specimens tested in this study. From the assessment presented in chapter 3, figures 3.33 through to 3.38, it was shown that the characterisation data produced fell within the scope of a more general published study [72]. With this the correlation between studies identified, an opportunity was presented to collate data. As a result, statistically significant data sets were formed from which generalised material parameters could be drawn.

Through the collating exercise, data for seven intimas, eleven medias and twelve adventitias obtained from [72] were combined with the present study. Expressed in Holzapfel FE parameter form, data for some these specimens are shown in table 6.4. When this study was completed, parameter sets published by Weisbecker containing zero k_2 values were omitted from the collating exercise as it was found that the use of these particular parameter resulted in the analyses being aborted, with an error message of "incorrect parameter definition", in Abaqus 6.10 cae (only relevant to 5 intima and 1 media parameter sets).

Median parameters as put forward in table 6.5 can be seen as representing generalised parameters that can be used to model the abdominal aorta. Figure 6.14 presents these medians in graphical form alongside limit curves produced by collated parameters. Graphs "a" through to "c", all of whom have been scaled to the same strain values, can be compared against one another to illustrate the progression of compliance characteristics through the vessel wall.

Table 6.4: **Collated data sets for the intima, media and adventitia**

Intima					
	μ	k1	k2	φ	κ
VIII	0.068	25.91	67.45	37.5	0.23
IX	0.105	30.9	16.24	47.6	0.28
XVII	0.076	5.14	103.31	38.5	0.25
Specimen 1	0.0065	0.389	27.25	47.1	0.14
Specimen 2	0.025	35.42	10.625	49.1	0.228
Specimen 3	0.014	0.728	20.94	47.6	0.17
Median	0.0465	15.525	24.095	47.35	0.229

Media					
	μ	k1	k2	φ	κ
I	0.036	0.52	19.09	42.6	0.05
V	0.033	1.42	29.26	43.9	0.1
IX	0.028	0.92	10.33	35	0.28
XII	0.021	0.62	35.3	39.1	0.28
XIII	0.019	0.15	6.52	36.5	0.28
XIV	0.023	1.09	18.91	35.5	0.22
XVI	0.028	0.81	0.08	48.7	0.08
XVII	0.017	0.19	12.42	44.2	0.12
Specimen 1	0.091	0.145	5.58	44.2	0.12
Specimen 2	0.01	0.22	13.42	45.8	0.135
Specimen 3	0.0095	0.219	8.77	42.9	0.135
Median	0.021	0.52	12.42	42.9	0.135

| Adventita					
	μ	k1	k2	φ	κ
I	0.008	1.06	1.09	47	0.1
V	0.005	0.38	5.55	36.3	0.12
VIII	0.01	0.49	3.35	36.1	0.27
IX	0.016	0.44	3.41	45.9	0.12
XII	0.008	1.06	1.09	47	0.1
XIII	0.01	0.3	6.31	51.2	0.3
XIV	0.003	0.2	1.88	36.1	0.02
XVI	0.005	0.51	0.43	51.7	0.02
XVII	0.011	0.12	4.73	40.6	0.12
Specimen 1	0.003	0.0465	4.68	51.7	0.1425
Specimen 2	0.012	0.035	28.41	52.9	0.08
Specimen 3	0.001	0.11	7.4	59.6	0.21
Median	0.009	0.34	4.045	47	0.12
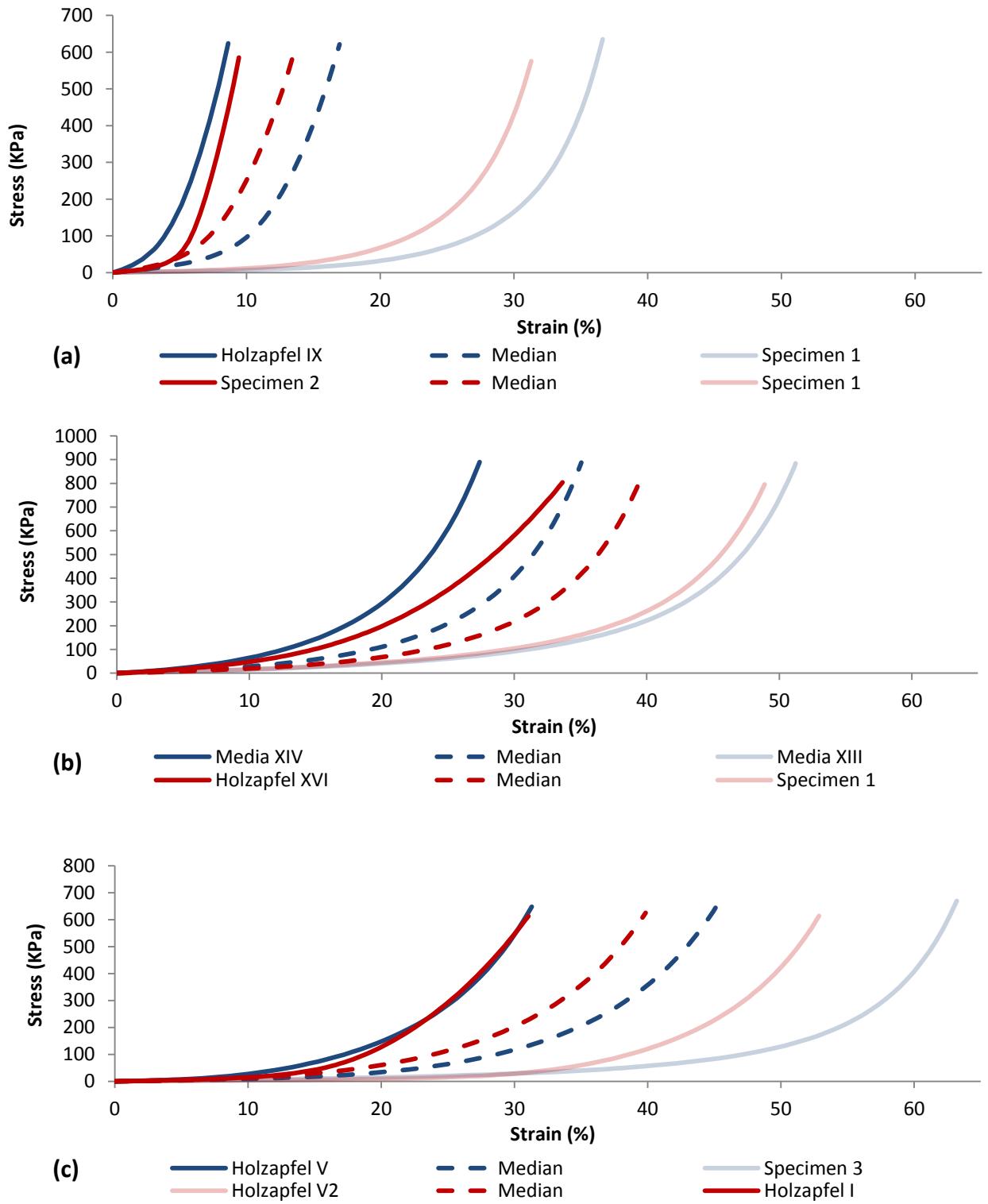
Figure 6.14: **Median plots against limit parameters for the intima (a), media (b) and adventitia (c). Within these graphs, blue is used to represent circumferential direction, while red denotes axial direction.**

To assess the merits associated of using a generalised data set, biaxial compliance studies presented in chapter 5, section 5.4.2, were revisited. Within section 5.4.2 FE pressure-diameter simulations for specimen 1, 2 and 3 are presented. The section assesses the ability of data specific material models to replicate data obtained during experimentation. Here, these simulations were repeated, substituting the particular data sets for the generalised one developed here. By noting the difference in deformations obtained between particular and generalised forms of representation, insight into the relative results can be presented here.

Table 6.6 shows the results of the present study. As can be seen, the generalised parameter set tended to marginally under-predict deformations obtained when using particular representations. This result is consistent with figure 6.14, which indicate that Median parameters tended to be less compliant than those obtained for specimens tested within the vascular tissue characterisation program.

Table 6.5: **Generalised parameter set for the human abdominal aorta**

	μ	k1	k2	Φ	κ
Intima	0.0465	15.525	24.095	47.35	0.229
Media	0.021	0.52	12.42	42.9	0.135
Adventita	0.009	0.34	4.045	47	0.12

Table 6.6: **Generalised parameter set for the human abdominal aorta**

	Pressure (mmHg)	Vessel external diameter as measured in experimental programme (mm)	FE estimation using particular model (mm)	FE estimation using generalised model (mm)
Specimen 1	80	16.98	16.47	16.32
	120	17.95	17.11	17.03
Specimen 2	80	20.07	19.75	19.61
	120	21.21	20.62	20.55
Specimen 3	80	20.88	19.10	19.02
	120	22.30	20.41	20.21

6.5 Chapter summary

A comprehensive literature review revealed that most studies involving Nitinol neglected taking Load Path Dependency effects into account. Through the use of a simple FE based case study, the substantial influence of LPD effects was clarified and the potential consequences for endovascular device design outlined. For the case study considered, it was shown that LPD effects could potentially influence the radial force applied by the proximal ring. A correlation between LPD effects as seen within FEA and as captured within experiments was also established. Due to the significance of the study into LPD effects, findings were presented at the international conference on Shape Memory and Super-elastic Technologies 2011 (SMST 2011).

In this chapter, a solution to the computational issues surrounding multi-turn bundle modelling was presented. The technique developed was seen as novel and having potential applications outside the scope of the current context. A further modelling technique referred to as the Bi-Material approach was presented within this chapter. The approach addressed deficiencies within the current constitutive models available for Nitinol. Both the merits and limitations of the approach were clearly outlined using two case studies. Case studies showed that although additional control over the compressive behaviour of Nitinol could be achieved, the development of singularities and stability issues made the applicability of the modelling technique case specific.

Finally, a generalised parameter set for the abdominal Aorta was presented. The set was developed by collating data from published studies, producing the largest database available for such parameters. Once developed, the generalised parameter set was incorporated into the integrated modelling framework. Through repeating biaxial compliance simulations conducted with particular artery parameters, comments on the applicability of such a generalised set could be made for the first time. This is seen as a considerable step forward for the incorporation

of the FE method into the field of endovascular device design, thus, meeting the final objective the current work set to achieve.

7 Thesis summary and conclusions

This chapter provides a summary of the research conducted. It clarifies the extent to which thesis objectives have been met and draws conclusions from the work presented. Statements of novelty and recommendations for further developments are also provided.

7.1 Thesis summary

This research project had the principle objective of investigating the use of emerging FE technologies for the design of endovascular devices. For this purpose, a thorough literature review was conducted, the primary outcomes of which have been presented. The review was comprehensive in nature, addressing relevant topics under the headings of Super-Elastic Nitinol and arterial tissue.

Through the literature review, the wealth of data available concerning Nitinol's mechanical properties was revealed. Gaps in the knowledge relevant to the work herein were shown to be largely limited to constitutive modelling, the mechanical response of thin wires in compression and the influence of load path dependency on the alloy's stress-strain response.

While it was shown that ample relevant data is available where Nitinol is concerned, the distinct lack of data available for human arterial tissue was highlighted. For the objectives studied in the present paper, this lack of data was seen as a considerable shortcoming as it meant that ambiguity still exists regarding basic questions such as the variability of mechanical properties in the presence of arterial features. The lack of layer-specific data also means that generalised material parameters have yet to be proposed. Generalised material parameters are fundamental for the development of FE design tools.

A review of published studies that have investigated FE device-artery interactions was also presented. Although several relevant studies were found during this review, none investigated the interactions between super-elastic Nitinol and a three-layered Holzapfel arterial model. An investigation into these interactions will

set a benchmark for current FE capabilities within the field of endovascular device design.

The knowledge gaps identified through the literature review were consolidated under the research objectives of the present thesis. With clear deficiencies noted in the data available where human arterial tissue is concerned, a vascular tissue testing programme was initiated. Within this programme, three human abdominal aortas were characterised. The experimental protocol used during the programme was established through extensive testing with porcine specimens, whilst the experimental pressure-diameter rig employed was developed especially for this purpose.

The vascular programme was the first comprehensive, layer-specific characterisation programme aimed at specifically meeting the data requirements for human abdominal aorta material model development and subsequent FE model validation. To this extent, the work presented can be viewed as a valuable contribution to the academic field. As the scope of the programme was broad, a vast array of data was made available that had previously only been accessible through a collection of disjointed studies.

With the required material modelling data produced, the focus of this thesis turned to the development of a FE-based device-artery interaction simulation. The approach adopted was to create a modular framework of material, geometrics, load case and interaction properties. During the development of the framework, a number of challenges were encountered, the solutions for which were presented. Some novel solutions included the Bi-Material approach, which addressed constitutive modelling limitations and the Bi-Element approach, which addressed wire bundle modelling challenges. Neither of these modelling approaches has previously been proposed within the literature and was viewed as having large scale application outside the boundaries of this research project.

With the framework developed, focus was placed on issues of validation and accuracy. Validation activities first verified the appropriateness of boundary

conditions sets used for the proximal ring. A concerted effort was also made to demonstrate agreement between beam and continuum element forms of ring representation. Once boundary conditions were verified as being appropriate, focus turned to the material models that had been developed. Device-artery simulations were compared against data, which had specifically been collated during the vascular testing programme for this purpose. Through this step-wise validation procedure, a critical review of the design framework was provided that clearly identified all its merits and limitations.

The final device-artery simulations created during this research project were the most comprehensive of their kind. With built-in versatility, robustness and an understanding of the accuracies involved, the framework was also deemed viable for industrial implementation. This outcome of the research satisfied one of the central academic questions that the research project set out to address, i.e., demonstrating the appropriateness of current technologies within the proposed industrial setting. Although capabilities have been demonstrated, it is acknowledged that due to a number of complexities involved in the FE modelling of endovascular devices, overall accuracies may be doubtful.

7.2 Thesis conclusions

The thesis provided an assessment of current FE technologies and the role it can play within the design of endovascular devices. During this assessment, the merits and limitations of two relevant constitutive models (the Auricchio Nitinol and Holzapfel arterial models) were extensively explored.

The Auricchio model was found to be adequate for the current application. Due to the number of relevant academic studies present in the literature, a comprehensive understanding of the accuracies associated with the model was available. Within the present work, the Auricchio material model could be integrated into a number of novel FE proximal ring studies without any significant difficulties. The most urgent development required in the FE representation of Nitinol is further control over the compressive response of material models.

The Holzapfel constitutive model has been subjected to a much lower level of peer review. The peer reviews that are available within the literature tend to focus on uniformity in plane deformations. To this extent, this thesis clearly demonstrated the Holzapfel model's ability to replicate uniaxial tensile stress-strain experimental data. Primarily, however, the validation procedures presented in this thesis were extended to assess the model's ability for capturing complex out-of-plane deformations. It was shown that the model is able to capture pressure-diameter results to reasonable levels of accuracy (within 32% of deformations). Results indicated that, in addition to the constitutive relations, the FE *in situ* modelling of the arterial vessel poses considerable challenges that are yet to be met (i.e., capturing residual *in situ* residual stresses).

When the two material models (Holzapfel and Auricchio) were combined within the same model to perform deployment simulations, typical accuracies within 40% of experimental deformation results were obtained. When relating these deformations to the accuracies of strain predictions, it was demonstrated that caution should be applied when interpreting results from FE models where the proximal ring is compacted past 15% oversize. It was shown that under these conditions, due to a power-law relationship, strain results can be considered unreliable. Although it is recognised that within this figure there is considerable room for improvement, the difficulty of the attempted simulation should be emphasised. Moreover, usefulness is provided through an understanding of limitations and merits, as opposed to accuracies *per se*.

The two material models discussed were also successfully integrated into a novel framework of Python scripts. These scripts were able to construct a number of FE studies within Abaqus 6.11, demonstrating the potential value of the framework as a tool that can be used in the design of endovascular devices. These studies were remarkably computationally efficient, considering that simulations involved contact between two highly non-linear material models under large levels of deformations. It is felt that the interactions between the hyper-elastic Holzapfel and super-elastic

Auricchio models currently represent a benchmark for endovascular device FE modelling. It is therefore the conclusion of this thesis that the highly non-linear material models required for endovascular device modelling can be integrated into a FE study, while at the same time remaining efficient and robust. This conclusion is significant, as these are the basic requirements if the models are to be used within parameter optimisation studies within the industry.

Towards the objectives of this thesis

- Regarding the principle objective of the thesis: the use of FE technologies within the design process of endovascular devices was successfully investigated. This was achieved through the development of a framework of Python scripts that can be used to investigate device-artery interactions. This framework can be used to determine the stress/strain states of an endovascular device *in situ* and through this be used as a design tool.

- An objective of the research project was to build upon previous studies. To this extent, several FE modelling methodologies were adopted from previous research projects (e.g., Equivalent-I). The creation of a generalised parameter set also relied on the notion of building upon previous experimental programmes, where data produced in the present study were combined with data available in the literature.

- During the Python script development, focus was placed on aspects of computational expense and robustness. This objective was clearly met with reference to section 4.4.3, where a significant reduction in computational time was achieved between like-for-like simulations conducted in the present study when compared to those conducted in previous research projects.

- Focus was placed on quantifying the levels of accuracy associated with device-artery simulations. Towards this objective, a chapter within this thesis (chapter 6) was dedicated to validation activities. Through a step-wise approach of validation, the boundary conditions used and material models

developed were independently checked prior to device-deployment simulations and were compared against experimental data.

- A generalised material model for the human abdominal aorta was proposed, thus meeting a central objective of this project.

- It is felt that the limitations/merits of current constitutive models available for Nitinol (Auricchio [62]) and arteries (Holzapfel [90]) were successfully demonstrated during this research project, thereby meeting another research objective. The limitations associated with Nitinol's asymmetric representation within the Auricchio constitutive model were not only highlighted, but also addressed through the Bi-Material approach. The ability of the Holzapfel constitutive model to predict complex, out of plane deformations was for the first time investigated in the literature. The stability of both models was also explored under complex contact conditions and large scale deformation.

- Further novel FE modelling methodologies for the representation of wire bundles were proposed.

With these objectives met, it is recognised that the integrated modelling framework proposed in the present thesis will require further development if it is to be successfully integrated into the design process. Until such a time, the framework stands as an excellent research tool which can be used for a variety of studies. An example of such a study can be to quantify the radial force exerted by endovascular devices once deployed. The consistency of this radial force along the circumference of the proximal ring during the cardiac cycle could also be established, and a correlation with potential "leaking locations" explored. This data will be useful in addressing issues such as type 1 endoleaks, a major cause of device failures *in situ*. Further studies could establish the relationship between the radial force exerted by the ring and anchoring characteristics. Such data could lead to improved designs and reduce the risk of stent migration. Towards the objective of a product development tool integrated into the design process, further research recommendations are provided in the following section.

7.3 Further research recommendations

Arterial testing: further research recommendations

- During the vascular testing programme, best practice of arterial pressurisation without an internal balloon conduit was assumed. Although this worked well during protocol development with porcine specimens, the method led to significant leaking issues during pressure-diameter testing with human specimens. As the literature remains ambiguous about best practice protocols, more should be done to define set procedures that future studies can follow.

- One recommendation is to add to the existing data pools through further experimental testing. With additional data, female/male variations, as well as age bands can be separated. Narrowing the specimen envelopes will lead to less scatter in results and more accurate simulations.

- Residual stresses were not included into the FE arterial model. Part of the reason for this was the general unreliability of current residual stress data. Further studies aimed at developing experimental protocols for the characterisation of *in situ* residual stresses are required.

- Further research should be conducted to better define a reliable method by which arterial layers can be separated. During this research project, layers were frequently damaged, leaving little left for characterisation.

- Although it was shown that regional characterisation can be regarded as adequate for material model development, future studies are urged to perform site specific characterisation. This is in part to remove the ambiguities associated with regional characterisation and in part to limit variables within data sets. It is also argued that, as more data becomes available, the narrowing of specimen envelopes (specifically age and gender) will reduce the scatter of data sets, during which time the site specific variation may become more apparent.

Nitinol: further research recommendations

- Relevant to the current work, further research is required to determine the behaviour of thin Nitinol wires (<0.18 mm) under compression.

- There is an urgent need for improving constitutive relations in order to fully capture Nitinol's asymmetric nature in the context of tension and compression. The current focus on the tensile aspect limits adequate characterisation where bending deformation is dominant.

- This project determined that load history effects are adequately captured within the current Auricchio constitutive relations over a single cycle. It is recommended that the work presented in this thesis be extended to determine the influence of load history effects over a larger number of cycles (>100). If it is shown that load history effects influence the material's stress-strain response over a large number of cycles, the consequences for fatigue performance should clearly be clarified.

FE modelling of device-artery interactions: further research recommendations

- With the deficiencies noted concerning the Equivalent-I approach, it is hoped that the stability of the Bi-Element and Bi-Material solutions can be improved to the point where they can be used in conjunction with the Holzapfel material definition. It is believed that such a development will significantly improve the accuracy of the simulations presented in this thesis.

- Little has been done to clearly define the merits of different forms of arterial representation. A dedicated study that considers solely the different FE representations of arteries is therefore required. Idealised forms of modelling, such as shell elements, should also be explored.

- The framework developed in this thesis is an excellent tool for future studies. A study that needs to be conducted is an in depth investigation into the maximum errors that can possibly be achieved when using the generalised material model proposed in chapter 3. These errors will be

obtained when comparing results obtained from the general model to those achieved using enveloping material parameters.

- To improve the usability of the framework, it should be incorporated into Abaqus cae as a plug-in application. In this way, users can directly interact with the framework without the need for manipulating Python scripts. This step will also promote the adoption of the framework by the industry.

- Finally, the incorporation of *in situ* residual stresses into an arterial model is seen as a major further research recommendation. Following on from recommendations made regarding the experimental data required to support such an endeavour, this recommendation is viewed as supporting large-scale independent study. The incorporation of residual stresses into the arterial model should initially be followed by a parameter study. This will clarify the significance of these stresses on the mechanical characteristics of the artery.

7.4 Final words

The research presented in this thesis was driven by academic interest and guided by industrial needs. It is believed that the project's outcome managed to bridge the gap between a variety of previously unconnected academic projects and final industrial applications.

Although it has been shown that a viable FE-based endovascular product design tool can be created using current technologies, the complexities in doing so must not be underestimated. At the centre of this project were two vastly different, highly non-linear materials that interacted with each other under complex loading conditions. Throughout the course of the project, experimentation with soft tissue was needed, which required considerable practical laboratory skills and knowledge. A broad range of expertise was therefore required, which took a considerable length of time to develop. It is, however, believed that the value of the work has been demonstrated and it is hoped that future studies will build upon the work presented.

Finally, it is hoped that the work presented within this thesis will positively impact the future design of endovascular devices.

8 References

[1]   "Endovascular stent–grafts for the treatment of abdominal aortic aneurysms," *Natl. Inst. Heal. Care Excell.*, vol. 167, no. September, 2009.

[2]   M. S. Makaroun, G. W. Barone, D. Bandyk, G. L. Moneta, and A. Frank, "The Aneurysm Detection and Management Study Screening Program," *Am. Med. Assoc.*, vol. 160, no. 1, pp. 1425–1430, 2000.

[3]   P. Cuypers, J. Buth, P. L. Harris, E. Gevers, and R. Lahey, "Reprinted article 'Realistic expectations for patients with stent-graft treatment of abdominal aortic aneurysms. Results of a European multicentre registry'.," *Eur. J. Vasc. Endovasc. Surg.*, vol. 42 Suppl 1, pp. S63–71, Sep. 2011.

[4]   A. R. Zankl, H. Schumacher, U. Krumsdorf, H. a Katus, L. Jahn, and C. P. Tiefenbacher, "Pathology, natural history and treatment of abdominal aortic aneurysms.," *Clin. Res. Cardiol.*, vol. 96, no. 3, pp. 140–51, Mar. 2007.

[5]   C. Dubost, M. Allary, and N. Oeconomos, "Resection of an aneurysm of the abdominal aorta: reestablishment of the continuity by a preserved human arterial graft, with result after five months.," *AMA. Arch. Surg.*, vol. 64, no. 3, pp. 405–8, Mar. 1952.

[6]   R. M. Greenhalgh, L. C. Brown, G. P. S. Kwong, J. T. Powell, and S. G. Thompson, "Comparison of endovascular aneurysm repair with open repair in patients with abdominal aortic aneurysm (EVAR trial 1), 30-day operative mortality results: randomised controlled trial.," *Lancet*, vol. 364, no. 9437, pp. 843–8, 2004.

[7]   J. C. Parodi, J. C. Palmaz, and H. D. Barone, "Transfemoral intraluminal graft implantation for abdominal aortic aneurysms.," *Ann. Vasc. Surg.*, vol. 5, no. 6, pp. 491–9, Nov. 1991.

[8]   M. Manish, "Risks and Benefits of Endovascular Abdominal Aortic Aneurysm Repair (EVAR), a video released by the Society for Vascular Surgery," Society for Vascular Surgery, US, 2010.

[9]   M. R. Greenhalgh, "Endovascular aneurysm repair versus open repair in patients with abdominal aortic aneurysm (EVAR trial 1): randomised controlled trial.," *Lancet*, vol. 365, no. 9478, pp. 2179–86, 2003.

[10]   G. Iannelli, M. Monaco, L. Di Tommaso, F. Piscione, P. Stassano, P. P. Mainenti, S. Laurino, and N. Spampinato, "Endovascular vs. open surgery of abdominal aortic aneurysm in high-risk patients: a single center experience.," *Thorac. Cardiovasc. Surg.*, vol. 53, no. 5, pp. 291–4, Oct. 2005.

[11]   C. K. Zarins and C. a Taylor, "Endovascular device design in the future: transformation from trial and error to computational design.," *J. Endovasc. Ther.*, vol. 16 Suppl 1, no. Suppl I, pp. I12–21, Feb. 2009.

[12]   N. Saratzis, N. Melas, A. Saratzis, J. Lazarides, K. Ktenidis, S. Tsakiliotis, and D. Kiskinis, "Anaconda aortic stent-graft: single-center experience of a new commercially available device for abdominal aortic aneurysms.," *J. Endovasc. Ther.*, vol. 15, no. 1, pp. 33–41, Feb. 2008.

[13]   M. L. Marin, L. H. Hollier, S. H. Ellozy, D. Spielvogel, H. Mitty, R. Griepp, R. a Lookstein, A. Carroccio, N. J. Morrissey, V. J. Teodorescu, T. S. Jacobs, M. E. Minor, C. M. Sheahan, K. Chae, J. Oak, and A. Cha, "Endovascular stent graft repair of abdominal and thoracic aortic aneurysms: a ten-year experience with 817 patients.," *Ann. Surg.*, vol. 238, no. 4, pp. 586–93; discussion 593–5, Oct. 2003.

[14]   D. Perrin, N. Demanget, P. Badel, S. Avril, and L. Orgeas, "Deployment of stent grafts in curved aneurysmal arteries: toward a predictive numerical tool," *Int. j. numer. method. biomed. eng.*, 2015.

[15]   G. Mouktadiri, B. Bou-Saïd, and H. Walter-Le-Berre, "Aortic endovascular repair modeling using the finite element method," *J. Biomed. Sci. Eng.*, vol. 6, no. September, pp. 917–927, 2013.

[16]   D. Roy, C. Kauffmann, S. Delorme, S. Lerouge, G. Cloutier, and G. Soulez, "A literature review of the numerical analysis of abdominal aortic aneurysms treated with endovascular stent grafts," *Comput. Math. Methods Med.*, 2012.

[17]   F. Migliavacca, L. Petrini, V. Montanari, I. Quagliana, F. Auricchio, and G. Dubini, "A predictive study of the mechanical behaviour of coronary stents by computer modelling.," *Med. Eng. Phys.*, vol. 27, no. 1, pp. 13–8, Jan. 2005.

[18]   C. Lally, F. Dolan, and P. J. Prendergast, "Cardiovascular stent design and vessel stresses: a finite element analysis.," *J. Biomech.*, vol. 38, no. 8, pp. 1574–81, Aug. 2005.

[19]   S. N. D. Chua, B. J. Mac Donald, and M. S. J. Hashmi, "Finite-element simulation of stent expansion," *J. Mater. Process. Technol.*, vol. 120, no. September 2001, pp. 335–340, 2002.

[20]   C. Rogers, D. Y. Tseng, J. C. Squire, and E. R. Edelman, "Balloon-Artery Interactions During Stent Placement : A Finite Element Analysis Approach to Pressure, Compliance, and Stent Design as Contributors to Vascular Injury," *Circ. Res.*, vol. 84, no. 4, pp. 378–383, Mar. 1999.

[21]   F. D. Whitcher, "Simulation of in vivo loading conditions Nitinol vascular stent structures," *Comput. Struct.*, vol. 64, no. 6, pp. 1005–1011, 1997.

[22] M. Brand, M. Ryvkin, S. Einav, I. Avrahami, J. Rosen, and M. Teodorescu, "Numerical Models of an Artery with Different Stent Types," in *XII Mediterranean Conference on Medical and Biological Engineering and Computing 2010*, pp. 545–548.

[23] X. Gong and A. Pelton, "Finite Element Analysis on Nitinol Medical Applications," in *Proceedings of IMECE*, 2002, vol. 53, pp. 75 – 80.

[24] E. McCummiskey, "The development of an analysis tool for the design of endovascular devices," *PhD Thesis, Univ. Strat.*, pp. 1–264, 2008.

[25] M. I. Ther, A. Technol, D. Stoeckel, C. Bonsignore, and S. Duda, "A Survey of Stent Designs," *A Nitinol Devices Components Publ.*, vol. 11, no. 4, pp. 137 – 147, 2002.

[26] C. K. J. Jr, H. Vm, G. Jl, and E. Anderson, "FDA Recommendations for Nitinol Stent and Endovascular Graft Fatigue Characterization and Fracture Reporting," *Jounral ASTM Int.*, vol. 3, no. 6, pp. 1–7, 2013.

[27] D. Stoeckel, "Nitinol medical devices and implants," *Minim. Invasive Ther. Allied Technol.*, vol. 9, no. 2, pp. 81–88, Jan. 2000.

[28] S. Ansari, D. J. McConnell, G. J. Velat, M. F. Waters, E. I. Levy, B. L. Hoh, and J. Mocco, "Intracranial stents for treatment of acute ischemic stroke: evolution and current status.," *World Neurosurg.*, vol. 76, no. 6 Suppl, pp. S24–34, Dec. 2011.

[29] "Drug-eluting stents for the treatment of coronary artery disease Part review of NICE technology," *Natl. Institure Heal. Clin. Excell. NICE Technol. apprasial Guid. 71*, no. April, 2009.

[30] M. Bäumler, T. Stargardt, J. Schreyögg, and R. Busse, "Cost effectiveness of drug-eluting stents in acute myocardial infarction patients in Germany : results from administrative data using a propensity score-matching approach .," *Appl. Health Econ. Health Policy*, vol. 10, no. 4, pp. 235 – 248, 2012.

[31] S. B. White and S. W. Stavropoulos, "Management of Endoleaks following Endovascular Aneurysm Repair.," *Semin. Intervent. Radiol.*, vol. 26, no. 1, pp. 33–8, Mar. 2009.

[32] D. Stockel, "Nitinol - A material with unusual properties," ndc Library, 1998.

[33] M. B. Streiff, "Review article Vena caval filters : a comprehensive review," *Am. Soc. Hematol.*, vol. 95, no. 12, pp. 3669–3677, 2000.

[34] T. Yoneyama and S. Miyazaki, "Shape Memory Alloys for Biomedical Applications," in *A volume in Woodhead Publishing Series in Biomaterials*, San Jose, 2009.

[35]   A. Ooi, D. Franklin, and S. Ohri, "Improved Technique of Nitinol Sternal Clip Application," *Ann. Thorac. Surg.*, vol. 87, no. 6, pp. 1971 – 1972, 2009.

[36]   T. Duerig and A. Pelton, "TiNi Shape Memory Alloys," *Prop. Handb. Titan. Alloy.*, no. 1, pp. 1035 – 1049, 1994.

[37]   S. Daly, D. Rittel, K. Bhattacharya, and G. Ravichandran, "Large Deformation of Nitinol Under Shear Dominant Loading," *Exp. Mech.*, vol. 49, no. 2, pp. 225–233, Oct. 2008.

[38]   Stoeckel and Yu, "Superelastic NiTi Wire," *Wire J. Int.*, pp. 45– 50, 1991.

[39]   L. Orgcas, Y. Liu, and D. Favier, "Experimental Study of Mechanical Hysteresis of NiTi During Ferroelastic and Superelastic Deformation," *J. Phys. III*, vol. 7, pp. 477–482, 1997.

[40]   S. Daly, G. Ravichandran, and K. Bhattacharya, "Stress-induced martensitic phase transformation in thin sheets of Nitinol," *Acta Mater.*, vol. 55, no. 10, pp. 3593–3600, Jun. 2007.

[41]   B. Reedlunn, C. B. Churchill, E. E. Nelson, J. A. Shaw, and S. H. Daly, "Tension , Compression , and Bending of Superelastic Shape Memory Alloy Tubes," in *ASME 2011 Conference on Smart Materials, Adaptive Structures and Intelligent Systems*, 2011, pp. 249–258.

[42]   P. Šittner, M. Landa, P. Lukáš, and V. Novák, "R-phase transformation phenomena in thermomechanically loaded NiTi polycrystals," *Mech. Mater.*, vol. 38, no. 5–6, pp. 475–492, May 2006.

[43]   L. Jordan, M. Chandrasekaran, M. Masse, and G. Bouquet, "Study of the Phase Transformations in Ni-Ti Based Shape Memory Alloys," *Le J. Phys. IV*, vol. 05, no. C2, pp. C2–489–C2–494, Feb. 1995.

[44]   J. Eaton-Evans, J. M. Dulieu-Barton, E. G. Little, and I. a Brown, "Observations during mechanical testing of Nitinol," *Proc. Inst. Mech. Eng. Part C J. Mech. Eng. Sci.*, vol. 222, no. 2, pp. 97–105, Feb. 2008.

[45]   A. R. Pelton, "Nitinol Fatigue: A Review of Microstructures and Mechanisms," *J. Mater. Eng. Perform.*, vol. 20, no. 4–5, pp. 613–617, Feb. 2011.

[46]   M. Wagner, T. Sawaguchi, G. Kausträter, D. Höffken, and G. Eggeler, "Structural fatigue of pseudoelastic NiTi shape memory wires," *Mater. Sci. Eng. A*, vol. 378, no. 1–2, pp. 105–109, Jul. 2004.

[47]   E. Henderson, D. H. Nash, and W. M. Dempster, "On the experimental testing of fine Nitinol wires for medical devices.," *J. Mech. Behav. Biomed. Mater.*, vol. 4, no. 3, pp. 261–8, Apr. 2011.

[48]   "Abaqus/CAE User's Manual 6.11." .

[49]   H. Soul, A. Isalgue, A. Yawny, V. Torra, and F. C. Lovey, "Pseudoelastic fatigue of NiTi wires: frequency and size effects on damping capacity," *Smart Mater. Struct.*, vol. 19, no. 8, Aug. 2010.

[50]   A. Wick, X. Gong, J. Fino, J. Sheriff, and A. R. Pelton, "Bending fatigue characteristics of Ntinol," *Proc. SMST*, pp. 361–366, 2006.

[51]   J. L. McNichols, P. C. Brookes, and J. S. Cory, "NiTi fatigue behavior," *J. Appl. Phys.*, vol. 52, no. 12, 1981.

[52]   S. Miyazaki, K. Mizukoshi, T. Ueki, T. Sakuma, and Y. Liu, "Fatigue life of Ti–50 at.% Ni and Ti–40Ni–10Cu (at.%) shape memory alloy wires," *Mater. Sci. Eng. A*, vol. 273–275, pp. 658–663, Dec. 1999.

[53]   S. W. Robertson, a. Mehta, a. R. Pelton, and R. O. Ritchie, "Evolution of crack-tip transformation zones in superelastic Nitinol subjected to in situ fatigue: A fracture mechanics and synchrotron X-ray microdiffraction analysis," *Acta Mater.*, vol. 55, no. 18, pp. 6198–6207, Oct. 2007.

[54]   Y. Freed and L. Banks-sills, "Crack growth resistance of shape memory alloys by means of a cohesive zone model," *J. Mech. Phys. Solids*, vol. 55, no. 10, pp. 2157–2180.

[55]   S. Robertson, J. Stankiewicz, X. Gong, and R. Ritchie, "Cyclic Fatigue of Nitinol," *Proc. Int. Conf. Shape Mem.*, pp. 79–87, 2004.

[56]   T. W. Duerig, A. Pelton, A. R. Pelton, X. Gong, and T. Duerig, "Fatigue Testing of Diamond Shaped Specimens," in *Proceedings of SMST 2003, Monterey, CA*, 2003, pp. 293–302.

[57]   M. M. Patel, M. R. Mitchell, K. Jerina, and S. W. Dean, "Characterizing Fatigue Response of Nickel-Titanium Alloys by Rotary Beam Testing," *J. ASTM Int.*, vol. 4, no. 6, p. 100390, 2007.

[58]   F. Nematzadeh and S. K. Sadrnezhaad, "Effects of material properties on mechanical performance of Nitinol stent designed for femoral artery: Finite element analysis," *Sci. Iran.*, vol. 19, no. 6, pp. 1564–1571, Dec. 2012.

[59]   C. Grabe and O. T. Bruhns, "Path dependence and multiaxial behavior of a polycrystalline NiTi alloy within the pseudoelastic and pseudoplastic temperature regimes," *Int. J. Plast.*, vol. 25, no. 3, pp. 513–545, Mar. 2009.

[60]   N. Rebelo, X. Gong, A. Hall, A. R. Pelton, T. W. Duerig, A. West, P. P. Parkway, F. Suite, N. Devices, and W. Drive, "Finite Element Analysis on the Cyclic Properties of Superelastic Nitinol," *2004 Abaqus Users' Conf.*, pp. 601–613.

[61] C. L. Zollikofer, F. Antonucci, M. Pfyffer, F. Redha, E. Salomonowitz, G. Stuckmann, and I. Largiadèr, "Arterial stent placement with use of the Wallstent: midterm results of clinical experience.," *Radiology*, vol. 179, no. 2, pp. 449–56, May 1991.

[62] F. Auricchio, R. L. Taylor, and J. Lubliner, "Shape-memory alloys: macromodelling and numerical simulations of the superelastic behavior," *Comput. Methods Appl. Mech. Eng.*, vol. 146, no. 3–4, pp. 281–312, Jul. 1997.

[63] F. Auricchio, G. Scalet, and M. Urbano, "A Numerical/Experimental Study of Nitinol Actuator Springs," *J. Mater. Eng. Perform.*, vol. 23, no. 7, pp. 2420–2428, Feb. 2014.

[64] M. J. Thubrikar, M. Labrosse, F. Robicsek, J. Al-Soudi, and B. Fowler, "Mechanical properties of abdominal aortic aneurysm wall.," *J. Med. Eng. Technol.*, vol. 25, no. 4, pp. 133–42, 2001.

[65] D. H. Wang, M. Makaroun, M. W. Webster, and D. A. Vorp, "Mechanical properties and microstructure of intraluminal thrombus from abdominal aortic aneurysm.," *J. Biomech. Eng.*, vol. 123, no. 6, pp. 536–9, Dec. 2001.

[66] S. R. H. Barrett, M. P. F. Sutcliffe, S. Howarth, Z.-Y. Li, and J. H. Gillard, "Experimental measurement of the mechanical properties of carotid atherothrombotic plaque fibrous cap.," *J. Biomech.*, vol. 42, no. 11, pp. 1650–5, Aug. 2009.

[67] G. A. Holzapfel, "Determination of material models for arterial walls from uniaxial extension tests and histological structure.," *J. Theor. Biol.*, vol. 238, no. 2, pp. 290–302, Jan. 2006.

[68] J. Gosline, M. Lillie, E. Carrington, P. Guerette, C. Ortlepp, and K. Savage, "Elastic proteins: biological roles and mechanical properties.," *Philos. Trans. R. Soc. Lond. B. Biol. Sci.*, vol. 357, no. 1418, pp. 121–32, Feb. 2002.

[69] B. Dobrin, "Mechanical Properties of Arteries," *Physiol. Rev.*, vol. 58, no. 2, pp. 397–447, 1978.

[70] M. P. E. Wenger, L. Bozec, M. a Horton, and P. Mesquida, "Mechanical properties of collagen fibrils.," *Biophys. J.*, vol. 93, no. 4, pp. 1255–63, Aug. 2007.

[71] A. J. Schriefl, G. Zeindlinger, D. M. Pierce, P. Regitnig, and G. a Holzapfel, "Determination of the layer-specific distributed collagen fibre orientations in human thoracic and abdominal aortas and common iliac arteries.," *J. R. Soc. Interface*, vol. 9, no. 71, pp. 1275–86, Jun. 2012.

[72] H. Weisbecker, D. M. Pierce, P. Regitnig, and G. a Holzapfel, "Layer-specific damage experiments and modeling of human thoracic and abdominal aortas

with non-atherosclerotic intimal thickening.," *J. Mech. Behav. Biomed. Mater.*, vol. 12, pp. 93–106, Aug. 2012.

[73]   M. Labrosse, "Structure and Mechanics of the Artery," *Vasc. Mech. Pathol. (1st ed), Springer*, 2007.

[74]   J. Kim and S. Baek, "Circumferential variations of mechanical behavior of the porcine thoracic aorta during the inflation test.," *J. Biomech.*, vol. 44, no. 10, pp. 1941–7, Jul. 2011.

[75]   J. H. Black, "Technique for repair of suprarenal and thoracoabdominal aortic aneurysms.," *J. Vasc. Surg.*, vol. 50, no. 4, pp. 936–41, Oct. 2009.

[76]   M. R. Labrosse, C. J. Beller, T. Mesana, and J. P. Veinot, "Mechanical behavior of human aortas: Experiments, material constants and 3-D finite element modeling including residual stress.," *J. Biomech.*, vol. 42, no. 8, pp. 996–1004, 2009.

[77]   H. P. Wagner, "Mechanical Characterisation, Modelling, and Examination of a Muscular Intracranial and Elastic ExtraCranial Artery with an Emphasis on Microstructure, Residual Stress and Smooth Muscle Cell Activation," PhD Thesis, Texas A&M University, 2011.

[78]   J. Kim, B. Peruski, and C. Hunley, "Influence of surrounding tissues on biomechanics of aortic wall," *Int. J. Exp. Comput. Biomech.*, vol. 2, no. 2, pp. 105–117, 2013.

[79]   A. Bollinger, J. P. Barras, and F. Mahler, "Measurement of foot artery blood pressure by micromanometry in normal subjects and in patients with arterial occlusive disease," *Circulation*, vol. 53, no. 3, pp. 506–512, Mar. 1976.

[80]   G. A. Holzapfel and R. W. Ogden, "Modelling the layer-specific three-dimensional residual stresses in arteries, with an application to the human aorta.," *J. R. Soc. Interface*, vol. 7, no. 46, pp. 787–99, May 2010.

[81]   G. Sommer, "Mechanical Properties of Healthy and Diseased Human Arteries Monographic Series TU Graz," PhD Thesis, Graz University of Technology, 2008.

[82]   G. a Holzapfel, G. Sommer, M. Auer, P. Regitnig, and R. W. Ogden, "Layer-specific 3D residual deformations of human aortas with non-atherosclerotic intimal thickening.," *Ann. Biomed. Eng.*, vol. 35, no. 4, pp. 530–45, Apr. 2007.

[83]   F. He and X. Li, "Residual strains in the arterial wall : A 3D finite element model," *Commun. Numer. Methods Eng.*, vol. 24, no. 11, pp. 1325–1337, 2008.

[84] L. G. Futterman and L. Lemberg, "The effects of aging on arteries.," *Am. J. Crit. Care*, vol. 12, no. 5, pp. 472–5, Sep. 2003.

[85] M. A. Hajdu, D. D. Heistad, J. E. Siems, and G. L. Baumbach, "Effects of aging on mechanics and composition of cerebral arterioles in rats," *Circ. Res.*, vol. 66, no. 6, pp. 1747–1754, Jun. 1990.

[86] G. Sommer and G. Holzapfel, "3D constitutive modeling of the biaxial mechanical response of intact and layer-dissected human carotid arteries.," *J. Mech. Behav. Biomed. Mater.*, vol. 5, no. 1, pp. 116–28, Jan. 2012.

[87] R. Wulandana and M. Robertson, "An inelastic multi-mechanism constitutive equation for cerebral arterial tissue.," *Biomech. Model. Mechanobiol.*, vol. 4, no. 4, pp. 235–48, Dec. 2005.

[88] J. Ferruzzi, D. a Vorp, and J. D. Humphrey, "On constitutive descriptors of the biaxial mechanical behaviour of human abdominal aorta and aneurysms.," *J. R. Soc. Interface*, vol. 8, no. 56, pp. 435–50, Mar. 2011.

[89] T. C. Gasser, R. W. Ogden, and G. a Holzapfel, "Hyperelastic modelling of arterial layers with distributed collagen fibre orientations.," *J. R. Soc. Interface*, vol. 3, no. 6, pp. 15–35, Feb. 2006.

[90] G. Holzapfel, T. . Gasser, and R. . Ogden, "A new constitutive framework for arterial wall mechanics and a comparative study of material models," *Jounral Elast.*, vol. 61, no. 8, pp. 1 − 48, 2000.

[91] "Bose ElectroForce 3200 Series III Test Instruments Users Manual." .

[92] R. C. Looft-Wilson and C. V Gisolfi, "Rat small mesenteric artery function after hindlimb suspension.," *J. Appl. Physiol.*, vol. 88, pp. 1199–1206, 2000.

[93] C. A. J. Schulze-Bauer, C. Mörth, and G. a. Holzapfel, "Passive Biaxial Mechanical Response of Aged Human Iliac Arteries," *J. Biomech. Eng.*, vol. 125, no. 3, pp. 0–12, 2003.

[94] G. A. Holzapfel, G. Sommer, and P. Regitnig, "Anisotropic Mechanical Properties of Tissue Components in Human Atherosclerotic Plaques," *J. Biomech. Eng.*, vol. 126, no. 5, p. 657, 2004.

[95] G. A. Holzapfel and R. W. Ogden, "On planar biaxial tests for anisotropic nonlinearly elastic solids. A continuum mechanical framework," *Math. Mech. Solids*, vol. 14, no. 5, pp. 474–489, Mar. 2008.

[96] M. A. Creager, T. F. Lüscher, F. Cosentino, and J. a Beckman, "Diabetes and vascular disease: pathophysiology, clinical consequences, and medical therapy: Part I.," *Circulation*, vol. 108, no. 12, pp. 1527–32, Sep. 2003.

[97]   G. J. Langewouters, K. H. Wesseling, and W. J. Goedhard, "The static elastic properties of 45 human thoracic and 20 abdominal aortas in vitro and the parameters of a new model.," *J. Biomech.*, vol. 17, no. 6, pp. 425–35, Jan. 1984.

[98]   R. W. Ogden, "Nonlinear Elasticity , Anisotropy , Material Stability and Residual stresses in Soft Tissue," *Biomech. Soft Tissue Cardiovasc. Syst.*, vol. 108, no. 441, pp. 65–108, 1997.

[99]   D. Y. Gao and R. W. Ogden, "Multiple solutions to non-convex variational problems with implications for phase transitions and numerical computation," *Q. J. Mech. Appl. Math.*, vol. 61, no. 4, pp. 497–522, Jul. 2008.

[100] G. Sommer, P. Regitnig, L. Költringer, and G. a Holzapfel, "Biaxial mechanical properties of intact and layer-dissected human carotid arteries at physiological and supraphysiological loadings.," *Am. J. Physiol. Heart Circ. Physiol.*, vol. 298, no. 3, pp. H898–912, Mar. 2010.

[101] H. Gavin, "The Levenberg-Marquardt method for nonlinear least squares curve-fitting problems," Masters Dissertation, Duke University, Department of Civil and Environmental Engineering, 2011.

Appendix 1 - Computer specifications

During this research project all simulations were conducted on a work station with the following specifications

Manufacturer :   Dell
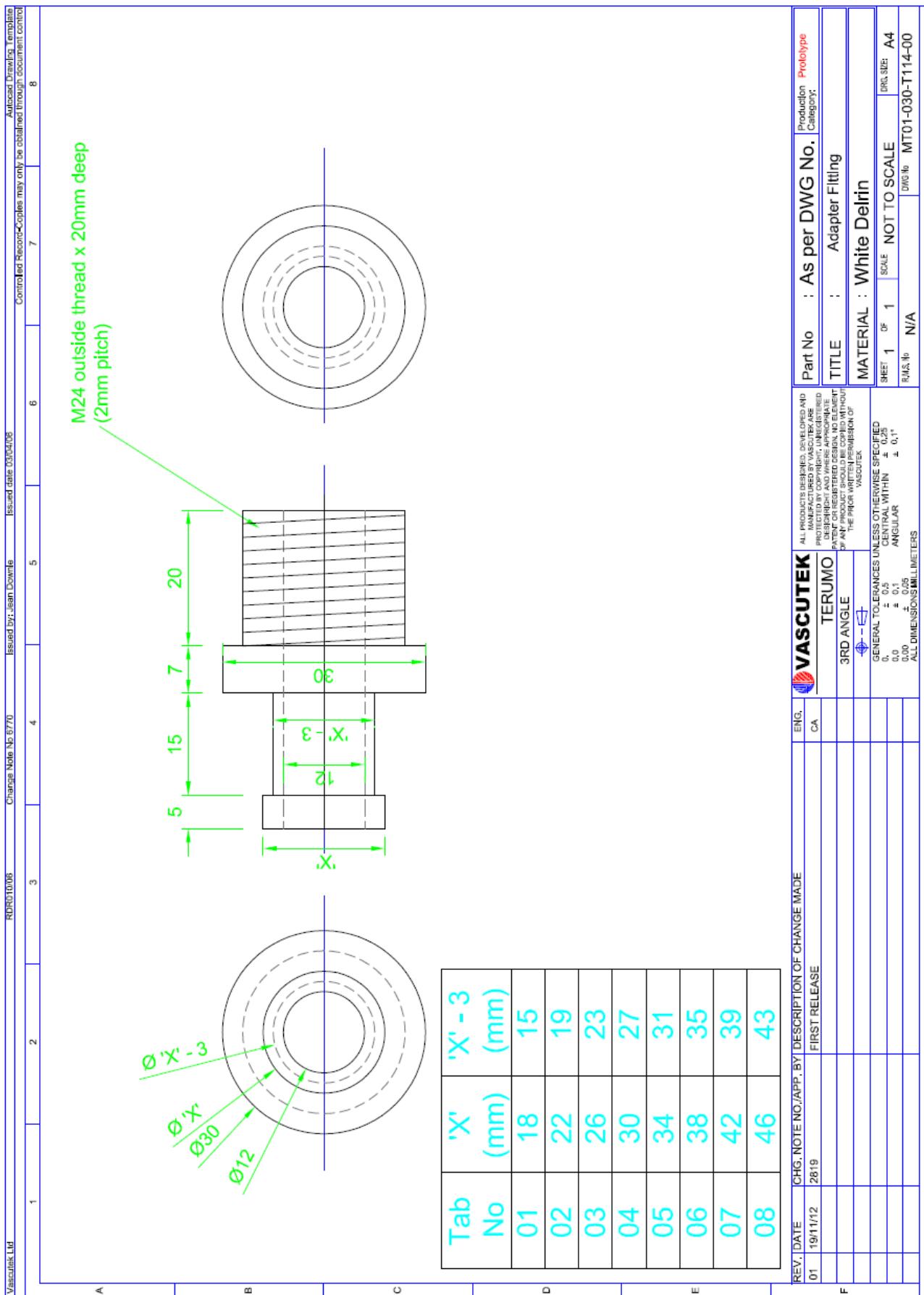
Model   :   Precision T3500

Processor   :   Intel(R) Xeon(R) CPU W350 @ 2.8GHz

Installed Ram :   12.0 GB

System Type :   64-Bit

Appendix 2 - Rig fittings drawings

M24 outside thread x 20mm deep
(2mm pitch)

Ø 'X' - 3
Ø 'X'
Ø30
Ø12

Tab No	'X' (mm)	'X' - 3 (mm)
01	18	15
02	22	19
03	26	23
04	30	27
05	34	31
06	38	35
07	42	39
08	46	43

20 7 15 5 'X' - 3 12 'X' 30

VASCUTEK
TERUMO
3RD ANGLE

ALL PRODUCTS DESIGNED, DEVELOPED AND MANUFACTURED BY VASCUTEK ARE PROTECTED BY COPYRIGHT, UNREGISTERED DESIGN RIGHT AND WHERE APPROPRIATE PATENT OR REGISTERED DESIGN. NO ELEMENT OF ANY PRODUCT SHOULD BE COPIED WITHOUT THE PRIOR WRITTEN PERMISSION OF VASCUTEK

GENERAL TOLERANCES UNLESS OTHERWISE SPECIFIED
CENTRAL WITHIN
ANGULAR
0,   ± 0,5   ± 0,25
0,0   ± 0,1   ± 0,1°
0,00 ± 0,05
ALL DIMENSIONS MILLIMETERS

Part No : As per DWG No.   Production Prototype Category:
TITLE : Adapter Fitting
MATERIAL : White Delrin
SHEET 1 OF 1   SCALE NOT TO SCALE   DWG. SIZE: A4
R.M.S. No N/A   DWG No MT01-030-T114-00

REV.	DATE	CHG. NOTE NO./APP. BY	DESCRIPTION OF CHANGE MADE
01	19/11/12	2819	FIRST RELEASE

ENG.
CA

Appendix 3 - Arterial specimen data

Within chapter 3, results obtained from uni-axial force stretch experiments were presented. As FE material modelling requirements dictate a single data set, per layer, per direction, only representative curves were presented within the chapter. Here, in appendix 3, all uni-axial data acquired during the programme are presented, and the choice of representative curves justified. Results are presented here per specimen, per layer, per direction, with the representative curves for that particular data set illustrated in black within each figure. In some cases, the same sample was subjected to altered displacement cycle regimes, with the term "run" in the figure legend used to indicate this.

Specimen 1

In total, eleven test samples were harvested from individual arterial layers, with stress-strain results shown below in figure Appendix 3.1 through to 3.6.
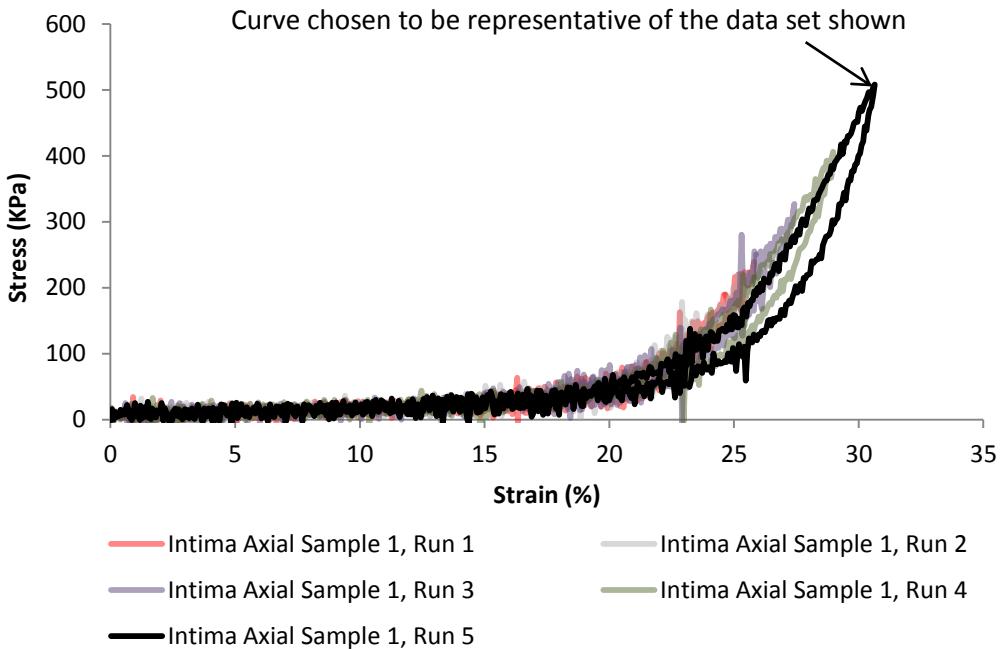
Figure Appendix 3.1: **Results obtained for the one sample harvested in the axial direction from the artery's intimal layer. The representative curve chosen was the one during which the sample experienced maximum extension and was in the most trained state.**
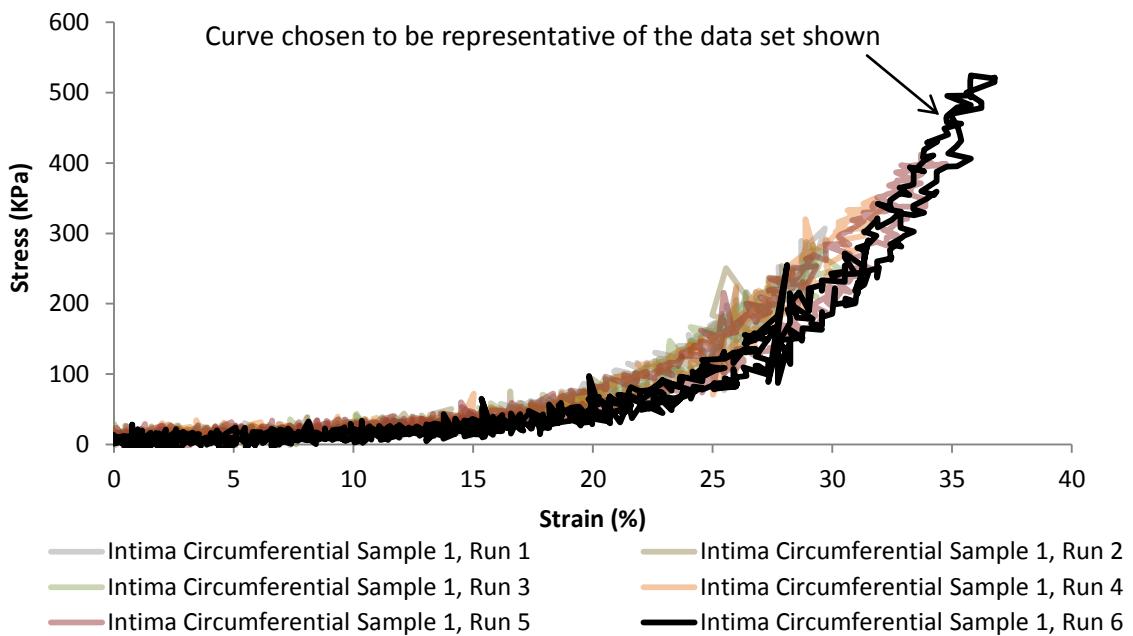
Figure Appendix 3.2: **Results obtained for the one sample harvested in the circumferential direction from the artery's intimal layer. The representative curve chosen was the one during which the sample experienced maximum extension and was perceived to be in a trained state.**
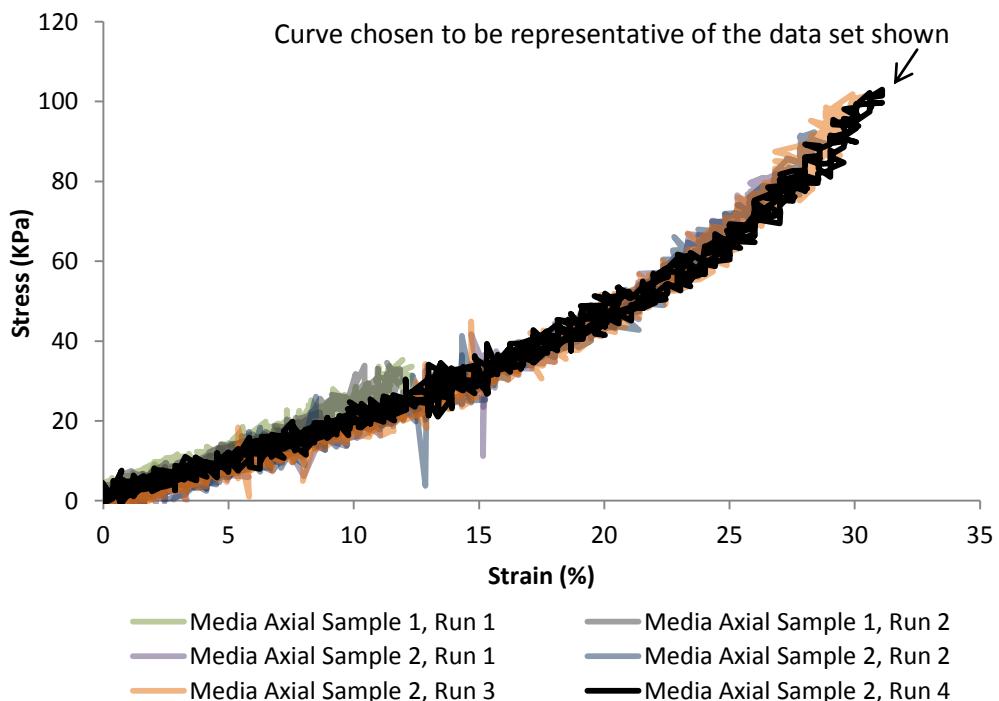

Figure Appendix 3.3: **Results obtained for the two samples harvested in the axial direction from the artery's medial layer. The representative curve chosen was the one during which the sample experienced maximum extension and was perceived to be in the trained state.**

Curve chosen to be representative of the data set shown
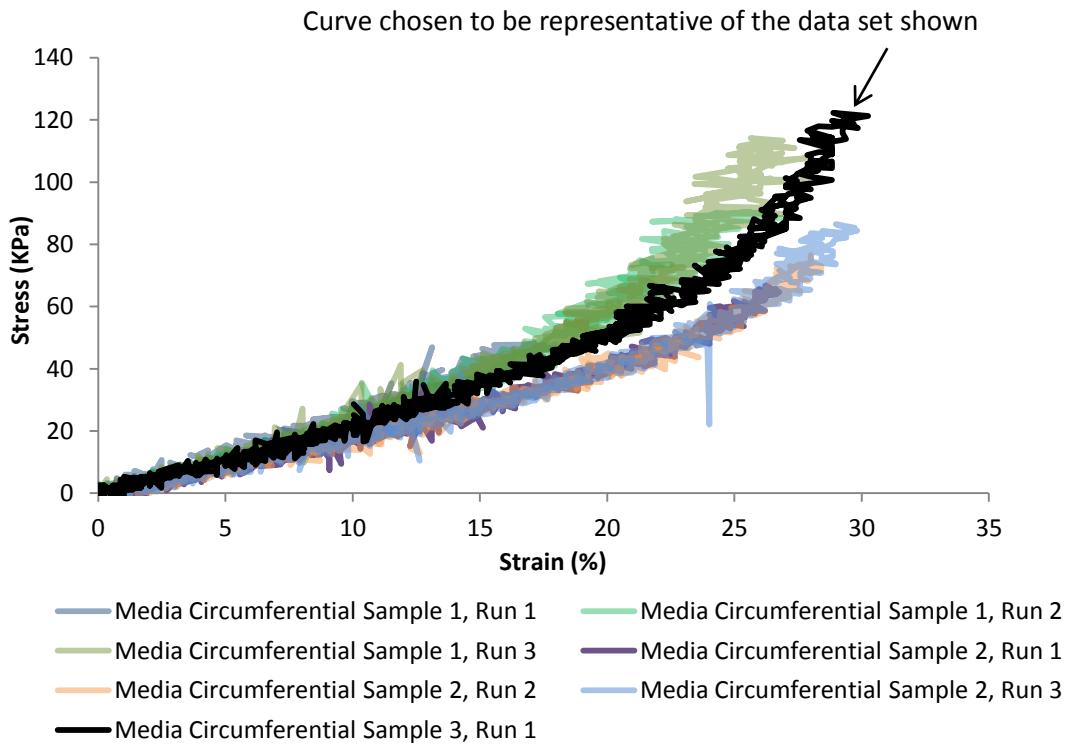
Figure Appendix 3.4: **Results obtained for the three samples harvested in the circumferential direction from the artery's medial layer. Results obtained from sample 3 were chosen to be representative as it was enveloped by both samples 1 and 2.**

Curve chosen to be representative of the data set shown
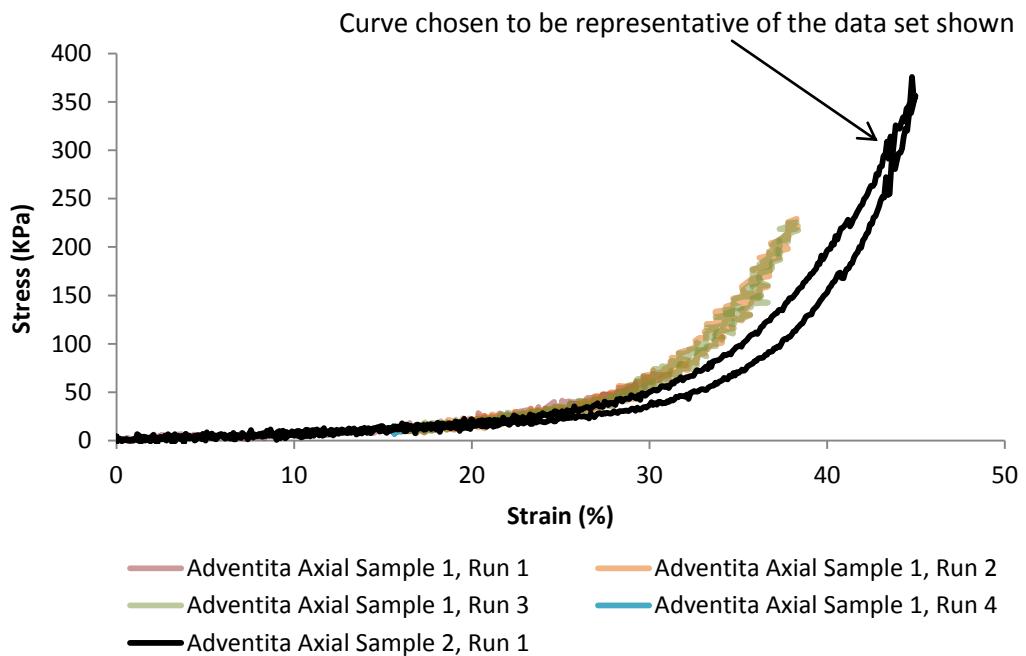
Figure Appendix 3.5: **Results obtained for the two samples harvested in the axial direction from the artery's adventitial layer. The representative curve chosen was the one during which the sample experienced maximum extension.**
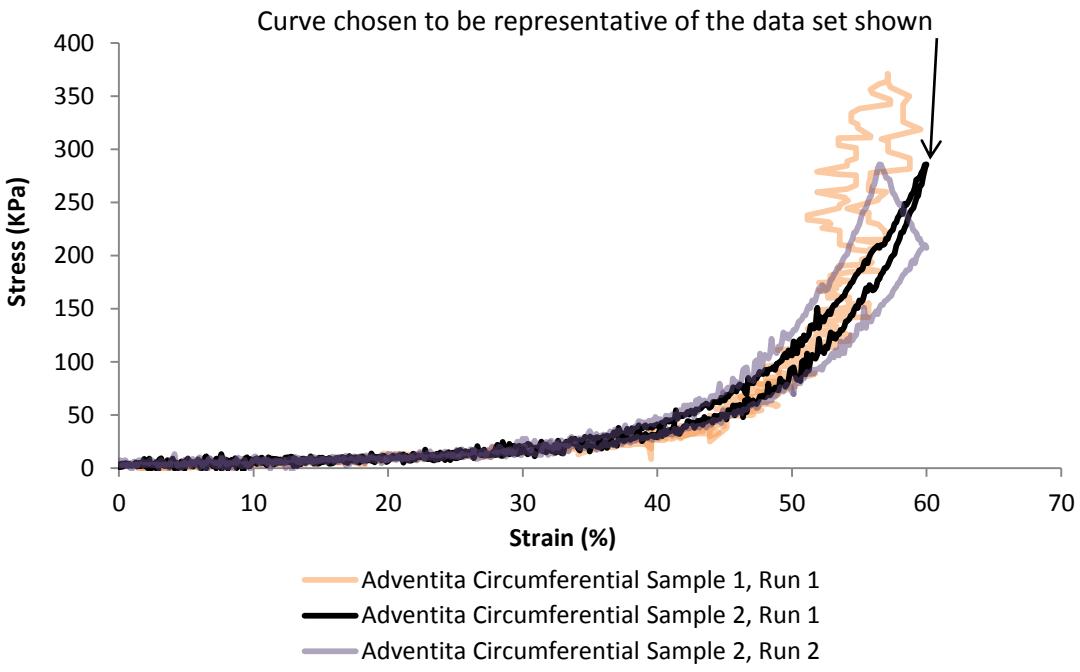
Figure Appendix 3.6: **Results obtained for the two samples harvested in the circumferential direction from the artery's adventitial layer. The representative curve chosen was the one least subject to scatter.**

Specimen 2

In total, twelve test samples were harvested from individual arterial layers, with stress-strain results shown below in figure Appendix 3.7 through to 3.12.
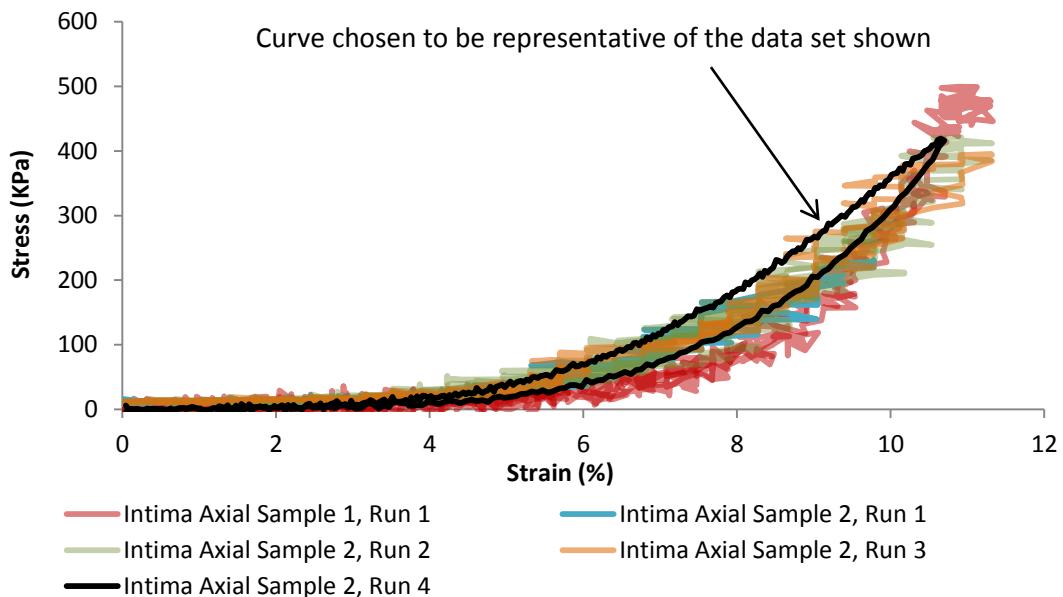

Figure Appendix 3.7: **Results obtained for the two samples harvested in the axial direction from the artery's intimal layer. The representative curve chosen was the one least subject to scatter.**
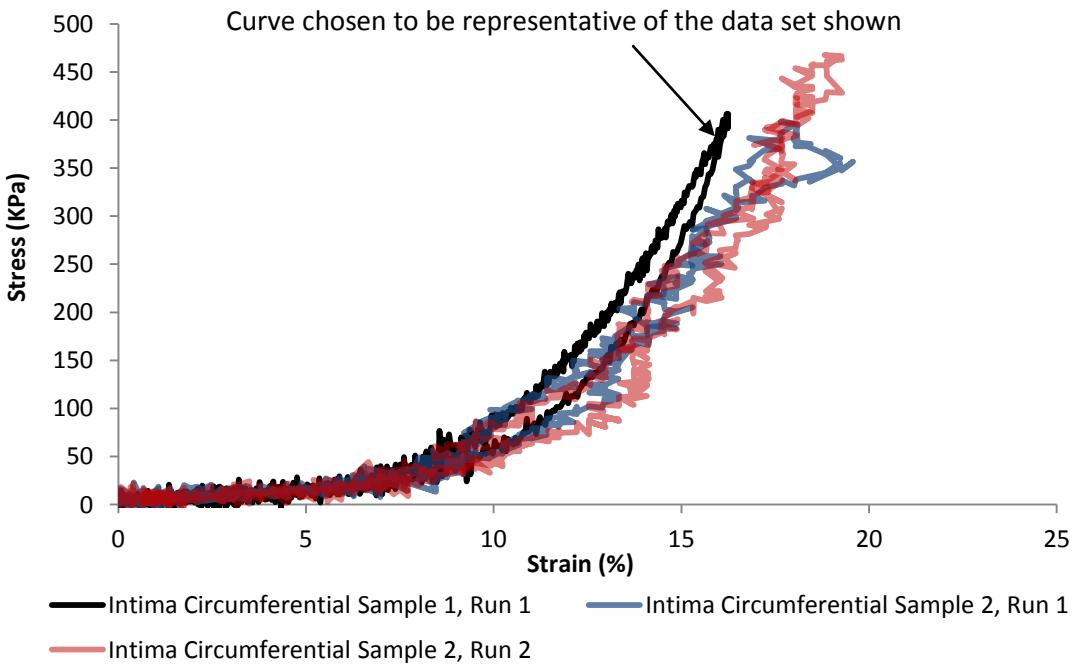
Figure Appendix 3.8: **Results obtained for the two samples harvested in the circumferential direction from the artery's intimal layer. The representative curve chosen was the one least subject to scatter.**
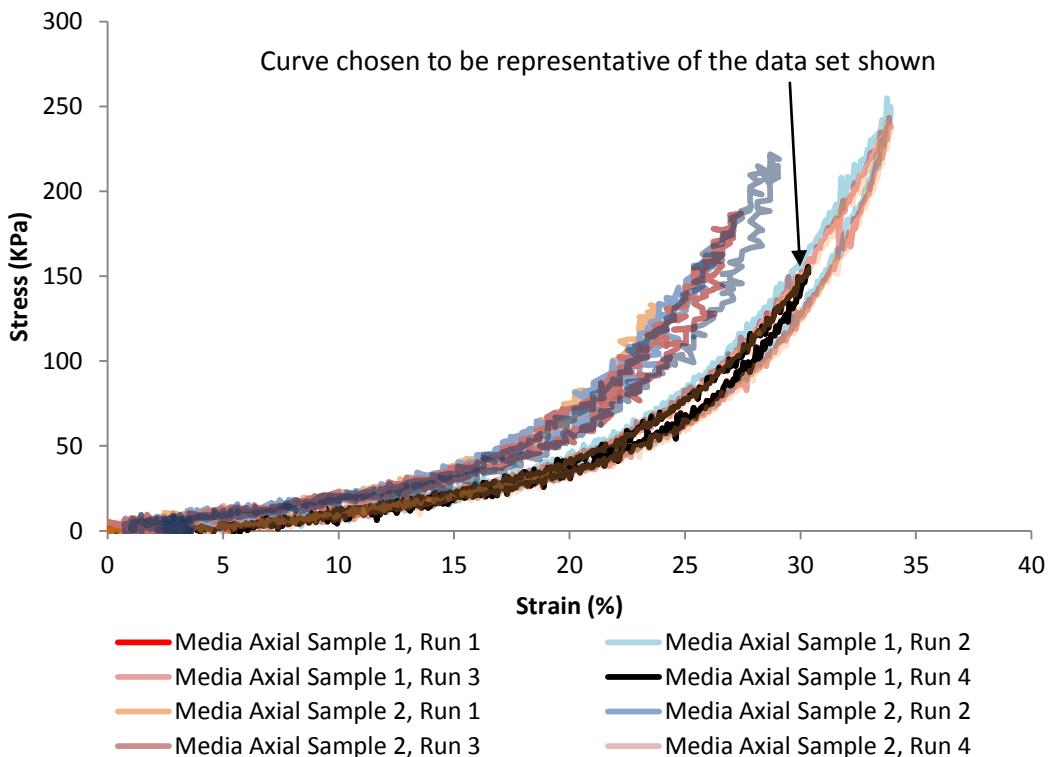

Figure Appendix 3.9: **Results obtained for the two samples harvested in the axial direction from the artery's medial layer. The representative curve chosen was the data set which was least subject to scatter, and represented the specimen in its most trained state.**
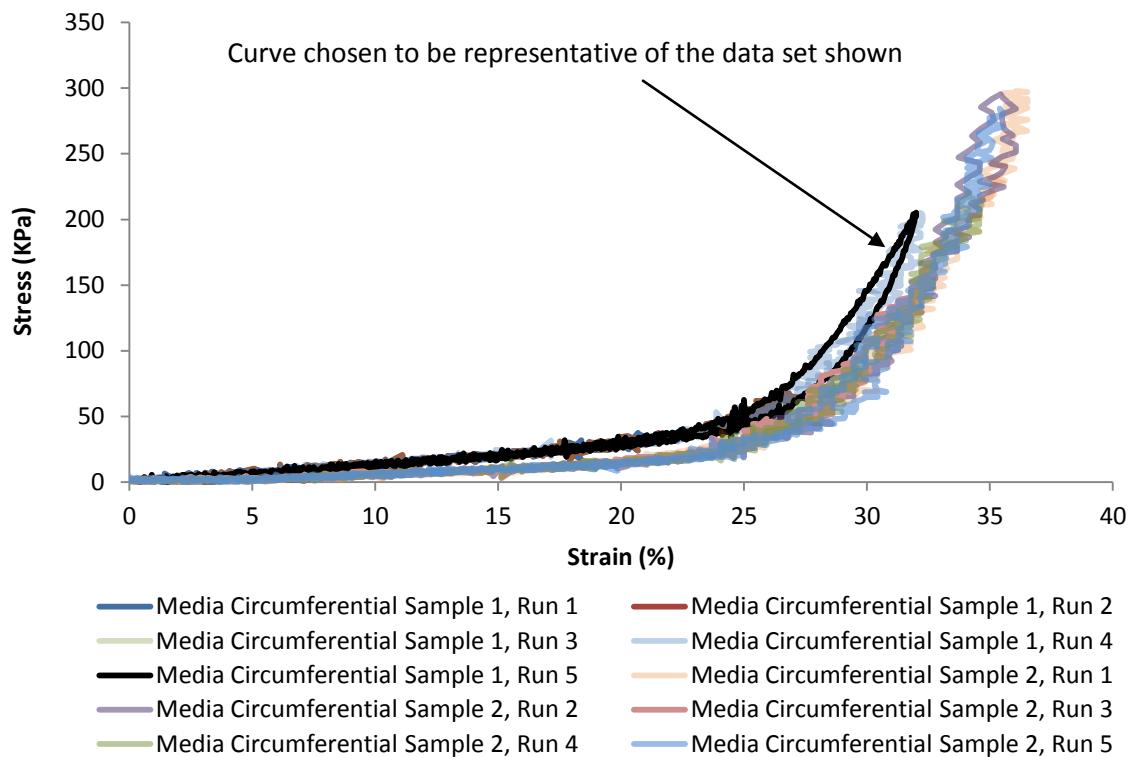
Figure Appendix 3.10: **Results obtained for the two samples harvested in the circumferential direction from the artery's medial layer. The representative curve chosen was the data set which was least subject to scatter, and represented the specimen in its most trained state.**
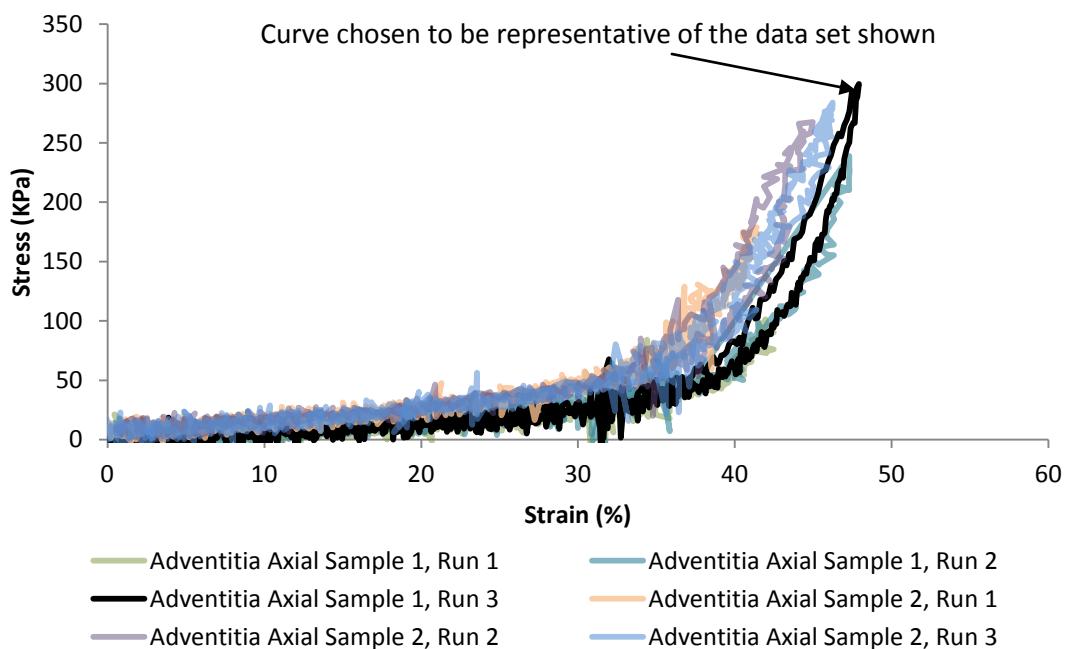

Figure Appendix 3.11: **Results obtained for the two samples harvested in the axial direction from the artery's adventitial layer. The representative curve chosen was the data set which was least subject to scatter and experienced maximum extension.**

211
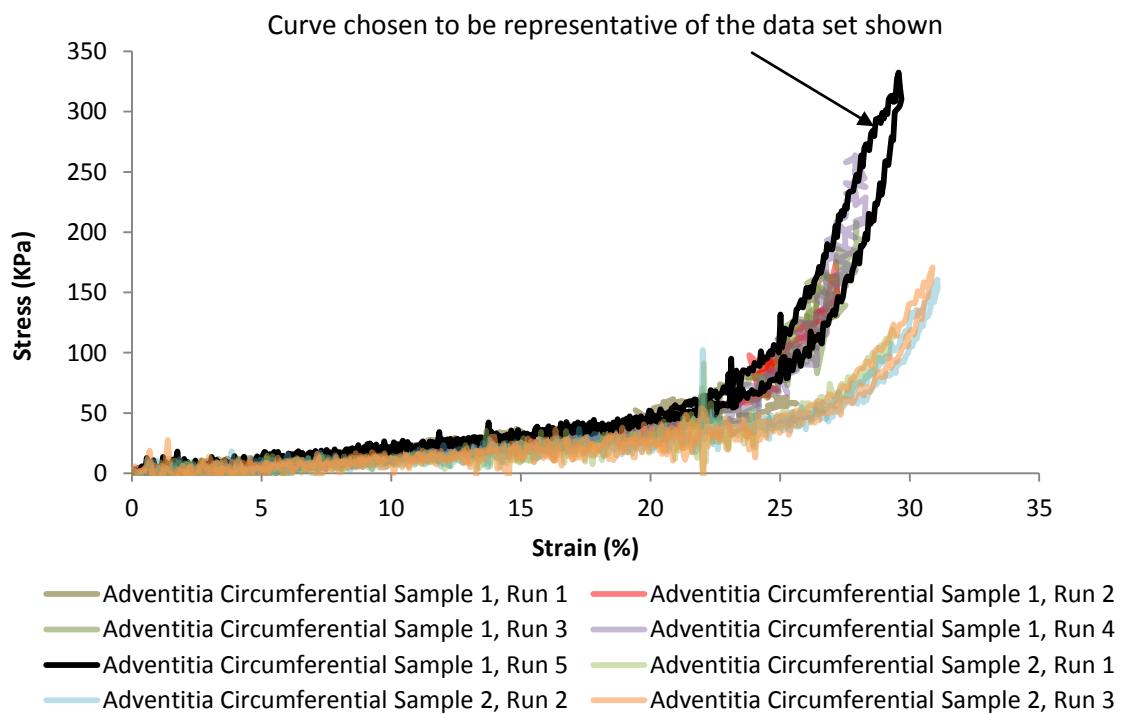
Figure Appendix 3.12: **Results obtained for the two samples harvested in the circumferential direction from the artery's adventitial layer. The representative curve chosen was the data set subject to least scatter and in the most trained state.**

Specimen 3

In total, eleven test samples were harvested from individual arterial layers, with stress-strain results shown below in figure Appendix 3.13 through to 3.18.
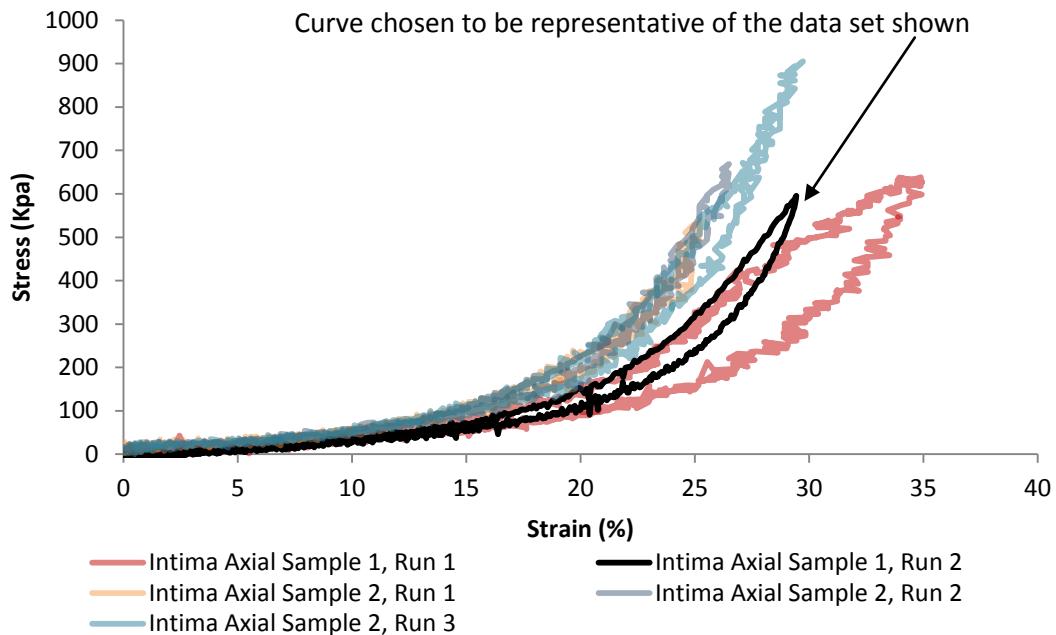

Figure Appendix 3.13: **Results obtained for the two samples harvested in the axial direction from the artery's intimal layer. The representative curve chosen was the data set subject to least scatter, and enveloped by other curves.**
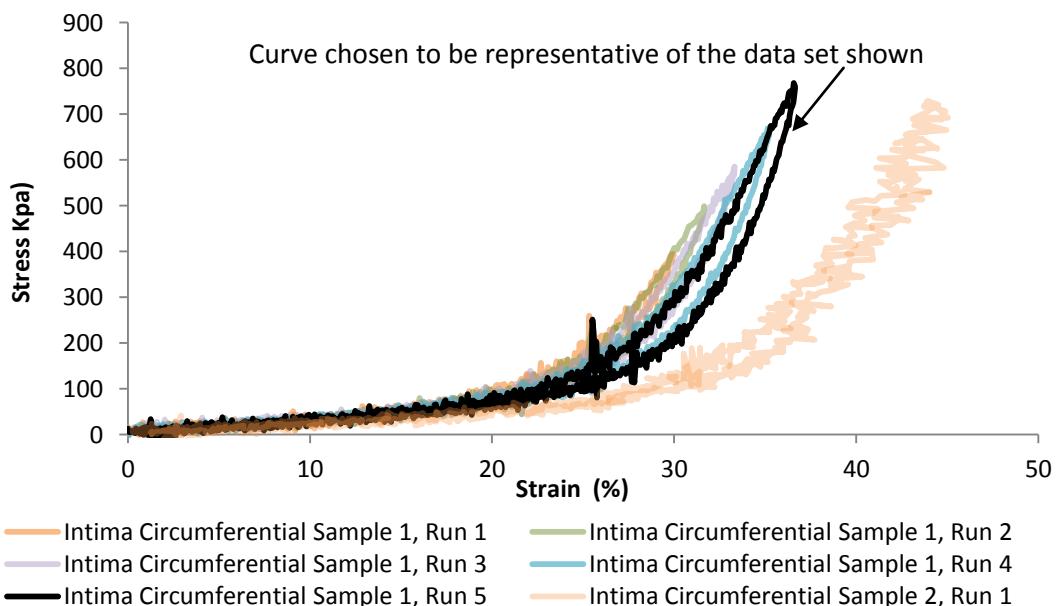

Figure Appendix 3.14: **Results obtained for the two samples harvested in the circumferential direction from the artery's intimal layer. The representative curve chosen was the curve from the most trained specimen, experiencing maximum extension.**
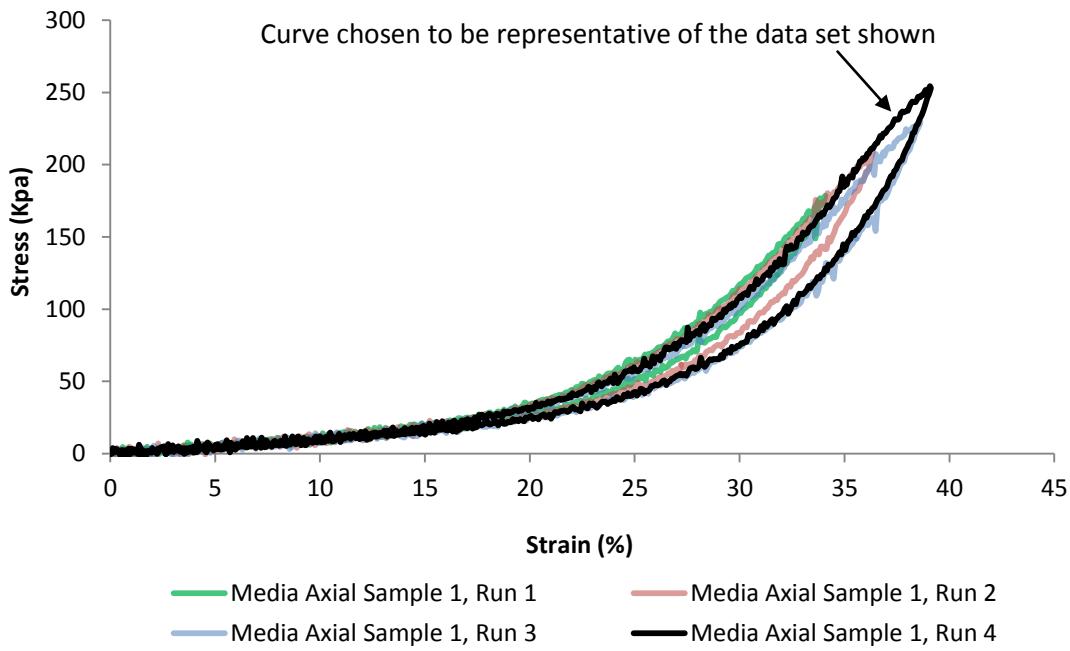
Figure Appendix 3.15: **Results obtained for the one sample harvested in the axial direction from the artery's medial layer. The representative curve chosen was the curve from the most trained specimen, experiencing maximum extension.**
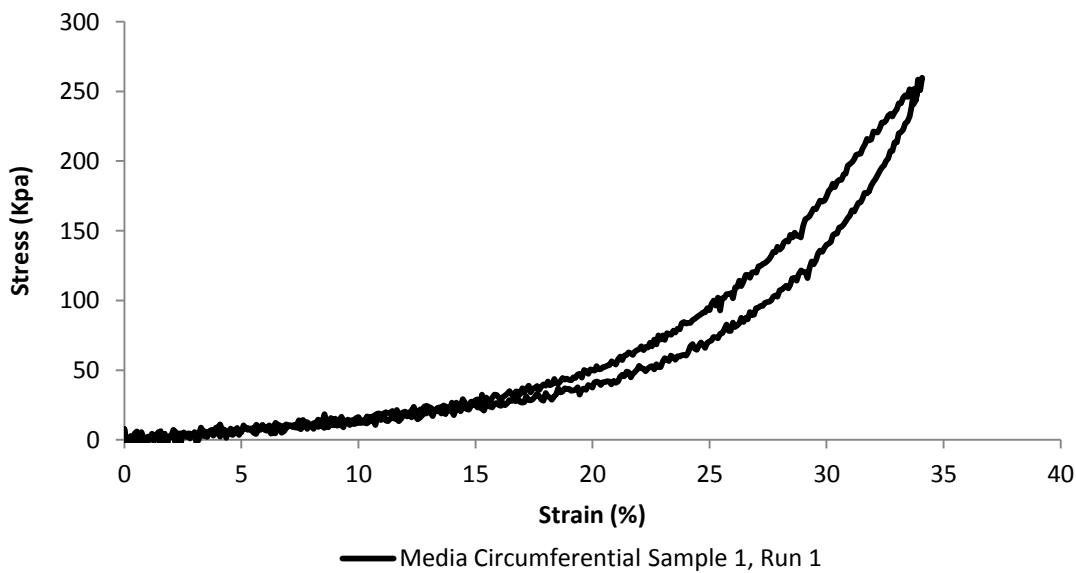

Figure Appendix 3.16: **Results obtained for the one sample harvested in the circumferential direction from the artery's medial layer. Only one successful run from this sample could be achieved (post training).**
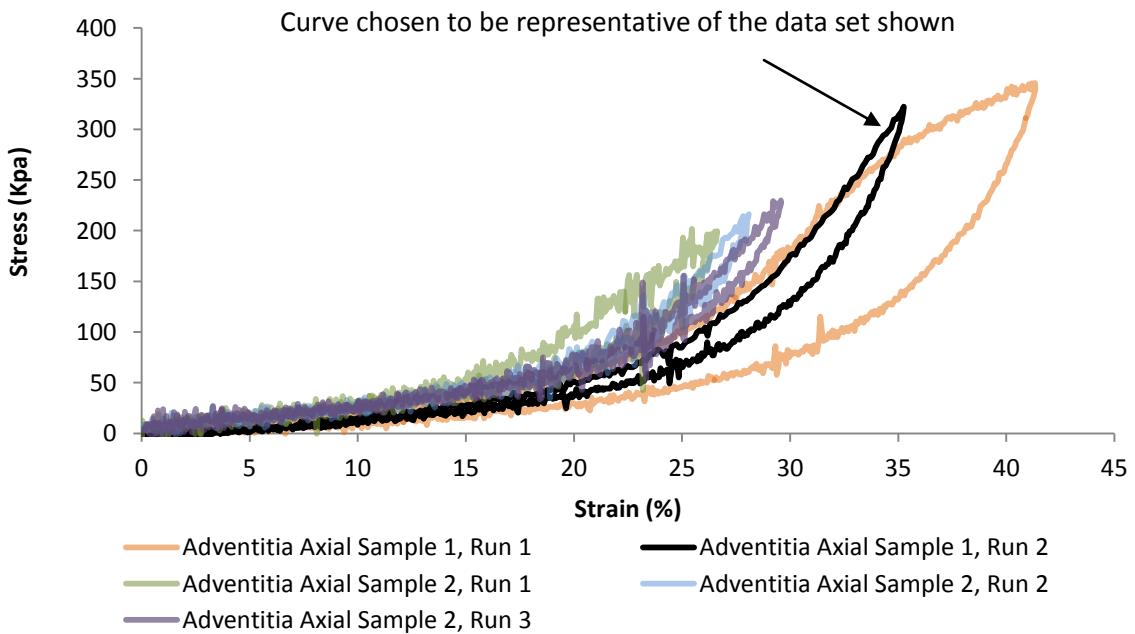
Figure Appendix 3.17: **Results obtained for the two samples harvested in the axial direction from the artery's adventitial layer. The representative curve chosen was the curve experiencing maximum extension and least subject to erroneous data points.**
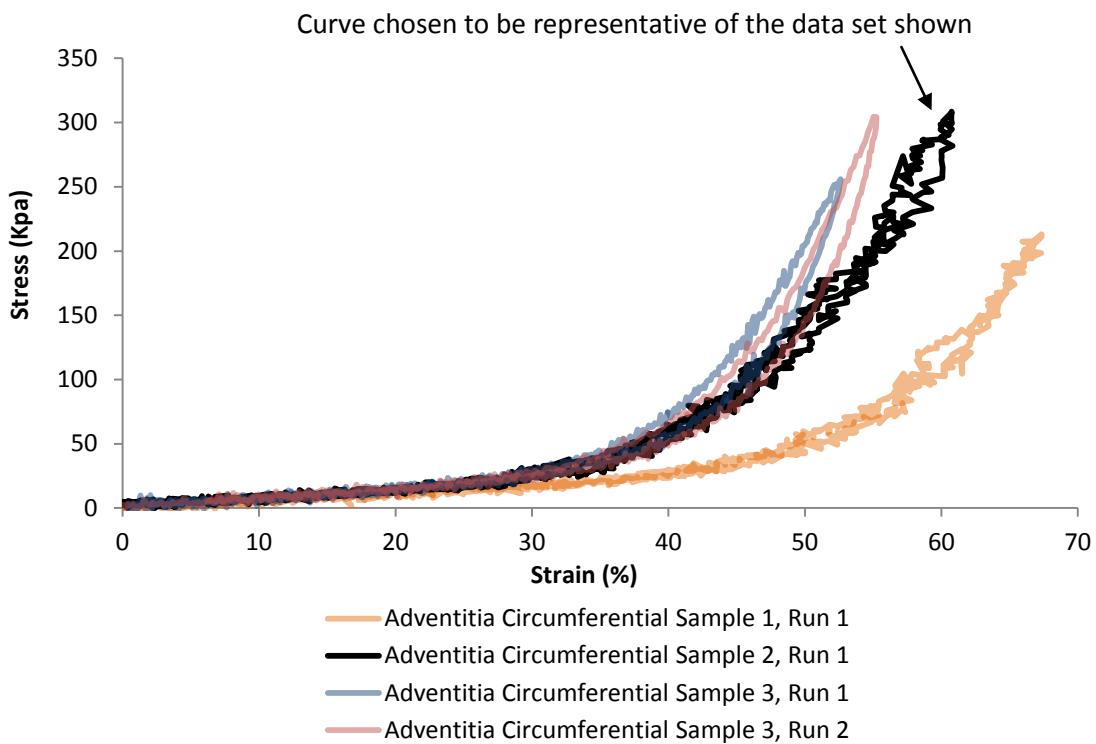

Figure Appendix 3.18: **Results obtained for the three samples harvested in the circumferential direction from the artery's adventitial layer. Sample 2 was chosen to be representative as its data curve was enveloped by the curves obtained for both sample 1 and 3.**
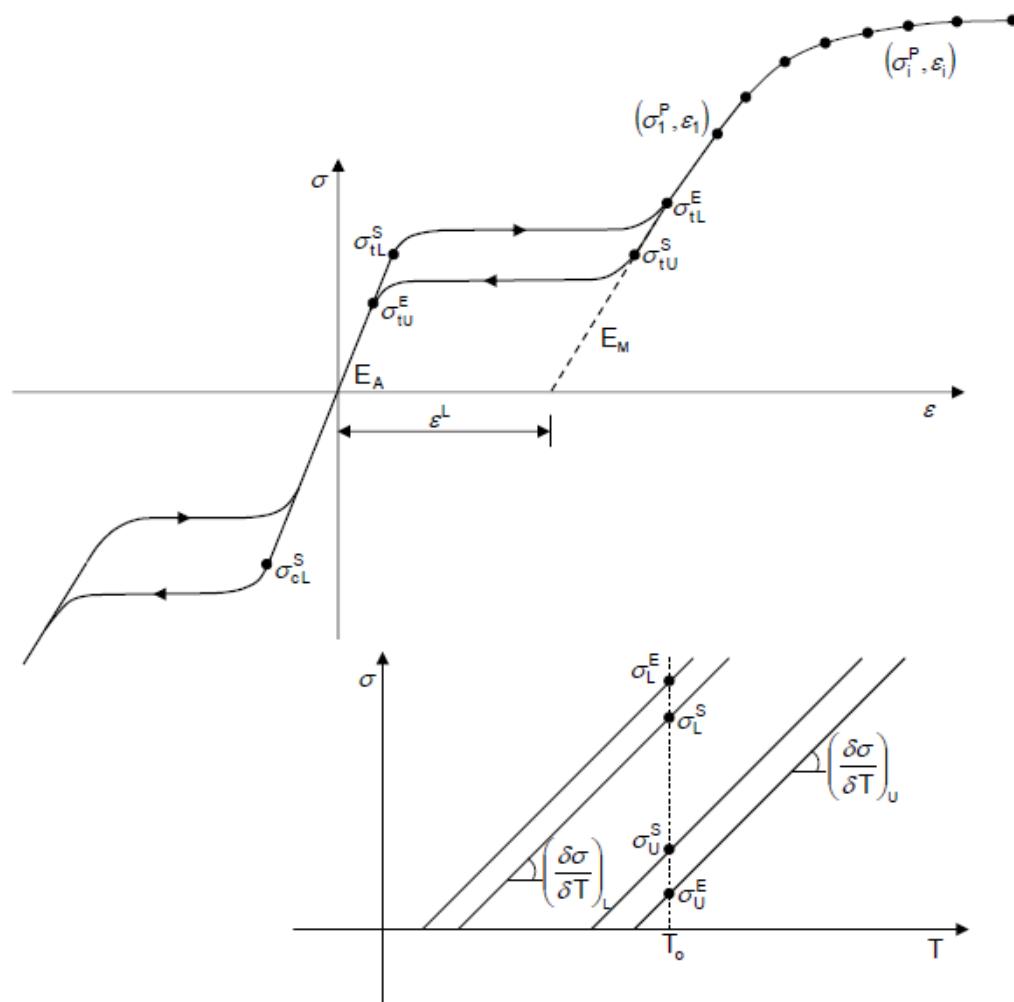
Appendix 4 - Determination of Nitinol material parameters

This section details the process by which Auricchio Nitinol material parameters can be derived from uniaxial stress-strain data.

UMAT for Superelasticity and Plasticity of Shape Memory Alloys

Superelastic-plastic behavior is based on the uniaxial behavior shown here:

Usage

Superelastic only behavior

```
*MATERIAL, NAME=name
*USER MATERIAL, CONSTANTS=15 + N_A
```

$$E_A,\ v_A,\ E_M,\ v_M,\ \varepsilon^L,\ \left(\dfrac{\delta\sigma}{\delta T}\right)_L,\ \sigma_L^S,\ \sigma_L^E$$

$$T_0,\ \left(\dfrac{\delta\sigma}{\delta T}\right)_U,\ \sigma_U^S,\ \sigma_U^E,\ \sigma_{CL}^S,\ \varepsilon_V^L,\ N_A,\ N_{S1},\ ...N_{SNA}$$

```
*DEPVAR
 24,
```

Superelastic-plastic behavior

```
*MATERIAL, NAME=name
*USER MATERIAL, CONSTANTS=16 + N_A + 2N_P
```

$$E_A,\ v_A,\ E_M,\ v_M,\ \varepsilon^L,\ \left(\dfrac{\delta\sigma}{\delta T}\right)_L,\ \sigma_L^S,\ \sigma_L^E$$

$$T_0,\ \left(\dfrac{\delta\sigma}{\delta T}\right)_U,\ \sigma_U^S,\ \sigma_U^E,\ \sigma_{CL}^S,\ \varepsilon_V^L,\ N_A,\ N_{S1},\ ...N_{SNA},\ N_P,\ \sigma_1^P,\ \varepsilon_1...\sigma_{NP}^P,\ \varepsilon_{NP}\ \textit{(8 values per line)}$$

```
*DEPVAR
```


Input to Superelasticity UMAT

|	
E_A	Austenite elasticity
v_A	Austenite Poisson's ratio
E_M	Martensite elasticity
v_M	Martensite Poisson's ratio
ε^L	Transformation strain
$\left(\dfrac{\delta\sigma}{\delta T}\right)_L$	$\delta\sigma/\delta T$ loading
σ_L^S	Start of transformation loading
σ_L^E	End of transformation loading
T_0	Reference temperature
$\left(\dfrac{\delta\sigma}{\delta T}\right)_U$	$\delta\sigma/\delta T$ unloading
σ_U^S	Start of transformation unloading
σ_U^E	End of transformation unloading
σ_{CL}^S	Start of transformation stress during loading in compression, as a positive value
ε_V^L	Volumetric transformation strain. If $\varepsilon_V^L = \varepsilon^L$, an associated flow algorithm is used, with ε_V^L computed based on σ_L^S and σ_{CL}^S. For all other cases, a nonassociated flow algorithm is used, which produces an unsymmetric Jacobian matrix. The USYMM parameter is thus required on the *USER MATERIAL keyword
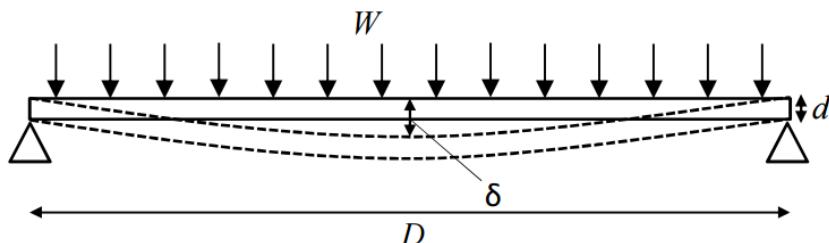
Appendix 5 – Lutz number equation derivation

The Lutz number is an assessment of ring stiffness. It was first proposed by Dr Karl-Lutz Lauterjung, inventor of the Anaconda ring stent design. Since its development, the Lutz number has been used by Terumo Vascutek as a key design parameter. Through adopting the parameter into this thesis, a method was established by which the rings used within the vascular testing programme (chapter 3) could be related to those used by Vascutek within the Anaconda device.

Here, a derivation for the Lutz number is provided, as proposed by Dr William Dempster from the University of Strathclyde. Although, fundamentally, the method relies on linear elastic beam bending theory, it is seen as reasonable approach to broadly define the stiffness of rings.

Within the derivation, the aim is to relate 'Ring Stiffness' to Ring diameter, D and wire diameter, d.

Consider a fine wire ring, approximated as being a simply supported beam with an evenly distributed load.

Where   W = Total Load

        D = Ring Diameter (approximated as beam length)

        d = Wire Diameter

        δ = Deflection

From beam bending theory, deflections for the configuration shown is given by

$$\delta = \frac{5WD^3}{384EI}$$

The beam stiffness, K, can then be defined as follows

$$K = \frac{W}{\delta} = \frac{384EI}{5\,D^3}$$

This relationship is limited to small deflections and the given boundary conditions. However, in general, the stiffness K can be approximated to be a function of parameters E, I and D, independent of boundary conditions and degrees of freedom as follows

$$K = F^n\left(\frac{EI}{D^3}\right)$$

Given that for a circular cross section, I, can be expressed as $I = \frac{\pi d^4}{64}$ then

$$K = F^n\left(\frac{Ed^4}{D^3}\right)$$

From this is can be seen that the stiffness K, is in general, dependent on the parameter group, $\frac{Ed^4}{D^3}$

For a given ring constructed from Nitinol wire of elastic modulus E

$$K \sim \left(\frac{d^4}{D^3}\right)$$

Finally, the combined stiffness for a bundle of wires, with a number of turns ,N can be expressed as

$$K \sim N\left(\frac{d^4}{D^3}\right)$$

Comparing this with equation 3.2, page 59, it can be seen that the stiffness K above is equivalent to the Lutz number of the ring.

Appendix 6 - Python scripts

This section provides the final python scripts as developed for the integrated modelling framework (figure 4.15). Annotations are provided for description. Further details around the operation and structure of these scripts can be found in chapter 4.

Appendix 6.1 - Parameter file

```
# Define Wire Constants
# Ring diameter is defined
rd = 25.0
# Wire diameter is defined
wd = 0.18
# Ring radius is calculated
rr = rd/2
# Wire radius is calculated
wr = wd/2
l = (pi/2)*(rr)
#Derived constants
# this file makes the vessel and also applies the contact conditions.
# Vod= vessel outside diameter, Vt vessel Thickness, Vl= vessel Length
Vod = 26.0
Vt = 1.00
Vl =45
# Derived Properties
Vor =  Vod/2
Vir = Vod/2-Vt
```

Base parameters are established for the analysis

```
# -*- coding: mbcs -*-, Abaqus python library imports,
# within this coding clock, python library imports are performed
# this enables Abaqus to interpret python commands.
from part import *
from material import *
from section import *
from assembly import *
from step import *
from interaction import *
from load import *
from mesh import *
```

Python libraries are called

```
from job import *
from sketch import *
from visualization import *
from connectorBehavior import *
import regionToolset
import datetime
from datetime import *
import math
```

Appendix 6.2 - Continuum element wire script

```
# The cross section is sketched as a 2D plane.
mdb.models['Model-1'].ConstrainedSketch(name='__profile__', sheetSize=200.0)
mdb.models['Model-
1'].sketches['__profile__'].CircleByCenterPerimeter(center=(0.0,    0.0),    point1=(0,
wr))

# The 2D plane is extruded into a wire strand
mdb.models['Model-1'].Part(dimensionality=THREE_D, name='Wire', type=
    DEFORMABLE_BODY)
mdb.models['Model-1'].parts['Wire'].BaseSolidExtrude(depth=l, sketch=
    mdb.models['Model-1'].sketches['__profile__'])
del mdb.models['Model-1'].sketches['__profile__']

# Datum planes are created for to assist the application
# of boundary conditions and meshing procedures
mdb.models['Model-1'].parts['Wire'].DatumPlaneByPrincipalPlane(offset=0.0,
    principalPlane=XYPLANE)
mdb.models['Model-1'].parts['Wire'].DatumPlaneByPrincipalPlane(offset=0.0,
    principalPlane=YZPLANE)
mdb.models['Model-1'].parts['Wire'].DatumPlaneByPrincipalPlane(offset=0.0,
    principalPlane=XZPLANE)
```

The wire model is created

```
# The wire is sectioned through partitions
mdb.models['Model-1'].parts['Wire'].PartitionCellByDatumPlane(cells=
    mdb.models['Model-1'].parts['Wire'].cells.getSequenceFromMask(('[#1 ]', ),
    ), datumPlane=mdb.models['Model-1'].parts['Wire'].datums[3])
```

The wire model is sectioned

```
mdb.models['Model-1'].parts['Wire'].PartitionCellByDatumPlane(cells=
    mdb.models['Model-1'].parts['Wire'].cells.getSequenceFromMask(('[#3 ]', ),
    ), datumPlane=mdb.models['Model-1'].parts['Wire'].datums[4])


# Materials are created, the first of which is a linear elastic model
#mdb.models['Model-1'].Material(name='simpleelastic')
#mdb.models['Model-1'].materials['simpleelastic'].Elastic(table=((30000000.0,
    #0.3), ))

#Superelastic Nitinol is defined
mdb.models['Model-1'].Material(name='ABQ_SUPER_ELASTIC_1')
mdb.models['Model-1'].materials['ABQ_SUPER_ELASTIC_1'].Depvar(n=24)
##mdb.models['Model-1'].materials['ABQ_SUPER_ELASTIC_1'].UserMaterial(
##    mechanicalConstants=(65800.0, 0.435, 39700.0, 0.435, 0.0538, 5.74, 637,
##    657, 0, 6.99, 327, 307, 853, 0.0538, 0.0))

mdb.models['Model-1'].materials['ABQ_SUPER_ELASTIC_1'].UserMaterial(
    mechanicalConstants=(65800.0, 0.435, 39700.0, 0.435, 0.0538, 5.74, 637,
    657, 0, 6.99, 327, 307, 0, 0.0538, 0.0))


# Model sections are associated with material properties
mdb.models['Model-
1'].HomogeneousSolidSection(material='ABQ_SUPER_ELASTIC_1', name=
    'wire', thickness=None)


# Assign section to part
mdb.models['Model-1'].parts['Wire'].SectionAssignment(offset=0.0, offsetField=
    '', offsetType=MIDDLE_SURFACE, region=Region(
    cells=mdb.models['Model-1'].parts['Wire'].cells.getSequenceFromMask(mask=(
    '[#f ]', ), )), sectionName='wire', thicknessAssignment=FROM_SECTION)


# A wire instance is imported and orientated
mdb.models['Model-1'].rootAssembly.DatumCsysByDefault(CARTESIAN)
mdb.models['Model-1'].rootAssembly.Instance(dependent=OFF,        name='Wire-1',
part=
    mdb.models['Model-1'].parts['Wire'])
```

Materials are defined

Wire sections are defined

Wire sections are defined

```
# rotate and move instance
mdb.models['Model-1'].rootAssembly.rotate(angle=-90.0, axisDirection=(10.0,
    0.0, 0.0), axisPoint=(0.0, 0.0, 0.0), instanceList=('Wire-1', ))
mdb.models['Model-1'].rootAssembly.translate(instanceList=('Wire-1', ), vector=
    (0.0, -l/2, 0.0))
mdb.models['Model-1'].rootAssembly.rotate(angle=45.0, axisDirection=(0.0, 0.0,
    10.0), axisPoint=(0.0, 0.0, 0.0), instanceList=('Wire-1', ))
mdb.models['Model-1'].rootAssembly.translate(instanceList=('Wire-1', ), vector=
    (rr*cos(pi/4), rr*sin(pi/4), 0.0))


# Instance seed is provided (nodal positions along an edge)
mdb.models['Model-1'].rootAssembly.seedEdgeByNumber(constraint=FINER,
edges=
    mdb.models['Model-1'].rootAssembly.instances['Wire-
1'].edges.getSequenceFromMask(
    ('[#101a00 ]', ), ), number=2)
#mesh instance


# Model mesh properties are defined
mdb.models['Model-1'].rootAssembly.setElementType(elemTypes=(ElemType(
    elemCode=C3D20R, elemLibrary=STANDARD), ElemType(elemCode=C3D15,
    elemLibrary=STANDARD),                      ElemType(elemCode=C3D10,
elemLibrary=STANDARD)),
    regions=(
    mdb.models['Model-1'].rootAssembly.instances['Wire-
1'].cells.getSequenceFromMask(
    ('[#f ]', ), ), ))


mdb.models['Model-1'].rootAssembly.generateMesh(regions=(
    mdb.models['Model-1'].rootAssembly.instances['Wire-1'], ))


# Local coordinate system at the geometry centre of the wire is defined.
# This coordinate is used for the application of boundary conditions
# and post processing scripts
mdb.models['Model-1'].rootAssembly.DatumCsysByThreePoints(coordSysType=
    CARTESIAN, name='Datum csys-3', origin=
    mdb.models['Model-1'].rootAssembly.instances['Wire-1'].InterestingPoint(
    mdb.models['Model-1'].rootAssembly.instances['Wire-1'].edges[0], MIDDLE),
    point1=mdb.models['Model-1'].rootAssembly.instances['Wire-1'].vertices[1],
    point2=mdb.models['Model-1'].rootAssembly.instances['Wire-1'].vertices[9])
```

Model assembly is created

Model is seeded

Model is meshed

Additional coordinate system is defined

```
# A single BC is applied at a node coinciding with the
# geometric centre of the wire

mdb.models['Model-1'].DisplacementBC(amplitude=UNSET,
createStepName='Initial',
    distributionType=UNIFORM, fieldName='', localCsys=None, name='HoldWireZ',
    region=Region(
    vertices=mdb.models['Model-1'].rootAssembly.instances['Wire-
1'].vertices.getSequenceFromMask(
    mask=('[#2 ]', ), )), u1=UNSET, u2=UNSET, u3=SET, ur1=UNSET, ur2=UNSET,
    ur3=UNSET)
```

```
# Surfaces are created to enable contact definitions
mdb.models['Model-1'].parts['Wire'].Surface(name='WireSurf', side1Faces=
    mdb.models['Model-1'].parts['Wire'].faces.getSequenceFromMask(('[#3014 ]',
    ), ))
```

Appendix 6.3 - Beam element wire script

```
# 2D wire cross section is sketched
mdb.models['Model-1'].ConstrainedSketch(name='__profile__', sheetSize=200.0)
mdb.models['Model-1'].sketches['__profile__'].Line(point1=(0.0, 0.0), point2=(
    l, 0.0))
mdb.models['Model-1'].sketches['__profile__'].HorizontalConstraint(
    addUndoState=False, entity=
    mdb.models['Model-1'].sketches['__profile__'].geometry[2])
```

```
# create part
mdb.models['Model-1'].Part(dimensionality=THREE_D, name='Wire', type=
    DEFORMABLE_BODY)
mdb.models['Model-1'].parts['Wire'].BaseWire(sketch=
    mdb.models['Model-1'].sketches['__profile__'])
#delete sketch
del mdb.models['Model-1'].sketches['__profile__']
```

```
# create material
mdb.models['Model-1'].Material(name='ABQ_SUPER_ELASTIC_1')
mdb.models['Model-1'].materials['ABQ_SUPER_ELASTIC_1'].Depvar(n=24)
mdb.models['Model-1'].materials['ABQ_SUPER_ELASTIC_1'].UserMaterial(
    mechanicalConstants=(65800.0, 0.3, 60000.0, 0.3, 0.05843, 1e-06, 567.34,
    574.54, 22.0, 1e-05, 268.28, 259.92, 0.0, 0.05843, 0.0))
```

```
# create profile
mdb.models['Model-1'].CircularProfile(name='Profile-1', r=wr)
#create section
mdb.models['Model-1'].BeamSection(integration=DURING_ANALYSIS, material=
    'ABQ_SUPER_ELASTIC_1', name='WireSection', poissonRatio=0.3, profile=
    'Profile-1', temperatureVar=LINEAR)
```

```
#assign orrientation
mdb.models['Model-1'].parts['Wire'].MaterialOrientation(additionalRotationType=
    ROTATION_NONE, axis=AXIS_1, fieldName='', localCsys=None, orientationType=
    GLOBAL, region=Region(
    edges=mdb.models['Model-
1'].parts['Wire'].edges.getSequenceFromMask(mask=(
    '[#1 ]', ), )), stackDirection=STACK_3)

mdb.models['Model-1'].parts['Wire'].assignBeamSectionOrientation(method=
    N1_COSINES, n1=(0.0, 0.0, -1.0), region=Region(
    edges=mdb.models['Model-
1'].parts['Wire'].edges.getSequenceFromMask(mask=(
    '[#1 ]', ), )))
```

```
#assign section
mdb.models['Model-1'].parts['Wire'].SectionAssignment(offset=0.0, offsetField=
    '', offsetType=MIDDLE_SURFACE, region=Region(
    edges=mdb.models['Model-
1'].parts['Wire'].edges.getSequenceFromMask(mask=(
    '[#1 ]', ), )), sectionName='WireSection', thicknessAssignment=
    FROM_SECTION)
```

```
#create instance
mdb.models['Model-1'].rootAssembly.DatumCsysByDefault(CARTESIAN)
mdb.models['Model-1'].rootAssembly.Instance(dependent=OFF,        name='Wire-1',
part=
    mdb.models['Model-1'].parts['Wire'])
```

```
# rotate and move instance
mdb.models['Model-1'].rootAssembly.translate(instanceList=('Wire-1', ), vector=
    (-l/2, 0.0, 0.0))
mdb.models['Model-1'].rootAssembly.rotate(angle=-45.0, axisDirection=(0.0,
    0.0, 1.0), axisPoint=(0.0, 0.0, 0.0), instanceList=('Wire-1', ))
mdb.models['Model-1'].rootAssembly.translate(instanceList=('Wire-1', ), vector=
    (rr*cos(pi/4), rr*sin(pi/4), 0.0))
```

```
#seed instance
mdb.models['Model-1'].rootAssembly.seedEdgeByBias(biasMethod=DOUBLE,
    constraint=FINER, endEdges=
    mdb.models['Model-1'].rootAssembly.instances['Wire-
1'].edges.getSequenceFromMask(
    ('[#1 ]', ), ), maxSize=0.20, minSize=0.02)
```

```
#chose element type
mdb.models['Model-1'].rootAssembly.setElementType(elemTypes=(ElemType(
    elemCode=B32H, elemLibrary=STANDARD), ), regions=(
    mdb.models['Model-1'].rootAssembly.instances['Wire-
1'].edges.getSequenceFromMask(
    ('[#1 ]', ), ), ))
#generate mesh
mdb.models['Model-1'].rootAssembly.generateMesh(regions=(
    mdb.models['Model-1'].rootAssembly.instances['Wire-1'], ))
```

```
# specify transverse shear stifness remember contains area calculation
mdb.models['Model-1'].sections['WireSection'].setValues(poissonRatio=0.3)
mdb.models['Model-1'].sections['WireSection'].TransverseShearBeam(k13=5636.7,
    k23=5636.7, scfDefinition=ANALYSIS_DEFAULT)
```

Appendix 6.4 - Holzapfel vessel script

```
Vod = 30.6
Vt = 3.0
Vl =45
# Derived Properties
Vor =  Vod/2
Vir = Vod/2-Vt
# Intimae/media/advetitia ratios
Ratio=[38.0,48.0,19.0]
Ithick=Ratio[0]/(Ratio[1]+Ratio[0]+Ratio[2])*Vt
Mthick=Ratio[1]/(Ratio[1]+Ratio[0]+Ratio[2])*Vt
Athick=Ratio[2]/(Ratio[1]+Ratio[0]+Ratio[2])*Vt
```

```
mdb.models['Model-1'].ConstrainedSketch(name='__profile__', sheetSize=200.0)
mdb.models['Model-1'].sketches['__profile__'].ArcByCenterEnds(center=(0.0, 0.0)
    , direction=CLOCKWISE, point1=(0.0, Vir), point2=(Vir, 0.0))
mdb.models['Model-1'].sketches['__profile__'].ArcByCenterEnds(center=(0.0, 0.0)
    , direction=CLOCKWISE, point1=(0.0, Vor), point2=(Vor, 0.0))
mdb.models['Model-1'].sketches['__profile__'].Line(point1=(0.0, Vor), point2=(
    0.0, Vir))
mdb.models['Model-1'].sketches['__profile__'].Line(point1=(Vor, 0.0), point2=(
    Vir, 0.0))
mdb.models['Model-1'].Part(dimensionality=THREE_D, name='Vessel', type=
    DEFORMABLE_BODY)
mdb.models['Model-1'].parts['Vessel'].BaseSolidExtrude(depth=Vl, sketch=
    mdb.models['Model-1'].sketches['__profile__'])
del mdb.models['Model-1'].sketches['__profile__']
```

```
# Partion face
mdb.models['Model-1'].ConstrainedSketch(gridSpacing=2.49, name='__profile__',
    sheetSize=99.86, transform=
    mdb.models['Model-1'].parts['Vessel'].MakeSketchTransform(
    sketchPlane=mdb.models['Model-1'].parts['Vessel'].faces[4],
    sketchPlaneSide=SIDE1,
    sketchUpEdge=mdb.models['Model-1'].parts['Vessel'].edges[10],
    sketchOrientation=LEFT, origin=(0.0, 0.0, Vl)))
mdb.models['Model-1'].parts['Vessel'].projectReferencesOntoSketch(filter=
    COPLANAR_EDGES, sketch=mdb.models['Model-1'].sketches['__profile__'])
mdb.models['Model-1'].sketches['__profile__'].CircleByCenterPerimeter(center=(
    0.0, 0.0), point1=(Vir+Ithick, 0.0))
mdb.models['Model-1'].sketches['__profile__'].CoincidentConstraint(
    addUndoState=False, entity1=
    mdb.models['Model-1'].sketches['__profile__'].vertices[5], entity2=
    mdb.models['Model-1'].sketches['__profile__'].geometry[3])
mdb.models['Model-1'].sketches['__profile__'].CircleByCenterPerimeter(center=(
    0.0, 0.0), point1=(Vir+Mthick+Ithick, 0.0))
mdb.models['Model-1'].sketches['__profile__'].CoincidentConstraint(
    addUndoState=False, entity1=
    mdb.models['Model-1'].sketches['__profile__'].vertices[6], entity2=
    mdb.models['Model-1'].sketches['__profile__'].geometry[3])
mdb.models['Model-1'].parts['Vessel'].PartitionFaceBySketch(faces=
    mdb.models['Model-1'].parts['Vessel'].faces.getSequenceFromMask(('[#10 ]',
    ), ), sketch=mdb.models['Model-1'].sketches['__profile__'],
    sketchOrientation=LEFT, sketchUpEdge=
    mdb.models['Model-1'].parts['Vessel'].edges[10])
del mdb.models['Model-1'].sketches['__profile__']
```

Vessel is partitioned to create the 3 discrete regions for the intima, media and adventitia

```
#Create Partition
mdb.models['Model-1'].parts['Vessel'].PartitionCellByExtrudeEdge(cells=
    mdb.models['Model-1'].parts['Vessel'].cells.getSequenceFromMask(('[#1 ]',
    ), ), edges=(mdb.models['Model-1'].parts['Vessel'].edges[4], ), line=
    mdb.models['Model-1'].parts['Vessel'].edges[14], sense=REVERSE)
mdb.models['Model-1'].parts['Vessel'].PartitionCellBySweepEdge(cells=
    mdb.models['Model-1'].parts['Vessel'].cells.getSequenceFromMask(('[#2 ]',
    ), ), edges=(mdb.models['Model-1'].parts['Vessel'].edges[13], ), sweepPath=
    mdb.models['Model-1'].parts['Vessel'].edges[21])
```

Partitioning continues

```
#create material
mdb.models['Model-1'].Material(name='simpleelastic')
mdb.models['Model-1'].materials['simpleelastic'].Elastic(table=((100000.0,
    0.3), ))
mdb.models['Model-1'].Material(name='Intimae')
#mdb.models['Model-1'].materials['Intimae'].Hyperelastic(anisotropicType=
#   HOLZAPFEL, localDirections=2, materialType=ANISOTROPIC, table=((0.00764,
#   0.0, 0.9966, 524.6, 0.226), ))
mdb.models['Model-1'].Material(name='Media')
#mdb.models['Model-1'].materials['Media'].Hyperelastic(anisotropicType=
#   HOLZAPFEL, localDirections=2, materialType=ANISOTROPIC, table=((0.00764,
#   0.0, 0.9966, 524.6, 0.226), ))
```

Three material models are created

```
mdb.models['Model-1'].Material(name='Adventitia')
#mdb.models['Model-1'].materials['Adventitia'].Hyperelastic(anisotropicType=
#   HOLZAPFEL, localDirections=2, materialType=ANISOTROPIC, table=((0.00764,
#   0.0, 0.9966, 524.6, 0.226), ))
```

Material models are created

```
# Create Section
mdb.models['Model-1'].HomogeneousSolidSection(material='simpleelastic', name=
    'SimpleVessel', thickness=None)

mdb.models['Model-1'].HomogeneousSolidSection(material='Intimae', name=
    'IntimaeSec', thickness=None)
mdb.models['Model-1'].HomogeneousSolidSection(material='Media',
name='MediaSec',
    thickness=None)
mdb.models['Model-1'].HomogeneousSolidSection(material='Adventitia', name=
    'AdvenSec', thickness=None)
```

Intima, media and adventitia sections are created

Section Assignment

```
# Section Assignment
#mdb.models['Model-1'].parts['Vessel'].SectionAssignment(offset=0.0,
#    offsetField='', offsetType=MIDDLE_SURFACE, region=Region(
#    cells=mdb.models['Model-1'].parts['Vessel'].cells.getSequenceFromMask(
#    mask=('[#1 ]', ), )), sectionName='Vessel', thicknessAssignment=
#    FROM_SECTION)
mdb.models['Model-1'].parts['Vessel'].SectionAssignment(offset=0.0,
    offsetField='', offsetType=MIDDLE_SURFACE, region=Region(
    cells=mdb.models['Model-1'].parts['Vessel'].cells.getSequenceFromMask(
    mask=('[#2 ]', ), )), sectionName='IntimaeSec', thicknessAssignment=
    FROM_SECTION)
mdb.models['Model-1'].parts['Vessel'].SectionAssignment(offset=0.0,
    offsetField='', offsetType=MIDDLE_SURFACE, region=Region(
    cells=mdb.models['Model-1'].parts['Vessel'].cells.getSequenceFromMask(
    mask=('[#1 ]', ), )), sectionName='MediaSec', thicknessAssignment=
    FROM_SECTION)
mdb.models['Model-1'].parts['Vessel'].SectionAssignment(offset=0.0,
    offsetField='', offsetType=MIDDLE_SURFACE, region=Region(
    cells=mdb.models['Model-1'].parts['Vessel'].cells.getSequenceFromMask(
    mask=('[#4 ]', ), )), sectionName='AdvenSec', thicknessAssignment=
    FROM_SECTION)
```

Sections are assigned

Sections are assigned

```
#Creat Assembly
mdb.models['Model-1'].rootAssembly.DatumCsysByDefault(CARTESIAN)
#Import Instance
mdb.models['Model-1'].rootAssembly.Instance(dependent=OFF, name='Vessel-1',
    part=mdb.models['Model-1'].parts['Vessel'])
# Move Instance
mdb.models['Model-1'].rootAssembly.translate(instanceList=('Vessel-1', ), vector=
    (0.0, 0.0, -Vl/2.0))
```

Instance is created

```
# Seed Instance
mdb.models['Model-1'].rootAssembly.seedPartInstance(deviationFactor=0.1,
    regions=(mdb.models['Model-1'].rootAssembly.instances['Vessel-1'], ), size=
    0.7)
#Change Element Type and Mesh
mdb.models['Model-1'].rootAssembly.setElementType(elemTypes=(ElemType(
    elemCode=C3D20H, elemLibrary=STANDARD), ElemType(elemCode=C3D15,
    elemLibrary=STANDARD),                         ElemType(elemCode=C3D10,
elemLibrary=STANDARD)),
    regions=(
    mdb.models['Model-1'].rootAssembly.instances['Vessel-
1'].cells.getSequenceFromMask(
    ('[#7 ]', ), ), ), ))
mdb.models['Model-1'].rootAssembly.generateMesh(regions=(
    mdb.models['Model-1'].rootAssembly.instances['Vessel-1'], ))
# Apply boundary conditions (symmeteryish)
mdb.models['Model-1'].XsymmBC(createStepName='Initial', name='Xhold', region=
    Region(
    faces=mdb.models['Model-1'].rootAssembly.instances['Vessel-
1'].faces.getSequenceFromMask(
    mask=('[#2048 ]', ), ),
    edges=mdb.models['Model-1'].rootAssembly.instances['Vessel-
1'].edges.getSequenceFromMask(
    mask=('[#800 ]', ), )))
mdb.models['Model-1'].YsymmBC(createStepName='Initial', name='Yhold', region=
    Region(
    faces=mdb.models['Model-1'].rootAssembly.instances['Vessel-
1'].faces.getSequenceFromMask(
    mask=('[#884 ]', ), )))
# Apply Z constraint... avoid rigid motion
mdb.models['Model-1'].ZsymmBC(createStepName='Initial', name='HoldVesselZ',
    region=Region(
    faces=mdb.models['Model-1'].rootAssembly.instances['Vessel-
1'].faces.getSequenceFromMask(
    mask=('[#20 ]', ), )))
# Create Vessel Contact Surface
mdb.models['Model-1'].parts['Vessel'].Surface(name='VesselSurf', side1Faces=
    mdb.models['Model-1'].parts['Vessel'].faces.getSequenceFromMask((
    '[#1000 ]', ), ))
```

Appendix 6.5 - Rigid and linear elastic vessel

```
#Create vessel
mdb.models['Model-1'].ConstrainedSketch(name='__profile__', sheetSize=200.0)
mdb.models['Model-1'].sketches['__profile__'].ArcByCenterEnds(center=(0.0, 0.0)
    , direction=CLOCKWISE, point1=(0.0, Vir), point2=(Vir, 0.0))
mdb.models['Model-1'].sketches['__profile__'].ArcByCenterEnds(center=(0.0, 0.0)
    , direction=CLOCKWISE, point1=(0.0, Vor), point2=(Vor, 0.0))
mdb.models['Model-1'].sketches['__profile__'].Line(point1=(0.0, Vor), point2=(
    0.0, Vir))
mdb.models['Model-1'].sketches['__profile__'].Line(point1=(Vor, 0.0), point2=(
    Vir, 0.0))
mdb.models['Model-1'].Part(dimensionality=THREE_D, name='Vessel', type=
    DEFORMABLE_BODY)
mdb.models['Model-1'].parts['Vessel'].BaseSolidExtrude(depth=Vl, sketch=
    mdb.models['Model-1'].sketches['__profile__'])
del mdb.models['Model-1'].sketches['__profile__']
```

Vessel sketch is made

```
#create material
mdb.models['Model-1'].Material(name='simpleelastic')
mdb.models['Model-1'].materials['simpleelastic'].Elastic(table=((100000.0,
    0.3), ))
```

Material is created

```
# Create Section
mdb.models['Model-1'].HomogeneousSolidSection(material='simpleelastic', name=
    'Vessel', thickness=None)

# Section Assignment
mdb.models['Model-1'].parts['Vessel'].SectionAssignment(offset=0.0,
    offsetField='', offsetType=MIDDLE_SURFACE, region=Region(
    cells=mdb.models['Model-1'].parts['Vessel'].cells.getSequenceFromMask(
    mask=('[#1 ]', ), )), sectionName='Vessel', thicknessAssignment=
    FROM_SECTION)
```

Section is created and assigned

```
#Creat Assembly
mdb.models['Model-1'].rootAssembly.DatumCsysByDefault(CARTESIAN)
#Import Instance
mdb.models['Model-1'].rootAssembly.Instance(dependent=OFF, name='Vessel-1',
    part=mdb.models['Model-1'].parts['Vessel'])
# Move Instance
mdb.models['Model-1'].rootAssembly.translate(instanceList=('Vessel-1', ), vector=
    (0.0, 0.0, -Vl/2.0))
```

```
# Seed Instance
mdb.models['Model-1'].rootAssembly.seedPartInstance(deviationFactor=0.1,
    regions=(mdb.models['Model-1'].rootAssembly.instances['Vessel-1'], ), size=
    0.8)
#Change Element Type and Mesh
mdb.models['Model-1'].rootAssembly.setElementType(elemTypes=(ElemType(
    elemCode=C3D8R, elemLibrary=STANDARD, secondOrderAccuracy=OFF,
    kinematicSplit=AVERAGE_STRAIN, hourglassControl=DEFAULT,
    distortionControl=DEFAULT),                         ElemType(elemCode=C3D6,
elemLibrary=STANDARD),
    ElemType(elemCode=C3D4, elemLibrary=STANDARD)), regions=(
    mdb.models['Model-1'].rootAssembly.instances['Vessel-
1'].cells.getSequenceFromMask(
    ('[#1 ]', ), ), ))
mdb.models['Model-1'].rootAssembly.generateMesh(regions=(
    mdb.models['Model-1'].rootAssembly.instances['Vessel-1'], ))
```

```
# Apply boundary conditions (symmeter)
mdb.models['Model-1'].DisplacementBC(amplitude=UNSET,
createStepName='Initial',
    distributionType=UNIFORM, fieldName='', localCsys=None, name='VesselBcY',
    region=Region(
    faces=mdb.models['Model-1'].rootAssembly.instances['Vessel-
1'].faces.getSequenceFromMask(
    mask=('[#8 ]', ), )), u1=SET, u2=UNSET, u3=UNSET, ur1=UNSET, ur2=UNSET,
    ur3=UNSET)
mdb.models['Model-1'].DisplacementBC(amplitude=UNSET,
createStepName='Initial',
    distributionType=UNIFORM, fieldName='', localCsys=None, name='VesselBcX',
    region=Region(
    faces=mdb.models['Model-1'].rootAssembly.instances['Vessel-
1'].faces.getSequenceFromMask(
    mask=('[#2 ]', ), )), u1=UNSET, u2=SET, u3=UNSET, ur1=UNSET, ur2=UNSET,
    ur3=UNSET)

# Apply Z constraint... avoid rigid motion
mdb.models['Model-1'].ZsymmBC(createStepName='Initial', name='HoldVesselZ',
    region=Region(
    faces=mdb.models['Model-1'].rootAssembly.instances['Vessel-
1'].faces.getSequenceFromMask(
    mask=('[#20 ]', ), )))

# Create Vessel Contact Surface
mdb.models['Model-1'].parts['Vessel'].Surface(name='VesselSurf', side1Faces=
    mdb.models['Model-1'].parts['Vessel'].faces.getSequenceFromMask(('[#4 ]',
    ), ))
```

Boundary conditions are applied

Surfaces are created

Appendix 6.6 - Proximal ring boundary condition set

```
#select facenodes top end and create the region
facenodes1=mdb.models['Model-1'].rootAssembly.instances['Wire-
1'].faces[11].getNodes()
facenodes2=mdb.models['Model-1'].rootAssembly.instances['Wire-
1'].faces[3].getNodes()
```

Node positions are retrieved

```
facenodes3=mdb.models['Model-1'].rootAssembly.instances['Wire-
1'].faces[14].getNodes()
facenodes4=mdb.models['Model-1'].rootAssembly.instances['Wire-
1'].faces[7].getNodes()
facenodes=facenodes1+facenodes2+facenodes3+facenodes4

#create step
mdb.models['Model-1'].StaticStep(name='Step1applylinebc', previous='Initial')
mdb.models['Model-1'].steps['Step1applylinebc'].setValues(nlgeom=ON)
mdb.models['Model-1'].steps['Step1applylinebc'].setValues(initialInc=0.05,
    maxInc=0.05)
```

```
#set constants
c=0
Xpositionlist=[]
Nlenght=len(facenodes)
```

```
#pin base
#mdb.models['Model-1'].DisplacementBC(amplitude=UNSET,
createStepName='Initial',
    #distributionType=UNIFORM, fieldName='', localCsys=None, name='pinbase',
    #region=Region(
    #faces=mdb.models['Model-1'].rootAssembly.instances['Wire-
1'].faces.getSequenceFromMask(
    #mask=('[#8460 ]', ), )), u1=SET, u2=SET, u3=SET, ur1=UNSET, ur2=UNSET, ur3=
    #UNSET)
```

```
#Cycle over nodes
rotate=-math.atan(1)
c=0
for i in range(0,Nlenght):
    c+=1
    b=i
    x=b+1
    node=facenodes[(b):(x)]
    print node[0]
    region = regionToolset.Region(nodes=node)
    nodecountstr=str(c)
    nodelabel="node"+nodecountstr

    BCx= -facenodes[i].coordinates[0]

    mdb.models['Model-1'].DisplacementBC(amplitude=UNSET, createStepName=
        'Step1applylinebc', distributionType=UNIFORM, fieldName='', fixed=OFF,
        localCsys=None,    name=nodelabel,    region=region,    u1=BCx,    u2=UNSET,
u3=UNSET, ur1=UNSET, ur2=UNSET,ur3=UNSET)



#select facenodes top end and create the region

facenodes1=mdb.models['Model-1'].rootAssembly.instances['Wire-
1'].faces[15].getNodes()
facenodes2=mdb.models['Model-1'].rootAssembly.instances['Wire-
1'].faces[6].getNodes()
facenodes3=mdb.models['Model-1'].rootAssembly.instances['Wire-
1'].faces[10].getNodes()
facenodes4=mdb.models['Model-1'].rootAssembly.instances['Wire-
1'].faces[5].getNodes()
facenodes=facenodes1+facenodes2+facenodes3+facenodes4
#create step
#mdb.models['Model-1'].StaticStep(name='Step1applylinebc2',
previous='Step1applylinebc')
#set constants
c=0
Xpositionlist=[]
Nlenght=len(facenodes)
```

Boundary conditions are applied required to shape arc from straight drawn condition

Nodal positions are retrieved

```
#Cycle over nodes
c=1000
for i in range(0,Nlenght):
    c+=1
    b=i
    x=b+1
    node=facenodes[(b):(x)]
    print node[0]
    region = regionToolset.Region(nodes=node)
    nodecountstr=str(c)
    nodelabel="node"+nodecountstr

    BCy= -facenodes[i].coordinates[1]

    mdb.models['Model-1'].DisplacementBC(amplitude=UNSET, createStepName=
        'Step1applylinebc', distributionType=UNIFORM, fieldName='', fixed=OFF,
        localCsys=None,    name=nodelabel,    region=region,    u1=UNSET,    u2=BCy,
u3=UNSET, ur1=UNSET, ur2=UNSET,ur3=UNSET)
```

Appendix 6.7 - Compaction definition

```
# Select Nodes
left=Region(
    vertices=mdb.models['Model-1'].rootAssembly.instances['Wire-
1'].vertices.getSequenceFromMask(
    mask=('[#2 ]', ), ))
right=Region(
    vertices=mdb.models['Model-1'].rootAssembly.instances['Wire-
1'].vertices.getSequenceFromMask(
    mask=('[#1 ]', ), ))
```

```
# Define step
mdb.models['Model-1'].StaticStep(name='Compaction', previous=
    'Step1applylinebc')

mdb.models['Model-1'].steps['Compaction'].setValues(initialInc=0.05, maxInc=
    0.05)
```

```
# apply bc's
mdb.models['Model-1'].DisplacementBC(amplitude=UNSET, createStepName=
    'Compaction', distributionType=UNIFORM, fieldName='', fixed=OFF, localCsys=
    None, name='pullleft', region=left, u1=UNSET, u2=UNSET, u3=10.05, ur1=UNSET,
ur2=UNSET,
    ur3=UNSET)
mdb.models['Model-1'].DisplacementBC(amplitude=UNSET, createStepName=
    'Compaction', distributionType=UNIFORM, fieldName='', fixed=OFF, localCsys=
    None,  name='pullright',  region=right,  u1=UNSET,  u2=UNSET,  u3=-10.05,
ur1=UNSET, ur2=UNSET,
    ur3=UNSET)
# release wire in z direction (deactivate z = 0 on vertice created)
mdb.models['Model-1'].boundaryConditions['HoldWireZ'].deactivate('Compaction')
```

Appendix 6.8 - Contact definitions

```
#Release and contact
#create interaction step,release compaction
mdb.models['Model-1'].StaticStep(initialInc=0.05,     minInc=1e-06,     maxInc=0.05,
name='Release',
    previous='Compaction')
#create interaction properties
mdb.models['Model-1'].ContactProperty('VesselWireProp')
mdb.models['Model-
1'].interactionProperties['VesselWireProp'].TangentialBehavior(
    formulation=FRICTIONLESS)
mdb.models['Model-1'].interactionProperties['VesselWireProp'].NormalBehavior(
    allowSeparation=ON, clearanceAtZeroContactPressure=0.0,
    constraintEnforcementMethod=PENALTY, contactStiffness=DEFAULT,
    contactStiffnessScaleFactor=1.0, pressureOverclosure=HARD,
    stiffnessBehavior=LINEAR)
```

```
# create interaction
mdb.models['Model-1'].SurfaceToSurfaceContactStd(adjustMethod=NONE,
    clearanceRegion=None, createStepName='Release', datumAxis=None,
    initialClearance=OMIT, interactionProperty='VesselWireProp', master=
    mdb.models['Model-1'].rootAssembly.instances['Vessel-1'].surfaces['VesselSurf']
    , name='VesselWire', slave=
    mdb.models['Model-1'].rootAssembly.instances['Wire-1'].surfaces['WireSurf']
    , sliding=FINITE, thickness=ON)
# Set solver to unsymetric
mdb.models['Model-1'].steps['Release'].setValues(matrixSolver=DIRECT,
    matrixStorage=UNSYMMETRIC)
## quick fix on rigid movement
```

Contact definitions

```
#edgenodes=                    mdb.models['Model-1'].rootAssembly.instances['Wire-
1'].edges[0].getNodes()
#node=edgenodes[153:154]
#noderegion = regionToolset.Region(nodes=node)

#mdb.models['Model-1'].DisplacementBC(amplitude=UNSET, createStepName=
        #'Release', distributionType=UNIFORM, fieldName='', fixed=OFF,
        #localCsys=None,  name="PinMiddle",  region=noderegion,  u1=UNSET,
u2=UNSET, u3=0.0, ur1=UNSET, ur2=UNSET,ur3=UNSET)
```

Nodes are pinned to avoid rigid body motion

```
### Release of top node
mdb.models['Model-1'].boundaryConditions['pullright'].deactivate('Release')
mdb.models['Model-1'].boundaryConditions['pullleft'].deactivate('Release')
### Pin middle node
##z=mdb.models['Model-1'].rootAssembly.instances['Wire-1'].edges[7].getNodes()
##zz=len(z)
##k=0
##for i in range(0,zz):
##    f=z[i].coordinates[0]
##    ff=round(f,2)
##    g=z[i].coordinates[1]
##    gg=round(g,2)
##    if gg == ff:
##        label=z[i].label
##        oo=i+1
##        middlenode=z[(i):(oo)]

##myRegion = regionToolset.Region(nodes=middlenode)

##mdb.models['Model-1'].DisplacementBC(amplitude=UNSET, createStepName=
##        'Release', distributionType=UNIFORM, fieldName='', fixed=OFF,
##             localCsys=None,  name="pinmiddle",  region=myRegion,  u1=UNSET,
u2=UNSET, u3=0.0, ur1=UNSET, ur2=UNSET,ur3=UNSET)
```

Nodes for compaction are selected

Appendix 6.9 - Pin centre node of proximal ring script

```
#mdb.models['Model-1'].rootAssembly.instances['Wire-1'].edges[1].getNodes()
angle=cos(math.radians(45))
xco=angle*rr
xco=round(angle*rr,2)
```

Node is identified

```
wiren=len(mdb.models['Model-1'].rootAssembly.instances['Wire-1'].edges)
for i in range(0,wiren):
    z=mdb.models['Model-1'].rootAssembly.instances['Wire-1'].edges[i].getNodes()
    if i ==0:
        GG=z
    else:
        GG+=z

z=GG
zz=len(GG)
k=0

for i in range(0,zz):
    f=z[i].coordinates[0]
    ff=round(f,2)
    g=z[i].coordinates[1]
    gg=round(g,2)
    m=g=z[i].coordinates[2]
    mm=round(m,1)
    if mm == 0.0:
        if gg==xco:
            if gg == ff:
                label=z[i].label
                oo=i+1
                middlenode=z[(i):(oo)]
                iii=ff
                ii=f
```

```
myRegion = regionToolset.Region(nodes=middlenode)

mdb.models['Model-1'].DisplacementBC(amplitude=UNSET, createStepName=
    'Release', distributionType=UNIFORM, fieldName='', fixed=OFF,
    localCsys=None, name="pinmiddle", region=myRegion, u1=UNSET, u2=UNSET,
u3=0.0, ur1=UNSET, ur2=UNSET,ur3=UNSET)
```

Appendix 6.10 - Element stress/strain history

Element history (provides stress output for all nodes within an element for the entire simulation)

```
from odbAccess import *
import math
bob=openOdb(path='C:/Users/lau06178/Desktop/Comparison Solid run
10/10solidcomparison6.odb')
mdb = openMdb('C:\\Users\\lau06178\\Desktop\\Comparison Solid run
10\\10solidcomparison6.cae')
```

```
##### select step to analyse
step=bob.steps[bob.steps.keys()[-3]]
frame=step.frames[-1]
outputs=frame.fieldOutputs
stress=outputs['S']
wireelements= stress.baseElementTypes[0]
Mises=[]
Mises1=[]
Elementlabel=[]
Misesi=0;
Misesi2=0;
Elementlabeli=1
ElementType=str
ET=1
# i lenght
ilen=len(stress.values)

for i in range (0,ilen):
    Elementlabeli = stress.values[i].elementLabel
    EType = stress.values[i].baseElementType
    if EType == 'C3D20R':
        if Elementlabeli == ET:
            Misesi=stress.values[i].mises
            if Misesi >= Misesi2:
                Misesi2=Misesi
                label=stress.values[i].elementLabel

        else:
            ET = Elementlabeli
            Mises.append(Misesi2)
```

```
        Elementlabel.append(label)
        Misesi2=0
 #find Element Locations
nlen=len(Mises)
Welements=mdb.models['Model-1'].rootAssembly.instances['Wire-1'].elements
Enodes=mdb.models['Model-1'].rootAssembly.instances['Wire-
1'].elements[1].connectivity
Enodelen=len(mdb.models['Model-1'].rootAssembly.instances['Wire-
1'].elements[1].connectivity)
w=0
c=0
i=0
x=[]
y=[]
z=[]
sumx=0
sumy=0
sumz=0
avrgx=0
avrgy=0
avrgz=0
nodes=[]

for i in range(0,nlen):
   for w in range (0,Enodelen):
     nodes.append(mdb.models['Model-1'].rootAssembly.instances['Wire-
1'].elements[Elementlabel[i]].connectivity[w])
   for c in range (0,Enodelen):
     sumx=sumx+mdb.models['Model-1'].rootAssembly.instances['Wire-
1'].nodes[nodes[c]].coordinates[0]
     sumy=sumy+mdb.models['Model-1'].rootAssembly.instances['Wire-
1'].nodes[nodes[c]].coordinates[1]
     sumz=sumz+mdb.models['Model-1'].rootAssembly.instances['Wire-
1'].nodes[nodes[c]].coordinates[2]
   avrgx=sumx/Enodelen
   avrgy=sumy/Enodelen
   avrgz=sumz/Enodelen
   x.append(avrgx)
   y.append(avrgy)
   z.append(avrgz)
   sumx=0
```

ODB is queried

Stress are obtained per time increment per load step

```python
        sumy=0
        sumz=0
        avrgx=0
        avrgy=0
        avrgz=0
        nodes=[]
        w=0
        c=0
### Convert locations to get the a horizontal profile of the beam.
xhor=[]
yhor=[]
Miseshor=[]
Elementlabelhor=[]
for i in range (0,nlen):
    alpha=atan(y[i]/x[i])
    beta=alpha+math.pi/4
    r=math.sqrt(math.pow(x[i],2)+math.pow(y[i],2))
    conx=r*cos(beta)
    cony=r*sin(beta)
    xhor.append(conx)
    yhor.append(cony)

### select highest value along the x direction to form profile.
Misesi2=0
Miseshor=[]
Elementlabelhor=[]
xhorprofile=0
xhorlist=[]
labelcheck=110000000
c=0
w=0
i=0
for i in range (0,500):
    for w in range (0,nlen):
        if (-14.4+c) < xhor[w] < (-14.3+c):
            if Mises[w] >= Misesi2:
                Misesi2=Mises[w]
                label=Elementlabel[w]
                xhorprofile=xhor[w]
    if not label == labelcheck:
```

```
        Miseshor.append(Misesi2)
        Elementlabelhor.append(label)
        xhorlist.append(xhorprofile)
        Misesi2=0
        labelcheck = label

    c+=.1

#if (0-l/2+l*(i/100.00)) < x[w] < 0-l/2+l*((i+1)/100.00):

#store xhor
xlist=[]
xlists=()
b=0
i=len(xhorlist)
for b in range (0,i):
    xlist.append(str(xhorlist[b])+"\n")

xlists=xlist

text_file=open("XhorlistMvz.txt","w")
text_file.write("who is your daddy\n")
text_file.writelines(xlists)
text_file.close()

#Store Mises
ylist=[]
ylists=()
b=0
for b in range (0,i):
    ylist.append(str(Miseshor[b])+"\n")
ylists=ylist
text_file=open("Miseshor.txt","w")
text_file.write("who is your daddy\n")
text_file.writelines(ylists)
text_file.close()
```

245

```
#Store z
zlist=[]
zlists=()
b=0
for b in range (0,i):
    zlist.append(str(Elementlabelhor[b])+"\n")

zlists=zlist

text_file=open("labelhor.txt","w")
text_file.write("who is your daddy\n")
text_file.writelines(zlists)
text_file.close()
#The.end
```

lists are saved to an output file